U.PORTO
FEUP FACULDADE DE ENGENHARIA
UNIVERSIDADE DO PORTO

Giga-cycle Fatigue Behaviour of the Structural Steel S690

Michael Ascenção Gouveia

Dissertation submitted to
Faculdade de Engenharia da Universidade do Porto
for the degree of:

Master in Mechanical Engineering

Advisor:
Professor Abílio de Jesus
(University of Porto)

Co-Advisors:
PhD. Filipe Silva
(INEGI)
MSc. Rita Dantas
(University of Porto)

Departamento de Engenharia Mecânica
Faculdade de Engenharia da Universidade do Porto

Porto, July 2022

The work presented in this dissertation was performed at the
Department of Mechanical Engineering
Faculty of Engineering
University of Porto
Porto, Portugal.

Michael Ascenção Gouveia
E-mail: up201706647@edu.fe.up.pt

Faculdade de Engenharia da Universidade do Porto
Departamento de Engenharia Mecânica
Rua Dr. Roberto Frias s/n,
4200-465 Porto
Portugal

Abstract

Nowadays, the need of very high cycle fatigue data is crucial since materials are increasingly being submitted to a high number of cycles during their lifetime. For example, steel tubular towers of a wind turbine could reach 2E6 cycles in 46 days of operation. The structural steels are of great interest due to their high tensile strength and excellent weldability, as is the case of the S690 steel.

The objective of this master's dissertation was to characterize the S690 steel in HCF and VHCF regimes. For that it was necessary to design smooth and notched specimens to test the material at 20 kHz with the piezoelectric ultrasonic testing system. The design was based on previous studies together with the machine's manufacturer indications. The smooth/hourglass S690 specimens' dimensioning was carried out either analytically and by finite elements methods. The last revealed to be more accurate in terms of resonance frequency. This is because the reduction of a two-dimensional problem to an unidimensional does not fully represent the reality.

The finite element method also proved to be the only good approach to estimate the frequency and nominal stress on notched specimens. However, it was developed an analytical formulation that cannot predict the stress state correctly, but can be used as a first iteration.

The surface quality and the fatigue crack's direction was qualitatively analysed under the magnifying eye. Resorting to scanning electron microscope, the fracture surfaces were also observed and revealed beach marks cause by the pulses post-test on the specimen. Only one specimen failed due to an internal inclusion, characteristic failure for very high cycle fatigue in high strength steels.

Strain gauges were employed to validate the theoretical stress displayed by the ultrasonic machine software. On smooth specimens, the stress was determined with minimum error. On the notched specimens, this task proved to be more laborious and with higher absolute error.

The fatigue limit at 20 kHz proved to be higher at 1E9 (500 MPa) than the 420 MPa verified at 150 Hz at 1E7. This confirmed the presence of a frequency and/or size effect for the S690 structural steel. The poor surface quality of the first batch of smooth specimens revealed to influence the fatigue life of the test piece. The fatigue limit determined for the notched specimens at 20 kHz was 440 MPa.

Keywords: fatigue, fracture, S690 steel, uniaxial, gigacycle, ultra high cycle fatigue, very high cycle fatigue, ultrasonic fatigue testing, 20 kHz, 150 Hz, notched specimens, stress concentration factor

Resumo

Actualmente, a necessidade de dados sobre fadiga de longa duração é crucial, uma vez que os materiais cada vez mais são submetidos a um elevado número de ciclos durante a sua vida útil. Por exemplo, as torres tubulares de aço de uma turbina eólica podem atingir 2E6 ciclos em 46 dias de funcionamento. Os aços estruturais são de grande interesse devido à sua elevada resistência à tracção e excelente soldabilidade, como é o caso do aço S690.

O objectivo desta dissertação de mestrado foi caracterizar o aço S690 nos regimes HCF e VHCF. Para isso, foi necessário conceber provetes lisos e entalhados (*notched*) para testar o material a 20 kHz com o sistema piezoelétrico de teste ultrassónico. O dimensionamento foi baseado em estudos anteriores juntamente com as indicações do fabricante da máquina. Para os provetes liso/ampulheta foi realizado o dimensionamento quer analiticamente quer pelo método de elementos finitos. O último revelou ser mais preciso em termos de frequência de ressonância. Isto porque a redução de um problema bidimensional a unidimensional representa uma simplificação da realidade.

O método de elementos finitos também provou ser a única abordagem admissível para estimar a frequência e a tensão nominal em provetes entalhados (*notched*). No entanto, foi desenvolvida uma formulação analítica que não pode prever correctamente o estado de tensão, mas pode ser utilizada como uma primeira iteração.

A qualidade da superfície e a direcção da fenda de fadiga foi analisada qualitativamente sob a lupa. Recorrendo ao microscópio eletrónico de varrimento, as superfícies de fractura também foram observadas e revelaram linhas de paragem causadas pelos pulsos pós-ensaio no provete. Apenas um provete falhou devido a uma inclusão interna, falha característica para ensaios de muito alto número de ciclos em aços de maior resistência.

Foram utilizados extensómetros para validar a tensão exibido pelo software da máquina ultrassónica. Em amostras lisas, a tensão foi determinada com um erro mínimo. Nas amostras entalhadas, esta tarefa revelou-se mais trabalhosa e com maior erro absoluto.

O limite de fadiga a 20 kHz provou ser mais elevado a 1E9 (500 MPa) do que os 440 MPa verificados a 150 Hz a 1E7. Isto confirmou a presença de um efeito de frequência e/ou tamanho no aço estrutural S690. A má qualidade superficial do primeiro lote dos corpos de prova lisos revelou influenciar a vida à fadiga do mesmo. O limite de fadiga obtido experimentalmente para os provetes com entalhe a 20 kHz foi 440 MPa.

Palavras-chave: fadiga, fratura, aço S690, uniaxial, gigacycle, fadiga de ciclos ultra elevados, fadiga de ciclos muito elevados, teste de fadiga ultra-sónico, 20 kHz, 150 Hz, provetes entalhados, factor de concentração de tensão

To my family.

"Eu não tenho ídolos. Tenho admiração por trabalho, dedicação e competência."

Ayrton Senna

Acknowledgements

First of all, I would like to express my deep gratitude to my mother who was always there to support me during my academic path.

I am also extremely thankful to the team I joined during this semester. To Professor Abílio de Jesus, who made this job possible, for selecting me for this project and providing support weekly. To PhD. Filipe Silva, my co-orientator for his daily collaboration and his good mood. To Engineer (MSc.) Rita Dantas, with whom I collaborated more permanently and was essential to clarify my doubts.

The contributions from MSc. Felipe Fiorentin to this project were also indispensables regarding the signal modelling. Furthermore, Mrs. Armanda was always helpful in the Metallurgy Laboratory helping to analyse the specimens under the magnifying glass. I am also grateful for the explanations given by Engineer (MSc.) Afonso Gregório, responsible for the workshop where the specimens for the Shimadzu machine were made.

I would like to express my acknowledgements to FCT - Foundation for Science and Technology which supported this work through the project PTDC/EME-EME/7678/2020, Giga-Cycle Fatigue Behaviour of Engineering Metallic Alloys. Besides, I would like to acknowledge INEGI – Institute of Science and Innovation in Mechanical and Industrial Engineering for providing the laboratory facilities, i.e. the Mechanical Testing Laboratory, where the experimental work of this master thesis was developed.

Additionally, I would also like to extend my gratitude to the project *AARM 4.0 - Aços de Alta Resistência na Metalomecânica 4.0*, with the reference POCI-01-0247-FEDER-068492, co-financed by the European Regional Development Fund (ERDF), through the Operational Programme for Competitiveness and Internationalization (COMPETE 2020), under the PORTUGAL 2020 Partnership Agreement.

This MSc. project (reference SFRH/BD/151377/2021) is co-financed by the Social European Fund – through the Northern Regional Operational Program (NORTE 2020), the Regional Operational Program of the Center (Centro 2020) and the Regional Operational Program of Alentejo (Alentejo 2020)- and by the Portuguese Foundation for Science and Technology – FCT under MIT Portugal.

FCT Fundação para a Ciência e a Tecnologia
MINISTÉRIO DA CIÊNCIA, TECNOLOGIA E ENSINO SUPERIOR

inegi INSTITUTO DE CIÊNCIA E INOVAÇÃO EM ENGENHARIA MECÂNICA E ENGENHARIA INDUSTRIAL

MIT Portugal

Cofinanciado por:

COMPETE 2020
PROGRAMA OPERACIONAL COMPETITIVIDADE E INTERNACIONALIZAÇÃO

PORTUGAL 2020

UNIÃO EUROPEIA
Fundo Europeu
de Desenvolvimento Regional

Contents

Abstract i

Resumo iii

Acknowledgements ix

List of Figures xv

List of Tables xxv

Nomenclature xxvii

1 Introduction 1
- 1.1 Motivation . . . 1
- 1.2 Objectives . . . 2
- 1.3 Host institution . . . 2
- 1.4 Content of the Dissertation . . . 3

2 State of the Art 5
- 2.1 Fundamentals of Fatigue . . . 5
  - 2.1.1 Mean S-N curve determination . . . 7
  - 2.1.2 Statistical analysis of the fatigue data . . . 8
- 2.2 Very high cycle fatigue: an overview . . . 9
- 2.3 Ultrasonic testing . . . 14
  - 2.3.1 Historical advancements in gigacycle machines . . . 25
- 2.4 Working principle of the VHCF machine . . . 26
- 2.5 Working principle of HCF resonance machine . . . 30
- 2.6 Effect of a stress concentration factor (notch) . . . 30
  - 2.6.1 Concentration factor definition (K_t) . . . 34
- 2.7 Variable amplitude loading . . . 37
- 2.8 The S690QL Steel . . . 39
  - 2.8.1 High Strength Steels . . . 41
  - 2.8.2 Mean curve estimation in function of the material properties . . . 42

3 Specimen design for gigacycle fatigue testing 45
- 3.1 Mechanical wave transmission model . . . 45
  - 3.1.1 Longitudinal elastic waves and resonance frequency . . . 45
  - 3.1.2 Analytical solution for the variable section smooth specimen . . . 48
  - 3.1.3 Analytical solution for the variable section for notched specimen . . . 53
  - 3.1.4 Shimadzu notch definition . . . 60
- 3.2 Steps for the finite element analysis . . . 62

3.3 Frequency estimation . . . 64
3.3.1 Frequency adjustment of the notched specimens . . . 66
3.4 Stress and displacement results along the machine's axis . . . 67
3.4.1 Machine and smooth specimen simulation . . . 68
3.4.2 Machine and notched specimen simulation . . . 69
3.4.3 FEM stress for the specimen's transverse section . . . 72

4 Experimental Programme 79
4.1 S690QL Steel Composition and Properties . . . 79
4.2 Young Modulus determination by dynamic and non-destructive methods . . . 81
4.3 Design of smooth specimens for testing at subsonic frequency (150 Hz) . . . 85
4.4 Specimens manufacturing . . . 86
4.4.1 Smooth specimens (20 kHz) . . . 91
4.4.2 Smooth specimens (150 Hz) . . . 95
4.4.3 Surface roughness smooth specimens comparison for 20 kHz and 150 Hz . . . 96
4.4.4 Notched specimens (20 kHz) . . . 99
4.5 Experimental apparatus for 20 kHz tests . . . 101
4.5.1 Sequence to execute a UHCF test in the Shimadzu USF-2000 . . . 103
4.6 Experimental apparatus for 150 Hz tests . . . 108
4.7 Stress validation for 20 kHz tests . . . 110
4.7.1 Strain gauge preparation . . . 110
4.7.2 Measurement results with strain gauges on smooth specimens (20 kHz) . . . 112
4.7.3 Measurement results with strain gauges on notched specimens (20 kHz) . . . 113

5 Results and discussion 121
5.1 Fatigue S-N curve - Frequency effect on S690 steel . . . 121
5.2 Fatigue S-N curve - Notch effect on S690 steel at 20 kHz . . . 126
5.3 Mean curve estimation . . . 128
5.4 Surface crack analysis . . . 129
5.4.1 Smooth specimens tested at 20 kHz fatigue surface crack analysis . . . 129
5.4.2 Notched specimens (20 kHz) fatigue surface crack . . . 131
5.4.3 Smooth specimens (150 Hz) fatigue surface crack . . . 132
5.5 Fracture surfaces . . . 132
5.5.1 Smooth specimens (20 kHz) fatigue fracture surfaces . . . 133
5.5.2 Notched specimens (20 kHz) fatigue fracture surfaces . . . 139
5.5.3 Smooth specimens (150 Hz) fatigue fracture surfaces . . . 143

6 Conclusion 149
6.1 Conclusions . . . 149
6.2 Future Work . . . 150

References 151

A Technical drawings 161

B FEM results for the notched specimens (20 kHz) 167

C FEM results comparison with the analytical solution (20 kHz) 169

D FEM cross section stress results **171**

E Smooth/hourglass specimens (20 kHz) data **173**

F Smooth specimens (150 Hz) data **177**

G Notched specimens (20 kHz) data **181**

H Fatigue limit estimation **183**

List of Figures

Figure 2.1.1 Terminology for alternating stress (adapted from Bannantine et al. (2022)) . . . 6
Figure 2.2.1 S–N curves that typify fatigue test results when testing medium-strength steels, categorizing the cycles to failure (adapted from Bathias and Paris (2004)) . . . 9
Figure 2.2.2 Typical fatigue test results for high strength steel (Furuya et al., 2019) . . . 11
Figure 2.2.3 Two-fold S-N curve concept (Furuya et al., 2019) . . . 11
Figure 2.2.4 Two-fold S-N curve concept (Zimmermann, 2018) . . . 12
Figure 2.2.5 10^9 cycles fatigue strength of japanese steels (Furuya et al., 2019) . 12
Figure 2.2.6 Typical propagation of a fatigue crack (Campbell, 2008) . . . 13
Figure 2.3.1 Load sequence of the UHCF (adapted from Stanzl-Tschegg et al. (2002)) . . . 16
Figure 2.3.2 Bending fatigue of the bar grades a) 38MSiVS5, b) 50CrV4 (Bergström et al., 2018) . . . 17
Figure 2.3.3 Gigacycle S-N curve the martensitic bearing steel 100Cr6 at different frequency and $R = -1$ (Bathias, 2012) . . . 18
Figure 2.3.4 S–N data for annealed and 10% pre-strained specimens (Tsutsumi et al., 2009) . . . 18
Figure 2.3.5 S–N diagram for low-temperature-tempered JIS SNCM439 steel. Arrow-marked plots show unbroken results (Furuya et al., 2002) . 19
Figure 2.3.6 S-N diagram of JIS S15C steel, $R_m = 441$ MPa, under several loading frequencies in tension compression with $R = -1$ (specimens with diameter of 5mm) (Palin-Luc and Jeddi, 2018) . . . 20
Figure 2.3.7 Fatigue test results for smooth specimens of 15C-P (Torizuka et al., 2012) . . . 20
Figure 2.3.8 Schematic illustration of the likely principle governing the fracture type change during ultrasonic fatigue tests on the smooth specimens (Torizuka et al., 2012) . . . 21
Figure 2.3.9 The concept of a twofold S–N curve (Nishijima and Kanazawa, 1999) 21
Figure 2.3.10 Crack growth diagram with the three fracture modes (adapted from (Abou Jaoude, 2015; Krasovskyy and Virta, 2014; Paris and Erdogan, 1963)) . . . 23
Figure 2.3.11 Typical biaxial cruciform specimens with: (a) slits; (b) elliptical notched corners; (c) circular-notched corners and reduced thickness at the centre (Rodrigues da Costa et al., 2020) . . . 24
Figure 2.3.12 UFT tension/torsion stress life results (Rodrigues da Costa et al., 2020) . . . 24

Figure 2.4.1 Ultrasonic fatigue machine model with smooth specimen. Displacement and stress representation. 1 - Piezoelectric transducer; 2 - Booster; 3 - High-gain Horn/Sonotrode; 4- Specimen (adapted from Dimitrov and Argirov (2014)) 28
Figure 2.6.1 Geometrical interpretation of stress distributions under uniaxial loadings on axisymmetric notched body with K_t=1.25 (adapted from Liao et al. (2020)) 31
Figure 2.6.2 S-N diagram for quenched and tempered steel 42CrMoS$_4$, $R = -1$, $f = 50$ Hz (Berger et al., 2008) 32
Figure 2.6.3 S–N curve of 40Cr material with smooth and notched specimens (Qian et al., 2010) 33
Figure 2.6.4 Fatigue strength reduction by notches (Akiniwa et al., 2006) 34
Figure 2.6.5 $S - N$ diagrams of plane and notched YXR3 steel (Ebara, 2017) . 34
Figure 2.6.6 S-N curves for $K_t = 1.09$ ($R = -1$ and 0.5), $K_t = 1.31$ and $K_t = 2.42$ ($R = -1$) of the martensitic steel X10CrNiMoV12-2-2 (Ritz and Beck, 2017) 35
Figure 2.6.7 S–N curves of smooth, notched and drill-holed specimens of SUJ2 (Akiniwa et al., 2006) 36
Figure 2.6.8 Gigacyle fatigue S-N curve of 100Cr6 with and without notch $R = -1$ (Bathias, 2012) 37
Figure 2.7.1 Schematic representation of two-level block loading: a) high-low; b) low- high; c) and d) Step in stress ratio (Ribeiro et al., 2011) . . 39
Figure 2.8.1 Stress–strain curves at various temperatures from steady state test (Qiang et al., 2012a) 41
Figure 2.8.2 Representation of elastic, plastic and total strain resistance to fatigue loading (Cui et al., 2014) 43

Figure 3.1.1 Displacement and strain variation along an elastic bar (Bathias and Paris, 2004) 46
Figure 3.1.2 Ultrasonic specimen geometry (adapted from Bathias and Paris (2004)) 49
Figure 3.1.3 Graphic of a line through the unit hyperbola at the point $(\cosh(a), \sinh(a))$, where a is twice the area between line ray, the hyperbola, and the x-axis 50
Figure 3.1.4 Geometrical variables of the notched specimen 54
Figure 3.1.5 Comparison between the real shape and the catenary approximation 55
Figure 3.1.6 Comparison between the real shape and the Shimadzu catenary approximation 60
Figure 3.2.1 Sketches: a) Booster, b) Horn 63
Figure 3.2.2 Assembly for the notched specimen on Abaqus 64
Figure 3.3.1 Simulation result for the notched specimen with $K_t = 1.25$. a) Axial displacement (μm). b) Axial stress (MPa). 65
Figure 3.3.2 Length adjustment plot 67
Figure 3.4.1 Axial stress obtained from simulation of the smooth specimen ($A_0 = 30$ μm) 68
Figure 3.4.2 Axial displacement obtained from the simulation of the smooth specimen ($A_0 = 30$ μm) 68
Figure 3.4.3 Axial stress for half of the smooth specimen by FEM and analytical solution ($A_0 = 30$ μm) 69

Figure 3.4.4 Axial stress obtained from simulation of the notched specimen with $K_t = 1.25$ ($A_0 = 30$ μm) 70
Figure 3.4.5 Axial displacement obtained from the simulation of the notched specimen with $K_t = 1.25$ ($A_0 = 30$ μm) 70
Figure 3.4.6 Axial stress for half the notched specimen with $K_t = 1.25$ by FEM and analytical solution for the real $L_1 = 43.44$ mm and $L = 48.58$ mm ($A_0 = 15$ μm) 71
Figure 3.4.7 Axial stress for half the notched specimen with $K_t = 1.50$ by FEM and analytical solution for the real $L_1 = 47.14$ mm and $L = 51.1$ mm ($A_0 = 15$ μm) 71
Figure 3.4.8 FEM simulations results (axial stresses, MPa) for the smooth specimen ($A_0 = 30$ μm) 73
Figure 3.4.9 FEM simulations results (axial stresses, MPa) comparison for the notched specimens with $A_0 = 15$ μm. a) $K_t = 1.25$. b) $K_t = 1.5$. . 74
Figure 3.4.10 Transversal section of the notched specimen with $K_t = 1.25$ (radius= 2 mm) 74
Figure 3.4.11 Axial stress obtained by FEM from the specimen's centre to the external radius ($A_0 = 30$ μm) 75
Figure 3.4.12 Longitudinal stress obtained by FEM from the notched specimen's centre to the external radius for different maximum displacements 75
Figure 3.4.13 FEM simulations results comparison (axial stresses, MPa) regarding the static simulation of a displacement with $A_0 = 15$ μm. a) $K_t = 1.25$. b) $K_t = 1.5$. 77

Figure 4.1.1 Microstructure of the S690 with (a) 100 μm and (b) 20 μm scales . 80
Figure 4.2.1 S690 steel beam supported by elastic bands at the vibration nodes 81
Figure 4.2.2 First 3 mode shapes for the free-free beam with $l = 207.2$ mm beam 83
Figure 4.2.3 Bending modes on y obtained by FEM: a) Mode 1, b) Mode 2 . . 84
Figure 4.3.1 Technical drawing from ISO (2006) 86
Figure 4.4.1 a) CNC lathe DMG MORI CTX 310 ecoline. b) Detail of the tailstock inside and the tool changing mechanism 86
Figure 4.4.2 From left to right: turned S690 bar, notched and smooth specimens, S690 cylinder. 87
Figure 4.4.3 Continuous chip formed during turning 88
Figure 4.4.4 a) Specimen's thread. b) Brass tool threaded. 88
Figure 4.4.5 Final specimen aspect on the CNC and scheme of the cutting parameters 89
Figure 4.4.6 Lathe Shaublin 135 89
Figure 4.4.7 a) Smooth specimen (20 kHz) after turning on the CNC. b) Specimen after polishing on the Lathe Shaublin being parted. 90
Figure 4.4.8 Tool inserts 90
Figure 4.4.9 Smooth specimens for ultrasonic tests at 20 kHz, arrival state P3-P34 91
Figure 4.4.10 Specimen P9 pre (a) and post (b) polishing operations (×64) on the magnifying eye 92
Figure 4.4.11 Specimen P27 pre (a) and post (b) polishing operations (×64) on the magnifying eye 92
Figure 4.4.12 Surface Roughness setup for the smooth specimens 94
Figure 4.4.13 Average SR of the smooth specimens (20 kHz) before polishing: P4, P5, P7, P14 and P23. SR after polishing for P4. 95
Figure 4.4.14 Smooth specimens for resonance tests at 150 Hz, arrival state P1-P24 95

Figure 4.4.15 Smooth specimen (150 Hz) P5 pre (a) and post (b) polishing operations ×40 on the magnifying eye 96
Figure 4.4.16 SR setup for the circumferential assessment of the smooth specimen (150 Hz) 96
Figure 4.4.17 Average SR in the longitudinal direction for smooth specimens at 20 kHz and 150 Hz (3 measurements for each). 19 test pieces for 20 kHz and 11 for 150 Hz. 97
Figure 4.4.18 Average SR in the circumferential direction for smooth specimens at 20 kHz and 150 Hz (3 measurements for each). 19 test pieces for 20 kHz and 11 for 150 Hz. 97
Figure 4.4.19 SR standard deviation in the longitudinal direction of smooth specimens at 20 kHz and 150 Hz. 3 measurements were taken for each specimen. 98
Figure 4.4.20 SR standard deviation in the circumferential direction for smooth specimens at 20 kHz and 150 Hz. 3 measurements were taken for each specimen. 99
Figure 4.4.21 First notched specimen P1 ($K_t = 1.25$) before polishing operations observed at ×8 (a) and ×64 (b) magnifications 99
Figure 4.4.22 Notched specimens ($K_t = 1.25$) for ultrasonic tests at 20 kHz, arrival state P2-P7 100
Figure 4.4.23 Notched specimen P3 ($K_t = 1.25$) with the correct length before polishing, at ×10 (a) and ×64 (b) magnifications 101
Figure 4.4.24 Average SR in the circumferential direction for the smooth specimens for testing at 20 kHz and 150 Hz, along with the notched specimens for 20 kHz. 101
Figure 4.5.1 Shimadzu USF-2000 Machine with its peripheral equipments . . . 102
Figure 4.5.2 UFT Machine. Labels: 1- Current stabilizer; 2- Operation box; 3- Signal Generator; 4- DAQ box from Kistler; 5- Eddy current signal generator; 6- Piezoelectric Transducer; 7- Booster; 8- Horn; 9- Hourglass Specimen; 10- Compressed air nozzle (and valve); 11- Electromagnetic probe; 12- Pyrometers; 13- PC to monitor the temperature; 14- PC to control the test and register its values; 15- Air dryer 102
Figure 4.5.3 Accessory to calibrate the torque wrench for 25 Nm (a), tools to tighten the horn (b) and tightening direction (c). 104
Figure 4.5.4 Sequence to tighten the specimen in the machine and probe placement 104
Figure 4.5.5 Example of the data for 15 % load of the specimen P17. Displacement amplitude is 9.37 μm 105
Figure 4.5.6 Calibration curve for the specimen P21 106
Figure 4.5.7 Supersonic system settings page where the calibration is performed and the data for horn amplitude is introduced 106
Figure 4.5.8 Supersonic test conditions 107
Figure 4.5.9 Supersonic test start page 108
Figure 4.6.1 Resonance system scheme (a) and Rumul Testronic 150 kN (b) (Rumul, 2022) 109
Figure 4.6.2 Specimen assembly on the machine (a); Tools to tighten the grip and specimen to the accessory (b); running test position (c) 110

Figure 4.7.1 Strain gauge (C5K-06-S5145-350-33F) gluing (a) and the smooth specimen assembled on the machine (b) . . . 111
Figure 4.7.2 Quarter bridge-one active gauge (Thitima, 2022) . . . 111
Figure 4.7.3 Strain measured on P26 and corresponding stress . . . 113
Figure 4.7.4 Strain gauges on the notched specimen P7 . . . 114
Figure 4.7.5 Stress predicted by FEM and calculated for the gauge on the notch in function of the probe displacement for the notched specimen P2 116
Figure 4.7.6 Stress predicted by FEM and calculated for the gauge on the cylindrical region in function of the probe displacement for the notched specimen P2, for measurement 1 and 2 . . . 118

Figure 5.1.1 S-N curve of the S690 obtained for smooth specimens at 20 kHz and 150 Hz . . . 121
Figure 5.1.2 Weibull (a) and Normal (b) Probability Density Functions for the 20 kHz smooth specimens for each load . . . 124
Figure 5.1.3 Weibull (a) and Normal (b) Probability Density Functions for the smooth specimens at 150 Hz for each load . . . 125
Figure 5.2.1 S-N curve of the tests at 20 kHz for smooth and all notched (K_t = 1.25) specimens . . . 126
Figure 5.2.2 S-N curve of the tests at 20 kHz for smooth and only the notched ($K_t = 1.25$) specimens without the strain gauge . . . 127
Figure 5.2.3 K_f and q in function of the number of cycles . . . 128
Figure 5.3.1 Fatigue estimation curves in comparison with the experimental data from: USM- Universal Slopes Method, MUSM- Modified Universal Slopes Method, HM- Hardness Method, UML- Uniform Law Material, MM- Mitchell's Method, MedM- Medians Method, Manson-Coffin 2010, Manson-Coffin 2015 . . . 129
Figure 5.4.1 Crack shapes: (a) P8 (×19) ($S = 550$ MPa, $N = 4.3$E5), (b) P15 (×40) ($S = 510$ MPa, $N = 1.82$E6) and (c) P22 (×40) ($S = 520$ MPa, $N = 1.18$E7) . . . 130
Figure 5.4.2 Crack shapes for smooth specimen (20 kHz): (a) P14 (×20) before and (b) P14 (×40) after test ($S = 510$ MPa, $N = 6.44$E5) . . . 130
Figure 5.4.3 Sequence to open the specimen P4 ($S = 520$ MPa, $N = 1.34$E6) . . 131
Figure 5.4.4 Crack shapes for notched $K_t = 1.25$ specimen (20 kHz): (a) P3 ×30 ($S = 530$ MPa, $N = 8.03$E5), (b) P4 ×10 ($S = 510$ MPa, $N = 1.11$E7) and (c) P6 ×10 ($S = 490$ MPa, $N = 3.88$E6) . . . 131
Figure 5.4.5 Crack shapes for notched $K_t = 1.25$ specimen (20 kHz): P7 (a) ×10 and (b) ×30 ($S = 460$ MPa, $N = 2.24$E6) . . . 132
Figure 5.4.6 Crack shapes for smooth specimens at 150 Hz (×10): (a) P5 (S = 470 MPa, $N = 4.78$E6), (b) P9 ($S = 510$ MPa, $N = 4.54$E5) and (c) P18 ($S = 490$ MPa, $N = 1.00$E6) . . . 132
Figure 5.5.1 SEM images of P22 ($S_f = 520$ MPa, $N = 1.18$E7) with different scales. . . . 133
Figure 5.5.2 Detail of the metallic inclusion (40 μm scale) ($S_f = 520$ MPa, $N = 1.18$E7) . . . 134
Figure 5.5.3 Tridimensional images of the inclusion surface area on P22 (S_f = 520 MPa, $N = 1.18$E7) . . . 135
Figure 5.5.4 Tridimensional images of fracture surfaces on (a) P8 ($S_f = 550$ MPa, $N = 4.30$E+05) and (b) P14 ($S_f = 510$ MPa, $N = 6.44$E+05) 135

Figure 5.5.5 Topographic image acquired on P8 (S_f = 550 MPa, N = 4.30E+05) through Leica Application Suite . . . 136
Figure 5.5.6 Magnifying eye (a) and SEM (b) images of P15 smooth specimen at 20 kHz (S_f = 510 MPa, N = 1.82E6) with scale of 2 mm. 136
Figure 5.5.7 Fatigue crack average size according to the stress load for smooth specimens at 20 kHz . . . 138
Figure 5.5.8 SEM images of the smooth specimens (20 kHz) . . . 139
Figure 5.5.9 Leica DVM6 fracture surfaces of the notched specimens ×100: (a) P4 (S_f = 510 MPa, N = 1.11E7), (b) P7 (S_f = 460 MPa, N = 2.24E6) and (c) P10 (S_f = 490 MPa, N = 4.34E6) . . . 140
Figure 5.5.10 Leica DVM6 fracture surfaces of the notched specimens ×100: (a) P4 (S_f = 510 MPa, N = 1.11E7), (b) P7 (S_f = 460 MPa, N = 2.24E6) and (c) P10 (S_f = 490 MPa, N = 4.34E6) . . . 140
Figure 5.5.11 Magnifying eye (a) and SEM (b) images of P4 notched specimen at 20 kHz (S = 530 MPa, N = 8.03E5) with scale of 2 mm . . . 141
Figure 5.5.12 Fatigue crack average size according to the stress load for notched specimens at 20 kHz . . . 142
Figure 5.5.13 SEM images of the notched specimens (20 kHz) . . . 143
Figure 5.5.14 Leica DVM6 fracture surfaces of smooth specimens at 150 Hz (×68): (a) P5 (S_f = 470 MPa, N = 4.78E6), (b) P20 (S_f = 520 MPa, N = 4.52E5) and (c) P23 (S_f = 440 MPa, N = 4.99E6) . . . 144
Figure 5.5.15 Leica DVM6 fracture surface of the smooth specimen for 150 Hz (×68) (a) P20 (S_f = 470 MPa, N = 4.78E6) and (b) topographic image (of Fig. 5.5.14b) . . . 144
Figure 5.5.16 Leica DVM6 fracture surface of the smooth specimens for 150 Hz (×68): (a) P23 (S_f = 440 MPa, N = 4.99E6) and (b) topographic image (of Fig. 5.5.14c) . . . 145
Figure 5.5.17 Magnifying eye (a) and SEM (b) images of P20 smooth specimen at 150 Hz (S = 520 MPa, N = 4.52E5) with scale of 2 mm . . . 145
Figure 5.5.18 Fatigue crack average size according to the stress load for smooth specimens at 150 Hz . . . 146
Figure 5.5.19 SEM images of the smooth specimens (150 Hz) . . . 147

Figure A.0.1 Technical drawing of the smooth specimen (20 kHz) . . . 162
Figure A.0.2 Technical drawing of the notched specimen with K_t = 1.25 and the corrected dimensions for the 20 kHz . . . 163
Figure A.0.3 Technical drawing of the notched specimen with K_t = 1.50 and the corrected dimensions for 20 kHz . . . 164
Figure A.0.4 Technical drawing of the booster of the Shimadzu UHSF-2000 . . . 165
Figure A.0.5 Horn dimensions of the Shimadzu UHSF-2000 . . . 165
Figure A.0.6 Technical drawing of the S690 smooth specimen (150 Hz) . . . 166

Figure B.0.1 FEM results for the 20 kHz notched specimen with K_t=1.5 (A_0 = 30μm) . . . 167

Figure C.0.1 Stress for half the notched specimen (20 kHz) by FEM and analytical solution . . . 169

Figure E.0.1 Legend for the dimensions of Table E.0.1 . . . 173

Figure F.0.1 Legend for the dimensions of Table F.0.1 . . . 177

Figure G.0.1 Legend for the dimensions of Table G.0.1 181

List of Tables

Table 2.1.1 Loading notable conditions (Bannantine et al., 2022) 7
Table 2.3.1 Comparison between the duration of different fatigue testing methods for continuous loading (approximate values) (Rodrigues da Costa et al., 2020) 15
Table 2.3.2 Overview on important steps in developing the ultrasonic fatigue technique for endurance and fracture mechanical investigations (Stanzl-Tschegg and Mayer, 2001) 25
Table 2.8.1 Calculated M-C parameters for steel for the Median's method (Meggiolaro and Castro, 2004) 44

Table 3.1.1 Comparison between the specimen's length for different test frequencies (approximate values) (Bathias and Paris, 2004) 48
Table 3.2.1 Stress Concentration Factors (K_t) for the notched specimens 62
Table 3.2.2 Mechanical properties of the parts 63
Table 3.2.3 Mechanical properties of the parts 64
Table 3.3.1 Frequency and number of elements for each simulation 65
Table 3.3.2 Length adjustment iterations 66
Table 3.4.1 Maximum stress for $A_0 = 30$ μm on specimen's centre by FEM . . . 67
Table 3.4.2 Stress and lengths comparison for the notched specimens' analytical solution ($A_0 = 15$ μm) 72
Table 3.4.3 Relevant stress values for the transversal section of the smooth specimen ($A_0 = 30$ μm) 76
Table 3.4.4 Comparison between stress values in the cross section of the notched specimen for the maximum displacements: 15 μm, 30 μm and 50 μm 76
Table 3.4.5 Real K_t for each notch type regarding static analysis ($A_0 = 15$ μm) . 77

Table 4.1.1 Designation of S690QL (Qiang et al., 2012b; Steel, 2022) 79
Table 4.1.2 Mechanical Properties of the S690 steel 80
Table 4.1.3 Alloy Elements of the S690 steel (% weight) 80
Table 4.2.1 Solutions for Equation 4.8 82
Table 4.2.2 Vibration nodes 83
Table 4.2.3 Procedure to obtain the Young Modulus E 84
Table 4.2.4 Frequency determined by FEM vs Experimental (Iteration 1) 84
Table 4.2.5 Frequency determined by FEM vs Experimental (Iteration 2) 85
Table 4.3.1 Geometric dimensions recommended from ISO (2006) 86
Table 4.4.1 Sequence to manufacture the specimens for fatigue testing at 20 kHz 87
Table 4.4.2 Cutting parameters used in the machining operation of the specimens for the 20 kHz fatigue testing. 91
Table 4.4.3 Sandpaper grit standard in Europe (Orvis and Grissino-Mayer, 2002) 92
Table 4.4.4 Specimens dimensions and frequency comparison 93
Table 4.4.5 Smooth specimens (150 Hz) P1 to P24 dimensions 95

Table 4.4.6 Notched specimens $K_t = 1.25$ P2 to P10 average dimensions (3 measurements for each dimension) . . . 100
Table 4.4.7 SR of the notched specimens ($K_t = 1.25$) before polishing (3 measurements for each) . . . 100
Table 4.5.1 Sequence to turn on the experimental apparatus . . . 103
Table 4.5.2 Calibration data smooth specimen P21 . . . 106
Table 4.6.1 Legend Rumul system . . . 109
Table 4.7.1 Strain gauge measurements on specimen P26 . . . 112
Table 4.7.2 Calibration data for notched specimens . . . 114
Table 4.7.3 Strain gauge on the critical section results for notched specimen P2 . 114
Table 4.7.4 Results for the strain gauge in function of the probe displacement on the critical section for the notched specimen P2 . . . 115
Table 4.7.5 Strain gauge results compared with the strain of the FEM model on the critical section for notched specimen P2 . . . 115
Table 4.7.6 Cylindrical stress and strain compared with the FEM model for the specimen P2 . . . 116
Table 4.7.7 Cylindrical stress and strain compared with the FEM model for a wider range of stress levels with constant increment, for the specimen P2 . . . 117
Table 4.7.8 Determination of the cylindrical stress difference regarding the FEM stress calculated from the strain for the specimen P2 . . . 117
Table 4.7.9 Notched specimens P7 and P8 calculated stress . . . 118

Table 5.1.1 Run-outs for smooth specimens at 20 kHz (1E9) and at 150 Hz (1E7) 123
Table 5.2.1 Probability of survival curves equations for the notched specimens . 126
Table 5.2.2 K_f and q for the S690 for $K_t = 1.15$ at 2E7 . . . 128
Table 5.5.1 Inclusions size (5 measurements) and composition . . . 134
Table 5.5.2 Longitudinal and transversal length of the fracture surface for smooth specimens at 20 kHz . . . 137
Table 5.5.3 Longitudinal and transversal length of the fracture surface for notched specimens at 20 kHz . . . 141
Table 5.5.4 Longitudinal and transversal length of the fracture surface for smooth specimens at 150 Hz . . . 146

Table C.0.1 Constants and values calculated for the analytical determination of the stress in the notched specimens (20 kHz) . . . 170

Table D.0.1 Trendline power equations for the horizontal stress distribution for the 20 kHz notched specimens ($R^2 = 1$) . . . 171

Table E.0.1 Smooth/hourglass specimens (20 kHz) P3 to P34 dimensions (the average of 3 measurements for each variable) . . . 173
Table E.0.2 Smooth/hourglass specimens (20 kHz) P3 to P34 results data . . . 175
Table E.0.3 Surface roughness of the smooth/hourglass specimens (20 kHz) before polishing (3 measurements for each) . . . 175
Table E.0.4 Surface roughness of the smooth/hourglass specimens (20 kHz) after testing in both directions (3 measurements for each) . . . 176

Table F.0.1 Smooth specimens (150 kHz) P1 to P21 dimensions (the average of 3 measurements for each variable) . . . 177
Table F.0.2 Smooth specimens (150 Hz) P1 to P24 results data . . . 178

Table F.0.3 Surface roughness of the smooth specimens (150 kHz) after testing (the average of 3 measurements for each variable) 179

Table G.0.1 Notched specimens $K_t = 1.25$ (20 kHz) P2 to P10 dimensions (the average of 3 measurements for each variable) 181
Table G.0.2 Notched specimens $K_t = 1.25$ (20 kHz) P2 to P10 results 182

Table H.0.1 Constant for the estimation of the fatigue life of the material based on its mechanical properties 183

Nomenclature

Greek Symbols

α	Variable to adjust the hyperbolic cosine for the specimen
β	Variable to facilitate the integration of the displacement second order differential equation
$\Delta\sigma$	Stress range
$\Delta\sigma_i$	Stress range for block i
$\dot{\varepsilon}$	Strain rate
$\frac{\Delta\varepsilon_e}{2}$	Elastic strain amplitude
$\frac{\Delta\varepsilon_p}{2}$	Plastic strain amplitude
$\frac{\Delta\varepsilon}{2}$	Total strain amplitude
$\hat{\sigma}_x$	Standard Deviation
∇^2	Laplacian/Laplace Operator
ν	Poisson's coefficient
ω	Angular frequency
ω_n	Natural Frequency (rad*s^{-1})
ω_r	Resonance Frequency (rad*s^{-1})
ϕ	Constant parameter of the strain and stress analytical solution of the smooth specimen (20 kHz)
ψ	Constant of the Uniform Material Law
ρ	Volume mass
σ	Stress on the specimen
σ_f	Fatigue limit
σ_f'	Fatigue strength coefficient
σ_a	Stress amplitude
σ_{max}	Maximum stress

σ_{min} Minimum stress

σ_m Mean stress

$\sigma_{notched}$ Fatigue limit of the notched specimen

σ_{smooth} Fatigue limit of the smooth specimen

θ Opening angle of the notch in the notched specimens

ε Strain

ε_a Total strain amplitude

ε_f' Fatigue ductility coefficient

ξ Damping Coefficient

Acronyms

ASTM American Society for Testing and Materials

DN Displacement Nodes

FCG Fatigue Crack Growth

FGA Fine Granular Area

GBF Bright Granular Facet

GTAW Gas Tungsten Arc Welding

HCF High Cycle Fatigue

HM Hardness Method

HSLA High Strength Low Alloy

HSS High Strength Steel

LBW Laser Beam Welding

LCF Low Cycle Fatigue

M-C 1 Manson-Coffin method with Basan et al. (2011) constants

M-C 2 Manson-Coffin method with Basan et al. (2015) constants

MedM Medians Method

MM Mitchell's Method

MUSM Modified Universal Slopes Method

ODA Optically Dark Area

PZT Lead Zirconate Titanate

SN Stress Nodes

UFT Ultrasonic Fatigue Testing

UML Uniform Material Law

USM Universal Slopes Method

VHCF Very High Cycle Fatigue

Latin Symbols

ΔK Stress intensity range

ΔK_{cr} Critical stress intensity range

ΔK_{th} Fatigue crack growth threshold

ΔV_{cr} Critical speed

ΔV_{th} Threshold speed

$\frac{da}{dN}$ Fatigue crack growth rate

a Crack Length

A_0 Initial amplitude at time $t = 0$

A_r Amplitude ratio

A_{n-1}, B_{n-1} Wave constants

b Fatigue strength exponent

C Material parameter (b on y-axis) for the Paris law

c Velocity of the wave propagation

c_d Fatigue ductility exponent for the fatigue limit estimation based on monolithic parameters

D Total fatigue damage

D_1 Maximum diameter of the notched specimen

D_2 Minimum diameter of the notched specimen

E Young's Modulus

e Volume dilatation

f Frequency

f_i Fatigue damage of one block

f_n Natural Frequency (Hz)

f_r Resonance Frequency (Hz)

i Single stress block

k Wavenumber

K_t	Stress concentration factor
L	Length of half the specimen
l	Specimen's length
L_1	Length of the cilindrical part of the smooth and notched specimens
L_2	Length of half the bowstrings for the smooth specimen. Length of the straight notch part of the notched specimen
L_3	Length of the circumferential part of the notched specimen
l_s	Length of half the notch
m	Material parameter (slope) for the Paris law
mt	Total number of stress blocks
N_f	Fatigue life, number of cycles until failure
n_i	Number of cycles of block i
N_{fi}	Number of cycles to failure at i
R	Load ratio
R^2	Coefficient of determination
R_1	Minimum radius of the smooth specimen
R_2	Maximum radius of the smooth specimen
S	Specimen's cross section area
$S-N$	Fatigue Strength Curve
S_f	Fatigue limit
S_N	Fatigue strength at N cycles
T	Wave period
T_a	Active time
T_{off}	Stop time
T_{on}	Oscillation time
U	Displacement
u	Displacement in function of x and t
$U'(x)$	Derivative of the displacement in function of x
$U(x)$	Displacement in function of x
u, v, w	Displacements along the axis x, y, z respectively

Chapter 1

Introduction

This chapter describes the motivation of this dissertation that is the departure point to the defined objectives. The objectives turned into the structure of the dissertation which is described.

1.1 Motivation

Currently, the study of the fatigue behaviour of engineering materials, namely metallic alloys when subjected to a number of cycles exceeding the High Cycle Fatigue (10^7 cycles), has raised an enormous interest. A growing number of components (e.g. transportation, energy), in operation, are subjected to load application scenarios of small stress amplitude, but which may reach a number of cycles higher than 10^9, leading to non-negligible fatigue damage. This is a fatigue domain referred to as Very High Cycle Fatigue or Ultra High Cycle Fatigue. It has been found that in this fatigue regime, cracks may initiate within the material, instead of the typical surface cracks. Thus, fatigue behaviour in the extreme super-cyclic regime exhibits a special dependence on the microstructure of the material, making extrapolations of high-cycle fatigue behaviours to this extreme regime questionable. Conventional fatigue limits are often set against the time and economic constraints imposed by very long duration testing, leading to potentially unsafe designs.

Ultrasonic fatigue testing machines (20 kHz) have recently been proposed as an alternative method to evaluate fatigue behaviour in the extreme super-cyclic domains, however they raise many challenges. Namely, the possibility of a frequency or temperature effect on the strength data obtained. Besides this, the meticulous machining precision required for the specimens manufacturing is a challenge. There are also difficulties in the stress determination (load cell, strain gauges) during the tests due to the high frequencies and the loading system. These are related to the need of acquisition equipment with high frequencies and low noise, and the acquisition prices of such systems are quite high. Without this equipment it is not possible to validate the applied loads, displacements and strains during the tests.

In spite of these demanding particularities, there is acceptance of the market about fatigue testing at ultrasonic frequencies due to the significant speed of the results obtained.

The choice of material to be analysed, taking into account the demand associated with extreme fatigue behaviour, is the S690QL steel, which is used in high demanding structural applications. Specifically, in offshore structures this steel grade can be found in the substation, tower, foundation and transition piece (NYSERDA, 2022) and enable weight reduction (Monteiro, 2019). Offshore wind turbine support structure can be exposed to various factors that carry fatigue damage, which is one of the main causes of structural

failure (Mendes et al., 2021). In addition, between January and June 2022, 21 318 GWh of eletricity from wind sources were generated in Continental Portugal, that corresponds to 30.30 % of the total produced electricity (APREN, 2022). The wind power capacity in Europe increases annually, being in 2022 at 236 GW (WindEurope, 2022).

Studying the S690QL high strength steel is of extreme importance for future applications taking into account the market's dimension, for example, on February 2022 about 142.7 Mt of steel were produced (World Steel Association, 2022). This is an indicator that this steel will be present in a large number of structures being built which may soon require this data.

1.2 Objectives

This master thesis was developed in order to accomplish the main goal of characterizing the fatigue behaviour of S690 steel under extreme long duration low stresses. For this, the following objectives were outlined:

- Design of test specimens like smooth/hourglass. Due to the necessity of matching the resonance frequency of the system, which works on a single frequency 20 kHz, the specimen's dimensions and the machining quality (namely the surface roughness) are extremely important. This also involves the accurate assessment of the Young's modulus and the density of the material.
- Analyse the influence of two stress concentration factors (K_t) on the material ultra high cycle fatigue behaviour. Regarding this step, achieving the equations for the specimen's shape (notched specimens design) determination is also relevant. Verifying the validity of the analytical equations is essential and also comparing the solution with the Finite Elements Method.
- Validate the stress accuracy of the fatigue test on the S690 steel employing strain gauges.
- Verify the existence, or not, of a frequency effect for the S690 steel by means of comparing the 20 kHz tests results against the data obtained in the smooth specimens that were submitted to fatigue tests at 150 Hz.
- Verify the notch sensitivity factor of the S690 by means of testing notched specimens at 20 kHz.
- Determine the S-N curve of the S690 steel at 20 kHz and 150 Hz.

This work is developed in the context of the GCYCLEFAT project coordinated by INEGI with the participation of IDMEC/IST-UL.

1.3 Host institution

The experimental programme was performed in the Mechanical Testing Laboratory of INEGI – Institute of Science and Innovation in Mechanical and Industrial Engineering. INEGI is a Research and Technology Organisation (RTO), founded in 1986, focused on research and technology-based innovation activities, technology transfer, consulting and technological services, oriented to the development of industry and economy in general. It is a non-profit, private and recognised as a public utility entity (Inegi, 2022).

INEGI has a wide range of competencies and acts in the following main areas: product development, additive manufacturing, manufacturing processes, composite materials, industry 4.0, biomechanics and energy and sustainability. Furthermore, INEGI integrates and leads LAETA - Associated Laboratory for Energy, Transports and Aeronautics, which organises its activity in 5 Research & Development groups (Inegi, 2022; Portal da Inovação, 2022):

- Materials and manufacturing processes.
- Structures and mechanical systems.
- Energy, Environment and Sustainability.
- Intelligent control systems.
- Biomechanics.

1.4 Content of the Dissertation

The research work developed within the scope of this master thesis is described throughout six chapters.

The Chapter 2, aims to give insight about the state of the art of fatigue on the recent years. It covers the fundamentals of fatigue, reveals numerous investigations regarding the very high cycle fatigue and the ultrasonic fatigue testing. Non-withstanding, this chapter discusses particularities of the Shimadzu USF-2000 and Rumul Testronic 150 kN principles of functioning, as well as the structural steel S690, tested on both.

In Chapter 3, the Bathias and Paris (2004) solution for smooth specimens is described since it is the one adopted by Shimadzu that supplies the USF-2000. Additionally, based on the smooth specimen's approach, the analytical formulation for the notched specimens was deduced thoroughly. The Young Modulus determination of the S690 steel is done by an iterative method that involves the resonance frequency estimation in Abaqus. The Finite Element Method performed in Abaqus to simulate the fatigue testing conditions is explained step by step, along with the results. It is useful to predict the resonance frequency of the specimens for USF-2000 and the stresses they are submitted in accordance to the applied displacements. A comparison is done with the analytical solution.

On the other hand, Chapter 4 presents the material and specimens manufacturing procedure, followed by a description of the experimental apparatus and the sequence to execute a test on both machines aforementioned (20 kHz Shimadzu USF-2000 and 150 Hz Rumul Testronic 150 kN). Plus, the procedure of gluing strain gauges with an adhesive to the specimens is described, along with the measured stress that allows to validate the theoretical stress applied.

The results are on Chapter 5, that presents the outcome of the experimental tests carried out during the dissertation and the discussion. It also presents the further analysis of the specimens under the magnifying eye (optical microscopy) and Scanning Electron Microscopy.

Finally, the Conclusions chapter enumerates the principal deductions from the work carried out namely for smooth/hourglass, notched and the specimens for Rumul.

Additionally, in Appendices the technical drawings can be found, as well the dimensions, results and surface roughness measurements of the tested specimens.

Chapter 2

State of the Art

In this chapter the main advances regarding fatigue studies of high strength steels are exposed. The frequency effect on fatigue testing is discussed as well as the outcome of a stress concentration factor. A revision about the S690 steel is detailed lastly, covering its characteristics and properties.

2.1 Fundamentals of Fatigue

Fatigue is an inevitable process that materials subjected to loading cycles suffer. It is particularly critical in structural parts submitted to variable loads. If ignored, it can lead to catastrophic failure with inevitable economic costs and threat to human life. It is estimated that about 90 % of all metallic failures are due to fatigue (Rodrigues da Costa et al., 2020).

According to the American Society for Testing and Materials (ASTM) Standard E-1823, fatigue is defined as "*the process of progressive localized permanent structural change occurring in a material subjected to conditions that produce fluctuating stresses and strains at some point or points and that may culminate in cracks or complete fracture after a sufficient number of fluctuations*" (ASTM International, 2013). The plastic strain resulting from cyclic stress initiates the crack while the tensile stress promotes crack growth propagation. Microscopic plastic strains also can be present at low levels of stress where the strain might otherwise appear to be totally elastic (Bathias, 2014). The ASTM International (2013) defines fatigue strength, S_N, as "*a value of stress for failure at exactly N cycles as determined from an S-N diagram*" and fatigue limit, S_f, as "*the limiting value of the median fatigue strength as the fatigue life, N_f, becomes very large*". The ASTM does not define endurance limit, the stress value below which the material will withstand many load cycles, but implies that it is similar to fatigue limit (Bathias, 2014).

The S-N curve, also known as Wöhler curve, was first established by a Germany engineer August Wöhler in 1870. Based on the results obtained from the rotating bending fatigue test on railroad axles, Wöhler revealed that the cyclic stress range ($\Delta\sigma$) was more important than the peak stress. S-N curves were then established by plotting the results in terms of the stress range against the number of cycles to failure. Nowadays, the development of technology in fatigue testing allows establishing the S-N curves for a specific component or structure under axial and bending loading (Liu, 2019).

The S-N curves are primarily based on the fatigue test data obtained from constant amplitude (CA) loading. They are typically plotted in log-log scales, which produces a reverse proportional linear relationship between the stress range and the fatigue life, following (Liu, 2019):

$$\sigma_a = CN^m \tag{2.1}$$

On Eq. 2.1 m and C are material constants that can be calculated using a linear regression analysis based on experimental results. The parameter m is the slope of the S-N curve (Liu, 2019).

The stress-based approach is broadly applied to model the fatigue life of a component loaded in elastic regime (bellow the yield stress). On this approach (Figure 2.1.1), the number of cycles a component can withstand is a function of its stress magnitudes, higher stress magnitude implies in smaller number of cycles until failure.

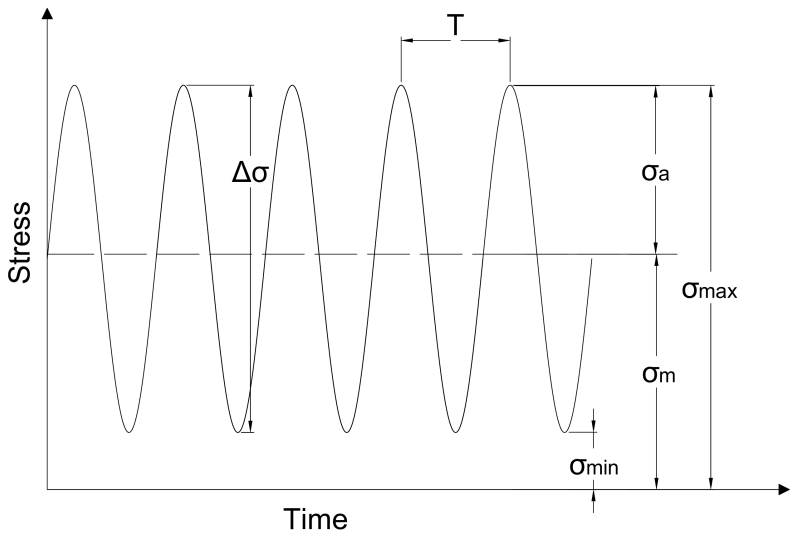


Figure 2.1.1: Terminology for alternating stress (adapted from Bannantine et al. (2022))

The mean stress, σ_m, represents the mean value between maximum and minimum stress, σ_{max} and σ_{min}, respectively being determined by Equation 2.2 (ASTM International, 2013).

$$\sigma_m = \frac{\sigma_{max} + \sigma_{min}}{2} \tag{2.2}$$

The stress range, $\Delta\sigma$, is the difference between maximum and minimum stress,

$$\Delta\sigma = \sigma_{max} - \sigma_{min} \tag{2.3}$$

The stress amplitude, σ_a, is described in Equation 2.4.

$$\sigma_a = \frac{\Delta\sigma}{2} = \frac{\sigma_{max} - \sigma_{min}}{2} \tag{2.4}$$

The period, T, the inverse of the frequency f, is the time taken to complete one cycle (it can be measured between two consecutive maximum or minimum values, for example). Another essential variable is the stress ratio, R, characterized by the ratio between minimum and maximum values of the stress:

$$R = \frac{\sigma_{min}}{\sigma_{max}} \tag{2.5}$$

it can only assume values smaller than 1. The stress ratio has two characteristic values: when it is equal to 0, it is called pulsated loading (or unidirectional stress), meaning that

the region of study is never under compressive stresses, being the minimum stress equal to zero. When the R corresponds to -1, the loading condition is denominated fully reversed, being the amplitude of maximum and minimal stresses identical, but with opposite signals.

The amplitude ratio A_r also gives information about the type of loading, being given by Equation 2.6 (Bannantine et al., 2022).

$$A_r = \frac{\sigma_a}{\sigma_m} = \frac{1-R}{1+R} \tag{2.6}$$

The states of loading are summarized by Table 2.1.1.

Table 2.1.1: Loading notable conditions (Bannantine et al., 2022)

Condition	R	A_r
Fully reversed	-1	∞
Zero to max	0	1
Zero to min	∞	-1

2.1.1 Mean S-N curve determination

The mean S-N curve can be obtained using the ISO (2012) 12107 Standard, following the formulae below:

$$\sigma_a = 10^A N^B \tag{2.7a}$$

$$\log(\sigma_a) = \log(10^A) + \log(N^B) \tag{2.7b}$$

$$\log(\sigma_a) = A + B\log(N) \tag{2.7c}$$

With $y = \log(\sigma_a)$ and $x = \log(N)$, the constants B and A are given by the Eqs. 2.8. The B is obtained by considering the stress as the independent and cycles as dependent variable.

$$B = \frac{\sum_{i=1}^{n}(x_i - \overline{x})(y_i - \overline{y})}{\sum_{i=1}^{n}(x_i - \overline{x})^2} \tag{2.8a}$$

$$A = \overline{y} - B\overline{x} \tag{2.8b}$$

Where the average values are:

$$\overline{x} = \frac{1}{n}\sum_{i=1}^{n} x_i \tag{2.9a}$$

$$\overline{y} = \frac{1}{n}\sum_{i=1}^{n} y_i \tag{2.9b}$$

The estimated values allow to obtain coefficient of determination, R^2, in order to get a perception of the estimation accuracy, via the calculus of the predicted logarithm of the stress level (y_p). The higher R^2, the closer curve gets to the points.

$$y_p = A + Bx \tag{2.10a}$$

$$R^2 = 1 - \frac{\sum_{i=1}^{n}(y_i - y_p)^2}{\sum_{i=1}^{n}(y_i - \overline{y})^2} \tag{2.10b}$$

The estimation of the standard deviation of the logarithm of the fatigue life from the mean S-N curve is given by first calculating the cycles prediction:

$$x_p = -\frac{A}{B} + \frac{1}{B}y \tag{2.11}$$

Hence, the standard deviation comes as Eq. 2.12 where $n-2$ stands for the degrees of freedom.

$$\hat{\sigma}_x = \sqrt{\frac{\sum_{i=1}^{n}(x_i - x_p)^2}{n-2}} \tag{2.12}$$

The curve for a certain probability of survival (PS) and a confidence level (CL) is obtained through the implementation of a shift factor:

$$\log(\sigma_a) = A + B * factor + B\log(N) \tag{2.13}$$

The factor is calculated through:

$$factor = k_{(PS,CL,n-2)}\hat{\sigma}_x\sqrt{\left(\frac{1}{n}+1\right)^2} \tag{2.14}$$

2.1.2 Statistical analysis of the fatigue data

The statistical analysis of the fatigue data provides a better perception of what is the most probable fatigue life at the test stress level. One common distribution used for fatigue is the Weibul probability density function (pdf) (Eq. 2.15) viewed as a function of two parameters. The maximum likelihood estimates (MLEs) are often for parameter estimation that maximize the likelihood function, for fixed values of x. The maximum likelihood estimators of a and b for the Weibull distribution are the solution of the simultaneous equations 2.16 where $\hat{a}$ and $\hat{b}$ are unbiased estimators of the scale a and shape or slope b parameters (Galar and Kumar, 2017; Matlab, 2022; Weibull, 1951). The Weibull shape parameter b indicates, for example, when $b < 1$, the system has a decreasing failure rate and it is failing earlier than expected. If $b = 1$, there is a constant failure rate. If $b > 1$, there is an increasing failure rate (Galar and Kumar, 2017).

$$f(x|a,b) = \begin{cases} \frac{b}{a}\left(\frac{x}{a}\right)^{b-1} e^{(-x/a)^b} & \text{if } x \geq 0, \\ 0 & \text{if } x < 0. \end{cases} \tag{2.15}$$

$$\hat{a} = \left[\left(\frac{1}{n}\right)x_i^{\hat{b}}\right]^{\frac{1}{\hat{b}}} \tag{2.16a}$$

$$\hat{b} = \frac{n}{\left(\frac{1}{\hat{a}}\right)\sum_{i=1}^{n} x_i^{\hat{b}}\log x_i - \sum_{i=1}^{n}\log x_i} \tag{2.16b}$$

2.2 Very high cycle fatigue: an overview

The gigacycle fatigue behaviour is characterized by the fatigue limit of a material being in the gigacycle region, i.e., above 10^9 cycles. An example is the high strength steels, whose tensile strength exceeds approximately 1200 MPa and show very high cycle fatigue (VHCF) failure at over 10^7 cycles (Furuya et al., 2019). Since high cycle fatigue (HCF) and VHCF failures affect safety, reliability, readiness, and support cost for many machine systems made from metal alloys, the fundamental understanding of fatigue resistance and potential prevention strategies are essential (Ilie et al., 2020). Bellow 10^4 cycles, the region is denominated low cycle fatigue (LCF). These fatigue regimes are portrayed on (Figure 2.2.1).

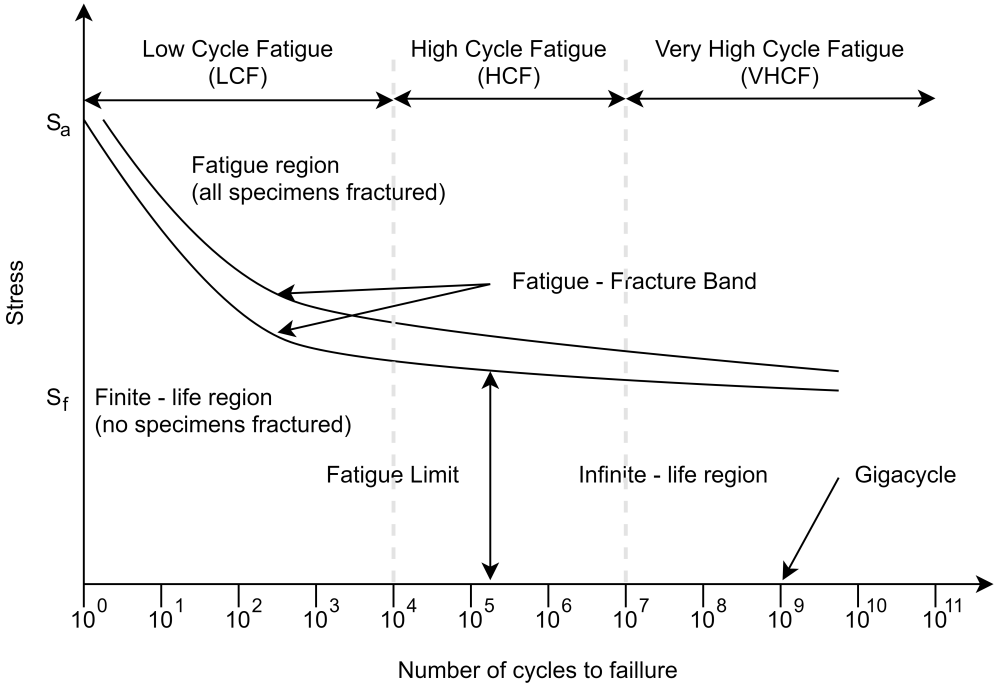


Figure 2.2.1: S–N curves that typify fatigue test results when testing medium-strength steels, categorizing the cycles to failure (adapted from Bathias and Paris (2004))

In many industrial sectors such as automotive, aeronautics and energy, the design of mechanical components against fatigue crack initiation is based on fatigue strength data in the HCF regime (i.e. around 10^7 cycles). However, despite stresses below the conventional HCF, there are fatigue failures beyond 10^9 cycles or more (VHCF regime). The fatigue life of various load bearing applications like gas turbines discs (10^{10}), cylinder heads and blocks in a car engine (10^8), bearings, drilling equipment, engines of high-speed trains, and ships (10^9), fall under VHCF (Sharma et al., 2020). A specific example is the high speed Japanese Shinkansen Train, which is subjected to gigacycle loads on its axles in 10 years of service, hence the steel fatigue behaviour should be known to guarantee its safety (Setowaki et al., 2011). Very high cycles experienced by certain automotive components and the ultra-high cycles seen by aerospace parts, gas turbine blades (due to vibrations), created the need for an even faster new testing techniques based on ultrasonic loading frequencies of 20 or 30 kHz (Ilie et al., 2020; Palin-Luc and Jeddi, 2018). In the renewable energy field, increasing turbine capacities demand larger rotor diameters and tower heights.

Wind turbines suffer a noteworthy amount of load cycles, namely due to the numerous revolutions of the rotor. In case of a turbine with a nominal rotor-blade frequency $f = 0.5$ Hz, 2E6 cycles are achieved in 46 days and 1E9 cycles after 20 operating years. This translates into the necessity of studying the fatigue life after 1E7 (Dong et al., 2011; Harte and Van Zijl, 2007).

Bathias (1999) found out that the fatigue strength decreases about 50–200 MPa from 10^6 to 10^9 cycles depending on the material. For high strength steels, this value is believed to be around 60 MPa. For a carbon steel, the S-N curve is usually a fatigue life curve defined as a relationship between the applied stress amplitude and the number of cycles to failure (Furuya et al., 2019). The S–N curve is conventionally limited to 10^7 cycles, and it is admitted, according to the standard ASTM E-1823 (ASTM International, 2013), that a horizontal asymptote can define a fatigue limit value for an alternating stress between 10^6 and 10^7 cycles. Beyond 10^7 cycles, the standard considers that the fatigue life is infinite due to time and cost restrictions when executed in the conventional regime 1-30 Hz. In fact, it is a convenient and economical approximation, but it is not a rigorous approach. For other alloys like aluminium, it is assumed that the asymptote of the S–N curve is not horizontal (Bathias, 1999).

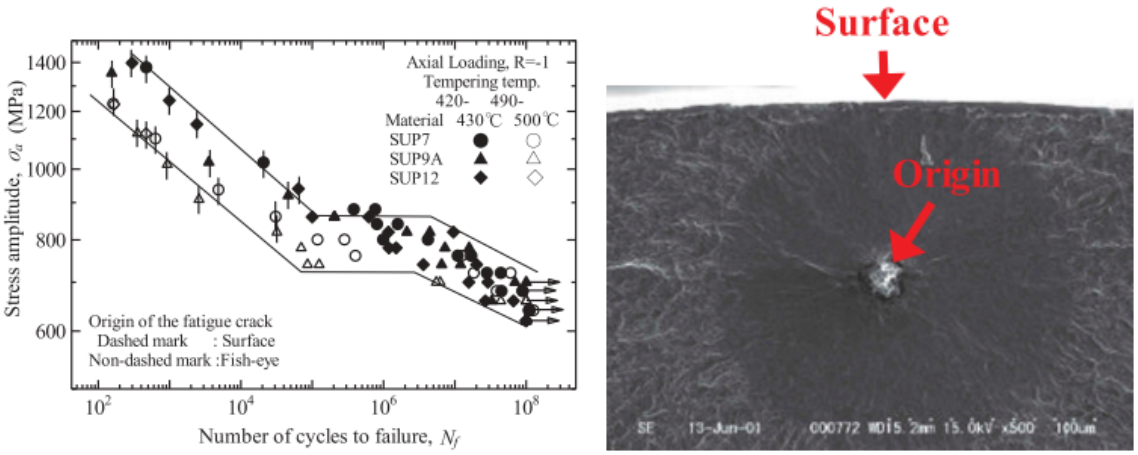
In conventional steels, the fatigue limit is clear and the fracture modes are surface fractures, i.e., fatigue cracks initiate from surfaces. The fatigue limit is, in general, around half the tensile strength up to a tensile strength of circa 1200 MPa (Eq. 2.17). For stress levels above 1200 MPa, the fatigue limit tends to flatten off, or at least increase more slowly in relation to the endurance limit and tensile strength for steels. This happens because the increase in strength is usually accompanied by a decrease in ductility and fracture toughness, facilitating the initiation of a fatigue crack (Furuya et al., 2019).

$$\sigma_f = 0.5 R_m \tag{2.17}$$

The equation 2.17 is the simplest estimation where σ_f is the fatigue limit and R_m is ultimate tensile strength.

It has been well documented now that the sudden reduction of fatigue strength of high strength steel in VHCF regime is due to the internal fatigue crack initiation at nonmetallic inclusions (Ebara, 2017). Murakami et al. (1999) published the relationship between the material's fatigue limit with its Vickers Hardness, stress ratio and square root of the projection area of a defect. Gao et al. (2019) in their investigations found out that the inclusion induced crack initiation is a leading failure mode within VHCF regimes for the specimens with large inclusion size. However, in an experiment with high strength steel (HSS), it was noticed that the non-inclusion induced crack initiations occurred solely in the specimens whose microstructure was coarse.

In contrast, the fracture mode of high strength steels in the short life region comprises normal surface fracture, whereas internal fractures occur in the VHCF region. The internal fractures mostly originate from inclusions. On Figure 2.2.2 it can be seen the S-N curve of fatigue tests for three spring steels, besides the fracture mode exposed (Bathias, 1999; Furuya et al., 2019). The fatigue life difference between surface crack initiation and subsurface crack initiation is due to the fact that the subsurface cracks grow in a vacuum and generally at an order of magnitude slower than surface initiating cracks at the same loading level (Qian et al., 2010).



(a) S-N curve

(b) Internal fracture surface

Figure 2.2.2: Typical fatigue test results for high strength steel (Furuya et al., 2019)

On Figure 2.2.3, the border of stress level between the surface and internal fractures is close to the conventional fatigue limit. Beyond that point, internal fractures eliminate the conventional fatigue limit. Hence the two-fold S-N curve concept is also known as stepwise S-N curve, illustrated on Figure 2.2.3. It assumes that the S-N curves of internal and surface fractures exist independently, but that a combination of the two S-N curves determines their final shape (Furuya et al., 2019).

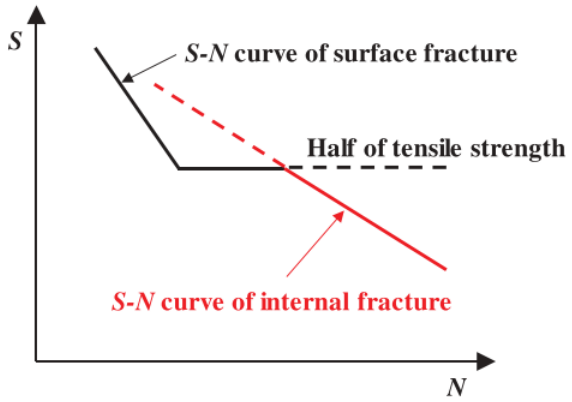


Figure 2.2.3: Two-fold S-N curve concept (Furuya et al., 2019)

The two-fold S–N curve depicted in Figure 2.2.4 exemplifies the general S-N curve for a high strength steel (Zimmermann, 2018).

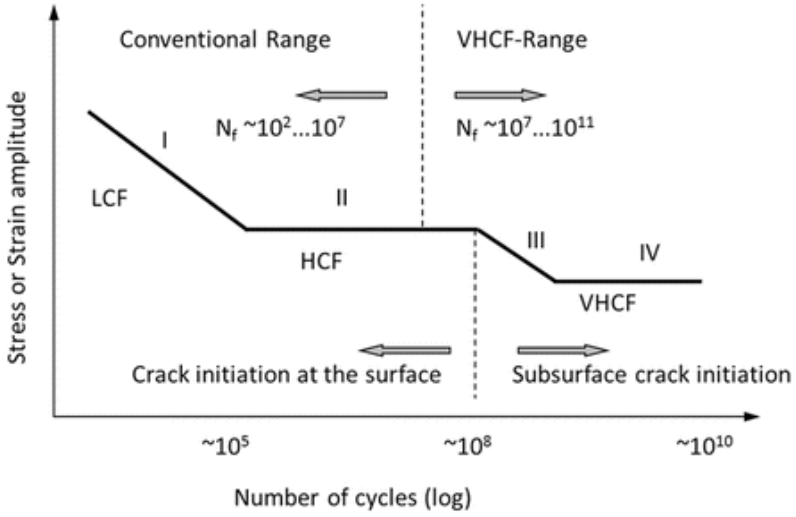


Figure 2.2.4: Two-fold S-N curve concept (Zimmermann, 2018)

Furuya et al. (2019) concluded that although the fatigue strengths of conventional surface fractures are closely dependent on tensile strength, the influence of this on internal fractures is very minor. Their studies indicate that the internal fractures are instead affected by the size of inclusions at fracture origins in japanese high strength steels: larger specimens show clearly lower fatigue strengths, revealing larger inclusions at the internal fracture origins. Furthermore, the authors reported extremely slow crack growth rates for small internal cracks, indicating that the growth of these small internal cracks controlled the internal fractures. For the materials studied by Furuya et al. (2019) on Figure 2.2.5, the decrease in fatigue strengths became less steep as a function of rising inclusion size, resulting in an estimated fatigue strength of 500 MPa, which is relatively to LCF minus 37.5 % at 10^9 cycles, even for 100 μm inclusions.

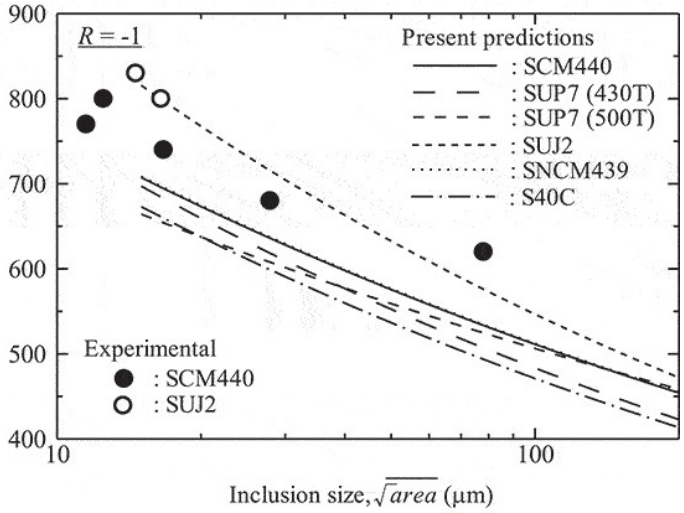


Figure 2.2.5: 10^9 cycles fatigue strength of japanese steels (Furuya et al., 2019)

It has been generally accepted the great importance to understand and predict a fatigue life in terms of crack initiation and small crack propagation. Bathias and Paris (2004) claimed that at high stress levels, fatigue life is determined primarily by crack growth,

while at low stress levels, the life span is mainly consumed by the process of crack initiation. This process is illustrated on Figure 2.2.6.

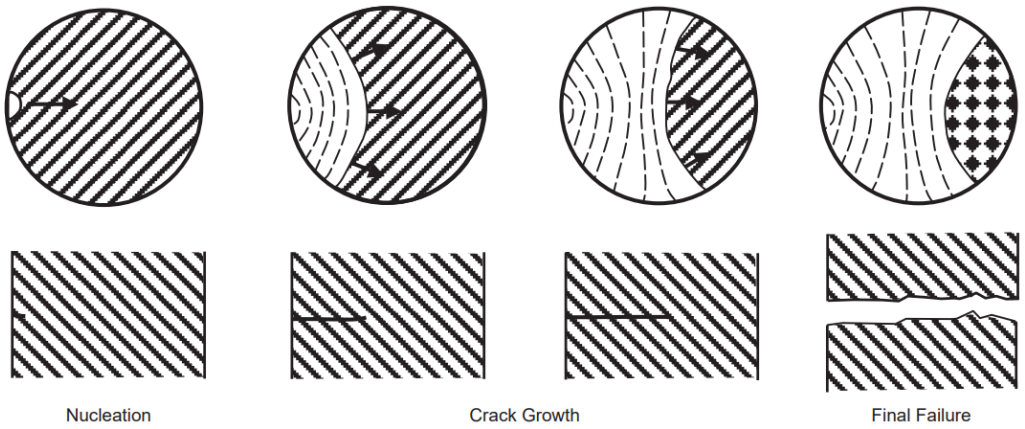


Figure 2.2.6: Typical propagation of a fatigue crack (Campbell, 2008)

The overall fatigue life is dominated by the crack initiation phase rather than the growth phase (Zimmermann, 2018). Several authors have demonstrated that the portion of life attributed to crack nucleation is above 90% in the high cycle regime (10^6 to 10^7 cycles) for steel, aluminium, titanium, and nickel alloys (Bathias and Paris, 2004). Non-metallic inclusions or matrices (inhomogeneities) acting as crack nucleation singularities, they are usually observed in the centre of a "bright granular facet" surrounded by a flat appearance so-called "fish-eye". In almost all cases, the fish-eye appears circular, with a dark area in the centre, inside which the crack initiation site is located. Controversy exists as to the presence of this dark area, and hence terms of fine granular area (FGA) was referred as optically dark area (ODA) (Murakami et al., 1999) and later as granular bright facet (GBF) (Shiozawa et al., 2006) reflect different crack initiation mechanisms and early-stage crack growth behaviour that cause such a macroscopic feature (Zhao et al., 2020). It is suggested that the non-metallic inclusions have a significant influence on the fatigue strength and life of high strength steels (Gao et al., 2019). In VHCF regime, the cycles spent for the crack initiation can account for a very large fraction of the 90 % to 99% of the fatigue life, involving both the initiation and early-stage growth process (Zhao et al., 2020). Gao et al. reported that at macroscopic scale, the surface of inclusion induced GBF is normal to the loading direction, but the non-inclusion induced GBF is along close to the plane of maximum shear stress (Gao et al., 2019).

From a macroscopic perspective for a large number of cycles, deformation is limited to purely elastic strain amplitudes. With increasing number of loading cycles, the scatter band of test results increases significantly, sometimes spreading over more than three decades (Zimmermann, 2018). This wide dispersion is due to the influence of several factors being well known that fatigue life depends on notches, residual stresses, temperature, corrosive medium, as well as the type of loading and mean loading (Berger et al., 2008). For martensitic steels, the effect of inclusion size on the fatigue strength strongly depends on the microstructure and vice versa (Gao et al., 2019).

Within the ODA area, a fine granular topographic structure is observed and hence the alternative designation fine granular area (FGA) was established. Further, outside of the fish-eye the fatigue crack continues until the final fracture is reached (Furuya et al., 2002; Sadek et al., 2020). In cases where the crack nucleates from a defect, such as an inclusion, casting pore, second phase particle or microstructural inhomogeneities (Zhao

et al., 2020), it is said that a relation should exist between the fatigue limit and the crack growth threshold, however this is difficult to establish. First, it is not certain that a sharp defect implies immediate fatigue crack growth from the very first cycle. Second, when a defect is small, a short crack does not grow at the same rate as a long crack. Bathias and Paris (2004) defend several crack initiation mechanisms dependent upon the alloys and particular types of defects.

The major variables which cause internal fatigue crack initiation are nonmetallic inclusions in high strength steels, surface roughness (SR), and notch in structural components and corrosive environments (Ebara, 2017). However, it is believed that fatigue crack does not initiate from inclusions below a critical size. Adopting zero-inclusion where the inclusion size is well controlled to within 1 μm can be a solution to extend super long fatigue life (Qingyuan and Zhiyong, 2013). Regarding the surface roughness, in general, as its the magnitude decreases it leads to an increase in fatigue life. Decreasing SR minimizes local stress raisers. Therefore, special attention must be given to the surface preparation with the goal of obtaining a metallographic finish, free of machining grooves and grinding scratches (Boyer, 1997).

Xiong et al. (2021) concluded that in the gigacycle fatigue regime, all of the specimens of stainless steel 316L prepared using Gas-Shielded Tungsten Arc Welding (GTAW) failed due to the surface crack initiation, while internal defects were the primary reason to induce the failure of Laser Beam Welding (LBW) made samples. So, LBW has some advantages in terms of fatigue resistance compared with GTAW. On top of that, their studies observed pore clusters in the fracture surface, which might have an influence on the gigacycle fatigue behaviour.

Ilie et al. (2020) developed an ultrasonic fatigue machine to conduct a fatigue testing of specimens made from 2024-T351 and 7075-T6 aluminium alloys. They found out that high test frequencies result in temperature increase, thus employed cooling with compressed air to control heat generation due to internal damping of specimens at high frequencies, consequently reducing the frequency effect.

Dimitrov and Argirov (2014) investigated the fatigue behaviour of a hourglass specimen made of the high strength steel 33NiCrMoV14-5 in 10^6–10^8 cycles at 20 kHz. Their studies concluded the fatigue limit decreased more than 100 MPa (18.5 %) between 10^6 and 10^8 cycles, having no horizontal asymptote in the S–N curve. Their fracture origins were located at the surface, so they deduced the internal inclusions were not the main stress concentrator because of their globular shape. They established that since their specimens had larger cross sections, these were more suitable of being affected by surface and/or subsurface inclusions. Henceforth, the inhomogeneous stress field around such surface inclusions combined with the surface roughness resulted in a higher maximal stress where the micro cracks could initiate, developing a fatigue crack.

Bathias (1999) found out the effects of frequency and heat dissipation were very small in a specimen with temperature less than 60 °C when the fatigue life was greater than 10^7 cycles. The gigacycle regime requires more attention with respect to the choice of alloys and the techniques used in the prediction of fatigue endurance.

2.3 Ultrasonic testing

The ultrasonic fatigue testing (UFT) method differs from the conventional that has low frequency limit of cyclic stressing the material. The frequency of UFT ranges from 15 kHz to 30 kHz, with a typical frequency being 20 kHz, which is enough to be above the human hearing spectrum and dismiss a soundproofing chamber. With this high frequency, the

time and cost to obtain a fatigue limit (if one does exist) or crack growth rate threshold data can be dramatically reduced. For instance, the test time for 10^7 cycles is within 9 minutes by ultrasonic method, i.e. 500 seconds at 20 kHz, while conventional fatigue testing at 100 Hz will take about 1.2 days (see Table 2.3.1) (Stanzl-Tschegg et al., 2002). For even higher cycles like 10^9, the ultrasonic method requires only 14 hours, whereas it would take more than 3000 hours at 100 Hz. A more drastic example is the application of 10^{10} cycles that would take 3 years at 100 Hz, but that is possible in 7 days considering the ultrasonic method at 20kHz (Bathias and Paris, 2004).

Besides the lower test times exposed on Table 2.3.1, the high frequency entails the need for coolant and the possibility of a frequency effect on the test results.

Table 2.3.1: Comparison between the duration of different fatigue testing methods for continuous loading (approximate values) (Rodrigues da Costa et al., 2020)

N	Ultrasonic (20kHz)	Resonance (150 Hz)	Rotating Bending (30 Hz)
10^7	8.3 min	1 days	4 days
10^8	1.5 h	1 weeks	1.5 months
10^9	0.5 days	2.5 months	1 years
10^{10}	1 week	2 years	1 decade

Traditional fatigue tests are performed typically in rotating bending machines that operate at frequencies up to 30 Hz or servo-hydraulic machines which work at frequencies up to 50 Hz. Zimmermann (2018) revealed that bending machines are limited to 200 Hz and work by the principle of inducing an oscillatory bending load on a clamped sample. They observed in their studies that the loading conditions may alter the failure characteristics of the alloy, especially in the VHCF range. Actuators are used to stress test specimens by reproducing any reference signal (waveforms, random spectra, etc.) at frequencies that in some cases can exceed 200 Hz (Rodrigues da Costa et al., 2020; Wagener et al., 2011). However, especially for servo-hydraulic test machines, since the oil pressure has to be generated for each cycle, the necessary energy for each cycle must be provided so that the overall power consumption is rather high. An enormous amount of energy is lost in the form of heat, which has consequences in running and maintenance costs and has to be dissipated by an appropriate cooling system. Servo-hydraulic machines with frequencies up to 1000 Hz, due to a high-flow voice coil servo-valve, have been developed since about 1997 (Stanzl-Tschegg, 2014).

Conventional resonance pulsation test systems are capable of vibrations at test frequencies somewhere between 100 and 300 Hz depending on the material damping behaviour and the size and geometry of the sample (Zimmermann, 2018). However, there are some electromagnetic or hydraulic shaker (resonant machines) that operate in the frequency range of 500 Hz to 1.8 kHz. In some studies these machines demonstrated that when employed to test aerospace alloys at a frequency of 800 Hz, the results have been shown to be comparable to a standard 2-Hz fatigue testing device (Ilie et al., 2020). Resonant fatigue testing machines are characterized by a relatively higher frequency and lower power consumption (0.5 kW) as compared to hydraulic equipment. Traditional resonant testing machines have a spring-mass system which is excited to vibrations at its eigenfrequency by an electromagnet, whereby the test specimen with its elastic properties is part of the system. For more than half a century there have been resonance machines of 250 kN and 100 kN with an electromagnetic driver capable of performing high cycle fatigue tests on stiff specimens (Stanzl-Tschegg, 2014).

New machines incorporate electromagnetic linear actuators in their uniaxial testing machines. The success of these actuators is mainly due to the much lower operating costs, little consumables needed, lower electrical consumption, less heat generation, no noise, high cleanliness and almost no wear. The principal drawback is the limitation in load capacity, in which the most powerful machines can only go up to 10 kN, much lower than what can be achieved with hydraulics, but enough to test small samples (Rodrigues da Costa et al., 2020; Wagener et al., 2011).

Regarding the load, generally the servo-hydraulic machines allow the highest, followed by resonance and ultrasonic machines. This justifies the diminished diameter of the specimens tested in the ultrasonic regime.

Ultrasonic technique is most appropriate to determine fracture mechanical quantities, especially the question of the existence or non-existence of thresholds under randomly varying amplitudes can be treated most efficiently with this technique (Stanzl-Tschegg et al., 2002). It is also effective to inspect for inclusions. Internal fracture surfaces reveal inclusions at the fracture origin and a significant distribution of inclusion sizes can be obtained. This testing creates internal fracture surfaces very rapidly (Furuya et al., 2019).

In spite of the advantages, the extremely high frequency can cause a stress load shift, heat generation in specimens, strain rate effect and so on (Torizuka et al., 2012). Metals present a decrease in their resistance to fatigue with the increase of temperature. To mitigate the temperature raise, the tests are carried out with intervals of stress blocks and a rest time for cooling. This translates to into a stop time (T_{off}), often more representative than the oscillation time (T_{on}), both illustrated on Figure 2.3.1. The active time is represented by T_a. Typical pulse-lengths are 25-100 ms (500-2000 cycles) and pause-lengths may vary between 25 and 1000 ms, depending on the damping capacity of the tested material. Short oscillation times are prejudicial since they add uncertainty to loading time. In addition, compressed air or liquid cooling is possible, but this last brings concerns at the corrosion level (Stanzl-Tschegg, 2014).

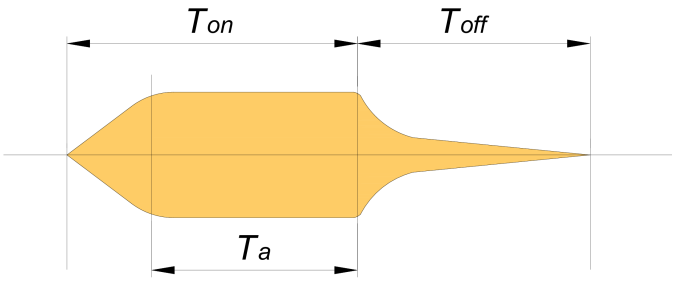


Figure 2.3.1: Load sequence of the UHCF (adapted from Stanzl-Tschegg et al. (2002))

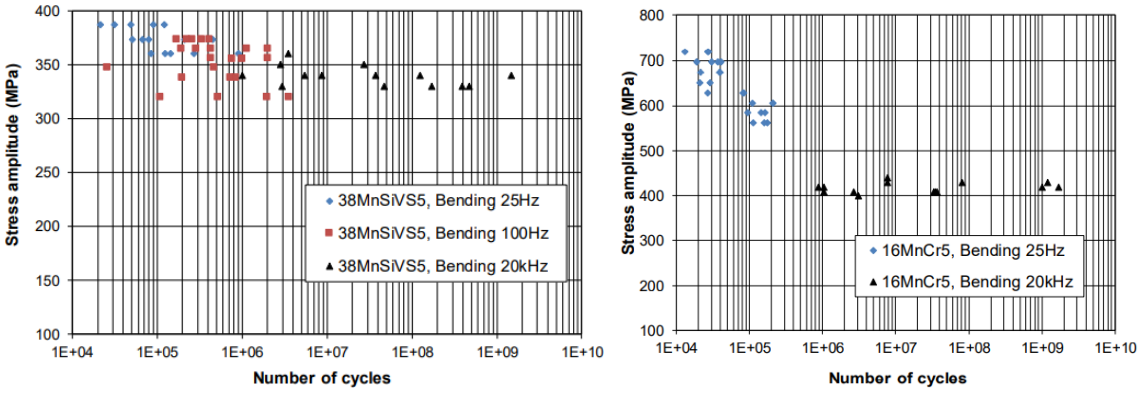
Moreover, the UFT is limited by the specimen size and shape restricted displacement control instead of strain or stress control and the potential frequency effects (Stanzl-Tschegg, 2014).

The frequency effect is a controversy in nowadays research, i.e., the question of whether the results of ultrasonic fatigue testing are comparable to those obtained by conventional fatigue testing. The literature claims results for both arguments, that it depends on the material if the stress is modified owing to the frequency. Ultrasonic fatigue testing is concluded to be effective for researching gigacycle fatigue that is caused by internal fractures, since the frequency effect was proved negligible under these conditions (Furuya et al., 2019; Torizuka et al., 2012). In the field of VHCF, the mechanism of loading frequency effect on fatigue life is often linked to the specimen self-heating and material's

strain-rate sensitivity. Zhao et al. (2020) reported that for the Ni-base superalloy DZ125 the UFT of 20 kHz does not seem to cause noticeable changes in fatigue life, deformation mode, as well as fracture mechanism, when compared to that at 100 Hz.

Setowaki et al. (2011) observed on the middle carbon steel (JIS S38C), quenched and tempered, the fatigue limit dependence on load frequency. The fatigue limits under each frequency were 250 MPa (10 Hz), 320 MPa (50 Hz) and 370 MPa (20 kHz). The difference of fatigue limits between 10 Hz and 50 Hz seemed to be due to the difference of loading method, i.e. axial or rotating bending. However, the fatigue limit under 20 kHz proved to be much higher than that of 10 Hz by 120 MPa. This difference seemed to be caused only by the load frequency. The amount of plastic strain of 50 Hz was much higher than that of 20 kHz at the same stress level, which does not happen comparing at the same cycles to failure. This means that fatigue damage was related not to the product of stress amplitude and number of cycles but that of plastic strain and number of cycles in different frequencies. Therefore, there should be the dependence of stress-strain hysteresis loop on load frequency during cyclic loading (i.e. cyclic yield stress dependence on strain rate). Nonaka et al. (2014) did a similar test for the same material but at 400 Hz and 19.8 kHz, reporting among the results the same frequency effect of 120 MPa.

The European Comission reported that for the steel 38MnSiVS5, used for forgings in the automotive industry, the bending fatigue strengths going from 25 Hz, 100 Hz and to 20 kHz are overlapping showing no frequency effect (Figure 2.3.2a). Moreover, the 16MnCr5 bending fatigue results of 25 and 20 kHz testing indicated an agreement as if extrapolation of the lower fatigue life data of 25 Hz testing would yield similar fatigue strength levels as the longer life data of 20 kHz testing (Figure 2.3.2b). The torsion fatigue results were however more irregular and not consistent as compared between the different test conditions (Bergström et al., 2018).



(a) (b)

Figure 2.3.2: Bending fatigue of the bar grades a) 38MSiVS5, b) 50CrV4 (Bergström et al., 2018)

Bathias (2012) studied the bearing steel 100Cr6 through fatigue tests at various test frequencies during tension-compression UFT. He confirmed that the shape of the S-N curve is continuously decreasing from the mega to the gigacycle regime, without effect of frequency since no step is observed in the S-N curve (Figure 2.3.3).

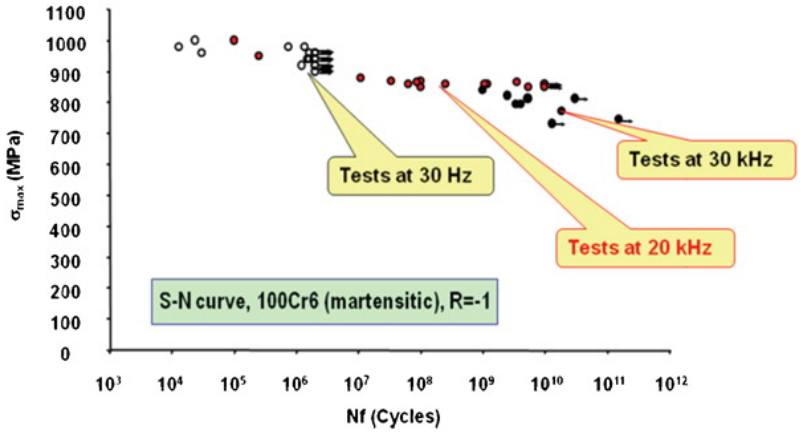


Figure 2.3.3: Gigacycle S-N curve the martensitic bearing steel 100Cr6 at different frequency and $R = -1$ (Bathias, 2012)

Tsutsumi et al. (2009) found out that the fatigue life and the fatigue limit for the annealed and the 10 % pre-strained specimens of 0.13 % carbon steel under ultrasonic fatigue tests were higher than those under conventional tension-compression fatigue tests. The crack growth rate under ultrasonic fatigue tests was slower than that under conventional tension-compression fatigue tests. Figure 2.3.4 shows the S-N curve. The fatigue life strength for the specimens under ultrasonic fatigue tests (20 kHz, strain rate: 126 $\sec^{-1}$) was up to ten times higher than that under conventional tension–compression fatigue tests (10 Hz, strain rate: 6.3 x 10^{-2} $\sec^{-1}$) for a given stress range. The increase in fatigue strength might have been, to a large extent, due to a reduction in crack tip cyclic plasticity during ultrasonic fatigue tests.

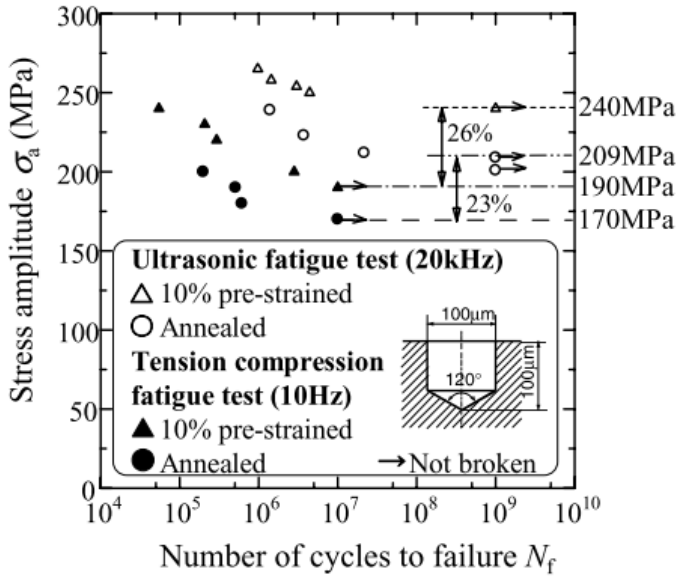


Figure 2.3.4: S–N data for annealed and 10% pre-strained specimens (Tsutsumi et al., 2009)

Marti et al. (2015) showed that on low carbon steel S15C, both of the fatigue strength and the fatigue life increased with testing frequency. However, such frequency effect tends to diminish at higher stress level in the frequency range of 0.2 to 140 Hz without the

ultrasonic frequency (Guennec et al., 2014; Marti et al., 2015; Palin-Luc and Jeddi, 2018). Bathias and Paris (2004) concluded that the frequency effect was much more significant between 0.001 and 10 Hz than between 10 and 20 kHz (Zhao et al., 2020).

Furuya et al. (2002) studied the frequency effect at 100 Hz, 600 Hz or 20 kHz. They found out that the failures in almost all the specimens were caused by internal non-metallic inclusions leading to fish-eye fractures. Fatigue life was distributed in a wide range in the S–N diagram (Figure 2.3.5) independently of frequency. The origins of fractures were Al_2O_3 or $Al_2O_3{\cdot}CaO$ inclusions in all fish-eye fractured specimens, which caused the scattering in S-N diagram by the differences in the inclusion sizes. Their S–N diagram showed clear fatigue limits which could be determined with fatigue tests exceeding 10^9 cycles even in the case of fish-eye fractures.

The scatter of S–N data is also due to the large scatter in size of inclusions contained in the specimens, the variation of residual stress from compression at the surface to tension in the interior, the different surface condition, etc (Qian et al., 2010).

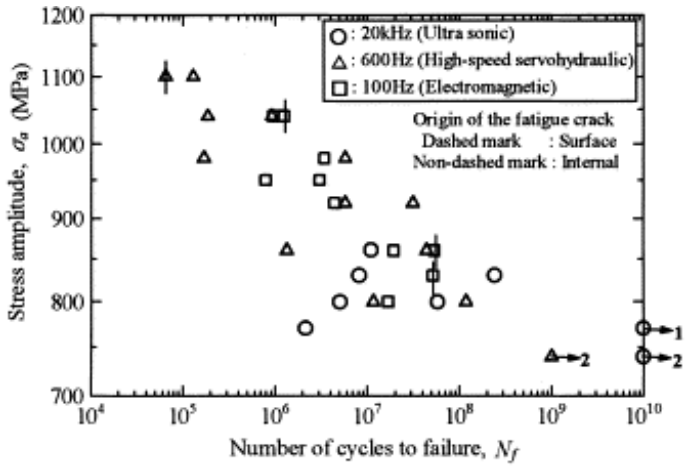


Figure 2.3.5: S–N diagram for low-temperature-tempered JIS SNCM439 steel. Arrow-marked plots show unbroken results (Furuya et al., 2002)

Palin-Luc and Jeddi (2018) reported, by means of Figure 2.3.6, that on the JIS S15C steel there was a decrease of about a fifth of the fatigue limit when performing 140 Hz fatigue tests instead of ultrasonic testing.

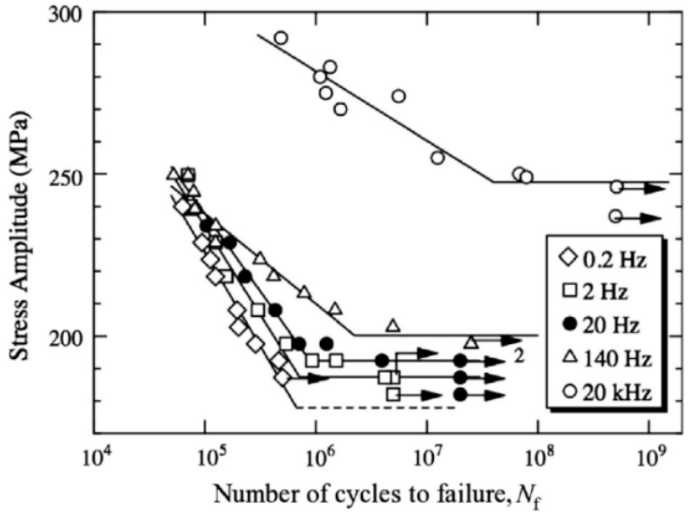


Figure 2.3.6: S-N diagram of JIS S15C steel, $R_m = 441$ MPa, under several loading frequencies in tension compression with $R = -1$ (specimens with diameter of 5mm) (Palin-Luc and Jeddi, 2018)

Torizuka et al. (2012) studied the behaviour of the 15C steel in smooth specimens under ultrasonic (20 kHz) and electromagnetic resonance (150 Hz) fatigue tests. The results of the ultrasonic fatigue tests revealed clearly longer fatigue life in the very high cycle region above 10^7 cycles. In addition, although the fracture type of the electromagnetic resonance fatigue tests is only surface fracture, the ultrasonic fatigue tests revealed internal fractures in the very high cycle region with origin in an oxide-type globular inclusion. Large specimens are more likely to contain large inclusions, so the fatigue strength drops. Thus, in their studies the frequency effect was visible, and the fatigue limit was unclear under these conditions, and instead the material revealed a typical stepwise S–N curve on Figure 2.3.7. The crack type change from surface to internal crack in UFT with the smooth specimens is attributable to elevation of the surface fracture strength due to the frequency effects.

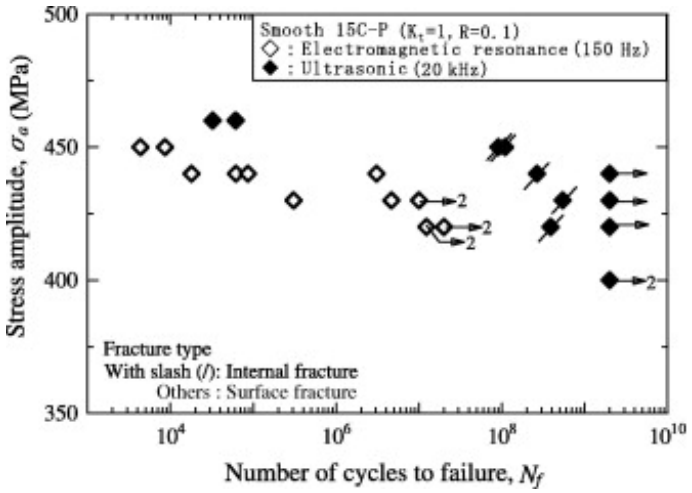


Figure 2.3.7: Fatigue test results for smooth specimens of 15C-P (Torizuka et al., 2012)

In their studies, many and spread slip bands were formed before the crack initiation in conventional fatigue testing, while the slip bands were reduced and concentrated in the

UFT. The fracture type change in the smooth specimens was caused by the frequency effects on the surface fracture. Figure 2.3.8 considers the S–N curves of the surface and internal fractures independently, i.e., based on a twofold S–N curve concept. In this steel, the S–N curve of the surface fracture is expected to be low enough to hide that of the internal fractures. However, when applying ultrasonic fatigue testing, the S–N curve of surface fracture is elevated due to the frequency effect. As a result the number of cycles increased to the point of reaching the stepwise S–N curve for internal fracture, which is not frequency sensitive. Thus, internal fractures occur during the ultrasonic fatigue tests on the smooth specimens (Torizuka et al., 2012).

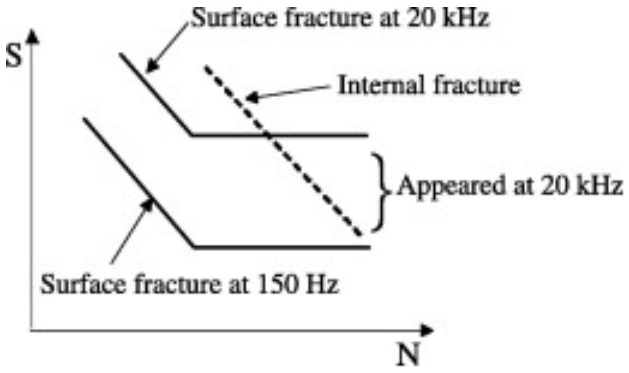


Figure 2.3.8: Schematic illustration of the likely principle governing the fracture type change during ultrasonic fatigue tests on the smooth specimens (Torizuka et al., 2012)

Other authors like Nishijima and Kanazawa (1999) presented a revised S–N curve for the twofold approach for carbon and low-alloy steels, considering a single frequency on Figure 2.3.9.

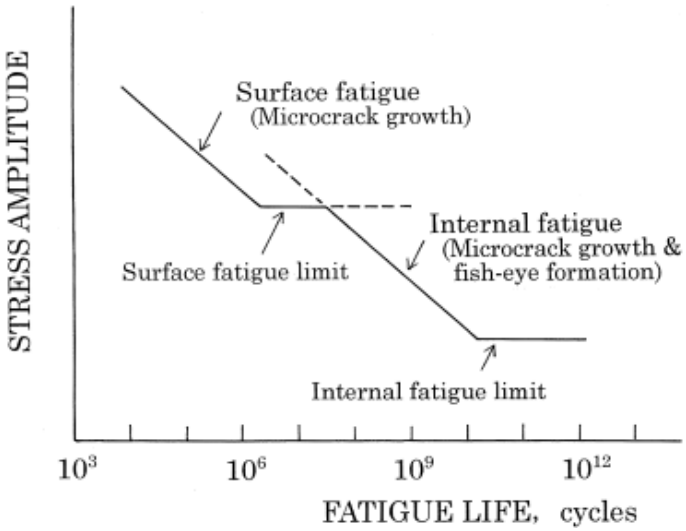


Figure 2.3.9: The concept of a twofold S–N curve (Nishijima and Kanazawa, 1999)

As it can be observed, the fatigue limit progresses in a series of not continuous stages, hence the name stepwise. For the surface fatigue mode, microcracks are formed at the specimen surface where slip bands are preferentially developed. These grow gradually and become macrocracks when conditions of microstructure and stress are favourable which then propagate until fracture. For the internal fatigue mode, the process is similar. These

two modes of fatigue can take place simultaneously. Fracture by the internal fatigue process is observed, however, only when the surface fatigue process is suspended, because the rate of internal fatigue is lower than that of surface fatigue. Formation of microcracks, their growth and ordinary crack propagation, as well, are all slower than at the surface, because some restoration by reverse slip is possible, albeit partially. This gives one fundamental reason as to why the S–N curve for the internal fatigue mode is shifted to the right, as compared to the curve for the surface fatigue mode (Nishijima and Kanazawa, 1999).

Ultrasonic fatigue is not only possible at a mean load of zero ($R = -1$), but also under positive or negative preloads ($R \neq -1$), if both ends of the specimen are attached to the load fixture. Other technique has also been developed to perform torsional fatigue loading at ultrasonic frequencies (Stanzl-Tschegg and Mayer, 2001).

The crack growth process is described by the diagram on Figure 2.3.10, divided in 3 phases. The range of stress intensity range in the loading cycle (ΔK), is used as the driving force parameter. The K is proportional to the applied load, the square root of the crack length, and a geometric factor. ΔK is the difference between the maximum and minimum K in each load cycle, and hence is proportional to the applied load range. The rate of crack growth, $\frac{da}{dN}$, where a is the crack length and N is the cycle number, is measured over a range of ΔK and a plot constructed. There are three characteristic regimes, the near-threshold region at low ΔK, the Paris regime where the logarithm of $\frac{da}{dN}$ is linearly dependent on ΔK, and the regime of high crack growth rates near failure (Smithells, 2004).

Stage I is the transition from no propagation below a threshold value of ΔK_{th} to a finite crack growth rate. This is commonly observed for metals. The crack threshold (ΔK_{th}) is, according to ASTM International (2013), "*the highest value of the stress intensity range (ΔK) at which crack growth is not observed*" and it is overcome at the threshold speed (ΔV_{th}). Stage II, referred to as macro-cracking, involves the propagation of a fatigue crack through the majority of the cross-section. Generally, it takes up the majority of the crack growth stage and the Paris' Law is the most used method to relate the fatigue crack growth rate. Stage III defines the final moments of fatigue crack growth when the remaining cross-section is unable to sustain the applied load, and brittle fracture or ductile collapse occurs (Liu, 2019). This last phase is characterized by the critical stress intensity range (ΔK_{cr}) at the critical speed (ΔV_{cr}).

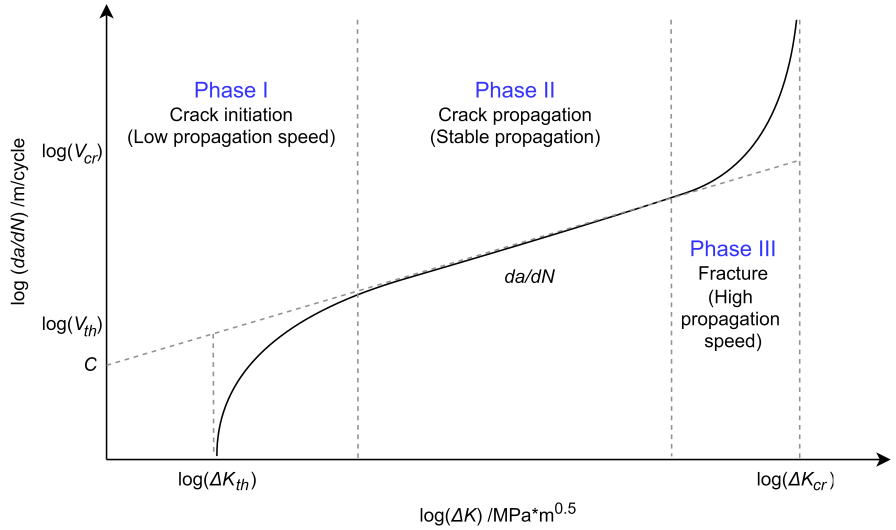


Figure 2.3.10: Crack growth diagram with the three fracture modes (adapted from (Abou Jaoude, 2015; Krasovskyy and Virta, 2014; Paris and Erdogan, 1963))

In terms of the linear elastic fracture mechanics crack growth can be described by the Paris power law (Krasovskyy and Virta, 2014; Paris and Erdogan, 1963):

$$\frac{da}{dN} = C(\Delta K)^m \tag{2.18}$$

where C and m are the material and environment parameters ($0 < C << 1, 2 < m < 4$) (Abou Jaoude, 2015).

Nishijima and Kanazawa (1999) in their studies verified a trend for the crack growth rate to be higher for hard materials, as closure is weak due to lack of plasticity, hence internal fatigue for hard materials is not so slow as compared to less-hard materials. In other words, the transition gap can be smaller between the S–N curves for the surface failure mode and the internal failure mode.

Most of the fatigue test equipment are uniaxial test machines. However, it is generally recognised that multiaxial stresses occur in many full-scale structures, being rare the occurrence of pure uniaxial stress states (Rodrigues da Costa et al., 2020).

The first method of multiaxial testing uses solid and thin-walled cylinder specimens (tubes), whereas the second one employs cruciform specimens. The combined tension-torsion test is commonly used to assess the fatigue life of shafts. Nevertheless, besides allowing for only a few stress states to be simulated, it requires the material to come in the form of circular tubes, being difficult to be applied to rolled sheet and composite materials. However, a cruciform specimen is able to be subjected under combined tension-torsion for UFT in the VHCF regime (Costa et al., 2017). Typical biaxial in-plane fatigue machines require four actuators precisely synchronised to ensure the symmetry and the immobility of the specimen, typically as the one on Figure 2.3.11 (Marques et al., 2021; Rodrigues da Costa et al., 2020).

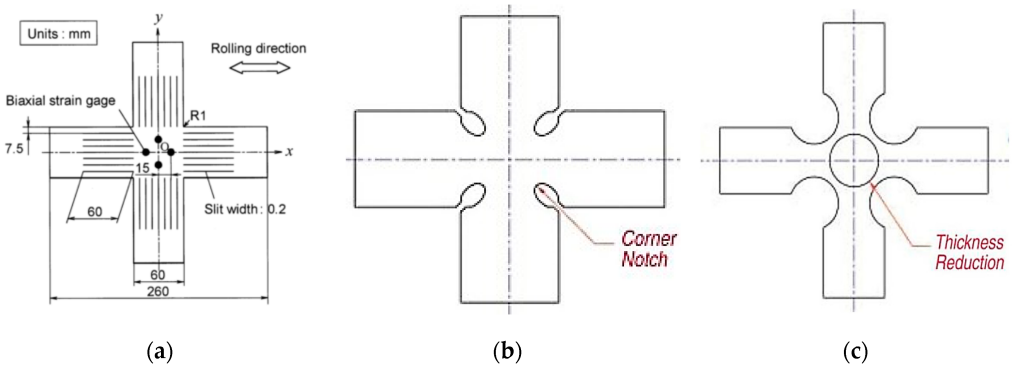


Figure 2.3.11: Typical biaxial cruciform specimens with: (a) slits; (b) elliptical notched corners; (c) circular-notched corners and reduced thickness at the centre (Rodrigues da Costa et al., 2020)

There is an absence of standards in the multiaxial testing methodology and more importantly in specimens, in contrast with uniaxial testing (Rodrigues da Costa et al., 2020). Rodrigues da Costa et al. (2020) tested a total of 7 specimens for each condition to failure, made from a ER9 steel, that complies with the European Standard EN 13262 + A1, from the rim of a railway wheel. Fatigue results on Figure 2.3.12, show the S-N curve, where fatigue strength increases for both uniaxial and multiaxial UFT, as well as for run-out specimens under VHCF conditions. In uniaxial run-out conditions, stress results have an increase of 11 % when tested in ultrasonic fatigue at 20 kHz in relation to conventional 5 Hz. The difference is more pronounced with 45 % higher stresses at 20 kHz, regarding the multiaxial experiment, and no failures during the entire duration of the tests. Their results support the existence of the frequency effect on the fatigue life. Since the material in this study has a predominant perlite phase, it results in little or no failure in the VHCF regime. On the other hand, the slope of the S-N curve from 10^6 cycles is very small (almost a flat plateau), making it extremely difficult to configure a stress state so that failure occurs at 10^7 and 10^8 cycles. Therefore, points at 10^9 cycles in Figure 2.3.12 are representing those that did not fail at all in the VHCF regime (run-out).

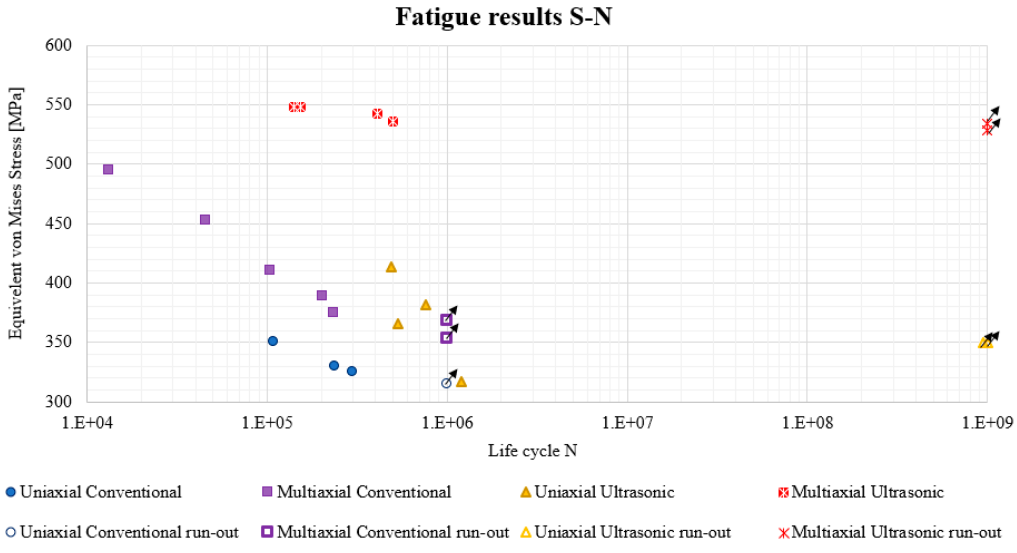


Figure 2.3.12: UFT tension/torsion stress life results (Rodrigues da Costa et al., 2020)

2.3.1 Historical advancements in gigacycle machines

In the beginning of the 20^{th} century, Hopkinson applied the piezoelectric techniques to fatigue tests, being this the first piezoelectric fatigue testing machine working in longitudinal resonance with 33 Hz (Anes et al., 2011). Fifty years later, in 1950, Mason introduced the piezoelectric and magneto restrictive types of transducers capable of convert 20 kHz electrical voltage signals into displacement controlled 20 kHz mechanical vibration and used high power 20 kHz ultrasonic waves to induce fracture of materials in fatigue. In 1959, Neppiras proposed to apply ultrasound for the determination of S-N curves aimed at developing methods of measuring fatigue life and fatigue limits under constant amplitude loading conditions at $R = -1$. In the attempt to reach higher frequencies, in the same year Girard presented a testing machine with 92 kHz as testing frequency but technology available did not guarantee a convincing correlation between results and experiments (Anes et al., 2011). In 1973, Mitsche applied ultrasound for the purpose of fatigue crack propagation testing (Stanzl-Tschegg and Mayer, 2001). Table 2.3.2 summarizes the developments in the 20^{th} century along with the main remarks.

Table 2.3.2: Overview on important steps in developing the ultrasonic fatigue technique for endurance and fracture mechanical investigations (Stanzl-Tschegg and Mayer, 2001)

Authors	N	$\frac{da}{dN}$ (m/cycle)	Remarks
Mason (1956)			First application of ultrasound to fracture materials in fatigue
Neppiras (1959)	1E8		First S–N-curves of brass, Al-alloy DTD 423, Araldite
Thiruvengadam (1972)	1E9		First corrosion fatigue studies on 1020 carbon steel in 3% NaCl solution
Mitsche (1973)		1E-8 to 1E-7	First application of 20 kHz ultrasound to measure (da/dN vs ΔK) curves (mild steel)
Stanzl and Mitsche (1977)		4E-10	First threshold measurements on 13% Cr steel and mild steel in different environments (water, oil) and at different temperatures (ambient air, liquid nitrogen)
Stanzl (1981)	1E9	5E-13	First random amplitude loading with 20 kHz, using feedback and computer control
Ebara et al. (1982)	1E10		Corrosion fatigue of 13% Cr steel and Ti-6Al-4V in NaCl solution. Influence of cyclic frequency on corrosion fatigue properties
Tschegg et al. (1991); Tschegg and Stanzl-Tschegg (1990)		5E-13	Superposition of static axial and shear loads (mode II, III) to ultrasonic vibrations
Mayer et al. (1996); Stanzl-Tschegg et al. (1993)	1E9		First torsion fatigue investigations at ultrasonic frequency (2024-T351, ZrO_2)

2.4 Working principle of the VHCF machine

The VHCF machine consists of a piezoelectric stack displacing a test specimen. Test specimens are designed on the basis of the wavelength of their operating frequencies and the speed at which sound travels through the given material. Over time, 20 kHz has become the norm for ultrasonic fatigue testing mainly because of the wide selection of power supplies, transducers, and various safety considerations (Ilie et al., 2020).

There are three main systems in the configuration proposed by Mason (1956) (section 2.3.1) and, later, by Bathias: the resonant system, the data acquisition system and the cooling system. To develop high stresses in the tested specimen, UFT requires cycle loading at its longitudinal resonance frequency (20 kHz) (Dimitrov and Argirov, 2014). The design of the machine is developed with the geometry of the resonant element as output. The other resonant components are purchased in the market and adapted to the machine (Bathias and Paris, 2004). The welded machine stand houses the converter, booster and horn in a rigid, column-mounted cabinet. A pneumatically activated carriage mechanism applies pressure to the part, and an electronic programmer controls ultrasonic exposure and clamping time (Emerson Industrial Automation, 2022).

The system resonance frequency is given in function of the natural frequency by Eq. 2.19.

$$\omega_r = \omega_n \sqrt{1 - 2\xi^2} \tag{2.19}$$

Since the system is undamped (Eq. 2.20), we get to Eq. 2.21.

$$\xi = 0 \tag{2.20}$$

$$\omega_r = \omega_n \tag{2.21}$$

The data acquisition system (DAQ) provides the displacement control and stores the data through means of a software. Usually, other software is also needed to calibrate the machine and acquire the displacement for each load %. On the other hand, the temperature control system is composed of a cooling fluid jet and pyrometers to measure the temperature. During UFT, due to the effect of internal friction, frequently the temperature increases significantly, which may influence the behaviour of the specimen. Therefore, the sample should be cooled down with usually clean and dry compressed air, however some specimens need be submerged in water for improved cooling (Bathias and Paris, 2004). For this reason, the specimen is stressed for a short-time to avoid unallowable heating. Afterwards, a cooling phase has to be integrated, which can last longer than the testing phase to allow the temperature of the specimen to be within an acceptable range. Taking into account the time for cooling, the effective testing time is considerably lower than the nominal testing frequency (Wagener et al., 2011).

The resonant system is subdivided into four main components: a signal generator, a piezoelectric transducer/piezoceramic converter, booster and an amplifier cone, also denominated as horn or sonotrode (Sharma et al., 2020). They are detailed as follows:

- **Signal Generator**: Transforms a 50 Hz or 60 Hz voltage signal into a 20 kHz sinusoidal electrical signal. It controls the displacement amplitude and guarantees the system's resonance regime. The ultrasonic generator has closed loop control of driving voltage and frequency in order to keep the resonance conditions and the constant vibration amplitude during the test (Dimitrov and Argirov, 2014). The machine gets feedback

and in function of the theory and material properties, the software (Supersonic in the case of Shimadzu USF-2000) applies the desired stress for the certain signal generated that causes a displacement.

- **Piezoelectric transducer**: Modifies the electrical signal into longitudinal ultrasonic waves and mechanical vibrations with the same frequency. Tests with $R = -1$ are characterized by the fact that the specimen has one of the ends free. For tests with $R > 0$, there is a second cone attached to the other end of the specimen (Bathias and Paris, 2004).

- **Booster and Amplifier cone/horn**: The vibration amplitude of the piezoelectric transducer is small (between 5 μm and 20 μm), so the booster and cone are designed in order to increase the vibration amplitude (and consequently the stress). The booster, besides its amplifying characteristics, will be responsible for clamping the system to the static steel plate of the machine at a nodal zone. The result will depend on the components geometry and the electrical signal received from the converter (Bathias and Paris, 2004; Emerson Industrial Automation, 2022).

All resonant elements are mechanically connected by a screw connection; the piezoelectric actuator is connected to the booster which in turn is connected to the horn. The specimen is screwed to the end of the horn (Anes et al., 2011).

The vibration of the specimen generates acoustical waves in it through a power concentrator (sonotrode) in order to obtain desired displacement and an amplification of the stress in the middle of the specimen (Dimitrov and Argirov, 2014).

In a vibration system, the number of displacement nodes must be reduced since it is easier to excite the system when the order of vibration mode is low. For a fatigue test, the specimen centre must be a displacement node because of the mechanical symmetry of the specimen. The vibration at the position where static load is applied has to be avoided. The displacement nodes are interleaved with a stress nodes so that there is a stress node at each end of the specimen. Consequently, there will be four nodes of displacement (DN) and five nodes of stress (SN), as shown in Figure 2.4.1, which is a representation of the UFT machine for a load ratio $R = -1$ (Bathias and Paris, 2004).

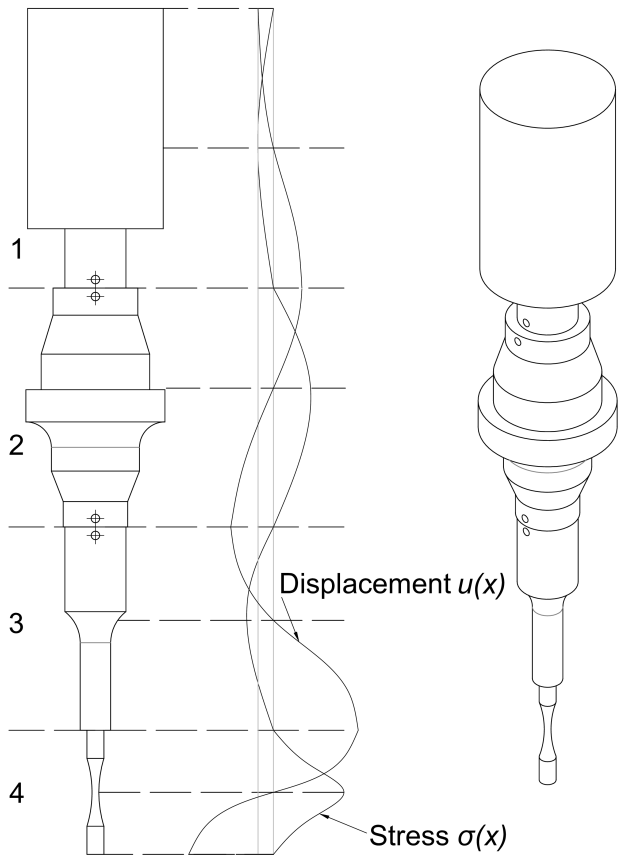


Figure 2.4.1: Ultrasonic fatigue machine model with smooth specimen. Displacement and stress representation. 1 - Piezoelectric transducer; 2 - Booster; 3 - High-gain Horn/Sonotrode; 4- Specimen (adapted from Dimitrov and Argirov (2014))

The generator excites the transducer causing a vibration which is then amplified. Between the transducer and the cone, the booster is dispensable but it allows a better connection and the support of the whole resonance system. The displacement amplitude reaches its maximum point at the end of the test specimen, which can be measured by a dynamic sensor (probe). While the maximum stress is reached in the intermediate section of the specimen (like it can be seen on Figure 2.4.1). The same happens with the horn since its two ends move in opposite directions, lengthening and shortening the horn (Emerson Industrial Automation, 2022). A strain gauge directly bonded to the specimen surface can be used to measure stresses (Bathias and Paris, 2004). In this case, the cyclic stress amplitude is calculated from the measured strain amplitudes by assuming linear elastic behaviour and by using Hooke's law and the Young's modulus (Stanzl-Tschegg et al., 2002).

The mechanical system formed by the transducer, the cone and the specimen is linear, as well as the stresses and displacement fields because the components vibrate in resonance in the elastic domain of the materials. Therefore, it is necessary to only measure the displacement amplitude of one of them. The lower end of the specimen being free avoids a large and heavy arrangement to secure as it is common in conventional testing equipment. Thus, an UFT machine is portable and relatively low cost.

The piezoelectricity is the ability of some crystals to generate electrical voltage in response to a mechanical pressure or vice versa. The piezoelectric effect is understood as

the linear electromechanical interaction between the mechanical force and the electrical state in crystalline materials such as ceramics and polymers. The most common material is lead zirconate titanate (PZT), an electrostrictive element which expands and contracts at its resonant frequency when excited by electrical energy (Emerson Industrial Automation, 2022). Thus, the transducer consists of ceramic plates that expand and contract when they are electrically induced. The voltage is proportional to the expansion or contraction, that is, the voltage is proportional to the displacement of the mechanical system (Bathias and Paris, 2004).

For transducers, the limits of usefulness of the material (strain saturation, fatigue, limiting temperature, etc) may serve to establish its power capability. The piezoelectric materials used within this application may be classified into seven groups: quartz crystal, water-soluble crystals, single crystals with high melting point, piezoelectric semiconductors, piezoelectric ceramics, piezoelectric polymer materials and piezoelectric ceramic composites. It can be shown that piezoelectric ceramics present the widest variety in their elastic, electric and piezoelectric constants and, in general terms: have the most favourable properties for ultrasonic transducers. In addition, the ceramic materials can be formed into a large variety of shapes and sizes and the polar axis can be directed according to the geometry and the vibration mode. Ceramics to be used as transducers require electrodes plated onto the element. These electrodes generally consist of a thin metal film, such as gold, silver, chromium or nickel (Gallego-Juarez, 1989).

The leading position of the lead zirconate titanates is due to their strong piezoelectric effect and high Curie point, together with the wide range of properties they offer. The advantage of such compositions is that mixtures richer in titanium have tetragonal crystal symmetry, while those richer in zirconium are rhombohedral. Changes in properties may be induced by replacing small fractions of the constituents with other elements (Gallego-Juarez, 1989).

The booster and horn are manufactured with the same material, which must be a good combination of acoustical and mechanical properties, so as the transducer (Bathias and Paris, 2004). Titanium has the best acoustical properties of the high strength alloys and its high fatigue strength enables it to withstand high cycle rates at high amplitudes. Furthermore, its high hardness proportionates better endurance against wear. Branson utilizes Titanium 7-4 to fabricate most of the catalogue horns. This higher end grade of titanium is roughly 15% stronger than the more common Titanium 6-4 grade (Ti6Al4V), allowing it to withstand higher stresses. In the other hand, this material is more expensive owing to the higher cost of the material and machining time (Emerson Industrial Automation, 2022).

Some types of amplifiers have complex shape whose analytical solutions are unknown, so the dimensioning is strictly done by finite elements. In comparison to the machine, the specimen must be relatively small to present high intrinsic frequencies (Bathias and Paris, 2004).

Generally, ultrasonic machines use a criterion to stop the test when the frequency decreases more than 0.5 kHz, since fatigue cracks increase the compliance/decrease the stiffness and reduce the cycling resonance frequency. Thus, if the displacement control system detects a frequency lower than 19.5 kHz, the test is stopped. However, if the crack grows rapidly, the change in vibration amplitude may be too large, beyond the control range (Bathias and Paris, 2004).

2.5 Working principle of HCF resonance machine

HCF machines can be of resonance pulsation type. Resonant Fatigue Tester Machines are very often used for fatigue tests (S-N curves) or in the fracture mechanics for pre-cracking and crack propagation tests. The advantages over servo-hydraulic systems with its actuators, valves and pumps is that maintenance is not required due to the wear-resisting construction. Plus, they provide a short testing time, better efficiency, variable frequency and they do not require a cooling system. However they do need a soundproofing chamber due to the frequency being in the audible spectrum, unlike ultrasonic machines (Rumul, 2022).

This type of test stand is powered by an electromagnetic drive and brings a system consisting of two oscillating masses, the specimen and further components such as clamping devices into resonance vibration. The number of oscillating weights can be adjusted to retrieve the highest possible test frequency with the resonating system. The test frequency cannot be chosen freely, like in servo hydraulic machines, which is probably one of the major disadvantages of all test systems based on resonance vibration. However, contrary to the UFT system, the load amplitudes can vary significantly with a load range from 5 kN up to 1,000 kN (Zimmermann, 2018).

Moreover, although the specimen geometry should be designed as a rotationally symmetric sample, there are more degrees of freedom to develop component-like test strategies, e.g., in turbine industry (Zimmermann, 2018).

Only the lower VHCF range can be tested in a reasonable time frame. Much more promising in this respect is a newly developed resonance pulsation test stand operating at a test frequency around 1,000 Hz developed by the Swiss company Russenberger Prüfmaschinen. This innovative test system load allows to perform cycles even up to 10^8 in reasonable time. Still, the determination of the true strain applied at frequencies beyond 1,000 Hz is a concern (Zimmermann, 2018).

More information about the Rumul machine's components is detailed in Chapter 4.6.

2.6 Effect of a stress concentration factor (notch)

The notch effect on the fatigue resistance of components varies considerably with its geometric features. Under external loads, geometric discontinuities unavoidably raise stress concentrations as well as complex stress-strain responses within the structure (see Figure 2.6.1) and thus result in complex fatigue problems and induce surface fatigue cracks. The concept of theoretical stress concentration factor K_t is defined by ASTM International (2013) as "*the ratio of the greatest stress in the region of a notch or other stress concentrator (...) to the corresponding nominal stress*". It is represented by (Liao et al., 2020):

$$K_t = \frac{\sigma_{max}}{\sigma_{nominal}} \tag{2.22}$$

where σ_{max} and $\sigma_{nominal}$ are the maximum stress at notch tip and the nominal normal stress under pure elastic state, respectively. However, it is widely accepted that the use of K_t yields non-conservative predictions during fatigue lifetime evaluation of ductile materials or structures with sharp notches. Moreover, it cannot effectively characterize the relationship between fatigue strengths of smooth and notched specimens, since it generally yields conservative predictions on the endurance of engineering components under cyclic loadings (D. Pilkey, 2007; Liao et al., 2020).

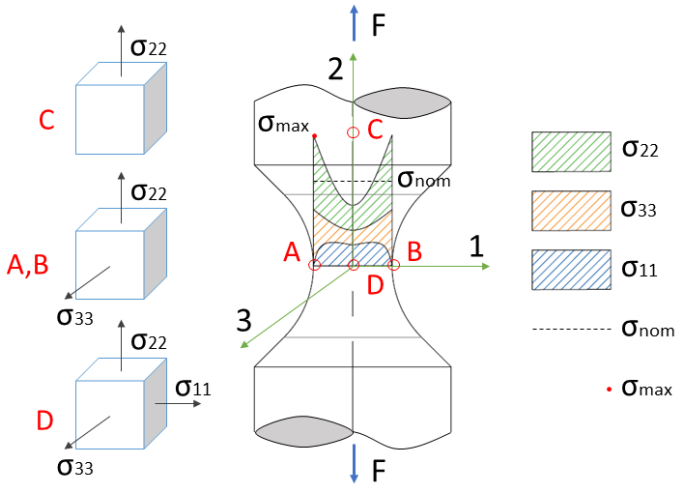


Figure 2.6.1: Geometrical interpretation of stress distributions under uniaxial loadings on axisymmetric notched body with K_t=1.25 (adapted from Liao et al. (2020))

The inhomogeneous stress distribution (on Fig. 2.6.1) explains why actual fatigue life of notched parts under cyclic loadings are generally longer than those predicted by utilizing the peak stress-strain data. The reason is when regions near the surface fleetly exceed the material yield strength and plastic deformation occurs, the internal part of the body still supports the highly stressed area since it is less stressed, often in elastic regime, and thus slows the progression of crack initiation, propagation, and eventual fracture (Liao et al., 2020).

The fatigue notch sensitivity, q, is also important to characterize a material. It is determined by comparing the fatigue notch factor, K_f, and the stress-concentration factor, K_t, for a specimen of a given size containing a stress concentrator of a given shape and size. ASTM International (2013) defines the K_f as "*the ratio of the fatigue strength of a specimen with no stress concentration to a specimen with a stress concentration for the same percent survival at N cycles and for the same conditions*". The fatigue notch sensitivity is given by Eq. 2.23 (ASTM International, 2013; Boyer, 1997; D. Pilkey, 2007).

$$q = \frac{K_f - 1}{K_t - 1} \tag{2.23}$$

in which q may be stated as percentage and its values varies between zero (where $K_f = 1$) and 1 (where $K_f = K_t$). By a mathematical reorganization, the K_f is as in Eq. 2.24 (Boyer, 1997).

$$K_f = 1 + q(K_t - 1) \tag{2.24}$$

Lindblom (1970) studied the notch sensitivity of nodular cast iron while Elangeswaran et al. (2020) studied the fatigue performance of 18Ni300 maraging steel. Both determine the K_f by the ratio between the smooth and notched specimens fatigue limit, as it is on Eq. 2.25.

$$K_f = \frac{\sigma_{smooth}}{\sigma_{notched}} \tag{2.25}$$

However, other authors like Hans (2003) and Sharifi and Rahgozar (2009) calculated the K_f and q based on the 50 % probability fatigue limits for powder metallurgy steels

and structural steels, respectively. Zhang et al. (2015) studied the distribution of the K_f in function of the number of cycles and temperature.

Torizuka et al. (2012) studied the gigacycle ultrasonic fatigue test on a notched specimen of the steel 30C with a yield strength of 929 MPa, having a stress concentration factor of $K_t = 2$. Most of the notched specimens failed in a fatigue life range from 10^5 to 10^6 cycles, not overcoming the 10^7 cycles. This means that the notched specimens do in fact have a fatigue limit. Their results had a good agreement with those of conventional electromagnetic resonance fatigue testing, i.e., the frequency effects are negligible. The fracture type was a conventional surface fracture originating from a notch root. The ultra-fine grained steel is less prone to internal fracture, so it showed a fatigue limit.

Investigations of smooth specimens show that failure in the VHCF region occurs in metals with a face-centred cubic lattice, where a real fatigue limit could not be found yet, and in metals with a body-centred cubic lattice, especially in (very) high-strength steels, with fatigue strength values below the conventional fatigue limit (Berger et al., 2008).

On the other hand, LCF and HFC region depending on the sharpness of the notch the fatigue strength of notched specimens is considerably lower in comparison to smooth specimens. This difference decreases with the increase of the lifetime, depending on the stress amplitude. In the VHCF region depending on the material condition, notches can have no influence on fatigue strength and subsurface failure can occur (Berger et al., 2008).

Berger et al. (2008) investigated smooth specimens made of the quenched and tempered steel 42CrMoS4 under rotating bending and tension compression loading (Figure 2.6.2). They found out the failure was due to internal inclusions, in contrary, failure in notched specimens always started at the surface, at lower stress amplitude.

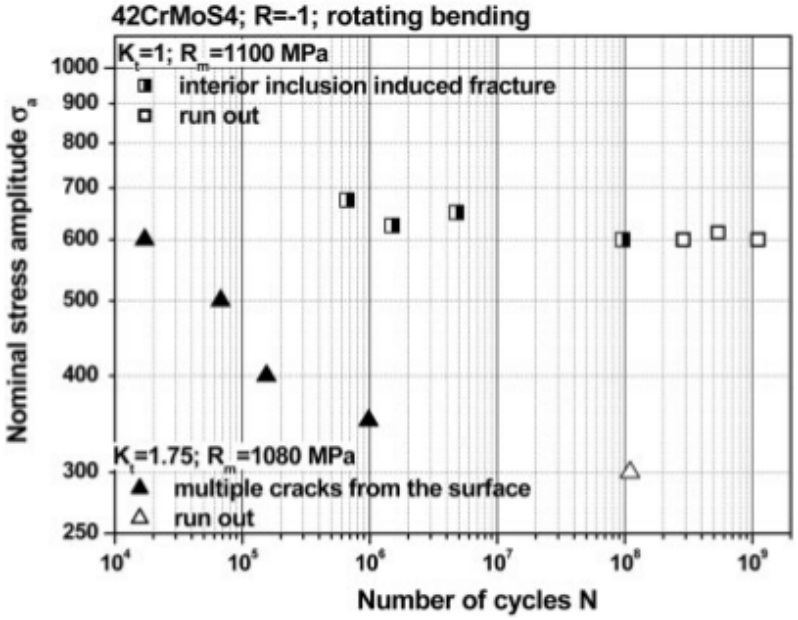


Figure 2.6.2: S-N diagram for quenched and tempered steel $42CrMoS_4$, $R = -1$, $f = 50$ Hz (Berger et al., 2008)

Qian et al. (2010) studied the VHCF behaviour of the structural steel 40Cr for smooth and V-notched specimens at conventional frequency of 52.5 Hz. For hourglass specimens, a stepwise S–N curve was revealed, having surface crack initiation in the regime of less than 10^7 cycles, while interior crack initiation was dominant in VHCF regime. For notched

specimens, they noticed a continuously decreasing curve and that there are multiple fatigue crack origins starting predominantly from the surface. The maximum stress for notched specimen is the nominal stress without consideration of the stress concentration factor (Figure 2.6.3).

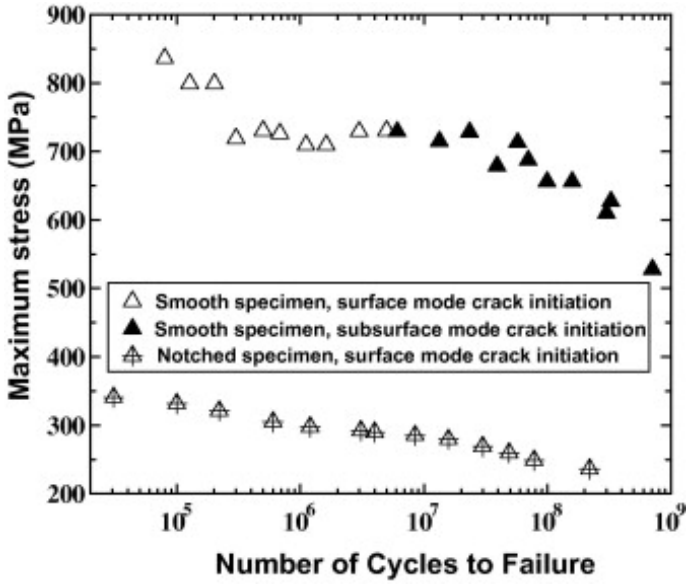


Figure 2.6.3: S–N curve of 40Cr material with smooth and notched specimens (Qian et al., 2010)

Their studies appointed out a fish-eye in the vicinity of a non-metallic inclusion at the fracture origin in VHCF regime. The inclusion depth and size increased and decreased, respectively, with an increment of fatigue life. The stress intensity range of fish-eye implied the failure was due to a process of small crack propagation. The non-metallic inclusion in the interior of specimen tends to de-bond from surrounding matrix and then to form a crack. At relatively low loading level, the possibility of crack initiation at subsurface increases with respect to large inclusion size, small grain size, smooth surface condition and large strength of material (Qian et al., 2010). The most influential parameters of inclusions are their size, their elastic properties, and their adhesion to the matrix. When Young's modulus of an inclusion is greater than the one of the matrix, a stress concentration is generated around the inclusion under a tensile stress. Young's modulus of the sulphides is usually lower than that of the matrix, which makes sulphides relatively harmless. Hard inclusions with low deformability may cause microcrack formation at the interface when the material is hot rolled, leading to fatigue cracks (Pineau and Forest, 2017).

Figure 2.6.4 illustrates the fatigue strength reduction by notches. In VHCF, the effect of notches may diminish when the fracture takes place in the interior region out of stress concentration. When the stress concentration is large and the stress required for crack initiation from a notch is small, the S–N curve will have a knee at around $N_f = 10^6$ as in ordinary HCF tests (Akiniwa et al., 2006).

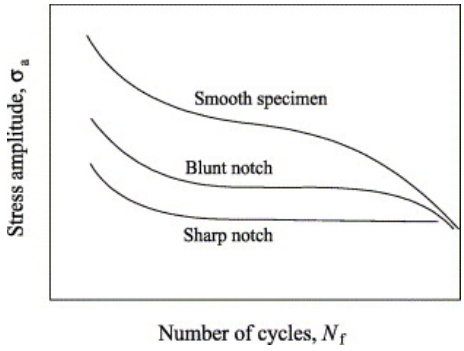


Figure 2.6.4: Fatigue strength reduction by notches (Akiniwa et al., 2006)

2.6.1 Concentration factor definition (K_t)

Ebara (2017) studied the ultrasonic (20 kHz & $R = -1$) very high cycle fatigue behaviour of the High Speed Steel YXR3 (HRC 60.7) with ultimate tensile strength of 2217 MPa for 3 concentration factors. It was studied to prevent forging die failure and to improve its life. The high cycle fatigue test specimens were notched round bars with 6 mm at minimum diameter. The S-N diagrams of plane and notched specimens of YXR3 steel in high cycle region are shown in Figure 2.6.5.

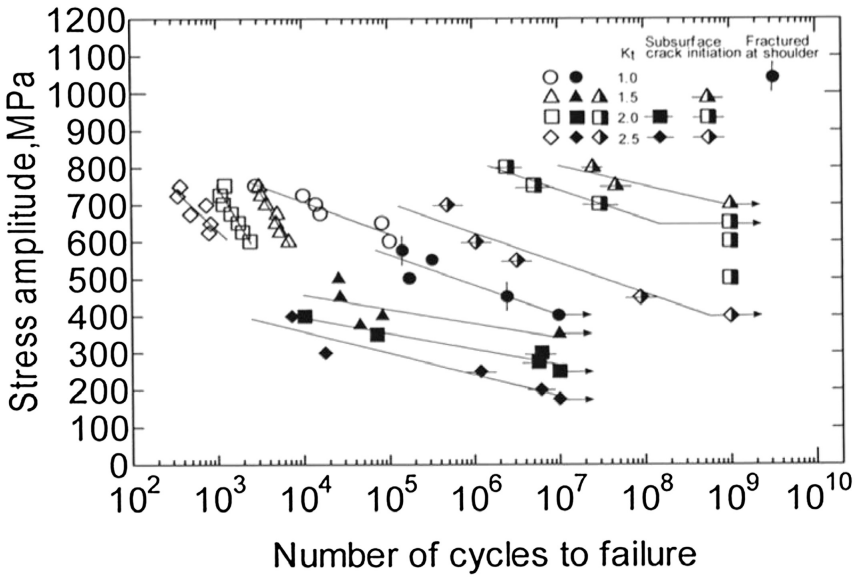


Figure 2.6.5: $S - N$ diagrams of plane and notched YXR3 steel (Ebara, 2017)

They found the fatigue limit at 10^9 cycles for the notched specimens with $K_t = 1.5$, 2.0, and 2.5 was 700, 650, and 400 MPa, respectively. The higher the K_t, the smaller fatigue limit at 10^9 cycles. This phenomenon was same as those of low and high cycle fatigue testing results of YXR3 steel. The higher fatigue strength in UHCF compared to HCF test is attributed to the frequency effect (previously discussed in section 2.3) (Ebara, 2017).

In plane bar specimen, crack initiated at subsurface as the fatigue failures observed on low cycle fatigue fracture surfaces. On the contrary, crack initiation site was changed from the notched surface to subsurface at failed number of cycles over than 10^6 for all notched specimens with K_t of 2.0 and 2.5. The subsurface crack initiated at carbides.

Thus, it can be emphasized that the subsurface crack initiation can be observed in high cycle regime over than 10^6 cycles even for the notched specimen in YXR3 steel with high ultimate tensile strength of 2192 MPa (Ebara, 2017).

Ebara (2017) observed that at the ultrasonic regime, the fatigue crack was initiated at nonmetallic inclusions located at subsurface for all notched specimens. Nevertheless, subsurface crack initiation was also observed in the high carbon chromium bearing steel SUJ2 (HRC 63.3) with K_t of 1.8.

Ritz and Beck (2017) studied different K_t such as 1.09, 1.31 and 2.42 in ultrasonic GCF testing up to a maximum number of load cycles of $2{\cdot}10^9$ for several load ratios ($-1 < R < 0.5$), on Figure 2.6.6. They noticed a transition from fatigue cracks initiated at the surface to internal cracks from oxide inclusions of the type AlCaO or AlCaMgO at N_f =$1{\cdot}10^7$ to $2{\cdot}10^7$. Plus, they noticed the fatigue life increases along with the R. While for $R = -1$ they had not experienced a failure for $N > 10^8$, samples failed even beyond $2{\cdot}10^9$ load cycles for $R = 0.5$. For all samples failed in the VHCF regime at $R = -1$, the fracture surface showed a region with increased roughness around the crack initiating inclusion indicating fine grained area formation (Figure 2.6.6) (Ritz and Beck, 2017).

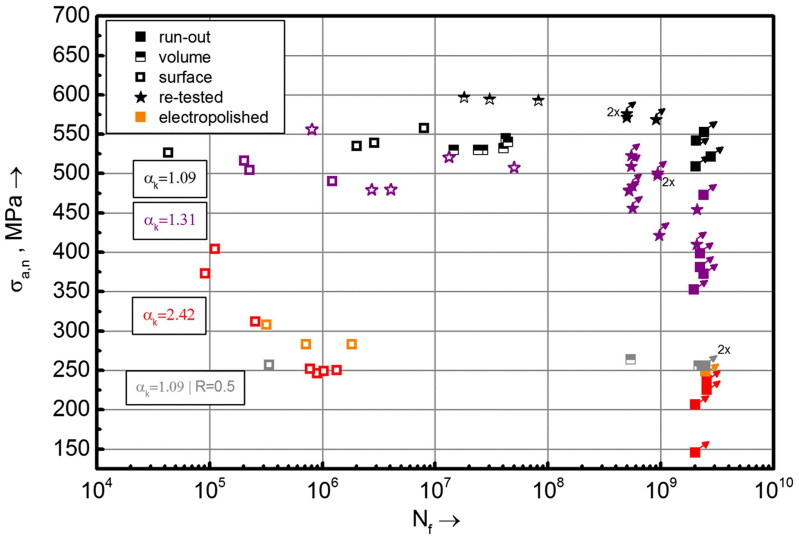


Figure 2.6.6: S-N curves for $K_t = 1.09$ ($R = -1$ and 0.5), $K_t = 1.31$ and $K_t = 2.42$ ($R = -1$) of the martensitic steel X10CrNiMoV12-2-2 (Ritz and Beck, 2017)

They found out the slope of the S-N curve for samples with stress concentration factor of $K_t = 2.42$ was, compared with $K_t = 1.09$, steeper in the LCF and HCF regime, which is typical for notched samples (Figure 2.6.6, red cubic symbols). Ritz and Beck (2017) did not get failure in the VHCF regime since the maximum fatigue life registered was $1{\cdot}10^6$. Their cracks were initiated exclusively at small defects within the notch resulting from the turning process. The probability of fatigue failure caused by an inclusion within this region was strongly reduced since the high stress concentration promoted a a smaller critical volume with sufficiently high local stresses for fatigue crack formation (Ritz and Beck, 2017).

Akiniwa et al. (2006) also studied notched specimens of a bearing steel SUJ2 under axial tension-compression by using UFT machines, with a $K_t = 2.39$. For all cases of circumferentially notched specimens, fatigue fracture started from the surface or very near, at the notch. The slip deformation was responsible for crack initiation in HCF and VHCF. Once again, the fatigue strength of notched specimens was lower than that of

smooth specimens, as it can be seen from Figure 2.6.7.

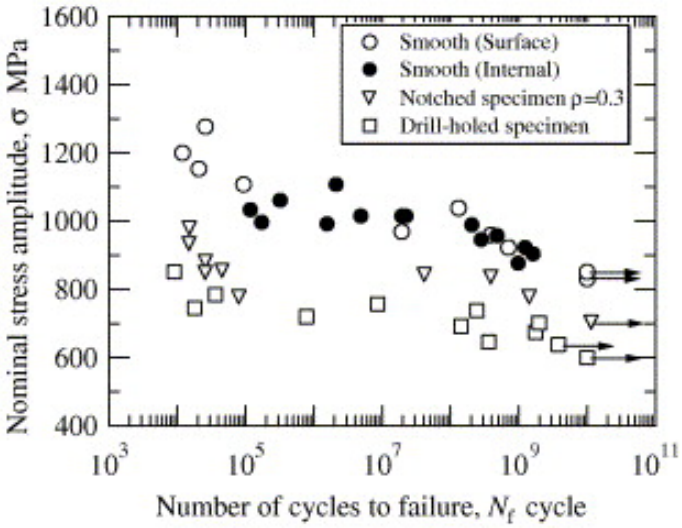


Figure 2.6.7: S–N curves of smooth, notched and drill-holed specimens of SUJ2 (Akiniwa et al., 2006)

Sadek et al. (2020) verified in their investigation that the influence of the notch ($K_t = 1.4$ with $R = 0.1$) at the gigacycle regime was negligible regarding the ferritic-pearlitic steel 38MnSiV5; in the martensitic 50CrV4, they had a slight increase in fatigue strength, and there was a decrease in carburized steel 16MnCr5. The fatigue strength decreases with higher R values for the 38MnSiV5 and 16MnCr5 grades, in spite of that, the 50CrV4 grade shows only a very small decrease in fatigue strength. For the notched specimens $K_t = 1.44$, all initiation sites should be located at, or close to, the surface because of the much higher local stresses at the surface, which is confirmed for 38MnSiV5 and 16MnCr5 grades.

Bathias (2012), besides the studies conducted for Figure 2.3.3, they also performed experimental tests on notched specimens (Figure 2.6.8). They observed a fatigue resistance far lower than for the smooth specimen, which is due to the larger stress concentration at notch surface. As for the smooth, the S-N curve slowly decreased after 10^6 cycles. This lead to a difference between the two S-N curves at 10^9 cycles smaller than that at 10^6 cycles (about 150 and 300 MPa), but the fatigue strength for notched specimens was ranging 600 MPa. For these results, the fatigue notch factor K_f, defined in Eq. 2.24, is around 1.35 at 1E+10.

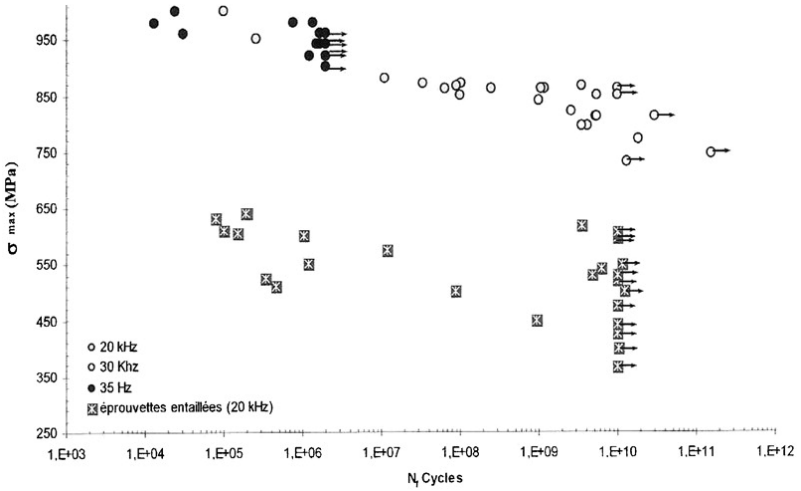


Figure 2.6.8: Gigacyle fatigue S-N curve of 100Cr6 with and without notch $R = -1$ (Bathias, 2012)

2.7 Variable amplitude loading

A specimen fatigue tested under continuous amplitude loading until a certain percentage (x %) of its fatigue life will have fatigue damage, although the damage is usually still invisible. This is because the material's original life (N) has been reduced to (100 - x)% of the fatigue life N (Schijve, 2009). When a component is subjected to variable loading conditions, the determination of its fatigue life is a complex issue (Lee, 2005). Owing to the low amplitudes, variable amplitude fatigue loading does not lead to a fatigue limit after testing times comparable to constant amplitude tests (Stanzl-Tschegg, 2014).

Variable amplitude loading is another domain to which the ultrasonic fatigue concept can contribute. Conventional tests often involve the modification of the load time sequence; however, ultrasonic tests can follow exactly the load sequences desired. Industrial applications of the ultrasonic fatigue data (constant amplitude and random amplitude) have been extended to aircraft, automobile, railway, offshore, and other structures, which have to withstand fatigue loads up to 10^9-10^{10} cycles (Stanzl-Tschegg and Mayer, 2001). Among them, some in-service loading conditions of aircraft do fall into the ultrasonic frequency region, giving more direct importance to ultrasonic fatigue technologies (Bathias and Paris, 2004).

For variable amplitude loading, it is found that ignoring the minor stress range that below continuous amplitude fatigue limit can be unsafe. Therefore, the S-N curves are advised to extrapolate beyond the knee point with a shallower slope at $m+2$ (i.e. 5 when $m = 3$) at 10^7 cycles (Liu, 2019).

The Palmgren-Miner linear damage rule, often referred to as simply Miner's rule (Miner, 1945) is a valuable tool in fatigue design. It is the first, simplest, and most widely used model to predict fatigue damage for structural components (Daniel and Paulus, 2019). The model is applied through a linear summation of the consumed life fraction per stress amplitude, where is assumed that failure occurs when the summation reaches unity (Bjørheim et al., 2022).

The Palmgren-Miner rule essentially acknowledges that the structure has a defined spectrum of total loading cycles, which cause damage to the structure over time. It works as follows (Daniel and Paulus, 2019):

- Convert the variable amplitude fatigue stress spectrum into a number mt of stress blocks, so that each block i has a constant stress range $\Delta\sigma_i$.
- Each block causes fatigue damage f_i. Being n_i the number of cycles of block i in the considered period (e.g., service life); and N_{fi} is the number of cycles to failure at i.

Then:

$$f_i = \frac{n_i}{N_{fi}} \tag{2.26}$$

This rule states that the considered object will fail when:

$$D = \sum_{i=1}^{mt} f_i = \sum_{i=1}^{mt} \frac{n_i}{N_{fi}} = 1 \tag{2.27}$$

Below the fatigue limit, load cycles are unable to create a growing microcrack under continuous amplitude loading, and thus can not cause failure, $N_2 = \infty$ and $n_2/N_2 = 0$. However, in many cases the linear rule often leads to non-conservative life predictions, i.e. failure before $D = 1$, since the fatigue damage accumulation material mechanisms are non-linear. The results from this approach do not take into account the effect of load sequence on the accumulation of damage due to cyclic fatigue loading (because $N = \infty$) (Bjørheim et al., 2022; Daniel and Paulus, 2019; Lee, 2005; Schijve, 2009). Thus, the outcome is a failure occurring at a sum lower than unity for decreasing load amplitude histories, but higher than unity for their increasing amplitude counterparts.

Some factors that are not considered and which limit this law's application and validation are: the variation of relative damage rate with stress and associated changes in fatigue mechanism, effect of the load at which a component fails, the low-level stress cycles, the strain hardening, the fretting as well as crack propagation considerations. Plus, Miner's rule is not able to fully cover the residual stresses introduced on high strength steels either deliberately to improve fatigue performance or unintentionally during the manufacturing process. They can also may be produced by local yielding at points of fatigue initiation under high loads in either direction (Heim, 2020).

In fact, if there was a decrease of amplitude from high to low fatigue loading, a crack might have initiated in the initial stress amplitudes, which would not happen for the equivalent percentage for a low amplitude fatigue loading. As an example, the first block of loading cycles can create a growing crack, which can then be propagated by a second lower stress block. In view of the stress singularity at the tip of the existing crack, a contribution to further crack growth is possible, which can indeed lead to failure. This also applies for more complex load histories including load cycle amplitudes above and below the fatigue limit. Experimental evidence of completely reversed loading conditions indicates $D > 1$ for a low-to-high loading sequence, and $D < 1$ for the opposite, high-to-low sequence (Fatemi and Yang, 1998).

Despite the shortcomings of Miner's rule, it is still commonly recommended in both Eurocode 6 and DNVGL (Bjørheim et al., 2022; Schijve, 2009).

It is not well documented, if a fatigue limit or a threshold value exists under variable amplitude conditions (Stanzl-Tschegg et al., 2002). Stanzl et al. demonstrated that no fatigue limit was obtained for the C45 steel at 10^{10} cycles for the Miner's distribution, though a fatigue limit exits under constant amplitude loading. They justify this outcome because the maximum stress value of several pulses or at least one pulse during the random sequence was higher than the fatigue limit. They would expect a long fatigue limit of about

10^{15} for random loading, if the maximum value of the sequence was below the constant amplitude fatigue limit (Stanzl-Tschegg et al., 2002).

The variable load sequences can be overloads and underloads. Besides these, the most commonly used sequences to study the load composed of interaction phenomenon are high-low (Hi-Lo), low-high (Lo-Hi) and change in stress ratio block load sequences as schematically represented on Fig. 2.7.1.

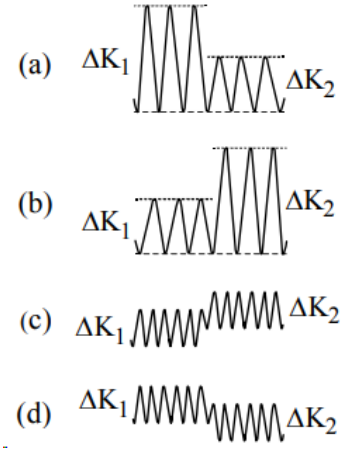


Figure 2.7.1: Schematic representation of two-level block loading: a) high-low; b) low-high; c) and d) Step in stress ratio (Ribeiro et al., 2011)

Nakajima et al. (2002) studied the VHCF behaviour of a high carbon chromium steel, JIS SUJ2, until 2.0×10^9 cycles, under variable amplitude loading. Their tests were performed using cantilever-type rotating bending fatigue testing machine for a steel with fatigue limit of 1275 MPa at constant amplitude loading. At stress levels above and below the fatigue limit, the fracture modes were the surface related and the subsurface crack initiation (fish-eye), respectively. They found out that subsurface crack nucleation took place at the early stage of fatigue life. Their studies conclude that the fracture modes derived from the high to low stress levels sequence were subsurface crack initiation and the cumulative damage ($\sum n/N$) is around 1. On the other hand, applying low to high stress levels, the fracture modes were different and the cumulative damage became considerably larger than the unit.

2.8 The S690QL Steel

Steels of high mechanical strength combined with high toughness, such as those in quenched and tempered condition (like the S690QL) are required to reduce weight in industrial machinery (Pinto et al., 2009). The advantages, in particular in high overloads, are safely and economically borne even with a low tare weight, whether in the steel industry, in machine building or in the production of transport equipment (Union Stahl, 2022). These materials develop their high strength from complex heat-treatments, rather than rely merely on more alloy elements. Heat treatment grants steels better performance in yield/tensile strength without sacrificing weldability compared to high alloy steels (Zhao et al., 2013). S690QL plates have higher payload capacity and are energy efficient, hence can be used in leaner structures. This steel is used in other applications such as heavy transportation, construction industry, machine building, and lifting equipment (Steel, 2022). The S690 steel grade has been used for penstocks since the mid-1970s, mainly for pumped storage

power projects having high water head and therefore high pressure (IMOA, 2011).

The S690QL is commonly adopted where higher strength is required, i.e. for long-span bridge components, bearing elements in high-rise buildings, off-shore structures and cranes, in power plants, mining applications or LPG vessel, etc. In quasi-static conditions and 20 °C, the ultimate tensile strength is 770 MPa (Cadoni and Forni, 2020; Liu et al., 2018). The use of quenched and tempered high strength steel in off-shore structures is still questionable. This happens because in the fatigue domain, besides the material's strength importance, it is also relevant the size and geometric parameters of structures, residual stress, stress ratio and loading conditions (Zhao et al., 2013). The increase of yield strength does not guarantee the corresponding improvement of fatigue resistance. Pedro et al. (2017) designed two bridges decks with the Eurocodes, one using standard S355NL and the other HSS S690 QL. They experimentally confirmed the S690 allowed the reduction of 25 % of the steel weight compared to the standard plate girder deck in S355 NL (Guo et al., 2020; Pedro et al., 2017). Even so, the S690QL is a steel that lacks efficient design rules nowadays and it is unknown the potential adverse effects of welding on their microstructures which lead to significant reductions in their mechanical properties, preventing its widespread application in construction engineering (Chung et al., 2020; Zhang et al., 2020).

The high strength S690 steels do have a good ductility under both monotonic and cyclic actions. The microstructure of the S690 is martensitic and significantly more refined than the microstructure of the S355 steel. The weldability of the high S690 is in general poorer than the weldability of mild steel due to the higher level of alloy elements. According to Liu et al. (2018), one of the major factors affecting structural stability of slender columns of S690 steel welded H-sections are the residual stresses, especially in the vicinity of heat affected zones (HAZ), (Liu et al., 2018; Ma et al., 2018). De Jesus et al. studied the microstructure of the S690 steel dominated by block quenched martensite. They found out it includes grain-refining elements such as aluminium, niobium and titanium and lower contents of phosphorus and sulphur since these elements have adverse effects on ductility and toughness, especially on quenched and tempered steels (de Jesus et al., 2012).

Monteiro (2019) studied the implementation of the S690QL high strength steel in a wind turbine tower which allowed a reduction in thickness, however limited by the buckling phenomenon. Their wind turbine tower was addressed as a hollow cylinder and their results showed that S690QL steel would be able to outperform the S355NL steel with half the thickness but would lead to tower collapse if reduced to a fourth of the original thickness.

Higher resistance to crack initiation of a High Strength Low Alloy (HSLA) steel grade such as S690 signifies its capability of sustaining a higher cyclic load before a crack can initiate and subsequently propagate. Also slower crack growth rates signify the capability of the alloy to resist crack propagation per loading cycle. Fatigue crack growth tests carried out using cyclic sinusoidal loading pattern revealed that the S690 performs better than the other steels throughout the range of ΔK (Shi, 2015).

De Jesus et al. proved that the S690QL steel, due to its superior yield strength, shows a higher resistance to fatigue crack initiation for structural components under stress control, for a wide range of stress concentration factors and applied stress ranges, covering both low and high cycle fatigue regimes, in comparison with the S355. The use of high strength steels increases the fatigue sensitivity of the structural detail to sharp notches reducing the fatigue life with respect to details made of mild steel (de Jesus et al., 2012).

Qiang et al. (2012b) studied the post-firing influence on the HSS S460 and S690. They discovered the S690 is more sensitive to reduce its yield strength during the tensile test after being heated up to 1000 ^{o}C. In another of their studies, they proved the S690 steel

suffers a decrease of yield and tensile strength with an increase of temperature, as it can be inferred from Fig. 2.8.1 (Qiang et al., 2012a).

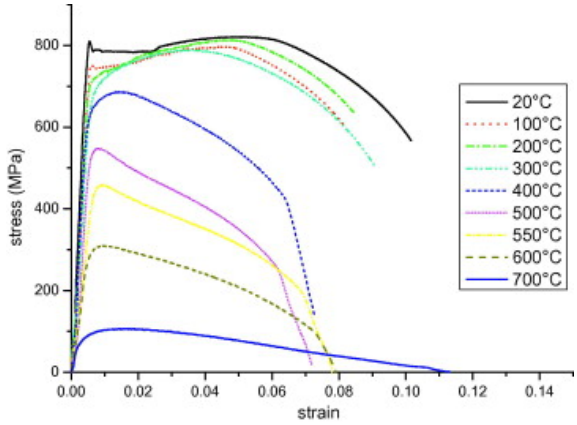


Figure 2.8.1: Stress–strain curves at various temperatures from steady state test (Qiang et al., 2012a)

2.8.1 High Strength Steels

High strength steels have this designation since their yield strength vary from 420 until 1100 MPa, besides presenting an interesting weldability and toughness. The carbon percentage between 0.18-0.25 % in the manufacturing of this type of steels leads to a substantial increase in strength. In spite of that, it restricts the material's weldability properties, so the quantity of carbon is limited in the range of 0.11 to 0.16 %. The loss of resistance is compensated by the addition of other elements such as manganese, niobium, molybdenum and vanadium. The guarantee of good weldability conditions for this type of steel is due to its low sulphur content, up to 0.006 % (Bjorhovde, 2004; Fu et al., 2018; Nova, 2018).

HSS have enhanced fracture toughness, cold bending property and weather resistance. Compared with conventional steel materials, these possess excellent strength to self-weight ratios, reduced tensile to yield strength ratios, and reduced elongations at fracture (Ma et al., 2018). Furthermore, they do not require pre heating for welding and they can do it at a lower temperature. This type of steels allows the cut-down of components' size, leaving more space and allowing more sustainable solutions (Fu et al., 2018).

In general, there are three main delivery conditions for these steel materials: a normalized rolled process, second a quenched and tempered process, and finally a thermo-mechanically controlled process (Liu et al., 2018). The process of steel production through heat treatment is the most used process nowadays, because it allows the maintenance of good weldability properties of steel (Nova, 2018). The base of strength enlargement is that the reduction of grain size of a given volume increases the surface of the grain boundaries and the phase boundaries, which at the same time increases the crystallographic defects, and due to this the energy of the material increases too. Consequently, the strength is increased, especially the yield strength. The reduction of the grain size also effects favourable on the impact test, besides that increases the Charpy impact energy, reducing the transition temperature as well (Dobosy and Lukács, 2014).

2.8.2 Mean curve estimation in function of the material properties

The fatigue limit (σ_f) found by Casagrande et al. (2011) on Equation 2.28 provides a reliable estimation relying on the Vickers Hardness of the material for HV < 400. However, it is interesting to predict the fatigue limit mean curve of the material based on its monolithic properties.

$$\sigma_f = 1.6HV \pm 0.1HV \tag{2.28}$$

The outcome of the methods depicted in this section for the mean curve estimation are displayed in Chapter 5, in comparison with the experimental data. The parameters for the S-N curves calculation are then exposed in Table H.0.1, in Appendix H.

A stress-based approach was the earliest but even now the most frequently used approach for fatigue limit prediction. A plot of the fatigue life vs true stress amplitude for a metal gives, in general, a curve in the Basquin (1910) form (Cui et al., 2014):

$$\sigma_a = \frac{E\Delta\varepsilon}{2} = \sigma'_f(2N_f)^b \tag{2.29}$$

where $2N_f$ is the number of load reversals to failure; σ_f' is the fatigue strength coefficient; b is the fatigue strength exponent with negative sign (Cui et al., 2014). In most practical cases of fatigue design, the critical location will be a notch in which plastic strains are imposed by surrounding elastic material. Thus, the situation will be strain controlled with a total strain range composed of an elastic and a plastic part (Cui et al., 2014).

The plastic strain amplitude ($\frac{\Delta\varepsilon_p}{2}$) is best described by the Coffin-Manson relationship (Cui et al., 2014; Manson, 1965):

$$\frac{\Delta\varepsilon_p}{2} = \varepsilon'_f(2N_f)^{c_d} \tag{2.30}$$

where ε_f' and c_d are the the fatigue ductility coefficient and exponent, respectively.

Manson (1965) proposed that a metal's amplitude to total strain cycling ($\Delta\varepsilon_a$) can be considered as a superposition of its elastic ($\Delta\varepsilon_e$) and plastic strain amplitude ($\Delta\varepsilon_p$). By combining Equations 2.29 and 2.30 (Cui et al., 2014).

$$\frac{\Delta\varepsilon}{2} = \varepsilon_a = \frac{\Delta\varepsilon_e}{2} + \frac{\Delta\varepsilon_p}{2} = \frac{\sigma'_f}{E}(2N_f)^b + \varepsilon'_f(2N_f)^{c_d} \tag{2.31}$$

The total strain life curve approaches the plastic strain life curve in the low cycle region and the stress life curve in the high cycle region as shown in Figure 2.8.2.

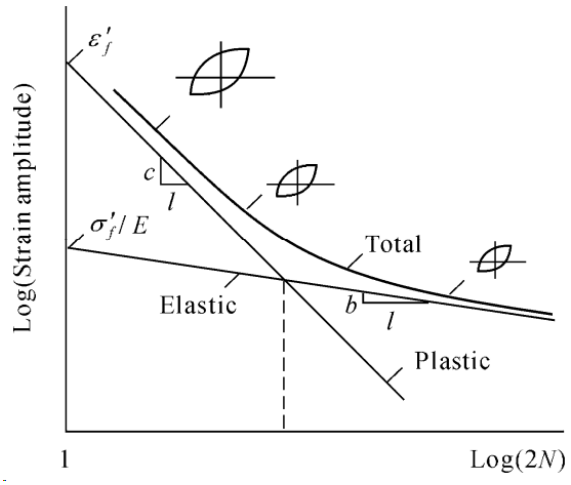


Figure 2.8.2: Representation of elastic, plastic and total strain resistance to fatigue loading (Cui et al., 2014)

Although the following equations of the methods are for the total curve of Figure 2.8.2, in the fatigue domain it is only considered the elastic part, i.e., without the plastic strain.

The Universal Slopes Method by Manson (1965) states the slopes of the elastic and plastic lines (b and c_d respectively in Equation 2.31) are assumed constant for all materials. From this assumption, the strain-life relation of Eq. 2.32 is developed when modified to match the standard M-C relationship form (Hartman, Derek, 2013; Meggiolaro and Castro, 2004; Ong, 1993). R_m stands for the tensile strength.

$$\frac{\Delta\varepsilon}{2} = 1.9018\frac{R_m}{E}(2N_f)^{-0.12} + 0.7579\varepsilon_f^{0.6}(2N_f)^{-0.6} \tag{2.32}$$

The Modified Universal Slopes Method (MUSM) (Eq. 2.33) by Muralidharan and Manson (1988) is just as the USM but the M-C parameters have been modified to give more accurate results (Hartman, Derek, 2013; Meggiolaro and Castro, 2004).

$$\frac{\Delta\varepsilon}{2} = 0.623\left(\frac{R_m}{E}\right)^{0.832}(2N_f)^{-0.09} + 0.0196\varepsilon_f^{0.155}\left(\frac{R_m}{E}\right)^{-0.53}(2N_f)^{-0.56} \tag{2.33}$$

Mitchell's Method (MM) by Mitchell (1979) follows the standard form of the M-C relationship (Eq. 2.31), where (Hartman, Derek, 2013; Meggiolaro and Castro, 2004):

$$\sigma_f = R_m + 345 \text{ (MPa)} \tag{2.34a}$$

$$b = -\frac{1}{6}\log\left(\frac{2\sigma_f}{R_m}\right) \tag{2.34b}$$

The development of Medians Method (MedM) by Meggiolaro and Castro (2004) is based on the assumption that the median value for each of the M-C parameters can be used for each material classification. MedM was developed under this assumption including 724 steels. The experimentally obtained M-C parameters to use in Eq. 2.31 are on Table 2.8.1 (Hartman, Derek, 2013).

Table 2.8.1: Calculated M-C parameters for steel for the Median's method (Meggiolaro and Castro, 2004)

	σ_f'	ε_f'	b	c_d
Steels	$1.5R_m$	0.45	-0.09	-0.59

The Uniform Material Law (UML) by Bäumel et al. (1990) was developed using 125 different materials. The method was developed so that only readily available properties (R_m, E) are required to allow for its easy use. For unalloyed and low alloy steels:

$$\frac{\Delta\varepsilon}{2} = 1.50\left(\frac{R_m}{E}\right)^{-0.087}(2N_f)^{-0.09} + 0.59\psi(2N_f)^{-0.58} \tag{2.35a}$$

$$\psi = 1.0 \qquad \text{for } \frac{R_m}{E} \leq 0.003 \tag{2.35b}$$

$$\psi = \left(1.375 - 125.0\frac{R_m}{E}\right) \qquad \text{for } \frac{R_m}{E} > 0.003 \tag{2.35c}$$

The Hardness Method (HM) by Roessle and Fatemi (2000) is a simple method for estimating the M-C parameters for steels using only readily available properties: Brinell hardness and elastic modulus. The fatigue strength and ductility exponents (b and c_d) were taken to be the same as MUSM since similar results were found for the steels studied (Hartman, Derek, 2013).

$$\frac{\Delta\varepsilon}{2} = \frac{4.25HB + 225}{E}(2N_f)^{-0.09} + \frac{0.32HB^2 - 487HB + 191000}{E}(2N_f)^{-0.56} \tag{2.36}$$

The approach by Basan et al. (2011) found that there is no link between any of the M-C parameters, the ε_f', b and c_d are independent of monotonic material properties and σ_f' is related to Brinell hardness. Therefore they take an approach similar to MedM and these M-C parameters are constant. It will be called M-C 2010. The equation is 2.31 and its constants are obtained by a linear regression of the data for the high-strength low-alloy steels AISI4140 and AISI4142 (Hartman, Derek, 2013).

In a later stage, Basan et al. (2015) defined a new table of constants, which will be denominated M-C 2015.

Chapter 3

Specimen design for gigacycle fatigue testing

The design of gigacycle fatigue specimens is very important since the specimen must match the machine fixed excitation frequency and it must have a zero displacement node on the middle of the specimen gauge section for the maximum stress. This chapter describes thoroughly the methodology adopted to calculate analytically the specimen's dimensions, and displacement and stress along the axis. Firstly, an introduction about the longitudinal elastic waves and resonance frequency is presented. Then, the equations for the smooth/hourglass specimen are exposed, followed by the notched specimens. These last specimens formulation use some of the assumptions taken for the smooth specimens.

The finite element method is described and results critically compared taking into consideration the previous analytical solution.

3.1 Mechanical wave transmission model

In conventional fatigue tests, the frequency is enforced by the external load system of the test machine, which is different from the natural frequencies of the specimen, and the specimen is in forced vibration. An ultrasonic fatigue test differs from this in since the external frequency supplied by the test machine must be one of the natural frequencies of the specimen (Bathias and Paris, 2004). The mechanical wave classical transmission model is the basis for the analytical determination of the equations that describe the strain, stress and displacement on a specimen.

3.1.1 Longitudinal elastic waves and resonance frequency

Recalling the elastic wave theory, the differential equations for a general three-dimensional isotropic elastic body in a Cartesian co-ordinate system are (Bathias and Paris, 2004):

$$\rho\frac{\partial^2 u}{\partial t^2} = \frac{E}{(1+\nu)}\left(\frac{1}{1-2\nu}\frac{\partial e}{\partial x} + \nabla^2 u\right) \tag{3.1a}$$

$$\rho\frac{\partial^2 v}{\partial t^2} = \frac{E}{(1+\nu)}\left(\frac{1}{1-2\nu}\frac{\partial e}{\partial y} + \nabla^2 v\right) \tag{3.1b}$$

$$\rho\frac{\partial^2 w}{\partial t^2} = \frac{E}{(1+\nu)}\left(\frac{1}{1-2\nu}\frac{\partial e}{\partial z} + \nabla^2 w\right) \tag{3.1c}$$

where u, v, and w are displacements along x, y, and z respectively, E and ν the ∇^2 the Laplacian, and (Bathias and Paris, 2004):

$$e = \frac{\partial u}{\partial x} + \frac{\partial v}{\partial y} + \frac{\partial w}{\partial z} \tag{3.2}$$

is the volume dilatation.

Elastic wave theory indicates that the following two types of wave may exist in an infinite isotropic elastic body. For a longitudinal wave, the curl of the displacement field is zero and the velocity of wave propagation is (Bathias and Paris, 2004):

$$\rho \frac{\partial^2 u}{\partial t^2} = \frac{E}{(1+\nu)} \left(\frac{1}{2(1-2\nu)} + \frac{1}{2} \right) \frac{1}{c^2} \frac{\partial^2 u}{\partial t^2} \tag{3.3}$$

$$c = \sqrt{\frac{E(1-\nu)}{(1+\nu)(1-2\nu)\rho}} \tag{3.4}$$

For a transverse wave, the volume dilatation e vanishes and the velocity of wave propagation is (Bathias and Paris, 2004):

$$\rho \frac{\partial^2 u}{\partial t^2} = \frac{E}{(1+\nu)} \left(\frac{1}{(1-2\nu)} * 0 + \frac{1}{2} \right) \frac{1}{c^2} \frac{\partial^2 u}{\partial t^2} \tag{3.5}$$

$$c = \sqrt{\frac{E}{2(1+\nu)\rho}} \tag{3.6}$$

If there is a boundary, a surface wave may also be produced. This wave is similar to the gravity surface wave in a fluid. The amplitude of vibration decreases rapidly with the distance from the surface, and the wave velocity is less than the velocity inside the body. The discussion is simplified employing a one dimensional specimen of straight cylinder. As shown in Figure 3.1.1, a longitudinal elastic wave comes from one end of the bar and travels through the length l, then it is reflected from the other end and returns to the initial place of entrance.

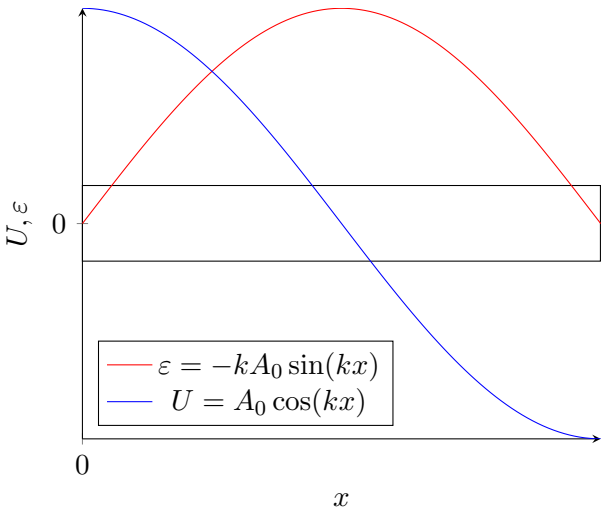


Figure 3.1.1: Displacement and strain variation along an elastic bar (Bathias and Paris, 2004)

The wave velocity c will be determined directly from Eq. 3.3 with ν=0 for consideration of this one-dimensional example (Bathias, 1999; Kolsky, 1964):

$$c = \sqrt{\frac{E}{\rho}} \tag{3.7}$$

The following deductions will be most likely affected by this reduction of a tridimensional problem to unidimensional approach. The differential Eqs. 3.1a to 3.1c reduce to a single equation:

$$\frac{\partial^2 u}{\partial t^2} = \frac{E}{\rho}\frac{\partial^2 u}{\partial x^2} \tag{3.8}$$

The solution of Eq. 3.8 is given by

$$u = \sum_{n=1}^{\infty} u_n(x,t) \tag{3.9}$$

where

$$u_n(x,t) = \left(A_{n-1}\cos\frac{n\pi ct}{l} + B_{n-1}\sin\frac{n\pi ct}{l}\right)\cos\frac{n\pi x}{l} \tag{3.10}$$

The boundary conditions of ultrasonic fatigue testing require the displacement to be maximum at both ends (A_0) whereas the strain vanishes at the same places (Bathias and Paris, 2004). That is,

$$\left(\frac{\partial u}{\partial x}\right)_{x=0,l} = 0 \tag{3.11}$$

Thus Eq. 3.9 and 3.10 for the first mode of vibration ($n = 1$) becomes

$$u_n(x,t) = A_0\cos(kx)\sin(\omega t) \tag{3.12}$$

where

$$k = \frac{\pi}{l}, \omega = \frac{\pi c}{l} \tag{3.13}$$

The amplitude of vibration at each point along the bar is

$$U(x) = A_0\cos(kx) \tag{3.14}$$

where A_0 is the displacement amplitude at the end of the bar. The strain ε of each point is given by the derivate of Eq. 3.14

$$\varepsilon(x,t) = -kA_0\sin(kx)\sin(\omega t) \tag{3.15}$$

with its maximum

$$\varepsilon(x,t) = -kA_0\sin(kx) \tag{3.16}$$

The strain rate is given by the derivate of Eq. 3.16

$$\dot{\varepsilon}(x,t) = -k\omega A_0\sin(kx)\cos(\omega t) \tag{3.17}$$

with its maximum

$$\dot{\varepsilon}(x,t) = -k\omega A_0 \sin(kx) \tag{3.18}$$

From Eqs. 3.7 and 3.13, the length of the bar is:

$$l = \frac{1}{2f}\sqrt{\frac{E_d}{\rho}} \tag{3.19}$$

for generating the first mode of vibration, where $f = \omega/(2\pi)$ is the frequency and E_d the dynamic elastic modulus for consideration of dynamic effects.

In conclusion, the length of resonance of the one dimensional specimen is given by Eq. 3.19 for the first vibration mode. The displacement node (where the displacement vanishes/equal to 0) at the centre of the specimen corresponds to the maximum strain, stress and strain rate. At both ends, there is the maximum of displacement and the nodes of strain, stress and strain rate. That is:

$$u = 0, \varepsilon = -kA_0, \sigma = -E_d k A_0, \dot{\varepsilon} = -k\omega A_0 \qquad \text{for } x = \frac{l}{2} \tag{3.20a}$$

$$U = A_0, \varepsilon = 0, \sigma = 0, \dot{\varepsilon} = 0 \qquad \text{for } x = 0, l \tag{3.20b}$$

Equation 3.19 indicates that the resonance length is inversely proportional to the frequency. This explains why some very high frequencies- for example, 92 kHz and 199 kHz- are not practicable. These frequencies lead to smaller specimen's which are prone to have difficulties in machining, displacement, or strain measurements, as well as energy dissipation. There are available different specimen's length according to its resonance frequency, as the example of Table 3.1.1 for a typical steel specimen of uniform section with $E = 200\,000$ MPa, $\rho = 7800$ kg/m^3 (Bathias and Paris, 2004).

Table 3.1.1: Comparison between the specimen's length for different test frequencies (approximate values) (Bathias and Paris, 2004)

f (kHz)	l (mm)
20	127
92	27.5
199	13.2

3.1.2 Analytical solution for the variable section smooth specimen

The theory explained in this chapter is the one used by Shimadzu (UFT machine's brand) and it comes detailed in Bathias and Paris (2004) work. For a fatigue specimen of variable section, amplitudes of strain and stress vary at each section. The resonance amplitude that is a function of the specimen geometry is generally determined numerically. In order to obtain stress concentration in the middle of the specimen to expedite a fatigue test, the specimen for ultrasonic fatigue initiation or fatigue crack growth is, in most cases, designed with a reduced section in the centre as shown in Figure 3.1.2. The L_1 represents the resonance length, the determination of which involves an exponential form to determine an analytical solution (Bathias and Paris, 2004).

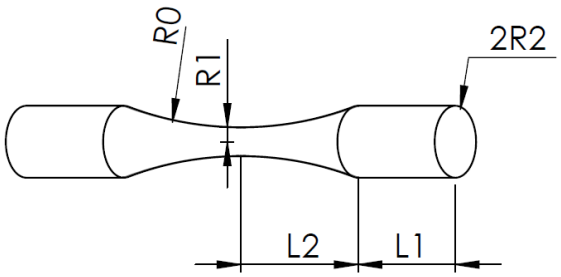


Figure 3.1.2: Ultrasonic specimen geometry (adapted from Bathias and Paris (2004))

The longitudinal wave equation for a specimen with a varying cross section can be written as

$$\rho S(x)\frac{\partial^2 u}{\partial t^2} = \frac{\partial f}{\partial x} \tag{3.21}$$

where $S(x)$ is the area of cross section at position x, and

$$f = E_d S(x)\frac{\partial u}{\partial t} \tag{3.22}$$

is the force acting on the section. Thus we have

$$\frac{\partial^2 u(x,t)}{\partial t^2} = c^2\left(p(x)\frac{\partial u(x,t)}{\partial x} + \frac{\partial^2 u(x,t)}{\partial x^2}\right) = 0 \tag{3.23}$$

where $p(x) = \frac{S'(x)}{S(x)}$ and $c = \sqrt{\frac{E}{\rho}}$ like in Eq. 3.7

Under the boundary conditions that ultrasonic fatigue specimens must satisfy, the solution to Eq. 3.23 takes the form $u(x,t) = U(x)\sin(x,t)$, and the equation for the amplitude of vibration $U(x)$ (see Eq. 3.14) at each point along the specimen can be easily obtained:

$$U''(x) + p(x)U'(x) + k^2 U(x) = 0 \tag{3.24}$$

where, as in Eq. 3.13, k is

$$k = \frac{\omega}{c} \tag{3.25}$$

To obtain the solution of Eq. 3.24, it must be defined the curve in the central part of the specimens given in Figure 3.1.2. For the axisymmetric specimen, the curve of the profile as a hyperbolic cosine in Eq. 3.26b facilitates the posterior integration.

$$y(x) = R_2, \qquad L_2 < |x| \leq L \tag{3.26a}$$

$$y(x) = R_1\cosh(\alpha x), \qquad 0 < |x| \leq L_2 \tag{3.26b}$$

where

$$L = L_1 + L_2, \alpha = \frac{1}{L_2}\operatorname{arccosh}\left(\frac{R_2}{R_1}\right) \tag{3.27}$$

To solve the differential equation, the circumferential solution for the variable section is discarded because it is difficult to integrate. It is implemented instead the hyperbolic

approach. On Figure 3.1.3, the inverse hyperbolic cosine function is represented by the blue line. The shaded area assumes the value $a/2$ and the vertex of this corresponds to the hyperbolic sine and cosine, on the y and the x axis respectively.

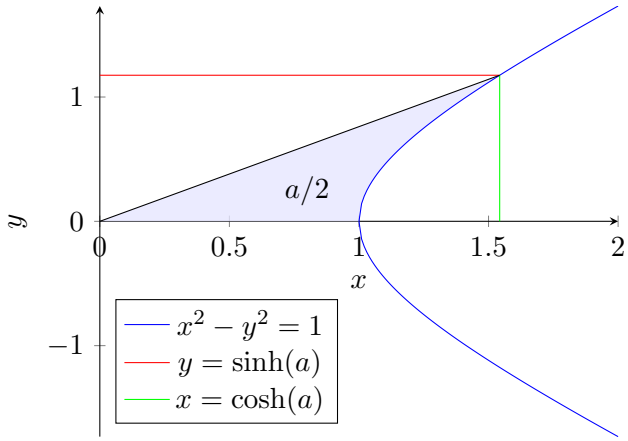


Figure 3.1.3: Graphic of a line through the unit hyperbola at the point $(\cosh(a), \sinh(a))$, where a is twice the area between line ray, the hyperbola, and the x-axis

Having this, the Eq. 3.26b corresponds to x, the hyperbolic cosine of Figure 3.1.3 and a is defined as

$$a = \operatorname{arccosh}(x) \tag{3.28}$$

Substituting the 1 for R_1 and accounting the specimen's maximum radius being R_2, using Eq. 3.29, the y comes as Eq. 3.26b. The L_2 corresponds to the length of half bowstrings and also marks the end of the hyperbola.

$$y(L_2) = R_1 \cosh\left(\frac{L_2}{L_2} \operatorname{arccosh}\left(\frac{R_2}{R_1}\right)\right) \tag{3.29}$$

Looking back to Eq. 3.24, to obtain the displacement the $p(x)$ comes solved taking into consideration the cross section area (Bathias and Paris, 2004):

$$S(x) = R_2^2, \qquad L_2 < |x| \leq L \tag{3.30a}$$
$$S'(x) = 0, \qquad L_2 < |x| \leq L \tag{3.30b}$$
$$p(x) = 0, \qquad L_2 < |x| \leq L \tag{3.30c}$$

The Eq. 3.24 comes then as

$$U''(x) + k^2 U(x) = 0, \quad L_2 < |x| \leq L \tag{3.31}$$

The ordinary differential equation of second order has complex conjugate roots, so the solution has the general form:

$$U(x) = C_1 \cos(kx) + C_2 \sin(kx), \quad L_2 < |x| \leq L \tag{3.32}$$

The derivate gives the strain and has the following form:

$$U'(x) = -C_1 \sin(kx) + C_2 \cos(kx), \quad L_2 < |x| \leq L \tag{3.33}$$

In the other hand, for the variable section of the specimen the Eq. 3.24 to calculate its area along the x axis:

$$S(x) = \pi[R_1 \cosh(\alpha x)]^2, \qquad |x| \leq L_2 \tag{3.34a}$$
$$S'(x) = 2\pi\alpha R_1^2[\sinh(\alpha x)\cosh(\alpha x)], \qquad |x| \leq L_2 \tag{3.34b}$$
$$p(x) = 2\alpha \tanh(\alpha x), \qquad |x| \leq L_2 \tag{3.34c}$$

Substituting once again in Eq. 3.24,

$$U''(x) + 2\alpha \tanh(\alpha x)U'(x) + k^2U(x) = 0, \quad |x| \leq L_2 \tag{3.35}$$

Removing the term $U'(x)$, it is possible to solve Eq. 3.35. For that, it is introduced function w:

$$w(x) = \cosh(\alpha x)U(x), \quad |x| \leq L_2 \tag{3.36}$$

That leads to:

$$w'(x) = U'(x)\cosh(\alpha x) + \alpha \sinh(\alpha x)U(x), \quad |x| \leq L_2 \tag{3.37}$$

$$w''(x) = [U''(x) + 2\alpha \tanh(\alpha x)U'(x) + \alpha^2 U(x)]\cosh(\alpha x), \quad |x| \leq L_2 \tag{3.38}$$

Comparing Eq. 3.35 to Eq. 3.38, it is obtained:

$$w''(x) = (\alpha^2 - k^2)\cosh(\alpha x)U(x) \qquad \text{or} \tag{3.39a}$$
$$w''(x) - (\alpha^2 - k^2)w(x) = 0 \tag{3.39b}$$

This equation has real roots so the general solution is:

$$w(x) = C_3 \exp(\beta x) + C_4 \exp(-\beta x), \quad |x| \leq L_2 \tag{3.40}$$

Where β is defined as:

$$\beta = \sqrt{\alpha^2 - k^2} \tag{3.41}$$

The definition (Eq. 3.36) gives the general solution of Eq. 3.35 on Eq. 3.42.

$$U(x) = \frac{C_3 \exp(\beta x) + C_4 \exp(-\beta x)}{\cosh(\alpha x)}, \quad |x| \leq L_2 \tag{3.42}$$

The displacement solutions for the cylindrical part (Eq. 3.32) and the reduced section part (Eq. 3.42) are found with four constants C_1, C_2, C_3 and C_4. These constants can be calculated by applying the appropriate boundary and continuity conditions.

The displacement at the specimen's end (L) is maximum and given by A_0 as in Eq. 3.20b, which must be equal to the displacement equation of the cylindrical part (Eq. 3.32):

$$C_1 \cos(kL) + C_2 \sin(kL) = A_0 \tag{3.43}$$

The same is verified to the strain that is null (Eq. 3.32) and allows to relate C_1 and C_2 using Eq. 3.33.

$$C_2 = C_1 \tan(kL) \tag{3.44}$$

From these two relationships,

$$C_1(\cos(kL) + \sin(kL)\tan(kL)) = A_0 \tag{3.45}$$

so that:

$$C_1 = A_0\cos(kL), C_2 = A_0\sin(kL) \tag{3.46}$$

Consequently, after a trigonometrical operation, the displacement amplitude for the cylindrical part is:

$$U(x) = A_0\cos(k(L-x)), \quad |x| \leq L_2 \tag{3.47}$$

The strain comes as displayed on Eq. 3.48.

$$U'(x) = kA_0\sin(k(L-x)), \quad |x| \leq L_2 \tag{3.48}$$

For the variable section, the centre of the specimen is a node ($U(0) = 0$ in Eq. 3.20a). Therefore, from Eq. 3.42:

$$C_3 = -C_4 \tag{3.49}$$

and Eq. 3.42 comes as:

$$U(x) = \frac{2C_3\sinh(\beta x)}{\cosh(\alpha x)}, \quad |x| \leq L_2 \tag{3.50}$$

The strain verified on the variable section is understandably given by Eq. 3.51:

$$U'(x) = \frac{2C_3(\beta\cosh(\beta x)\cosh(\alpha x) - \alpha\sinh(\beta x)\sinh(\alpha x))}{\cosh^2(\alpha x)}, \quad |x| \leq L_2 \tag{3.51}$$

From the continuity conditions at $x = L_2$, the displacement amplitude $U(L_2)$ so as the strain amplitude $U'(L_2)$ calculated from the solutions for both cylindrical (Eq. 3.47 and 3.48) and variable section (Eqs. 3.50 and 3.51) must be equal. This gives:

$$A_0\cos(k(L-L_2)) = \frac{2C_3\sinh(\beta L_2)}{\cosh(\alpha L_2)} \tag{3.52}$$

$$kA_0\sin(k(L-L_2)) = \frac{2C_3(\beta\cosh(\beta L_2)\cosh(\alpha L_2) - \alpha\sinh(\beta L_2)\sinh(\alpha L_2))}{\cosh^2(\alpha L_2)} \tag{3.53}$$

Combining Eqs. 3.52 and 3.53, reminding that $L = L_1 + L_2$, the value of k comes in Eq. 3.54,

$$k\tan(kL_1) = \beta\coth(\beta L_2) - \alpha\tanh(\alpha L_2) \tag{3.54}$$

which allows to calculate the specimen's resonance length L_1, dependant of the L_2 that is an input value.

$$L_1 = \frac{1}{k}\arctan\left(\frac{1}{k}\left(\beta\coth(\beta L_2) - \alpha\tanh(\alpha L_2)\right)\right) \tag{3.55}$$

The total length is defined as $2L$. Since C_3 is determined by Eq. 3.52, the solution for Eq. 3.50 is found. The solution of Eq. 3.24 is:

$$U(x) = A_0\phi(L_1, L_2)\frac{\sinh(\beta x)}{\cosh(\alpha x)}, \qquad |x| \leq L_2 \tag{3.56a}$$

$$U(x) = A_0\cos(k(L-x)), \qquad L_2 < |x| \leq L \tag{3.56b}$$

where,

$$\phi(L_1, L_2) = \frac{\cos(kL_1)\cosh(\alpha L_2)}{\sinh(\beta L_2)} \tag{3.57}$$

With this solution, deriving Eq. 3.56a and 3.56b it is easily obtained the strain and stress for the reduced section part and for the cylindrical part.

For the reduced section part ($|x| \leq L_2$):

$$\varepsilon(x) = A_0\phi(L_1, L_2)\frac{(\beta\cosh(\beta x)\cosh(\alpha x) - \alpha\sinh(\beta x)\sinh(\alpha x))}{\cosh^2(\alpha x)} \tag{3.58a}$$

$$\sigma(x) = EA_0\phi(L_1, L_2)\frac{(\beta\cosh(\beta x)\cosh(\alpha x) - \alpha\sinh(\beta x)\sinh(\alpha x))}{\cosh^2(\alpha x)} \tag{3.58b}$$

For the cylindrical part ($L_2 < |x| \leq L$):

$$\varepsilon(x) = kA_0\sin(k(L-x)) \tag{3.59a}$$

$$\sigma(x) = EkA_0\sin(k(L-x)) \tag{3.59b}$$

During the experimental test, the specimen will most likely present a fatigue failure in the maximum nominal stress section. As it was seen on Figure 3.1.1, this is verified on the middle of the specimen which corresponds to $x = 0$. Hence the strain and stress are, respectively, Equations 3.60a and 3.60b.

$$\varepsilon(0) = \beta A_0\frac{\cos(kL_1)\cosh(\alpha L_2)}{\sinh(\beta L_2)} \tag{3.60a}$$

$$\sigma(0) = \beta EA_0\frac{\cos(kL_1)\cosh(\alpha L_2)}{\sinh(\beta L_2)} \tag{3.60b}$$

3.1.3 Analytical solution for the variable section for notched specimen

The theory to determine the notched specimen's dimension was based on the Chapter 3.1.2, from the work of Bathias and Paris (2004). To once again solve Eq. 3.24, the specimen's shape in the central part must be defined. For the axisymmetric specimen, it has a circumferential part followed by a straight one, from where some relations can be deduced (Figure 3.1.4).

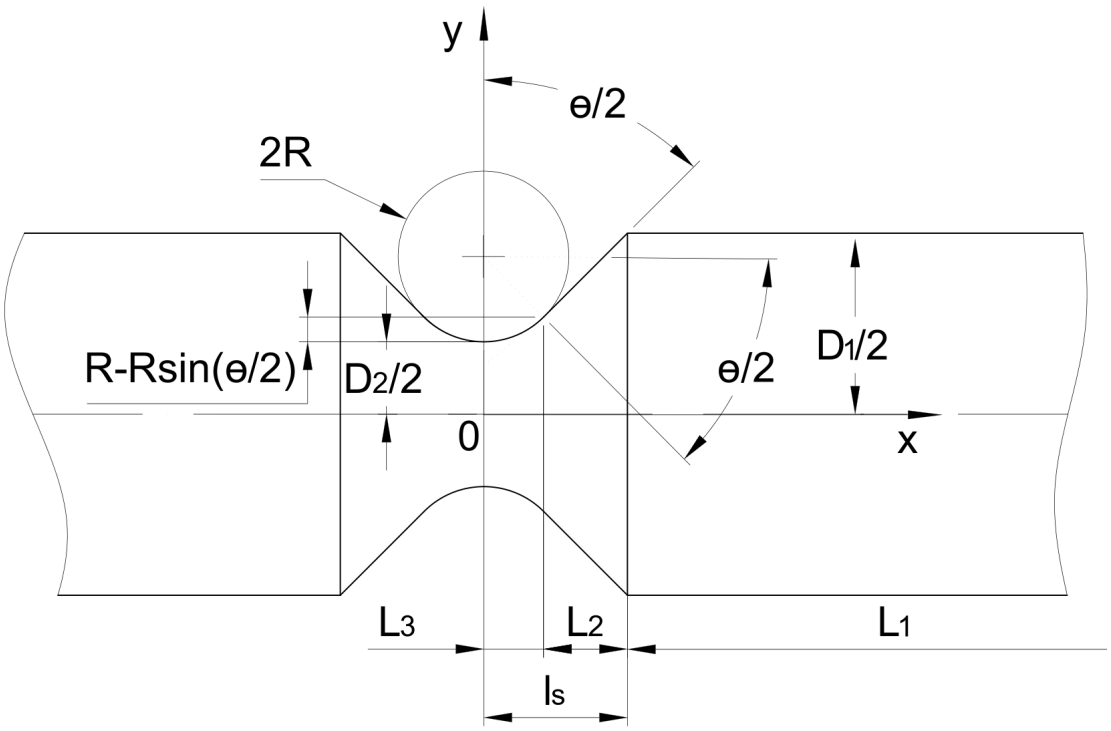


Figure 3.1.4: Geometrical variables of the notched specimen

For the cylindrical part there is Eq. 3.61:

$$y(x) = \frac{D_1}{2}, \quad l_s < |x| \leq L \tag{3.61}$$

The Eq. 3.62 defines the slope of the straight part of the notch:

$$\frac{1}{\tan(\frac{\theta}{2})} \tag{3.62}$$

The length of L_3 and L_2 is given in function of θ as it can be seen from Figure 3.1.4.

$$L_3 = R\cos\left(\frac{\theta}{2}\right) \tag{3.63a}$$

$$L_2 = \tan\frac{\theta}{2}\left(\frac{D_1 - D_2}{2} - R + R\sin\left(\frac{\theta}{2}\right)\right) \tag{3.63b}$$

$$l_s = \tan\frac{\theta}{2}\left(\frac{D_1 - D_2}{2} - R + R\sin\left(\frac{\theta}{2}\right)\right) + R\cos\left(\frac{\theta}{2}\right) \tag{3.63c}$$

where

$$L = L_1 + l_s \tag{3.64a}$$

$$l_s = L_2 + L_3 \tag{3.64b}$$

Having the coordinates where the cylindrical part starts $(l_s, D_1/2)$ the equation for the straight part can be found and then simplified to Eq. 3.65b.

$$y(x) = \frac{x}{\tan(\frac{\theta}{2})} + \frac{D_2}{2} + R - R\sin\left(\frac{\theta}{2}\right) - \frac{L_3}{\tan(\frac{\theta}{2})}, \qquad L_3 < |x| \leq l_s \tag{3.65a}$$

$$y(x) = \frac{D_1}{2} + \frac{x - l_s}{\tan(\frac{\theta}{2})}, \qquad L_3 < |x| \leq l_s \tag{3.65b}$$

The circumferential part can be defined as proposed on Eq. 3.66a. However, this turns out to be difficult to integrate, so the catenary approach on Eq. 3.66b is taken into consideration.

$$y = -\sqrt{R^2 - x^2} + \frac{D_2}{2} + R, \qquad 0 < |x| \leq L_3 \tag{3.66a}$$

$$y = \frac{D_2}{2}\cosh(\alpha_b x), \qquad 0 < |x| \leq L_3 \tag{3.66b}$$

where

$$\alpha_b = \frac{1}{R\cos(\frac{\theta}{2})}\operatorname{arccosh}\left(\frac{\frac{D_2}{2} + R - R\sin(\frac{\theta}{2})}{\frac{D_2}{2}}\right) \tag{3.67}$$

This is the same approach taken in Chapter 3.1.2. The denominator of α_b is related to the beginning of the catenary, while the end corresponds to the switch of equations. The graph on Figure 3.1.5 shows the real and the approximate shape of the notch employing a catenary for two different radius. It is demonstrated that the approximation is satisfactory.

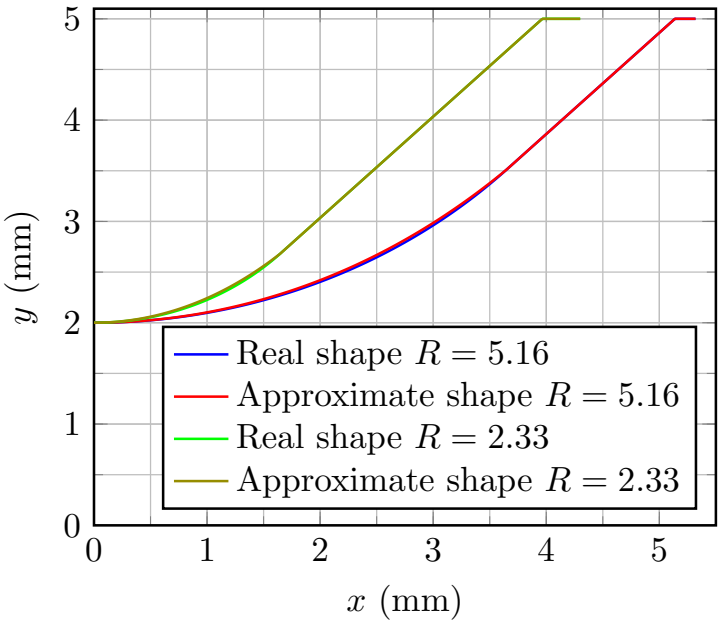


Figure 3.1.5: Comparison between the real shape and the catenary approximation

Having the equations for the specimens' shape defined, it is necessary to implement Eq. 3.24 in order to then integrate and obtain the length L_1 and L of the specimen. Taking as first step the cylindrical part, its solution (in Eq. 3.68a) is the same presented on Chapter 3.1.2. Its derivate and strain is on Eq. 3.68b. The constants C_1 and C_2 are also the same as Eq. 3.46.

$$U(x) = A_0 \cos(k(L-x)), \qquad l_s < |x| \leq L \tag{3.68a}$$
$$U'(x) = A_0 k \sin(k(L-x)), \qquad l_s < |x| \leq L \tag{3.68b}$$

Taking into account the straight part of the specimen's profile described on Eq. 3.65b, the cross section area, its derivate and ratio come as:

$$S(x) = \pi \left(\frac{D_1}{2} + \frac{x - l_s}{\tan(\frac{\theta}{2})} \right)^2, \qquad L_3 < |x| \leq l_s \tag{3.69a}$$
$$S'(x) = 2\pi \left(\frac{D_1}{2} + \frac{x - l_s}{\tan(\frac{\theta}{2})} \right) \frac{1}{\tan(\frac{\theta}{2})}, \qquad L_3 < |x| \leq l_s \tag{3.69b}$$
$$p(x) = \frac{4}{D_1 \tan(\frac{\theta}{2}) + 2(x - l_s)}, \qquad L_3 < |x| \leq l_s \tag{3.69c}$$

Substituting once again in Eq. 3.24.

$$U''(x) + \frac{4}{D_1 \tan(\frac{\theta}{2}) + 2(x - l_s)} U'(x) + k^2 U(x) = 0 \tag{3.70}$$

It is necessary to introduce the variable change in Eq. 3.71 to solve Eq. 3.24, for $L_3 < |x| \leq l_s$.

$$U(x) = \exp\left(-\int \frac{p(x)}{2}\, dx \right) w(x) = \exp\left(\ln\left(D_1 \tan(\frac{\theta}{2}) + 2(x - l_s) \right)^{-1} \right) w(x) \tag{3.71}$$

Consequently, $U(x)$ and its derivates come as in Eq. 3.72a, 3.72b and 3.73 for $L_3 < |x| \leq l_s$.

$$U(x) = \left(D_1 \tan\left(\frac{\theta}{2}\right) + 2(x - l_s) \right)^{-1} w(x) \tag{3.72a}$$

$$U'(x) = -2 \left(D_1 \tan\left(\frac{\theta}{2}\right) + 2(x - l_s) \right)^{-2} w(x) + \left(D_1 \tan\left(\frac{\theta}{2}\right) + 2(x - l_s) \right)^{-1} w'(x) \tag{3.72b}$$

$$U''(x) = 8 \left(D_1 \tan\left(\frac{\theta}{2}\right) + 2(x - l_s) \right)^{-3} w(x) - 4 \left(D_1 \tan\left(\frac{\theta}{2}\right) + 2(x - l_s) \right)^{-2} w'(x) + \left(D_1 \tan\left(\frac{\theta}{2}\right) + 2(x - l_s) \right)^{-1} w''(x) \tag{3.73}$$

Substituting Eq. 3.72a, 3.72b and 3.73 in Eq. 3.70, it is possible to obtain Eq. 3.74.

$$w''(x) + k^2 w(x) = 0 \tag{3.74}$$

The Eq. 3.74 is a homogeneous differential equation that has its solution just like in 3.37. Doing again a change of variable, $U(x)$ comes as Eq. 3.75, followed by its derivate on 3.76.

$$U(x) = \frac{C_3\cos(kx) + C_4\sin(kx)}{D_1\tan\left(\frac{\theta}{2}\right) + 2(x - l_s)}, \quad L_3 < |x| \leq l_s \tag{3.75}$$

$$\begin{aligned} U'(x) = &\frac{-C_3 k\sin(kx) + C_4 k\cos(kx)}{D_1\tan\left(\frac{\theta}{2}\right) + 2(x - l_s)} \\ &+\frac{-2\left(C_3\cos(kx) + C_4\sin(kx)\right)}{\left(D_1\tan\left(\frac{\theta}{2}\right) + 2(x - l_s)\right)^2}, \quad L_3 < |x| \leq l_s \end{aligned} \tag{3.76}$$

Since the circumferential part is defined as Eq. 3.66b, the differential equation comes in Eq. 3.77 just as Eq. 3.35.

$$U''(x) + 2\alpha_b\tanh(\alpha_b x)U'(x) + k^2U(x) = 0, \quad 0 < |x| \leq L_3 \tag{3.77}$$

Solving this equation like in Chapter 3.1.2, $U(x)$ comes solved in Eq. 3.78 just like for the smooth specimen in Eq. 3.50 from (Bathias and Paris, 2004).

$$U(x) = \frac{2C_5\sinh(\beta x)}{\cosh(\alpha_b x)}, \quad 0 < |x| \leq L_3 \tag{3.78}$$

The derivate for $U(x)$ is on Eq. 3.79.

$$U'(x) = 2C_5\frac{\beta\cosh(\beta x)\cosh(\alpha_b x) - \alpha_b\sinh(\beta x)\sinh(\alpha_b x)}{\cosh^2(\alpha_b x)}, \quad 0 < |x| \leq L_3 \tag{3.79}$$

There are 4 unknown constants which are C_3, C_4, C_5 and l. They can be determined establishing the continuity equations between the catenary, the straight part and the cylindrical. At $x = l_s$ the right side equations Eq. 3.68a and 3.68b are:

$$U(l_s) = A_0\cos(k(L_1 + l_s - l_s)) = A_0\cos(kL_1) \tag{3.80a}$$

$$U'(l_s) = A_0 k\sin(kL_1) \tag{3.80b}$$

While the left side equations 3.75 and 3.76 become as following.

$$U(l_s) = \frac{C_3\cos(kl_s) + C_4\sin(kl_s)}{D_1\tan\left(\frac{\theta}{2}\right)} \tag{3.81}$$

$$U'(l_s) = \frac{-C_3 k\sin(kl_s) + C_4 k\cos(kl_s)}{D_1\tan\left(\frac{\theta}{2}\right)} + \frac{-2\left(C_3\cos(kl_s) + C_4\sin(kl_s)\right)}{\left(D_1\tan\left(\frac{\theta}{2}\right)\right)^2} \tag{3.82}$$

By making Eq. 3.80a equal to Eq. 3.81 we can obtain A_0 on Eq. 3.83.

$$A_0 = \frac{C_3\cos(kl_s) + C_4\sin(kl_s)}{D_1\tan\left(\frac{\theta}{2}\right)\cos(kL_1)} \tag{3.83}$$

Then, substituting A_0 in Eq. 3.80b and making it equal to Eq. 3.82, the Eq. 3.84 is found which provides the length of the cylindrical part L_1, the resonance length.

$$L_1 = \frac{1}{k}\arctan\left(\frac{-C_3\sin(kl_s)+C_4\cos(kl_s)}{C_3\cos(kl_s)+C_4\sin(kl_s)} - \frac{2}{kD_1\tan(\frac{\theta}{2})}\right) \tag{3.84}$$

At $x = L_3$ the right side equations Eq. 3.75 and 3.76 are:

$$U(L_3) = \frac{C_3\cos(kL_3)+C_4\sin(kL_3)}{D_1\tan\left(\frac{\theta}{2}\right)+2(L_3-l_s)} \tag{3.85}$$

$$U'(L_3) = \frac{-C_3k\sin(kL_3)+C_4k\cos(kL_3)}{D_1\tan\left(\frac{\theta}{2}\right)+2(L_3-l_s)} + \frac{-2\left(C_3\cos(kL_3)+C_4\sin(kL_3)\right)}{\left(D_1\tan\left(\frac{\theta}{2}\right)+2(L_3-l_s)\right)^2} \tag{3.86}$$

In the other hand, for the left side we take into consideration Equations 3.78 and 3.79 for $x = L_3$, obtaining Equations 3.87 and 3.88.

$$U(L_3) = \frac{2C_5\sinh(\beta L_3)}{\cosh(\alpha_b L_3)} \tag{3.87}$$

$$U'(L_3) = 2C_5\frac{\beta\cosh(\beta L_3)\cosh(\alpha_b L_3)-\alpha_b\sinh(\beta L_3)\sinh(\alpha_b L_3)}{\cosh^2(\alpha_b L_3)} \tag{3.88}$$

Making Eq. 3.85 equal to Eq. 3.87 we can get $2C_5$ in function of C_3 and C_4 in 3.89.

$$2C_5 = \frac{C_3\cos(kL_3)+C_4\sin(kL_3)}{aux}\frac{\cosh(\alpha_b L_3)}{\sinh(\beta L_3)} \tag{3.89}$$

Where from now on it will be defined an auxiliary variable aux as the denominator of Eq. 3.85, represented on Eq. 3.90.

$$aux = D_1\tan\left(\frac{\theta}{2}\right)+2(L_3-l_s) \tag{3.90}$$

Once again making the equality of $U'(x)$ on each sides of $x = L_3$, i.e. Eq. 3.86 equal to Eq. 3.88 we can get Eq. 3.91 with the $2C_5$ (Eq. 3.89) substituted.

$$\begin{aligned}\frac{(C_4k*aux-2C_3)\cos(kL_3)+(-2C_4-C_3k*aux)\sin(kL_3)}{aux} = \\ (C_3\cos(kL_3)+C_4\sin(kL_3))\frac{\beta\coth(\beta L_3)\cosh(\alpha_b L_3)-\alpha_b\sinh(\alpha_b L_3)}{\cosh(\alpha_b L_3)}\end{aligned} \tag{3.91}$$

This is equivalent to

$$\begin{aligned}C_4\left(k\cos(kL_3)-\frac{2\sin(kL_3)}{aux}-\sin(kL_3)\frac{\beta\coth(\beta L_3)\cosh(\alpha_b L_3)-\alpha_b\sinh(\alpha_b L_3)}{\cosh(\alpha_b L_3)}\right) = \\ C_3\left(\cos(kL_3)\frac{\beta\coth(\beta L_3)\cosh(\alpha_b L_3)-\alpha_b\sinh(\alpha_b L_3)}{\cosh(\alpha_b L_3)}+\frac{2\cos(kL_3)}{aux}+k\sin(kL_3)\right)\end{aligned} \tag{3.92}$$

Which gives the ratio between C_4 and C_3 on Eq. 3.93.

$$\frac{C_4}{C_3} = \frac{k\tan(kL_3) + \frac{2}{aux} + \frac{\beta\coth(\beta L_3)\cosh(\alpha_b L_3) - \alpha_b\sinh(\alpha_b L_3)}{\cosh(\alpha_b L_3)}}{k - \frac{2\tan(kL_3)}{aux} - \tan(kL_3)\frac{\beta\coth(\beta L_3)\cosh(\alpha_b L_3) - \alpha_b\sinh(\alpha_b L_3)}{\cosh(\alpha_b L_3)}} \tag{3.93}$$

Since C_4 and C_3 are dependent, they can be displayed as a ratio on Eq. 3.84, allowing to obtain the length L_1 of the cylindrical part of the specimen on Equation 3.94.

$$L_1 = \frac{1}{k}\arctan\left(\frac{-\sin(kl_s) + \frac{C_4}{C_3}\cos(kl_s)}{\cos(kl_s) + \frac{C_4}{C_3}\sin(kl_s)} - \frac{2}{kD_1\tan(\frac{\theta}{2})}\right) \tag{3.94}$$

Finally, the total length of the specimen can be calculated through Eq. 3.95.

$$L = 2(L_1 + l_s) \tag{3.95}$$

Having L_1, C_3 comes from Equation 3.83 turned into Eq. 3.96. C_4 is found by Eq. 3.93 and C_5 by Eq. 3.89.

$$C_3 = \frac{A_0\cos(kL_1)D_1\tan\left(\frac{\theta}{2}\right)}{\cos(kl_s) + \frac{C_4}{C_3}\sin(kl_s)} \tag{3.96}$$

In brief, the strain and stress on the cylindrical part is the same as for the hourglass specimen on Eqs. 3.59a and 3.59b.

For the straight part of the notch, recurring to Eq. 3.76, we get the strain and stress as in Eq. 3.97 and 3.98, respectively.

$$\begin{aligned}\varepsilon(x) = &\frac{-C_3k\sin(kx) + C_4k\cos(kx)}{D_1\tan\left(\frac{\theta}{2}\right) + 2(x - l_s)} \\ &+\frac{-2\left(C_3\cos(kx) + C_4\sin(kx)\right)}{\left(D_1\tan\left(\frac{\theta}{2}\right) + 2(x - l_s)\right)^2}, \quad L_3 < |x| \leq l_s\end{aligned} \tag{3.97}$$

$$\begin{aligned}\sigma(x) = &E\frac{-C_3k\sin(kx) + C_4k\cos(kx)}{D_1\tan\left(\frac{\theta}{2}\right) + 2(x - l_s)} \\ &+E\frac{-2\left(C_3\cos(kx) + C_4\sin(kx)\right)}{\left(D_1\tan\left(\frac{\theta}{2}\right) + 2(x - l_s)\right)^2}, \quad L_3 < |x| \leq l_s\end{aligned} \tag{3.98}$$

Finally, the strain of the central part of the specimen Eq. 3.99 is once again given by the derivate of the displacement.

$$\varepsilon(x) = 2C_5\frac{\beta\cosh(\beta x) - \alpha_b\sinh(\beta x)\tanh(\alpha_b x)}{\cosh(\alpha_b x)}, \quad 0 < |x| \leq L_3 \tag{3.99}$$

According to this theory, the stress on the circumferential part of the specimen turns out to be on Eq. 3.100.

$$\sigma(x) = 2EC_5\frac{\beta\cosh(\beta x) - \alpha_b\sinh(\beta x)\tanh(\alpha_b x)}{\cosh(\alpha_b x)}, \quad 0 < |x| \leq L_3 \tag{3.100}$$

The nominal stress will achieve its peak in the middle of the specimen, corresponding to $x = 0$. So, substituting the constant C_5, the nominal stress is as displayed on Eq. 3.101.

$$\sigma(0) = 2EC_5\beta = E\beta\frac{C_3\cos(kL_3) + C_4\sin(kL_3)}{D_1\tan\left(\frac{\theta}{2}\right) + 2(L_3 - l_s)}\frac{\cosh(\alpha_b L_3)}{\sinh(\beta L_3)} \tag{3.101}$$

3.1.4 Shimadzu notch definition

Shimadzu has implemented a different definition for the specimen's geometry, which has been found not to be the most accurate regarding the length of the specimen and consequently its resonant frequency.

Although the correct definition for the length l_s, they approximate the whole notched section employing a catenary. This approach translates into the cylindrical part's length L_1 being computed with the same equation as the smooth specimen (Eq. 3.55). This leads to the wrong shape definition as seen on Figure 3.1.6 for the same radius adopted on Figure 3.1.5.

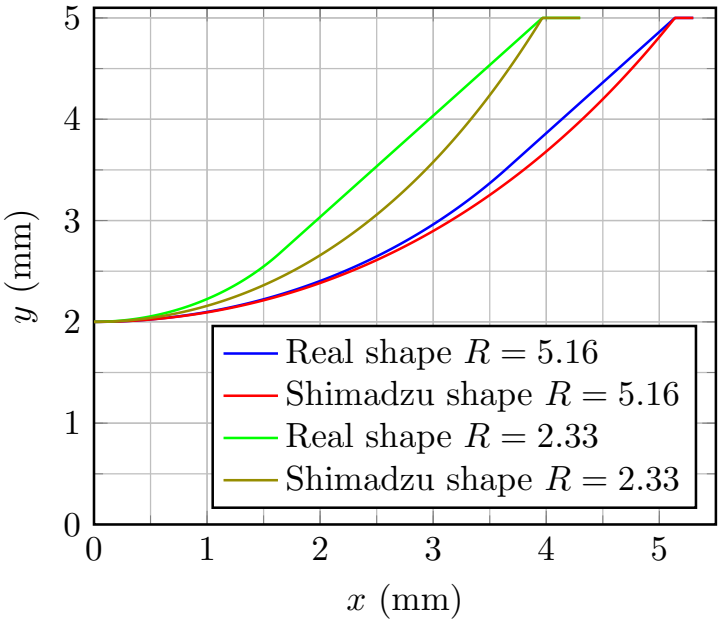


Figure 3.1.6: Comparison between the real shape and the Shimadzu catenary approximation

Furthermore, the nominal stress on the middle section of the notched specimens that Shimadzu defines on Eq. 3.102 is different from the analytical solution found in Eq. 3.101.

$$\sigma = AEk\left(\frac{D_1}{D_2}\right)^2 \tag{3.102}$$

They use the Eq. 3.22 and compute the force on the cylindrical section on Eq. 3.103.

$$f = AEk\pi\left(\frac{D_1}{2}\right)^2 \tag{3.103}$$

Then they divide by the smallest area (Eq. 3.104) located on the notch, getting Eq. 3.102.

$$S_2 = \pi \left(\frac{D_2}{2} \right)^2 \tag{3.104}$$

According to Shimadzu and the literature, the nominal stress in notched specimens (Eq. 3.102) is independent of the notch concentration factor.

Shimadzu states that the K_t factor comes from Eq. 3.105. This was primarily defined by Nihei et al. (1979), who determined the stress concentration factor in butt weld joins according to the geometric parameters of the cord height. Pluvinage (2003) also studied the subject of stress concentration factors. These were converted by Shimadzu to adapt them for the problematic of notched specimen's dimensioning.

$$K_t = 1 + f(\theta)(\alpha_c - 1) \tag{3.105}$$

$$f(\theta) = \frac{1 - \exp\left(-0.9(\pi - 2\theta)\sqrt{\frac{D_1}{D_1 - D_2}} \right)}{1 - \exp\left(-0.9\pi\sqrt{\frac{D_1}{D_1 - D_2}} \right)} \tag{3.106}$$

The α_c and n that Shimadzu supplies to the machine users come from D. Pilkey (2007), Peterson's Stress Concentration Factors.

$$\alpha_c = 1 + \left(\frac{\frac{D_1}{D_2} - 1}{1.55\frac{D_1}{D_2} - 1.3} \frac{D_2}{R} \right)^n \tag{3.107}$$

$$n = \frac{\left(\frac{D_1}{D_2} - 1 \right) + 0.5\sqrt{\frac{D_1 - D_2}{2R}}}{\left(\frac{D_1}{D_2} - 1 \right) + \sqrt{\frac{D_1 - D_2}{2R}}} \tag{3.108}$$

This formulation has a rough approximation of the specimen's shape, which is inadequate for the quality of the intended design. Therefore, it will be discarded since a new formulation was developed.

3.2 Steps for the finite element analysis

The Finite Element Method (FEM) is embedded in the commercial software Abaqus and it iterates the stress and displacement on the whole specimen in accordance with the mesh refinement defined. The simulation is essential to double check that the specimen's geometry obtained from the analytical solution is accurate, to experimentally reach the machine's natural frequency ($f_n = 19.98$ kHz). This is measured by the "Check Frequency" function of the machine's software, Supersonic.

Regarding the simulation on Abaqus, the first step was to create the parts' sketches for the Axisymmetric Deformable model which was chosen because it resembles the reality while saving time, allowing to get an accurate result. After some experiments for the smooth specimens, it was defined that the outer radius should be 10 mm, a recommendation from the manufacturer, and the minimum 4 mm. This last dimension was adopted to have a considerable range of stress on the specimen ($\sigma_{min} = 142$ MPa, $\sigma_{max} = 989$ MPa), without stressing the machine excessively. To have a comparison basis, these dimensions were maintained for the notched specimens, but in these lasts it was necessary to define a stress concentration factor. From the literature, the first K_t considered were too elevated, consequently, they were reduced with the goal to prevent the specimen from yielding (Table 3.2.1).

The technical drawings of the three specimens type are on Appendix A, namely Figures A.0.1, A.0.2, A.0.3.

Table 3.2.1: Stress Concentration Factors (K_t) for the notched specimens

K_t	Internal radius R (mm)	Specimen's length (mm)
1.25	5.16	104.64
1.5	2.33	109.91

The Booster sketch was done according to the Branson's booster technical drawing, presented in Appendix A (Fig. A.0.4), however some dimensions were tuned to obtain the 19.98 kHz. Same methodology was adopted to do the Horn sketch, whose length was undefined (in Fig. A.0.1), as it depends on the specific properties of the block to be machined to obtain the part. These are presented on Figure A.0.5.

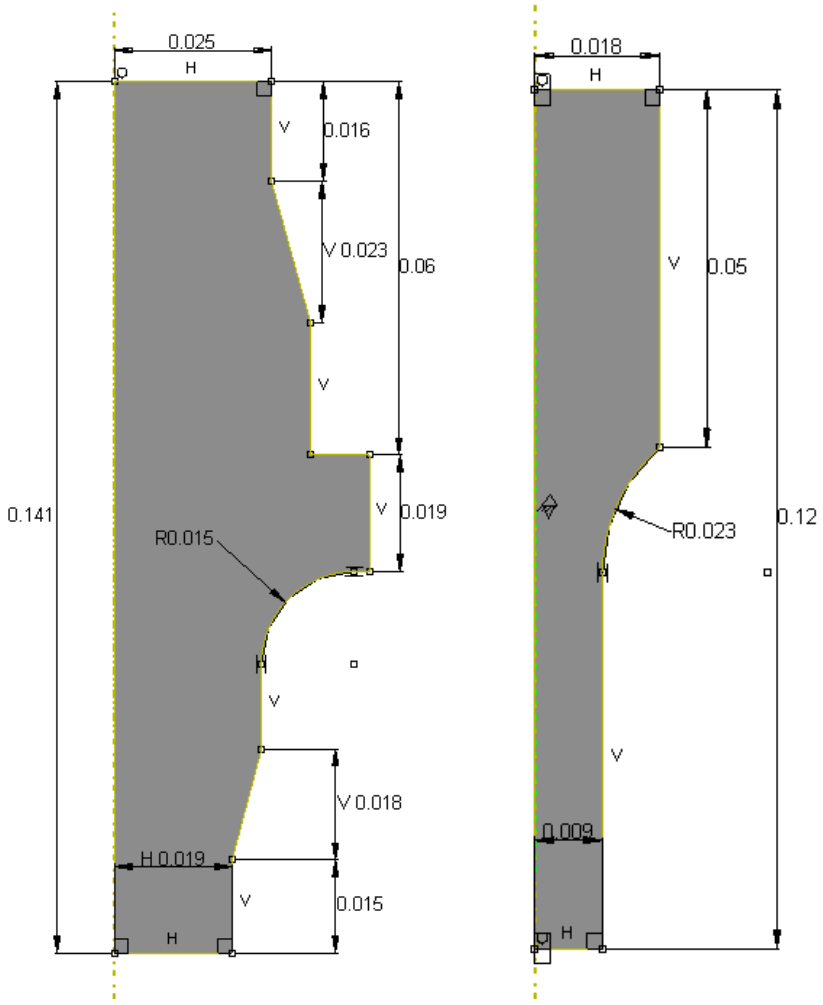


Figure 3.2.1: Sketches: a) Booster, b) Horn

Afterwards, it was necessary to access the alloy properties of these components. The volume mass ρ of the material, Titanium, was fixed, having an approximate Young's modulus, E. The correct E value was estimated by an iteration, having the result on Table 3.2.2, using Eq. 4.10b. The iteration methodology is explained on Section 4.2.

Table 3.2.2: Mechanical properties of the parts

Part	Horn		Booster	
Iteration	1	2	2	2
E (Pa)	1.06E+11	1.10890E+11	1.12033E+11	1.12235E+11
ρ (kg/m^3)	4500		4500	
f_n (Hz)	19534.5	19980	19962	19980

In the Property module, the materials need to be assigned to the corresponding sections of the parts. The mechanical properties and the volume mass attributed to each part are

summarized on Table 3.2.3.

Table 3.2.3: Mechanical properties of the parts

Part (kHz)	Material	E (MPa)	ν	ρ [kg/m^3] (mm)
Booster	Titanium alloy	110889.962	0.34	4500
Horn	Titanium alloy	112235.290	0.34	4500
Specimen	S690	211593.365	0.3	7815.66

Two models were made: one considering the whole machine and other with only the specimen to compare the differences. In the Assembly module, only for the whole machine model, the parts are put together resembling the real gigacycle fatigue machine. After this step, it is necessary to define in the Interaction module the constrains between parts, so that the whole group vibrates at the same frequency. The constrains on Figure 3.2.2 are ties, being the master surfaces on bottom and slave on top. In the module Step, it is created a "Frequency Step for Linear Perturbation", with 20 eigenvalues requested. This is done with the objective of finding the closest eigenvalue to 19.98 kHz, which corresponds to free-free axial vibration.

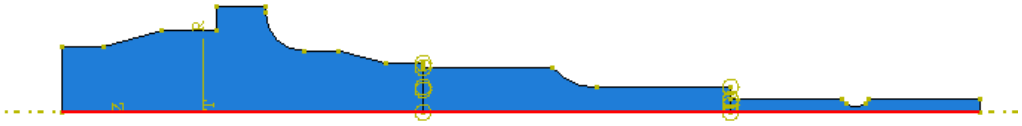


Figure 3.2.2: Assembly for the notched specimen on Abaqus

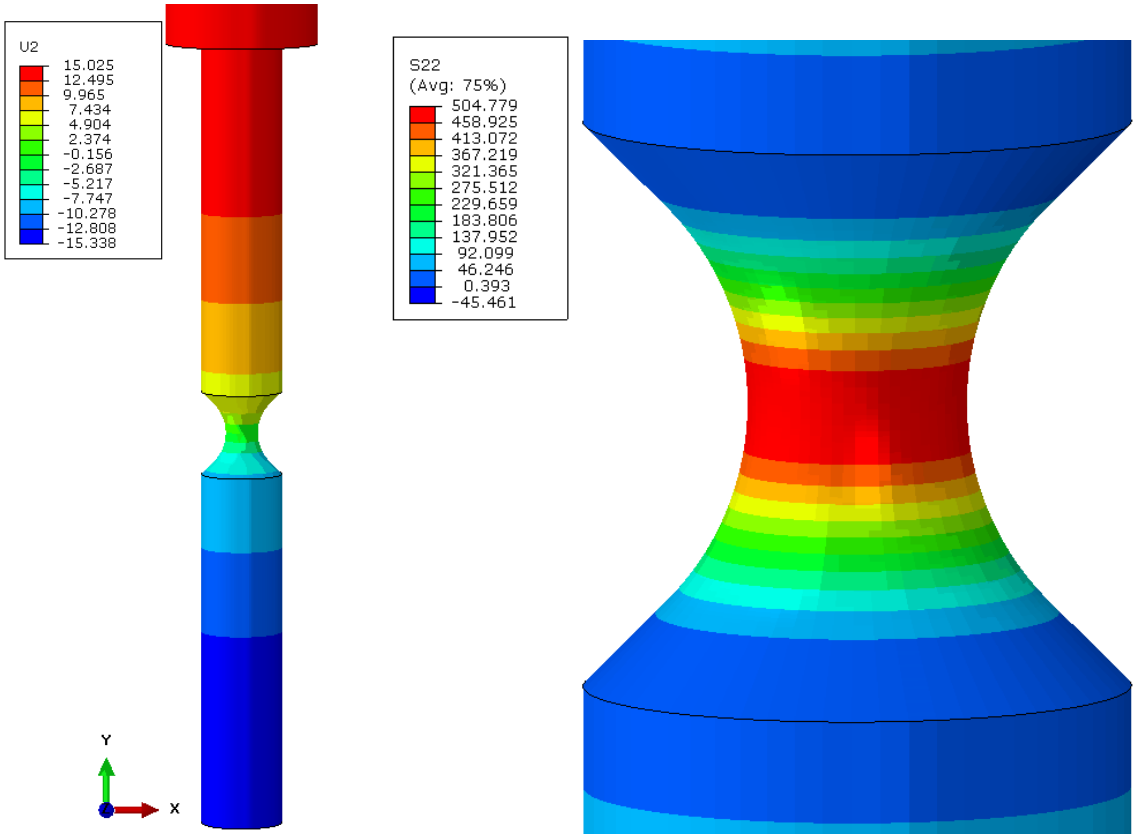
The mesh attributed to the booster and horn is more coarse, with approximate global size of 0.001 mm, since the tension and displacement are less significant in these. The mesh elements are quad-dominated with free technique. On other hand, for the specimen the size is smaller at 0.0001 mm, having elements quad dominated but structured. In all parts, the element type is CAX4R: a 4-node bilinear axisymmetric quadrilateral, reduced integration, hourglass control. The Booster had 4620 mesh elements while the Horn 1821.

The final step is to create and run the Job and then to check if the frequency matches the 20 kHz, using the fundamental longitudinal vibration mode that corresponds to the machine operation. On that step, the FEM frequency, the stress and the displacement can be verified.

3.3 Frequency estimation

This section presents the results originated from section 3.2. To simulate just the specimen, the booster and horn are suppressed from visualization, as well as the constrains between them. The results for the notched specimen transformed in 3D view are presented on Figure 3.3.1.

From now on, y represents the revolution axis (longitudinal direction) and x the radial coordinate.



(a) (b)

Figure 3.3.1: Simulation result for the notched specimen with $K_t = 1.25$. a) Axial displacement (μm). b) Axial stress (MPa).

On Figure 3.3.1, the theory extensively discussed on Chapter 3.1.1 is more perceivable visually. In other words, the stress increases in the negative direction of the y axis until the middle of the specimen, so the displacement is positive. After this central section, the stress decreases so the displacement is negative. The specimen presented is submitted to tensile loading, hence the positive stress on the central section and the positive and negative displacement, respectively on top and bottom of the specimen.

The frequencies for each specimen type were determined for the initial geometry calculated based on the analytical formulation of sections 3.1.2 and 3.1.4, respectively for smooth and notched specimens. These results are scrutinised for all specimens on Table 3.3.1.

Table 3.3.1: Frequency and number of elements for each simulation

Specimen	Nº of elements	Model	Frequency (Hz)
Smooth/Hourglass	38628	Specimen	20143
		Specimen + Horn + Booster	20015
Notch $K_t = 1.25$	64851	Specimen	19361
		Specimen + Horn + Booster	19787
Notch $K_t = 1.5$	69338	Specimen	19428
		Specimen + Horn + Booster	19805

For the hourglass specimen, the frequencies were slightly above the required, but fairly acceptable. However, for the notch specimen, it was acknowledged that the finite elements' frequency was considerably below the specified. Despite this, they were manufactured to later experimentally verify their resonance frequency. If the experimental frequency was as in Table 3.3.1, a turning operation in both ends of the specimens would be performed to remove some millimetres of length, reducing the specimen's mass and achieving the goal frequency.

It is noticed that the machine models always bring the simulation results closer to the 19.98 kHz. This is because the machine components represent the largest mass of the vibrating system and they are already dimensioned for the desired value. So, they bring the natural frequency of the whole system to approximate the objective. Furthermore, the specimens are dimensioned according non-standardized equations.

3.3.1 Frequency adjustment of the notched specimens

Upon the production of the notched specimens, it was verified experimentally that the frequency was low as predicted by the FEM on Table 3.3.1. The initial length was calculated by Eq. 3.55, so it was an outcome expected.

Subsequently, a second iteration by FEM was aimed for the 20.02 kHz and both ends of the specimen were machined to the length obtained with Abaqus. However, the experimental frequency on the second iteration was bellow the 20.02 kHz. For this reason, taking into account the real difference between FEM and the experimental frequency (Δf), a third iteration for a higher frequency in FEM was performed, achieving the desired frequency after machining the specimens' ends. The iterations are on Table 3.3.2, as well as the final specimen's dimension ($2L$) and the material length (ΔL_1) removed on each iteration.

Table 3.3.2: Length adjustment iterations

Iteration for $K_t = 1.25$	f_{FEM}	f_{exp}	Desired f	Δf	$2L$	L_1	ΔL_1
-	kHz	kHz	kHz	Hz	mm	mm	mm
1^{st}	19.787	19.68	20.00	107.00	104.64	47.18	0
2^{nd}	20.020	19.90	20.02	120.00	99.8	44.76	2.42
3^{rd}	20.151	**20.04**	20.02	111.00	**97.16**	43.44	1.32
Iteration for $K_t = 1.50$	f_{FEM}	f_{exp}	Desired f	Δf	$2L$	L_1	ΔL_1
-	kHz	kHz	kHz	Hz	mm	mm	mm
1^{st}	19.805	19.64	20.00	165.00	109.91	50.99	0
2^{nd}	20.020	19.86	20.02	160.00	105.45	48.76	2.23
3^{rd}	20.179	**20.02**	20.02	159.00	**102.20**	47.14	1.62

On Figure 3.3.2 it can be perceived there is almost a linear relationship between the frequency and the specimen's length.

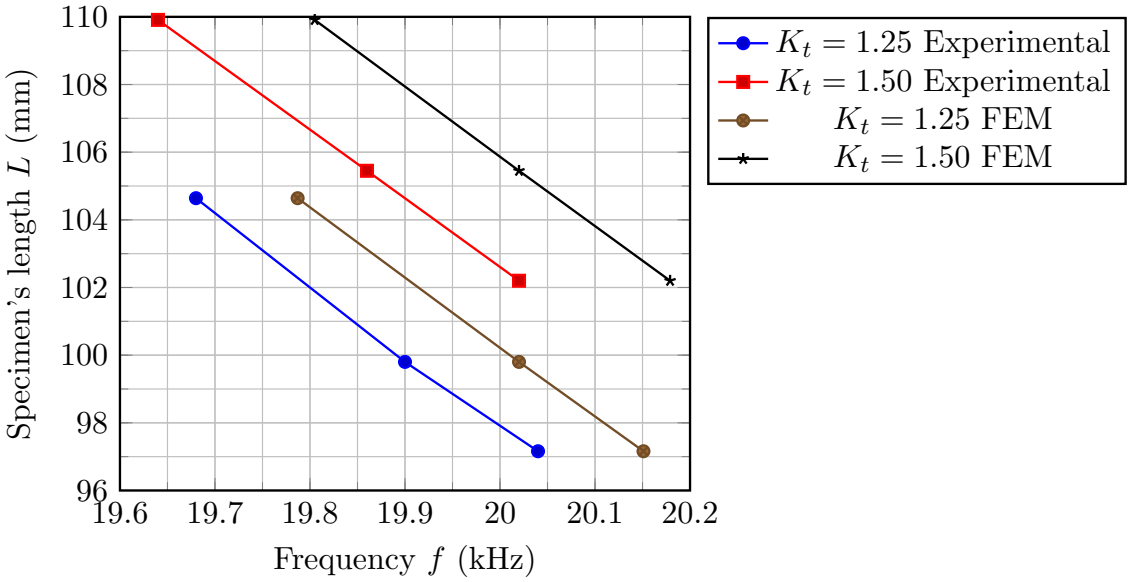


Figure 3.3.2: Length adjustment plot

Consequently, the technical drawings in Appendix A (Figures A.0.2 and A.0.3) have the dimensions for the correct frequency.

3.4 Stress and displacement results along the machine's axis

The simulation results discussed from now are the ones regarding the models Specimen+Booster+Horn in behalf of achieving a better representation of reality. The stress and displacement in function of the longitudinal coordinate (y) can be retrieved from the module Visualization. Beforehand, a Set must be created in the Tool menu of Abaqus, in which it is selected nodes belonging to the axis of the assembly illustrated on Figure 3.2.2. Having this, in the Visualization module, a Path with the Set chosen previously is created allowing to extract the variables for the correct desired Step, i.e., the vibration mode.

The maximum values acquired via FEM along the longitudinal axis are presented in Table 3.4.1. Regarding the notched specimens, the models considered were the ones with the adjusted final length calculated on Table 3.3.2.

Table 3.4.1: Maximum stress for $A_0 = 30$ μm on specimen's centre by FEM

Specimen	y for σ_{22} mm	σ_{22} MPa
Smooth/Hourglass	296.1	478
Notch $K_t = 1.25$	307.6	758
Notch $K_t = 1.50$	310.1	689

It is interesting that the axial stress on the notch with $K_t = 1.25$ is higher than the notch with a more critical stress concentration factor. The notched specimens obviously display a higher stress than the smooth specimen, for the same displacement. It is 58.6 % and 44.1 % higher than the smooth specimen, for the notched specimens with $K_t = 1.25$ and $K_t = 1.50$, respectively.

3.4.1 Machine and smooth specimen simulation

For the hourglass specimen, the graphical representation of the nodes' values at the revolution axis are on Figures 3.4.1 and 3.4.2.

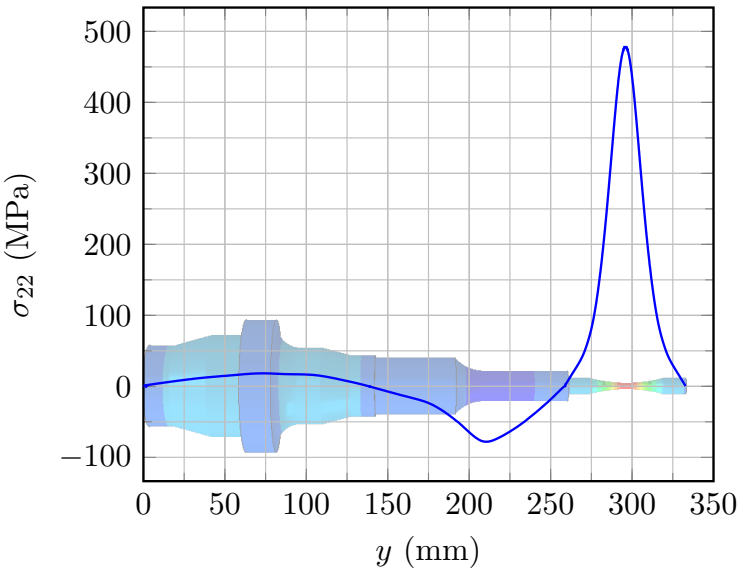


Figure 3.4.1: Axial stress obtained from simulation of the smooth specimen ($A_0 = 30$ μm)

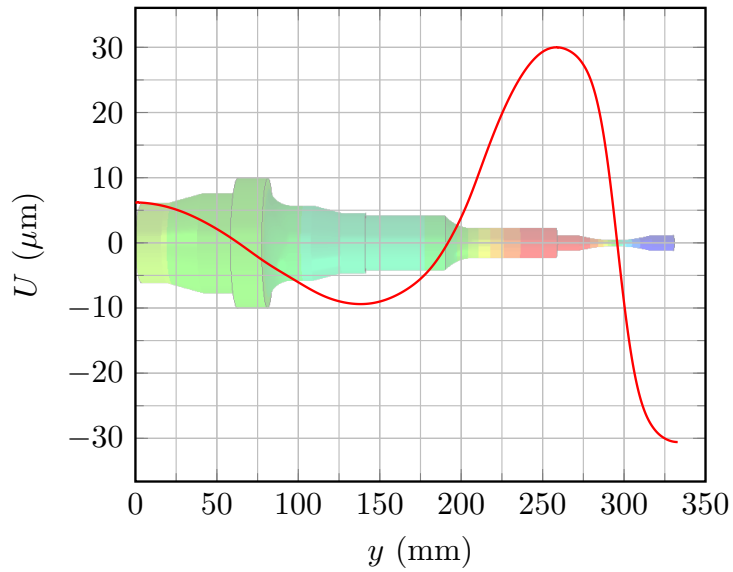


Figure 3.4.2: Axial displacement obtained from the simulation of the smooth specimen ($A_0 = 30$ μm)

Figures 3.4.1 and 3.4.2 are in accordance with the theory discussed in Chapter 2.4, resembling the predicted results on Fig. 2.4.1.

It is verified on Figure 3.4.1 there are 4 stress nodes in the transitions between the components. Figure 3.4.2 exhibits 3 displacement nodes and these are located in the y coordinate corresponding to the stress peaks. Plus, the maximum stress occurs in the centre of the specimen, which is coincident with the displacement nodes, a crucial condition

for the experimental procedure.

The maximum displacement for which the FEM simulations were done is 30 μm in order to compare smooth and notched specimens. This A_0 also proves a close stress to the one experimented on the smooth specimens. The FEM data was modified according to a gain rate to match the defined maximum displacement.

The Equations 3.58b and 3.59b give an analytical solution for the nominal stress along the axial coordinate. In opposition, FEM provides the stress on the nodes in the bidimensional specimen's area, depending on the mesh refinement. Figure 3.4.3 demonstrates a comparison between the analytical and FEM solution, being the latest the FEM stress along the longitudinal coordinate.

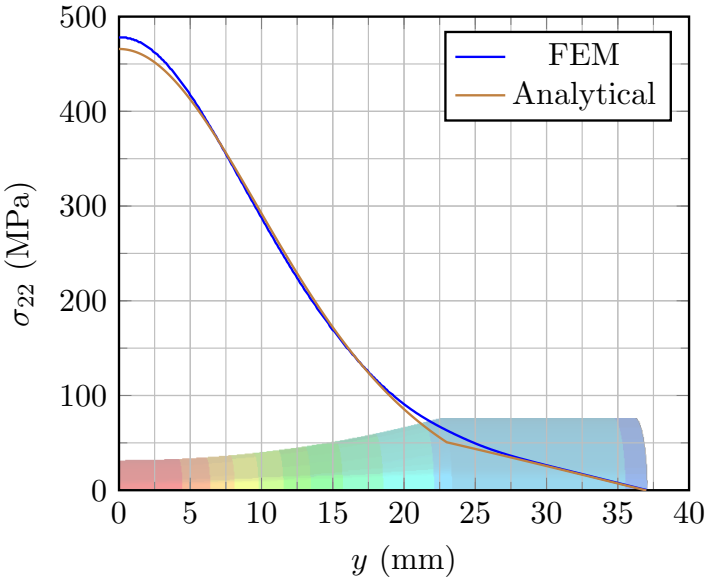


Figure 3.4.3: Axial stress for half of the smooth specimen by FEM and analytical solution ($A_0 = 30$ μm)

3.4.2 Machine and notched specimen simulation

For the notched specimen with $K_t = 1.25$, the stress and displacement distribution along the axial direction are presented in Figures 3.4.4 and 3.4.5, respectively. For $K_t = 1.5$ the graphics are fairly similar, having slight differences regarding the maximum values, hence they were placed in the Appendix B, on Figures B.0.1a and B.0.1b.

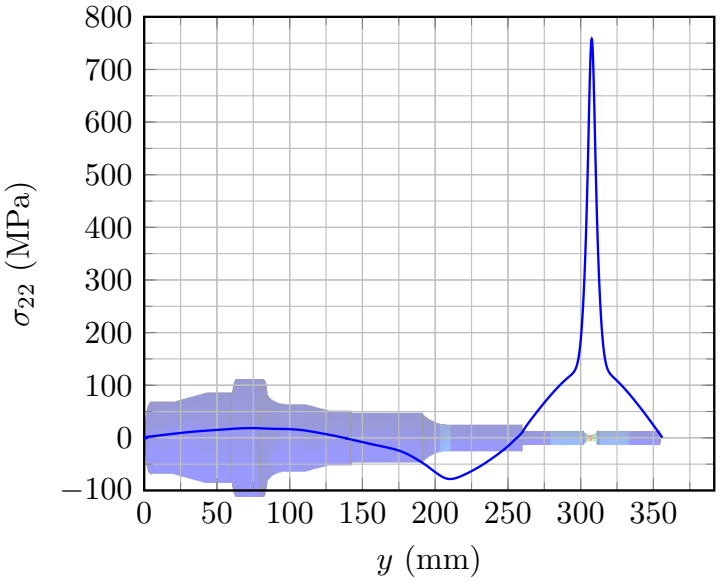


Figure 3.4.4: Axial stress obtained from simulation of the notched specimen with $K_t = 1.25$ ($A_0 = 30$ μm)

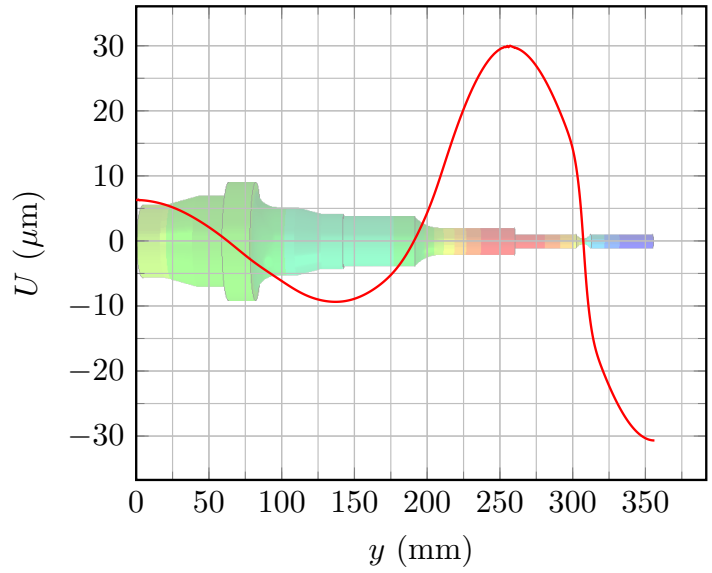


Figure 3.4.5: Axial displacement obtained from the simulation of the notched specimen with $K_t = 1.25$ ($A_0 = 30$ μm)

The notched specimens are longer than the smooth specimens but the displacement assumes the same shape. Regarding the stress, along the assembly axis the notched specimens present a higher value on the middle of the specimen's length and a more accentuated increase on that zone.

Having the smooth and notched specimens being compared, the analytical solution of Chapter 2.6 and the FEM must be compared. It was acknowledged that the displacement of 30 μm can be excessive for this last type of specimens. So, the A_0 of 15 μm was adopted.

The equation employed in Supersonic only accounts for the stress in the middle section of the specimen since it comes from 1D solution. Withal, employing the equations

developed in Chapter 2.6, namely Eq. 3.59b, 3.98 and 3.100 it is possible to predict the nominal stress along the specimen's axis considering the analytical formulation, while the FEM provides the stress on the test piece mesh nodes. The equations mentioned give a length (L_1 and L) different than the experimentally confirmed. So, forcing this variable to the real length on the analytical solution, both methods are comparable in Figures 3.4.6 and 3.4.7 the stress with $K_t = 1.25$ and $K_t = 1.50$. Note that the FEM stress represented is along the longitudinal axis.

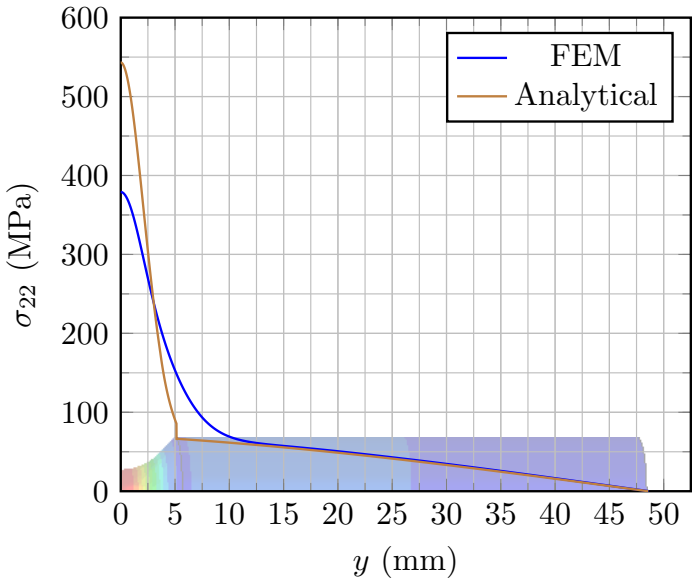


Figure 3.4.6: Axial stress for half the notched specimen with $K_t = 1.25$ by FEM and analytical solution for the real $L_1 = 43.44$ mm and $L = 48.58$ mm ($A_0 = 15$ μm)

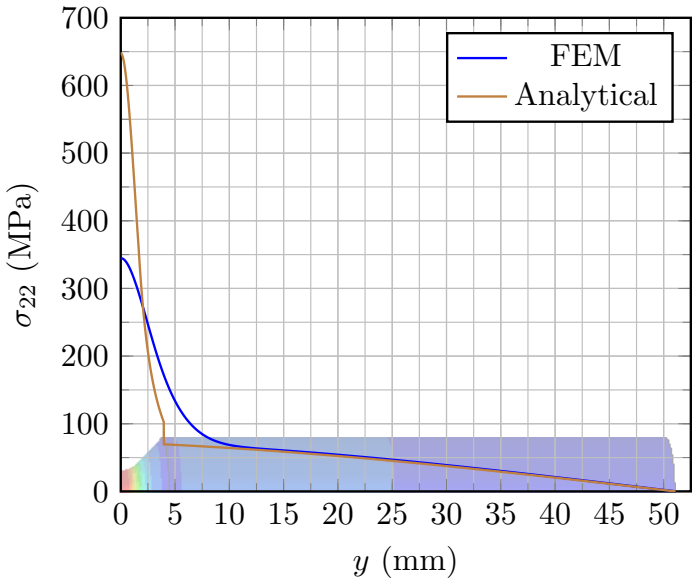


Figure 3.4.7: Axial stress for half the notched specimen with $K_t = 1.50$ by FEM and analytical solution for the real $L_1 = 47.14$ mm and $L = 51.1$ mm ($A_0 = 15$ μm)

The conclusion is that after 12.5 mm relatively to the middle of each notched specimen,

both solutions provide the same stress. The nominal stress for the analytical solution increases with the stress concentration factor. It is clear that the analytical solution is not a good reality representation due to the much higher stresses obtained. Plus, the analytical drops below the stress value calculated by FEM, which is highly improbable.

The analytical solution for the calculated L_1 is substantially similar, so it is presented in Figures C.0.1a and C.0.1b. However, it is higher than the experimental length that corresponds to the 20 kHz resonance frequency, as it can be observed on Table 3.4.2.

Table 3.4.2: Stress and lengths comparison for the notched specimens' analytical solution ($A_0 = 15$ μm)

Specimen	Model	L_1	L	Analytical stress
-	-	mm	mm	MPa
	Predicted	46.85	51.98	445
Notch $K_t = 1.25$	Experimental	43.44	48.60	543
	Variation	-3.41	-3.38	98
	Predicted	51.68	55.64	462
Notch $K_t = 1.50$	Experimental	47.14	51.1	648
	Variation	-4.54	-4.54	186

Table 3.4.2 elucidates that the analytical nominal stress prediction increases with the reduction of resonance length. For the notch with $K_t = 1.50$ the difference is higher since the greater the stress concentrator factor, the more difficult it becomes to reduce the problem to a unidirectional resolution. The constants and variables for the variables' calculus is on Appendix C, on Table C.0.1.

3.4.3 FEM stress for the specimen's transverse section

The smooth specimen has its maximum stress distributed for a wider area of the specimen cross section as it can be deduced from Figure 3.4.8, hence its stress concentration factor is fairly low.

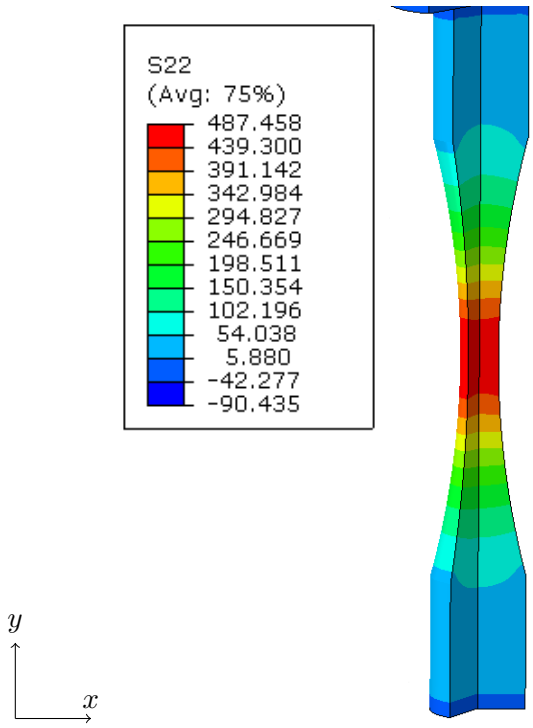


Figure 3.4.8: FEM simulations results (axial stresses, MPa) for the smooth specimen ($A_0 = 30$ μm)

The stress field obtained from FEM for the notched specimens is presented on Figure 3.4.9. This gives a better understanding how the lower radius brings a higher stress concentration value.

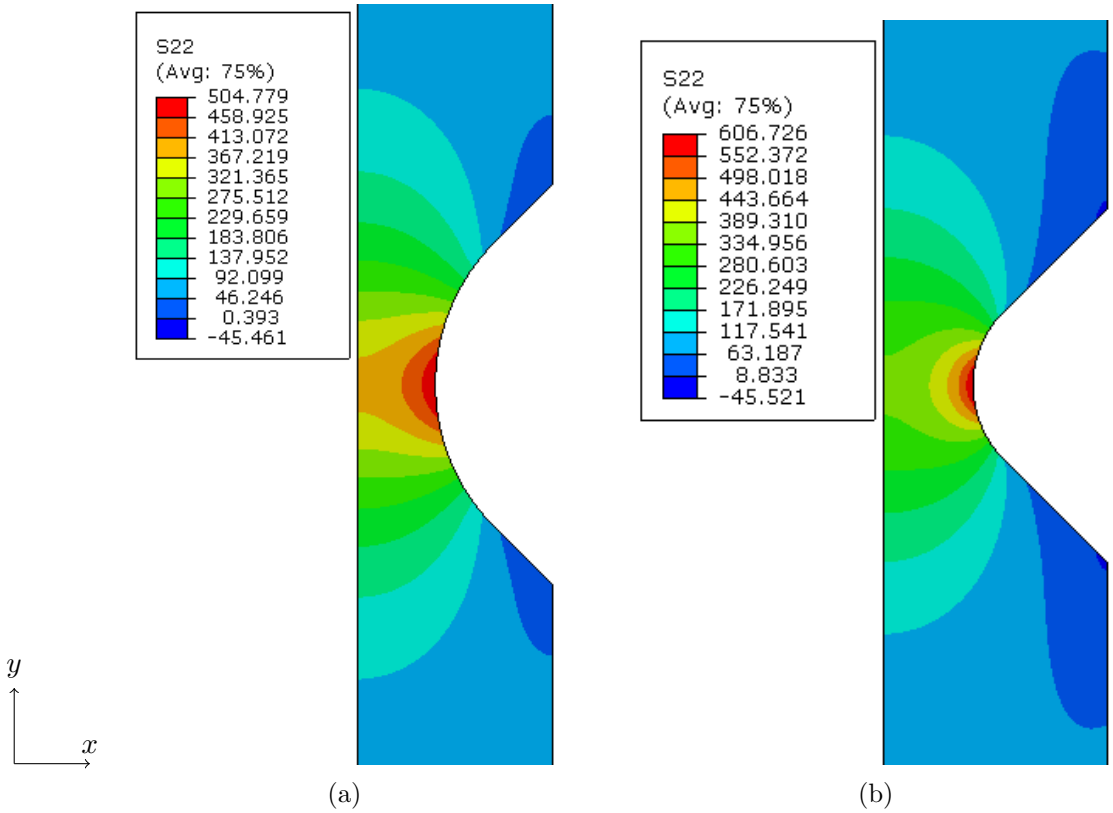


Figure 3.4.9: FEM simulations results (axial stresses, MPa) comparison for the notched specimens with $A_0 = 15$ μm. a) $K_t = 1.25$. b) $K_t = 1.5$.

Extracting the stress for the nodes belonging to the transversal section that divides the specimen in two halves (Figure 3.4.10), it is possible to obtain the stress distribution and its maximum in the outer wall of the notch. Plus, the nominal stress can be determined.

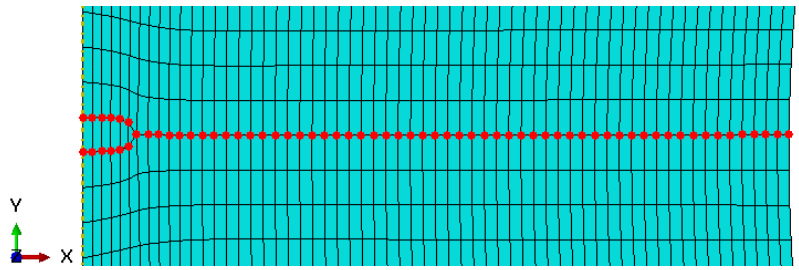


Figure 3.4.10: Transversal section of the notched specimen with $K_t = 1.25$ (radius= 2 mm)

In case there is not a node in the middle of the specimen, the average of the 2 closest nodes was considered. For a maximum displacement of 30 μm, the three specimen's plot is on Figure 3.4.11.

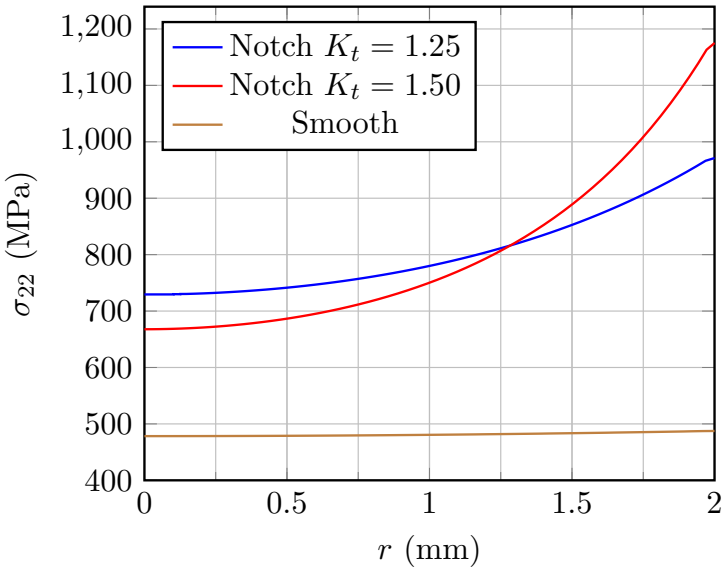


Figure 3.4.11: Axial stress obtained by FEM from the specimen's centre to the external radius ($A_0 = 30$ μm)

Figure 3.4.11 elucidates that the hourglass has only a slight increase of stress until the outer radius of the specimen. However, the notched specimen with $K_t = 1.5$ presents a higher stress than the one with $K_t = 1.25$ from $r = 1.285$ mm, being considerably greater at the specimen's surface.

On Figure 3.4.12 the plot of the stress for the maximum displacements 15 μm, 30 μm and 50 μm is performed.

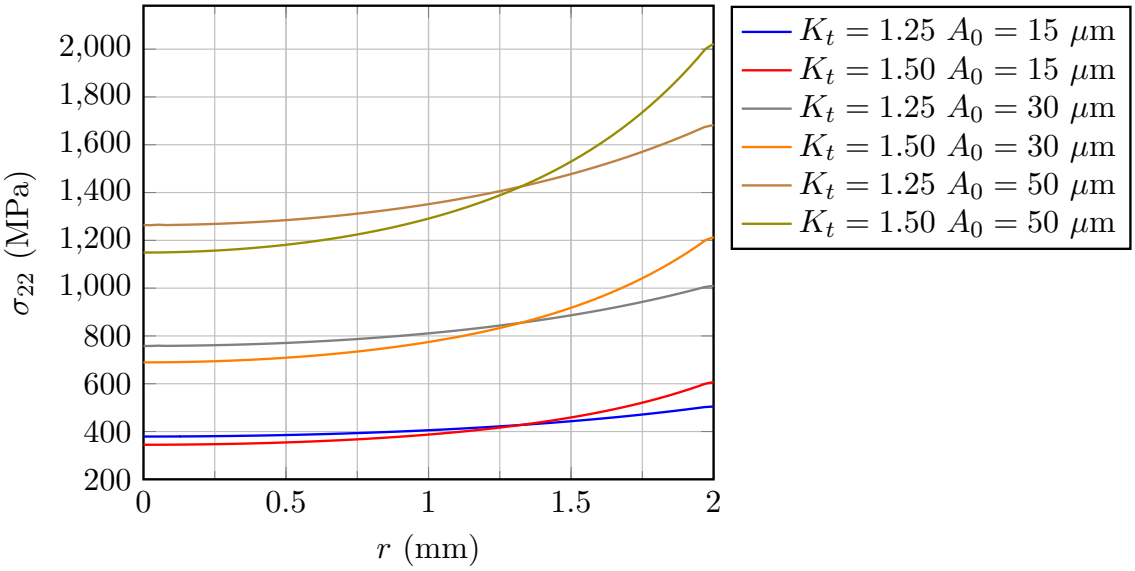


Figure 3.4.12: Longitudinal stress obtained by FEM from the notched specimen's centre to the external radius for different maximum displacements

The stress for different displacements is directly proportional. The plot allows to get the nominal stress, that was discussed on Figure 2.6.1. Its calculus begins by generating the trend line equation for each notch and displacement for example for Fig. 3.4.12, that

provides the most accurate approximation. Then, the area integral on Eq. 3.109a along the radius divided by the total area corresponds to the nominal stress.

$$\sigma_{nom} = \frac{1}{\pi R_2^2} \int_0^{R_2} 2\pi r \sigma(r)\, dr \tag{3.109a}$$

$$\sigma_{nom} = \frac{1}{2} \int_0^{2} r \sigma(r)\, dr \qquad \text{with } R_2 = 2 \tag{3.109b}$$

Regarding the smooth specimen, its stress analysis is discriminated on Table 3.4.3, including the analytical stress from Eq. 3.60b, discussed on Chapter 3.1.

Table 3.4.3: Relevant stress values for the transversal section of the smooth specimen ($A_0 = 30$ μm)

Specimen	FEM			Analytical	
	σ_{max} MPa	σ_{min} MPa	σ_{nom} MPa	σ_{nom} MPa	$\Delta\sigma_{nom}$ MPa
Smooth/Hourglass	487	481	483	466	-17

The analytical solution the Supersonic calculates is 17 MPa below the nominal stress registered by the FEM model. The computational solution may be better since it is closer to the resonance frequency.

For Fig. 3.4.12, the results allow to make a comparison with the Supersonic/Shimadzu and analytical solution (of Chapter 3.1.3) on Table 3.4.4. For example, to calculate the absolute deviation from the nominal FEM stress ($\Delta\sigma_{nom}$). Moreover, the stress concentration factors regarding the notched specimens were calculated by equation 3.105 for FEM simulations, for $K_t = 1.25$ and $K_t = 1.50$, as explained on Chapter 2.6. They revealed to be 1.15 instead of 1.25 and 1.33 in alternative to 1.5.

Table 3.4.4: Comparison between stress values in the cross section of the notched specimen for the maximum displacements: 15 μm, 30 μm and 50 μm

			FEM			Shimadzu		Analytical	
K_t -	Real K_t -	A_0 μm	σ_{max} MPa	σ_{min} MPa	σ_{nom} MPa	σ_{nom} MPa	$\Delta\sigma_{nom}$ MPa	σ_{nom} MPa	$\Delta\sigma_{nom}$ MPa
1.25	1.15	15	505	379	438	479	41	543	105
1.50	1.33		607	345	454		25	648	194
1.25	1.15	30	1010	758	876	958	82	1086	210
1.50	1.33		1213	689	909		49	1295	386
1.25	1.15	50	1683	1263	1459	1597	138	1810	351
1.50	1.33		2022	1149	1514		55	2159	645

It is determined that Shimadzu equation is not as accurate as the FEM simulations either for the frequency or the stress. Furthermore, the analytical equation (3.101) is believed to be a worse interpretation of the tridimensional problem exposed, hence the much higher deviation from the FEM values. This value was determined for the actual length L, which does not influence Shimadzu' stress estimation.

The stress concentration factors were bellow the expected, so a static analysis was carried out to verify if it was a dynamic analysis particularity, or the K_t is indeed different from the calculated. This is presented on Figure 3.4.13, where it is noticed a lower stress than for the dynamic analysis.

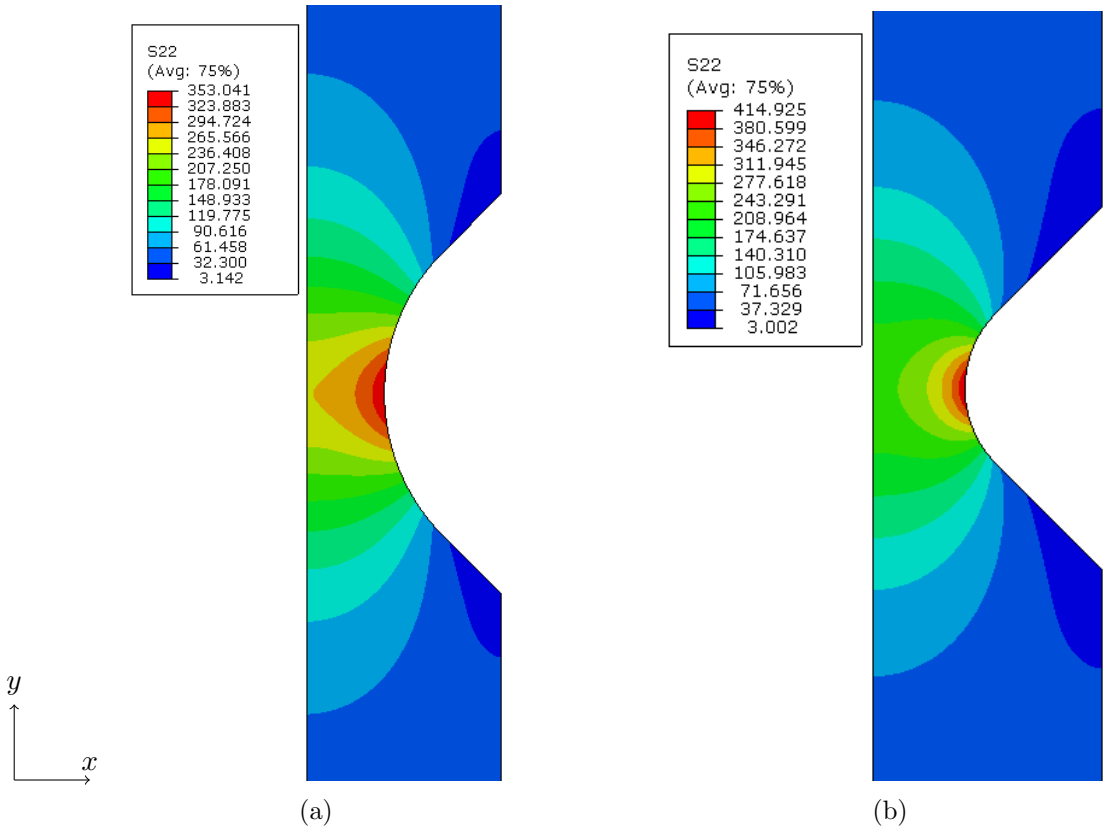


Figure 3.4.13: FEM simulations results comparison (axial stresses, MPa) regarding the static simulation of a displacement with $A_0 = 15$ μm. a) $K_t = 1.25$. b) $K_t = 1.5$.

This stress allows to calculate the nominal stress on Table 3.4.5.

Table 3.4.5: Real K_t for each notch type regarding static analysis ($A_0 = 15$ μm)

Specimen	σ_{max}	σ_{min}	σ_{nom}	Real K_t
Notch $K_t = 1.25$	353	265	306	1.15
Notch $K_t = 1.50$	415	236	311	1.33

The static stress values verified the stress concentration factor calculated for the 20 kHz dynamic simulation remains unchanged, so it is correct.

Chapter 4

Experimental Programme

This chapter presents the characteristics of the S690 steel. This is followed by the Young Modulus determination of the S690, done by matching the experimental data with the numerical results on Abaqus. It is described the design of the smooth specimens for HCF, 150 Hz. Next, the manufacturing process for smooth specimens and notched (only specimens with $K_t = 1.25$) is exposed for UFT.

The quality control of the surface is detailed for the three type of specimens. It was done via observation on the magnifying eye and by measuring the surface roughness.

The stress applied to the specimens to be tested at the Shimadzu machine is validated experimentally. It was performed by measuring the strain with the adhesion of a strain gauge to the surface of either smooth and notched specimens (20 kHz).

4.1 S690QL Steel Composition and Properties

The fine-grained high-strength structural steel S690QL possesses good low-temperature toughness at -40 ^{o}C according to EN 10025-6 (European Standard, 2019). Its microstructure is achieved by the addition of microalloying elements such as Nb and Ti. As S690QL is widely used in welded construction over a wide range of wall thicknesses, the weldability is a primary requirement criterion for a safe application of this material (Christ et al., 2020). The S690QL steel (DIN material number 1.8933) has its designation as exposed in Table 4.1.1, according to EN 10025-6. The S690 steel is obtained by thermomechanical rolling and supplied in quenched and tempered condition (de Jesus et al., 2012).

Table 4.1.1: Designation of S690QL (Qiang et al., 2012b; Steel, 2022)

S	690	Q	L
Structural Steel	Minimum Yield Strength (MPa)	Quenching and Tempering	Low notch toughness testing temperature

From Table 4.1.1, the steel S690 has a minimum yield strength of 690 MPa, but even 800 MPa can be reached. The "L" means that this steel group can be used at negative temperatures, like for example mobile cranes (Dobosy and Lukács, 2014). A tempered and quenched material has better fatigue characteristics than in its normalized/annealed state.

The yield strength ($Rp_{0,2}$), the tensile strength (R_m) and the elongation (A) are presented in Table 4.1.2, either the characteristics provided by the supplier and obtained through 3 tensile tests. The impact test energy was obtained from literature. The tensile

tests followed the ASTM International (2016) *"Standard Test Methods for Tension Testing of Metallic Materials"*.

Table 4.1.2: Mechanical Properties of the S690 steel

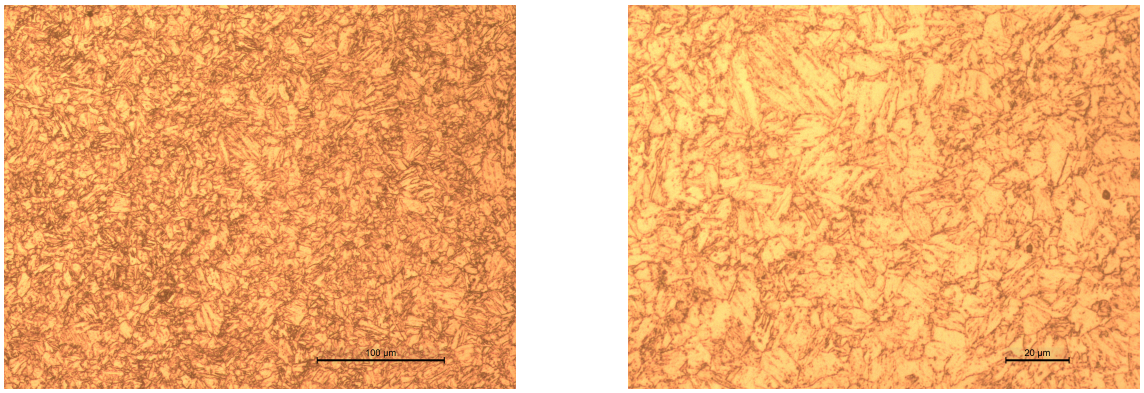
	Traction - Tensile test			Resilience - Impact test		
	$Rp_{0,2}$ (MPa)	R_m (MPa)	A (%)	C42 (J)	C42 (J)	C42 (J)
Supplier	783	824	16.2	180	178	174
Experimental	781	819	17.64	-	-	-

The S690QL is a low alloyed steel, as it can be concluded from Table 4.1.3.

Table 4.1.3: Alloy Elements of the S690 steel (% weight)

Mn	P	S	C	Si	Al	Cu	Nb
1.214	0.006	0.002	0.140	0.277	0.034	0.020	0.020
Ni	Cr	V	Mo	Ti	N	B	
0.012	0.292	0.030	0.115	0.018	0.0032	0.0020	

The S690 steel is a hypo-eutectoid steel (C approx 0.14%< 0.86% of eutectoid point) with low carbon content. Thus, if the steel was only tempered, it would be expect a dominantly martensitic structure with some ferrite to be observed. However, since the material is quenched, it was expected appearance of carbides as a way of relaxing the tetrahedral structure of martensite due to the rapid cooling during tempering. Consequently, in the microstructure of Figure 4.1.1, it would be present: martensite, ferrite and carbides.



(a) (b)

Figure 4.1.1: Microstructure of the S690 with (a) 100 μm and (b) 20 μm scales

In Figure 4.1.1, the typical lamellae allow to easily identify a martensitic microstructure along with the grain boundaries of the austenite that gave rise to the martensite during tempering (de Jesus et al., 2012). It was verified that the material has a homogenous microstructure and hardness on all directions. It was not possible to identify any direction of alignment of the steel grains due to hot plastic forming. Furthermore, the grain is very fine.

4.2 Young Modulus determination by dynamic and non-destructive methods

The modulus of elasticity of the material submitted to UHCF needs to be determined with high accuracy, since it influences the natural frequency (see Eq. 3.13), which affects the specimen's geometry and consequently its resonance frequency (Chapter 3.1.2). The material's volume mass ρ was also assessed for the same reason. To obtain a considerable accuracy, the last was assessed through the Archimedes Principle at the Laboratory of Materialography.

Regarding E, a test based on principles of vibration mechanics, which consisted in reproducing the conditions of a beam under natural vibration and "free-free" boundary conditions was done. It was based on the ASTM International (2022) Standard. Thus, the material under study was machined into a bar of constant circular cross section S and suspended by two elastic bands at the vibration nodes (Figure 4.2.1). The bar dimensions were length l 207.2 mm and diameter D_2 17.82 mm.

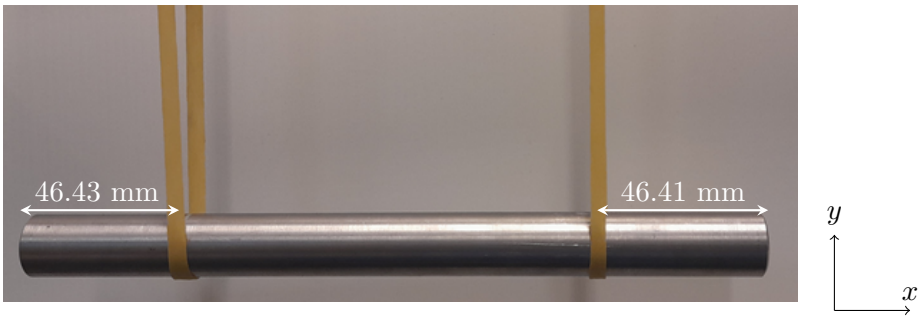


Figure 4.2.1: S690 steel beam supported by elastic bands at the vibration nodes

In the free regime, the external force or moment is null, $f(x,t) = 0$, and in case of the constant section beam, the bending vibrations of a beam are described by the following equation, where I represents the second moment of area (S) of the cross section (Caresta, 2022; Rodrigues, 2020):

$$EI\frac{\partial^4 v(x,t)}{\partial x^4} + \rho S\frac{\partial^2 v(x,t)}{\partial t^2} = 0 \tag{4.1}$$

The solution of Eq. 4.1 can be written as a steady wave $v(x,t) = w(x)u(t)$, separating the spatial and temporal components. This leads to the following characteristic equation that relates the circular frequency w to the wavenumber k:

$$\omega^2 = \frac{EI}{\rho S}k^4 \tag{4.2}$$

Equation 4.2 allows to numerically determine the Young Modulus of the material. The frequency f is then given by Eq. 4.3.

$$f = \frac{k}{2\pi}\sqrt{\frac{E}{\rho}}\sqrt{\frac{I}{S}} \tag{4.3}$$

The spatial part, i.e. the displacement, can be written as:

$$w(x) = C_1\sin(kx) + C_2\cos(kx) + C_3\sinh(kx) + C_4\cosh(kx) \tag{4.4}$$

For a free-free beam, as boundary conditions there are no restrictions to the beam movement, so the constants of Eq. 4.4 come as Eq. 4.5 to get Eq. 4.6. There is the absence of force, so acceleration is 0 ($w''(x)$) and moment ($w'''(x)$) (Caresta, 2022; Rodrigues, 2020).

$$\begin{Bmatrix} w''(0) = 0 \\ w'''(0) = 0 \\ w''(l) = 0 \\ w'''(l) = 0 \end{Bmatrix} \tag{4.5}$$

$$\begin{Bmatrix} -C_2 + C_4 = 0 \\ -C_1 + C_3 = 0 \\ -C_1 \sin(kl) - C_2 \cos(kl) + C_3 \sinh(kl) + C_4 \cosh(kl) = 0 \\ -C_1 \cos(kl) + C_2 \sin(kl) + C_3 \cosh(kl) + C_4 \sinh(kl) = 0 \end{Bmatrix} \tag{4.6}$$

Using the first two equations the 3rd and 4th can be arranged in matrix form:

$$\begin{bmatrix} \sinh(kl) - \sin(kl) & \cosh(kl) - \cos(kl) \\ \cosh(kl) - \cos(kl) & \sin(kl) + \sinh(kl) \end{bmatrix} \begin{bmatrix} C_1 \\ C_2 \end{bmatrix} = \begin{bmatrix} 0 \\ 0 \end{bmatrix} \tag{4.7}$$

For a non trivial solution (other than $k = 0$) the determinant of the matrix has to be equal to 0 to get Eq. 4.8.

$$\cosh(kl)\cos(kl) = 1 \tag{4.8}$$

The Equation 4.8 has infinite solutions (k_n), yet it can be solved numerically, so the first three values are reported on Table 4.2.1. The k_n is obtained dividing $k_n l$ by the bar length.

Table 4.2.1: Solutions for Equation 4.8

Mode (n)	$k_n l$	k_n
1	4.7300	22.828185
2	7.8532	37.901544
3	10.9956	53.067568

The constants in Equation 4.4 can be found after Equations 4.5 and 4.7, thereafter obtaining the simplified equation for the modes shapes on a free-free beam, according to the mode desired (Caresta, 2022; Rodrigues, 2020):

$$w(x) = \sinh(k_n x) + \sin(k_n x) + \frac{\sin(k_n l) - \sinh(k_n l)}{\cosh(k_n l) - \cos(k_n l)}(\cosh(k_n x) + \cos(k_n x)) \tag{4.9}$$

Equation 4.9 generates the mode shapes presented on Figure 4.2.2.

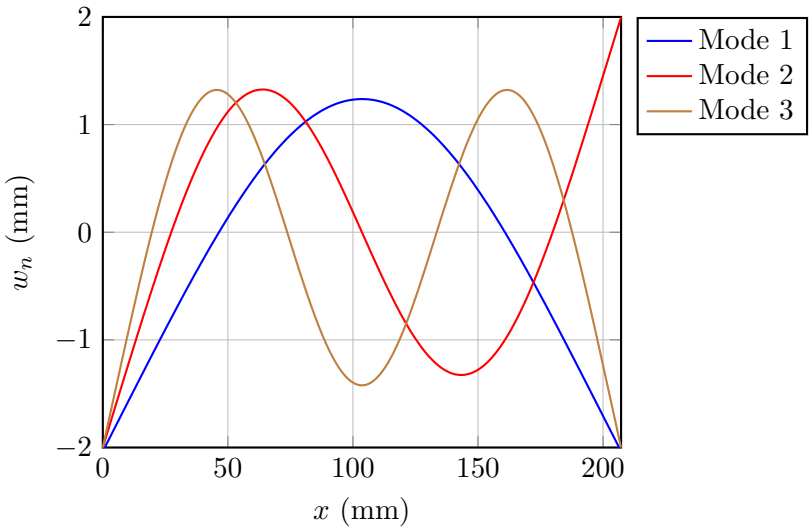


Figure 4.2.2: First 3 mode shapes for the free-free beam with $l = 207.2$ mm beam

This allows to get the vibration nodes coordinates on Table 4.2.2, essential for the elastic bands placement of Figure 4.2.1.

Table 4.2.2: Vibration nodes

Mode	% of l	x (mm)
Mode 1	22.41	46.434
	77.60	160.787
Mode 2	13.20	27.350
	50.00	103.600
	86.80	179.850
Mode 3	9.40	19.477
	35.60	73.763
	64.40	133.437
	90.60	187.723

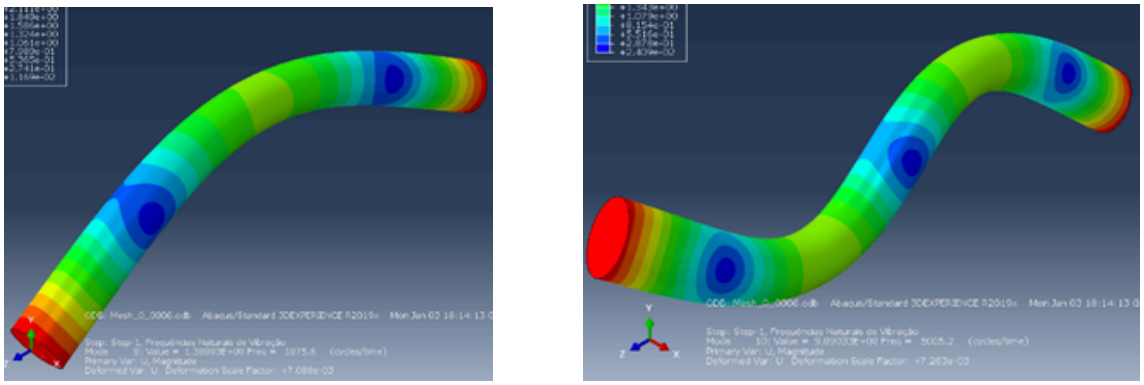
Subsequently, an initial excitation was performed with the goal to induce the beam to vibrate in its first vibration mode. The bump introduced (at the centre of the specimen) should be made with a hard metal or ceramic and executed in the centre of the cylinder. The sound emitted by the beam during its vibration was recorded to be processed by a Fast Fourier transform in the Scilabs program, obtaining the frequency response and the first and second f_n. The machined cylinder should meet dimensional accuracy and have a geometry such that its first natural frequencies are within the sound spectrum (audible, between 20 Hz and 20 kHz). Preferably, the target frequencies should be between 50 Hz and 18 kHz.

To determine correctly the E, it is done an evaluation of the ratio between Experimental (f_{exp}) and FEM (f_{FEM}) frequencies for the beam. When it is equal to 1, the iterations are ceased and the E is found (see Table 4.2.3).

Table 4.2.3: Procedure to obtain the Young Modulus E

Condition	Action
$\frac{f_{exp}}{f_{FEM}} \approx 1$	$E_{exp} = E_{FEM}$
$\frac{f_{exp}}{f_{FEM}} \neq 1$	New iteration (new E)

To create the FEM model in Abaqus, a 3D part was modulated with the exact dimensions of the S690 steel cylinder, along with its density and an initial E from the literature (210 GPa). It was created a step to acquire the 20 initial natural frequencies. The deformed representation of the bar in its firsts vibration modes is illustrated at Figure 4.2.3



(a) (b)

Figure 4.2.3: Bending modes on y obtained by FEM: a) Mode 1, b) Mode 2

The outcome of this simulation was finding the similar frequencies as the ones verified in the tested beam. It was seen that among the vibration modes obtained, some include bending and torsion. Notwithstanding, the simulation presented that the mode repeats itself, i.e., with the beam length through the x axis, it will have a bending mode in y identical to the one in z.

The frequencies analysed for first and second mode of vibration are presented in Table 4.2.4 and Table 4.2.5.

Table 4.2.4: Frequency determined by FEM vs Experimental (Iteration 1)

Properties FEM		FEM		Experimental		
E (Pa)	2,10E+11	Mode	f (Hz)	Mode	f (Hz)	$\frac{f_{exp}}{f_{FEM}}$
ρ (kg/m^3)	7815,656	1	1877,70	1	1884,805	1,003786557
$c = \sqrt{\frac{E_1}{\rho_1}}$ (m/s)	5180,000	2	5010,80	2	5028,40	1,003512413
					Average	1,003786557

From the first iteration (Table 4.2.4), it is concluded that the Young modulus defined *a priori* is still bellow the real value. Therefore, from Eq. 3.19, the Eq. 4.10b is solved, which allows to get the new elasticity modulus on Table 4.2.5. Then, the FEM simulation is repeated for the second iteration to verify the final ratio. Equation 4.10b can also be written as Eq. 4.10c.

$$\frac{f_{exp}}{f_{FEM}} = \frac{\sqrt{\frac{E_{exp}}{\rho_{exp}}}}{\sqrt{\frac{E_{FEM}}{\rho_{FEM}}}} \tag{4.10a}$$

$$E_{2,FEM} = \left(\frac{f_{exp}}{f_{FEM}} \sqrt{\frac{E_{1,FEM}}{\rho_{1,FEM}}} \right)^2 \rho_{2,FEM} \tag{4.10b}$$

$$c_2 = \frac{f_{exp}}{f_{FEM}} \sqrt{\frac{E_{1,FEM}}{\rho_{1,FEM}}} \tag{4.10c}$$

Table 4.2.5: Frequency determined by FEM vs Experimental (Iteration 2)

Properties FEM		FEM		Experimental		$\frac{f_{exp}}{f_{FEM}}$
E (Pa)	2,115933651E+11	Mode	f (Hz)	Mode	f (Hz)	
ρ (kg/m^3)	7815,656	1	1884,805	1	1884,805	1,000000000
c_2 (m/s)	5200,000	2	5029,770	2	5028,400	0,999727622
					Average	1

Now, the specimens dimensions can be found. It is worth reminding ρ was the fixed variable for the iterations. Nevertheless, only for the simulation, ρ could have been changed instead of E to obtain the same resonance frequency at modes 1 and 2.

4.3 Design of smooth specimens for testing at subsonic frequency (150 Hz)

The specimens for testing at 150 Hz in the Rumul machine in the HCF are easier to design. All their dimensions were recommended by the manufacturer for the standardized grips available (M16×1). Rumul also provides tolerances for the specimen to ensure the test piece fits on the machine, which are depicted in the technical drawing in Fig. A.0.6 in Appendix A.

The conventional fatigue limit of S690 steel is half of R_m (Furuya et al., 2019), so it is 412 MPa, hence the tests will be in the range of 350 to 783 MPa. The maximum dynamic amplitude of the machine is 75 kN, which translates into the maximum normal stress of equation 4.11.

$$\sigma_a = \frac{F}{\pi \frac{d^2}{4}} = \frac{75000}{\pi \frac{7^2}{4}} = 1949 \text{ MPa} \tag{4.11}$$

Since the R_m of the specimen is bellow 50 % the maximum dynamic stress of the machine, it can be successfully tested. The minimum stress expected was 390 MPa which is 20 % of the maximum dynamic load.

The fatigue standard "*Fatigue Testing-Axial Force-controlled Method*" ISO (2006) imposes the conditions of Table 4.3.1 which, as it can be deduced, are fulfilled by the dimensions recommended by Rumul for the standardized grip M16.

Table 4.3.1: Geometric dimensions recommended from ISO (2006)

Parameter	Dimension mm
Cylindrical diameter	$d \geq 3$ $9 \geq 3$
Transition radius	$r \geq 2d$ $14 \geq 14$
Grip end diameter	$D \geq 2d$ $16 \geq 14$
Minimum diameter	$L_C \leq 8d$ $14 \leq 56$
Gauge length radius	$r \geq 3d$ $45 \geq 21$

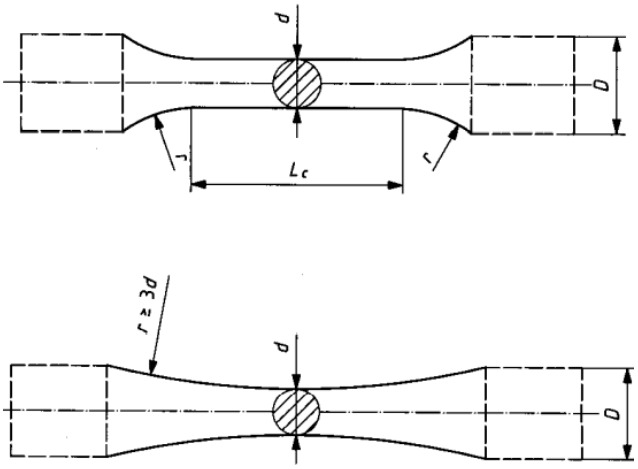


Figure 4.3.1: Technical drawing from ISO (2006)

4.4 Specimens manufacturing

The specimens for the Shimadzu USF-2000 testing (20 kHz) were obtained employing two machines, a conventional lathe Shaublin 135 (Fig. 4.4.6) and a CNC lathe, presented on Figure 4.4.1. The cutting tools used were new or in very good condition.



(a) (b)

Figure 4.4.1: a) CNC lathe DMG MORI CTX 310 ecoline. b) Detail of the tailstock inside and the tool changing mechanism

The material was supplied in rectangular bars with the dimensions 1m×0.025m×0.02m. They are machined according to the sequence detailed in Table 4.4.1.

Table 4.4.1: Sequence to manufacture the specimens for fatigue testing at 20 kHz

Order	Machine	Description
1	Conventional lathe	Turning the square section into a 19 mm cylinder.
2	Conventional lathe	Parting of the steel bar to make 2 specimens per bar.
3	CNC lathe	Facing the specimen.
4	CNC lathe	Turning the section where the thread will stand.
5	CNC lathe	Grooving to make the precise thread length.
6	CNC lathe	Machining the thread M6×0.75
7	Manual	Screw the brass tool that will hold the tailstock.
8	CNC lathe	Turning to obtain the cylindrical shape ($D = 10$mm).
9	CNC lathe	Turning the characteristic central shape ($D = 4$mm).
10	Conventional lathe	Polishing operation.
11	Conventional lathe	Parting of the specimen. The feed is adjusted manually.
12	Conventional lathe	Facing the specimen to get the final length.

Some stages of the specimens machining are given in Fig. 4.4.2.

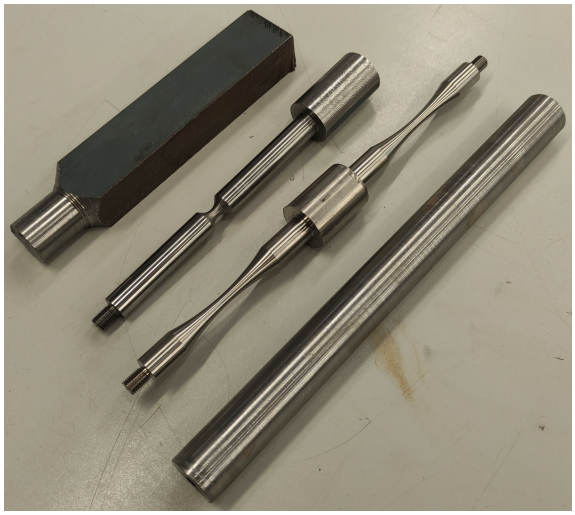


Figure 4.4.2: From left to right: turned S690 bar, notched and smooth specimens, S690 cylinder.

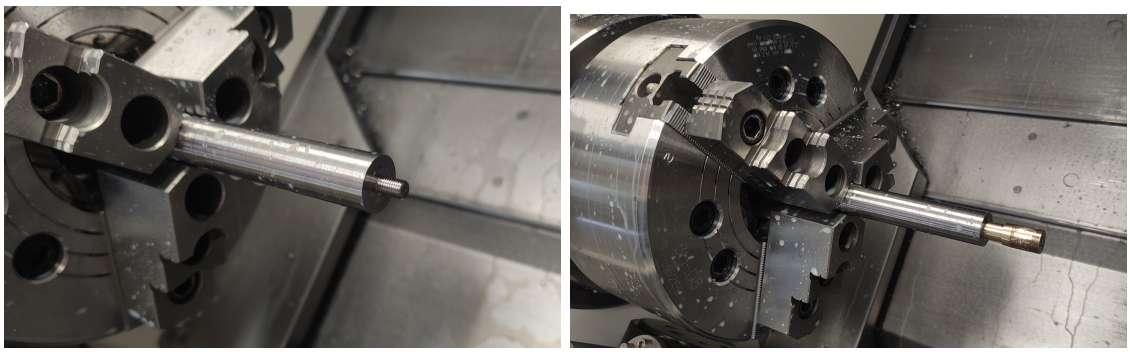
Among the problems in machining, it was reported cutting instability in the CNC turning, which caused mainly defects in the transition zone between the curved section and the cylindrical part. These were not visible after the roughing operation but they appeared after the polishing.

Several grooves were also caused by the feed chosen in the turning operations. The feed led to continuous chip that rolled up in the spindle (Fig. 4.4.3) which made its removal harder and scratches the specimen. The chip is prejudicial since it can rip off the material, leave marks and damage the insert. To solve this, the feed rate was increased so that the chip became discontinuous. There is a lower increase on the finish operations. The lubricant, white water and oil emulsion, is mostly water to ensure the cooling of the turning operations and a lesser quantity of oil (Castrol Hysol XF) to lubricate the lathe parts and reduce friction during cutting between tool and workpiece.



Figure 4.4.3: Continuous chip formed during turning

In Table 4.4.1, for step 7 a piece of brass with a female M6×0.75 tapped hole was threaded in the specimen with a hole in the other end where the tailstock was placed. This piece is illustrated in Fig. 4.4.4b and it is intended to reduce drastically the vibrations generated in the specimen (step 8 and 9). The pressure adjustment of the tailstock evidently also influences its effect. Owing to less vibrations, the specimen's geometry was achieved with more accuracy and less scratches.



(a) (b)

Figure 4.4.4: a) Specimen's thread. b) Brass tool threaded.

During the machining, the slender characteristic of the smooth specimen, small diameter and long length hindered the determination of ideal cutting parameters and propitiated vibrations. These cutting parameters as well as the sequence from Fig. 4.4.4 are exemplified in Figure 4.4.5.

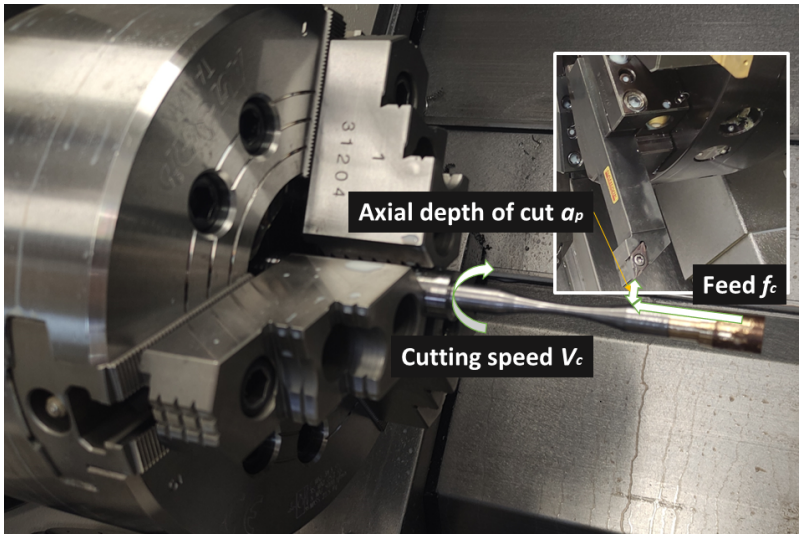


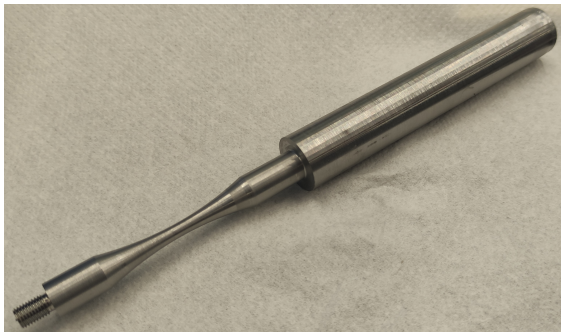
Figure 4.4.5: Final specimen aspect on the CNC and scheme of the cutting parameters

Part of the turning process can be watched accessing the following youtube link: Turning operation. The next step was to transfer the specimen to the conventional lathe illustrated in Figure 4.4.6.

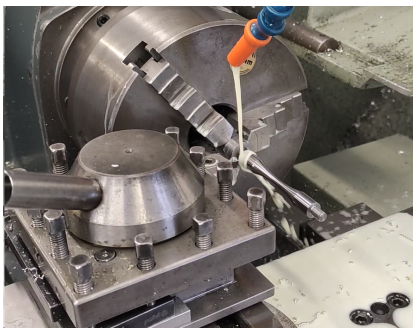


Figure 4.4.6: Lathe Shaublin 135

The finishing operations were minimal (Fig. 4.4.7a) because the polishing would give the final surface quality (Fig. 4.4.7b). Although, leaving too much material for the polishing operations is detrimental because it extends considerably production time. Both type of specimens used the same cutting parameters and tools, and due to material's properties they needed to be protected from ambient humidity.



(a)



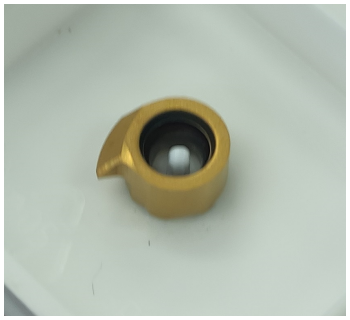
(b)

Figure 4.4.7: a) Smooth specimen (20 kHz) after turning on the CNC. b) Specimen after polishing on the Lathe Shaublin being parted.

A detail about these machining operations is that the S690 destabilizes and has more defects near the fixture. The roughing process' parameters are practically understood, yet for the ideal finishing the parameters were more difficult to tune.

For larger diameters it is easier to apply the traditional machining laws. In other words, higher cutting speed and less feed for finishing operations. However, for this reduced diameter it was used a smaller finishing feed and an equal speed relatively to the roughing operation. More feed looks better at naked eye but the texture is not the ideal. It was also used an equal depth of cut for the operations.

About the cutting tools, the one in Fig. 4.4.8c was used according to the different cutting parameters on the specimens P3 to P24. For the following specimens (P25 to P34 and notched), 2 types of tools were used according to the different cutting parameters, these are on Figures 4.4.8b and 4.4.8c, respectively for roughing and finishing. For the thread preparation, the tool on Figure 4.4.8c with the roughing parameters are employed, then the grooving tool and afterwards the M6×0.75 tool is applied (Fig. 4.4.8a).



(a) SECO LCEX0804-G60R CP500.



(b) Palbit DCMT11T304-MW PH5115 (Palbit, 2022)



(c) Palbit DCGT 070202-FS PHH910

Figure 4.4.8: Tool inserts

The new roughing tool (Fig. 4.4.8b) was adopted because the insert geometry favoured chip breaking. The parameters shown in Fig. 4.4.5 are listed in Table 4.4.2, where the a_p during the roughing operation is low due to the slenderness of the specimen.

Table 4.4.2: Cutting parameters used in the machining operation of the specimens for the 20 kHz fatigue testing.

Parameter	Roughing cutting insert Palbit DCMT11T304-MW PH5115	Finishing cutting insert Palbit DCGT070202-FS PHH910
V_c	120 m/min	120 m/min
f_c	0.15 mm/rev	0.025 mm/rev
a_p	1 mm	0.1 mm
Cutter radius	0.4 mm	0.2 mm

4.4.1 Smooth specimens (20 kHz)

The manufacturing sequence allowed to get the first batch of smooth specimens, exposed in Figure 4.4.9a. The second batch of smooth specimens have notoriously a better superficial quality. These are presented in Figure 4.4.9b.

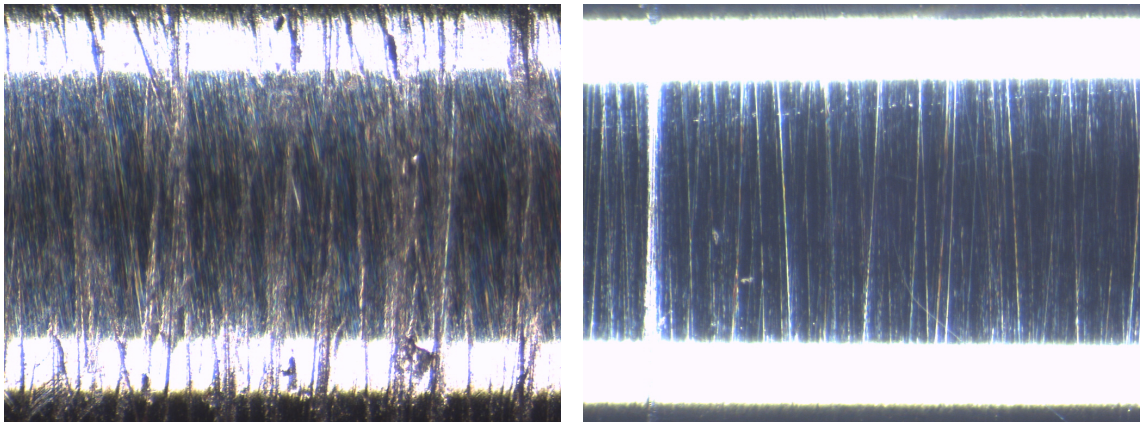


(a) (b)

Figure 4.4.9: Smooth specimens for ultrasonic tests at 20 kHz, arrival state P3-P34

All the specimens were measured (see Table E.0.1) and observed meticulously under the Olympus SZH, a magnifying eye. The Leica camera's software to take the pictures was Leica Application Suite v4.3.

For some specimens of the first batch, like the one on Figure 4.4.10, it was understood that they needed to be polished since they did not meet the requirements. Even after the first polishing operation, depending on what is visualized on the magnifying eye, some specimens needed to be repolished. The polishing removes mass from the specimen, so it lowers its resonance frequency. If this is critical, the specimen undergoes a machining operation on both ends. However this ended to be not necessary.



(a) (b)

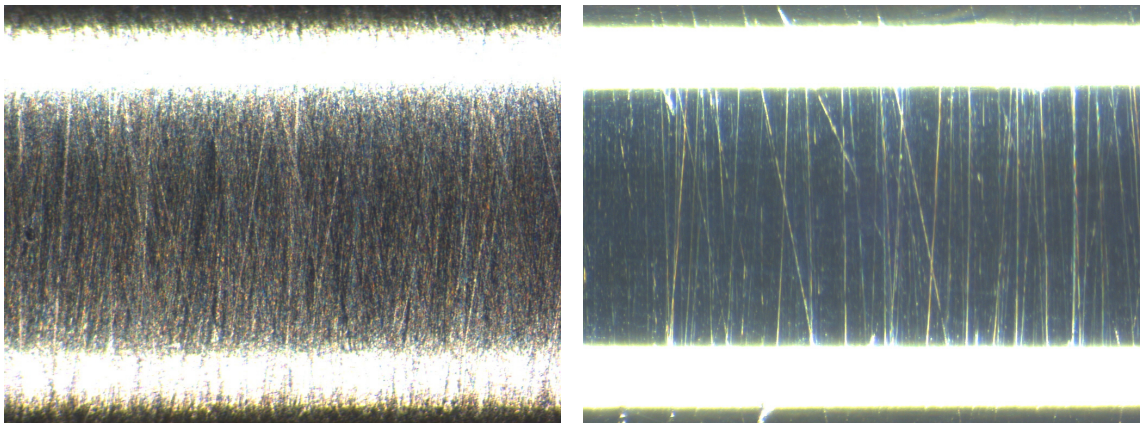
Figure 4.4.10: Specimen P9 pre (a) and post (b) polishing operations (×64) on the magnifying eye

The polishing sequence was established according to the available materials, being the microgrits used P600, P1200, P2500 and then a polishing cloth. These follow the ISO (2021) Mastergrits/FEPA Grit that defines the maximum grain size of each sandgrit, as specified on Table 4.4.3. The first microgrit (P600) is mainly for material removal, being the last focused on getting a better surface finishing (Orvis and Grissino-Mayer, 2002).

Table 4.4.3: Sandpaper grit standard in Europe (Orvis and Grissino-Mayer, 2002)

Designation	ISO/FEPA designation	ISO (μm)	FEPA (μm)
Extra Fine	P600	24.8-26.8	
Super Fine	P1200	14.3-16.3	
Ultra fine	P2500	7.9-9.1	7.9-8.9

The specimens of the second batch were submitted to the same polishing sequence and a much better qualitative surface quality was achieved, due to the lack of deep groves, as it can be seen in Figure 4.4.11.



(a) (b)

Figure 4.4.11: Specimen P27 pre (a) and post (b) polishing operations (×64) on the magnifying eye

Table 4.4.4 shows the average measurements for each batch to quantify the improvement regarding the dimensional accuracy. Table E.0.1 on Appendix E the dimensions and checked resonance frequencies for all specimens. The diameters where measured with a digital micrometer of flat and spherical tips, while the length with a digital calliper. The percentage variation is calculated according to Eq. 4.12, being x_f the final dimension and x_i the initial.

$$\Delta x(\%) = \frac{x_f - x_i}{x_i} * 100 \tag{4.12}$$

Table 4.4.4: Specimens dimensions and frequency comparison

Variable	Specimen	f	D_2 thread	D_2 flat	D_1	L
-	-	Hz	mm	mm	mm	mm
Average x_1	P3-P24	19.88	10.054	10.040	4.049	73.907
Average x_2	P25-P34	19.85	10.011	10.008	4.009	73.865
Δx	-	-0.03	-0.043	-0.032	-0.040	-0.042
Δx (%)	-	-0.18	-0.432	-0.316	-0.986	-0.057
Std. deviation $\hat{\sigma}_x$	P3-P24	0.01	0.008	0.015	0.009	0.019
Std. deviation $\hat{\sigma}_x$	P25-P24	0.01	0.006	0.006	0.004	0.012
$\Delta\hat{\sigma}_x$	-	-0.01	-0.002	-0.009	-0.005	-0.006
$\Delta\hat{\sigma}_x$ (%)	-	-52.07	-21.131	-61.433	-57.816	-34.038

It is clear from Table 4.4.4 that improving the manufacturing parameters enabled to get the specimens closer to the dimensioned values. The lower f may be due to the better surface quality but it is definitely also consequence of the machine's frequency drop from 19.98 kHz to 19.94 kHz from March to June. This is correlated with the ambient temperature that raised from 16 ºC to 26 ºC (approximately).

Besides the dimensional control, the surface roughness (SR) must comply with the $\text{Ra}_{max} = 0.1$ μm of the technical drawing. It was measured to ensure the fatigue tests are performed in the same conditions for different specimens and in addition, to ensure quality control. In order to do this, the SR was accessed in one specimen before and after polishing to verify if the polishing was effective to obtain the desired SR. The SR was measured on 5 specimens of the first batch and on the specimen P4 after polishing. Only one specimen had the SR accessed after polishing because the device uses a needle that can scratch the surface, which is detrimental to the surface quality and can influence the results. On Figure 4.4.12 it can be seen the direction adopted was along the specimen's axis to avoid scratches on the critical area.



Figure 4.4.12: Surface Roughness setup for the smooth specimens

The device used is a Mitutoyo Surftest SJ-210 that follows the standard Surface Texture Profile Method ISO (1997). It measures the profile and calculates the arithmetical mean deviation (Ra), root mean square deviation (Rq) and average peak to valley height of the roughness profile (Rz) along the sampling length (L_{SR}). These parameters are obtained as it is explained on Equations 4.13 where $z(x)$ is the absolute ordinate values axis (Mitutoyo, 2022).

$$Ra = \frac{1}{L_{SR}} \int_0^{L_{SR}} \left| z(x) \right| \, dz \tag{4.13a}$$

$$Rq = \sqrt{\frac{1}{L_{SR}} \int_0^{L_{SR}} \left| z^2(x) \right| \, dz} \tag{4.13b}$$

$$Rz = \left| \min \, z(x) \right| + \max \, z(x) \tag{4.13c}$$

Figure 4.4.13 exposes the average SR for the specimens, being done 3 measurements for each. It elucidates that after polishing, the longitudinal SR was lower than the specified for the SR of the circumferential middle section, so the polishing procedure was validated for the other specimens. The SR values for each specimen are presented in Table E.0.3 from Appendix E.

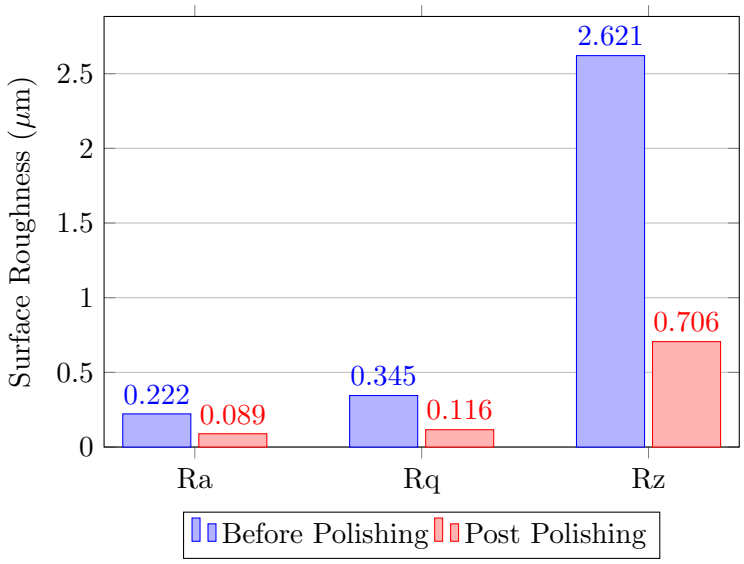


Figure 4.4.13: Average SR of the smooth specimens (20 kHz) before polishing: P4, P5, P7, P14 and P23. SR after polishing for P4.

4.4.2 Smooth specimens (150 Hz)

The smooth specimens for testing at 150 Hz, at Figure 4.4.14 machine, are bigger and more robust. They are threaded on both sides so they require the machining tolerances of the technical drawing of Figure A.0.6.



Figure 4.4.14: Smooth specimens for resonance tests at 150 Hz, arrival state P1-P24

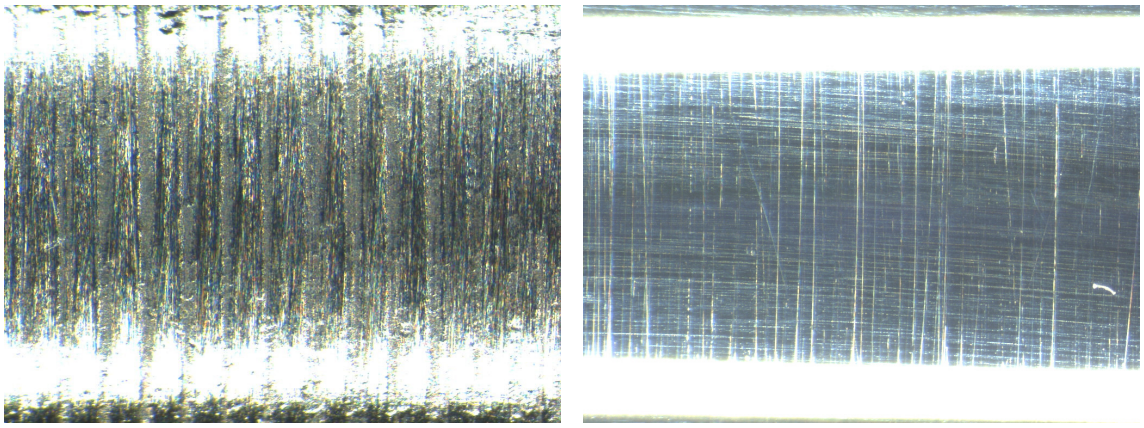
It was noticed once again that the dimensions were slightly above the required, as it is illustrated at Table 4.4.5. The dimensions for all specimens are supplied in Appendix F, Table F.0.1.

Table 4.4.5: Smooth specimens (150 Hz) P1 to P24 dimensions

Variable -	D middle mm	L mm	D thread mm	$D2$ thread mm
Average	7.036	109.45	9.023	9.018
Standard deviation $\hat{\sigma}_x$	0.0419	0.771	0.0453	0.0486

The surface finish remained poor on these larger specimens (Fig. 4.4.15a), thus, the polishing sequence was assigned and allowed to remove the grooves observable, for example,

on Figure 4.4.15b.



(a) (b)

Figure 4.4.15: Smooth specimen (150 Hz) P5 pre (a) and post (b) polishing operations ×40 on the magnifying eye

4.4.3 Surface roughness smooth specimens comparison for 20 kHz and 150 Hz

The SR of the smooth specimens for 150 Hz was assessed only after the experimental tests. These specimens, thanks to the diameter of 7 mm, are more straightforward to measure circumferentially, like it is shown on the setup of Fig 4.4.16.

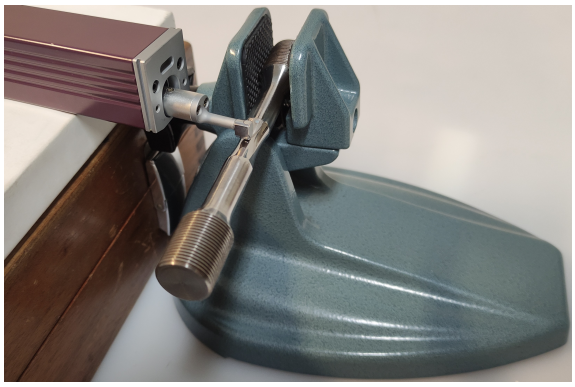


Figure 4.4.16: SR setup for the circumferential assessment of the smooth specimen (150 Hz)

For the 20 kHz specimens, all the SR were uniquely evaluated on the failed test pieces, but they are equivalent to the measurements after polishing. The average SR obtained for botch specimens type is easier to compare on Figure 4.4.17. The data for the SR of all specimens is given in Tables E.0.4 and F.0.3.

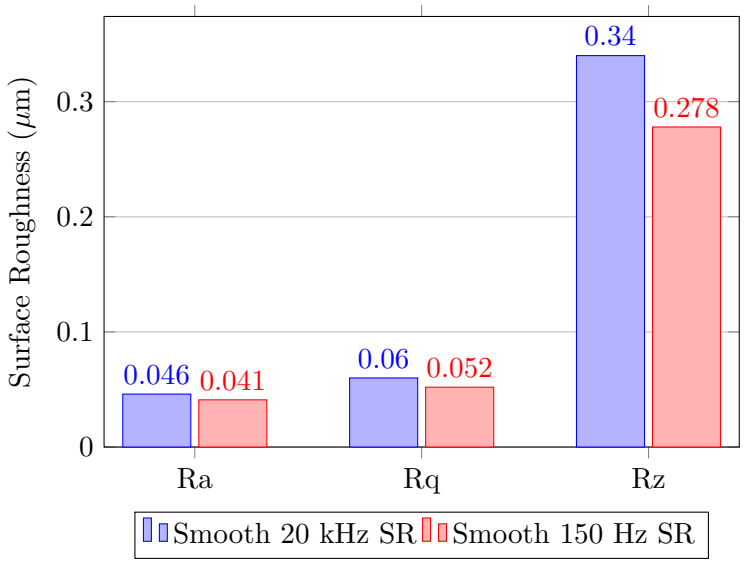


Figure 4.4.17: Average SR in the longitudinal direction for smooth specimens at 20 kHz and 150 Hz (3 measurements for each). 19 test pieces for 20 kHz and 11 for 150 Hz.

The inference from Figure 4.4.17 is that the SR on the longitudinal direction are fairly similar, hence this variable is not an influence in the comparison between both specimens' results. The specimens for 150 Hz have a SR slightly lower, that can be due to the surface available for measurement being near flat, which does not happen in the other small specimens. The Ra of the longitudinal direction is bellow 0.1 μm.

The required Ra is for the circumferential middle section, hence the accessed SR is presented on Figure 4.4.18, although it being more difficult and inaccurate to determine.

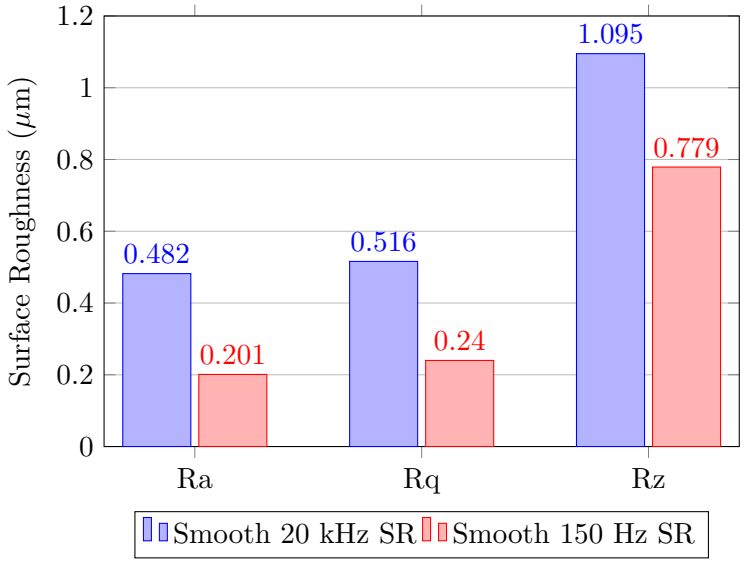


Figure 4.4.18: Average SR in the circumferential direction for smooth specimens at 20 kHz and 150 Hz (3 measurements for each). 19 test pieces for 20 kHz and 11 for 150 Hz.

For this last direction chosen, the SR of the specimens for 20 kHz is double the one verified for the ones materialized for 150 Hz, which is double the required except for the Rz. Since by Figures 4.4.11 and 4.4.15 taken on the magnifying eye it is perceived that

the surface quality is the same, these SR values are definitely strongly affected by the size effect effect of the specimen. To put it in other words, the 7 mm diameter of the smooth specimens for 150 Hz specimens have a more steady surface to access the surface roughness than the 4 mm diameter used at 20 kHz. Either way, the minimum SR average value measured with this device is double the required for the circumferential section (Ra= 0.1 μm) certainly because of the specimen's shape.

It is also important to mention that the variability in the longitudinal direction is very similar on both types of specimens, in Figure 4.4.19.

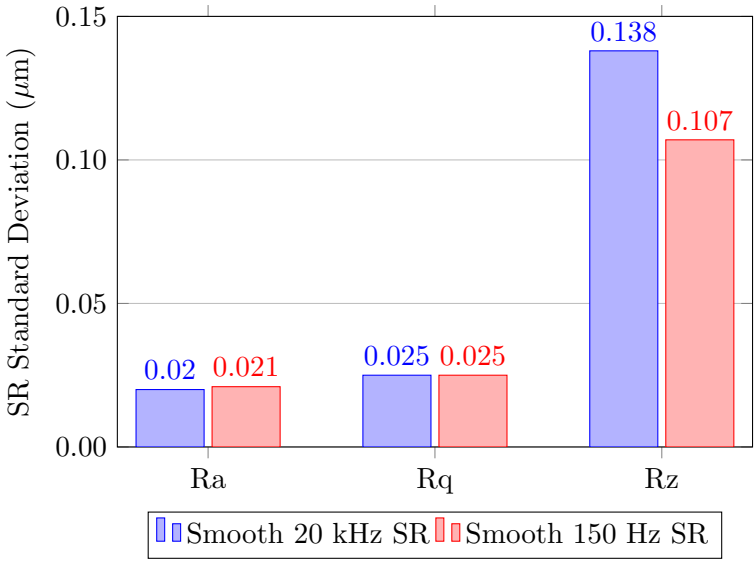


Figure 4.4.19: SR standard deviation in the longitudinal direction of smooth specimens at 20 kHz and 150 Hz. 3 measurements were taken for each specimen.

Contrariwise, in the circumferential direction the variability is indubitably higher than in the longitudinal, again owing to the size difference. On Figure 4.4.20 the variabilities of both specimens are dissimilar, this time the specimens for 150 Hz present a higher SR variation than the ones for VHCF 20 kHz. The SR assessment besides being influenced by the specimens diameter difference, it is affected simultaneously by human induced errors.

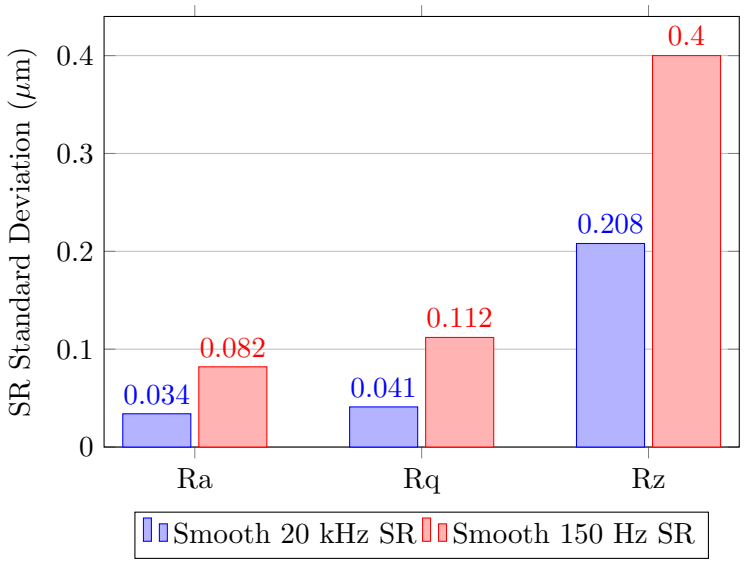
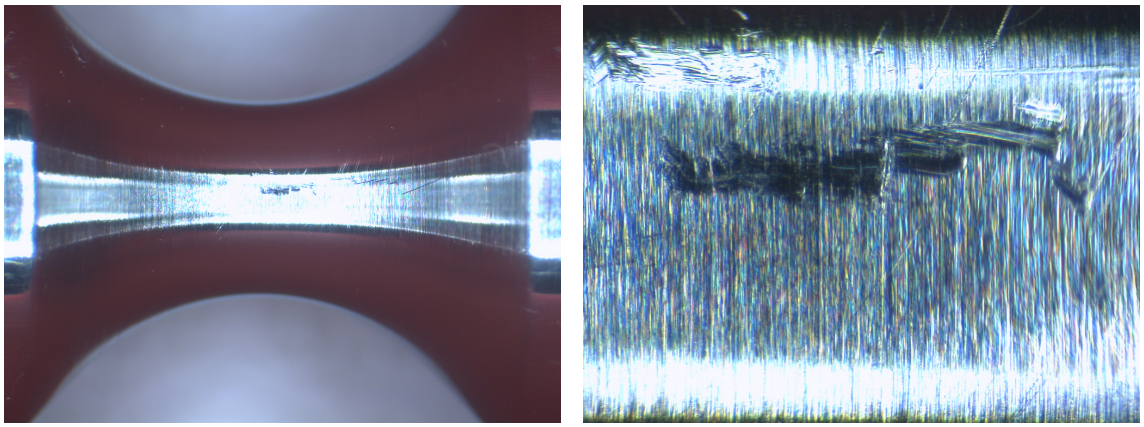


Figure 4.4.20: SR standard deviation in the circumferential direction for smooth specimens at 20 kHz and 150 Hz. 3 measurements were taken for each specimen.

4.4.4 Notched specimens (20 kHz)

The notched specimens have a smaller variable section length that requires more attention, portrayed on Figure 4.4.21. As it can be observed, beyond the slight grooves there is a scratch that is only superficial and was caused by the use of pachymeter for dimensional control in the manufacturing workshop. It can be removed with the defined polishing operations.



(a) (b)

Figure 4.4.21: First notched specimen P1 ($K_t = 1.25$) before polishing operations observed at ×8 (a) and ×64 (b) magnifications

Figure 4.4.22 shows the notched specimens with the reduced dimensions to achieve the 20 kHz resonance frequency.

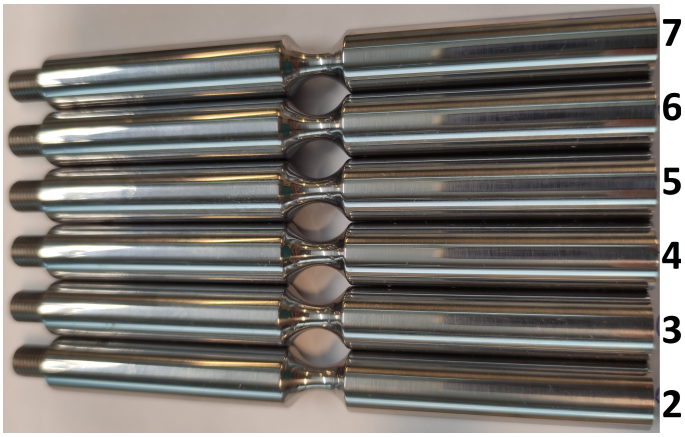


Figure 4.4.22: Notched specimens ($K_t = 1.25$) for ultrasonic tests at 20 kHz, arrival state P2-P7

The dimensions and standard deviation ($\hat{\sigma}_x$) of the referred specimens are given at Table 4.4.6, where it is perceived they are as accurate as the second batch of the smooth specimens. The resonance frequency is close to the desired.

Table 4.4.6: Notched specimens $K_t = 1.25$ P2 to P10 average dimensions (3 measurements for each dimension)

Variable	f	D_2	D_1 Thread	D_1 Flat	L_1 Flat	L_1 Thread	$2L$
-	Hz	mm	mm	mm	mm	mm	mm
Average	19.97	4.013	10.010	10.014	43.523	43.487	97.129
Std. deviation	0.013	0.016	0.006	0.005	0.091	0.076	0.020

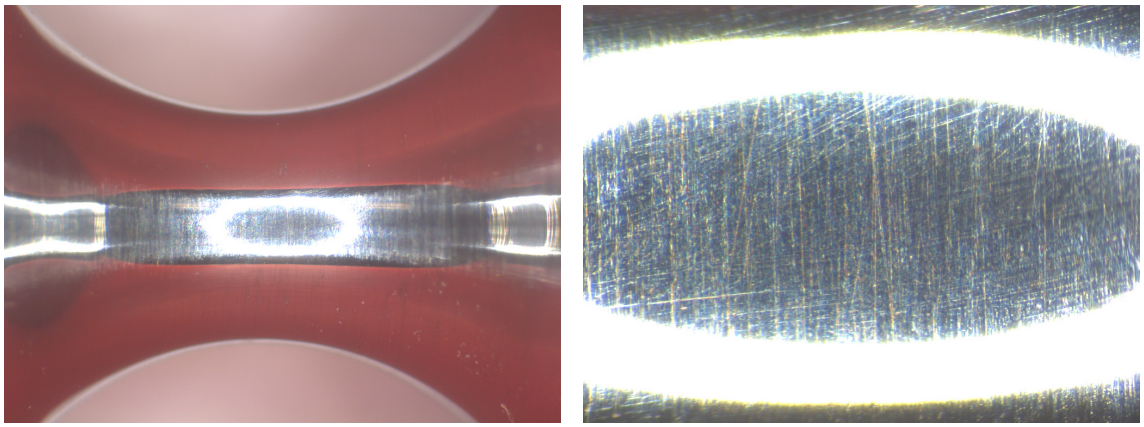
The surface roughness can be measured exclusively on the circumferential direction because of the short sized needle. These were done for quality control on the specimens of Figure 4.4.22. The specimen P1 of Figure 4.4.21 was not initially considered for testing since its thread was machined to diminish the length in order to raise the frequency. The SR of some specimens are on Table 4.4.7.

Table 4.4.7: SR of the notched specimens ($K_t = 1.25$) before polishing (3 measurements for each)

Specimen	Ra	Rq	Rz
	μm	μm	μm
2	0.491	0.757	1.440
3	0.465	0.487	0.892
4	0.419	0.436	0.862
8	0.479	0.502	0.997
9	0.489	0.511	1.044
Average	0.4685	0.5385	1.0468
Standard deviation	0.0278	0.1939	0.2570

The values are in accordance with the surface roughness presented in Section 4.4.3. Moreover, although having improved the surface, as the example of Figure 4.4.23, the

specimen still required a polishing to improve the surface quality and maintain the procedure.



(a) (b)

Figure 4.4.23: Notched specimen P3 ($K_t = 1.25$) with the correct length before polishing, at ×10 (a) and ×64 (b) magnifications

Summarizing the study of the surface roughness, the updated Figure 4.4.24 clarifies that the values measured after polishing are similar. The difference observed for the distinct testing frequencies is only a consequence of the wider diameter adopted for testing at 150 Hz.

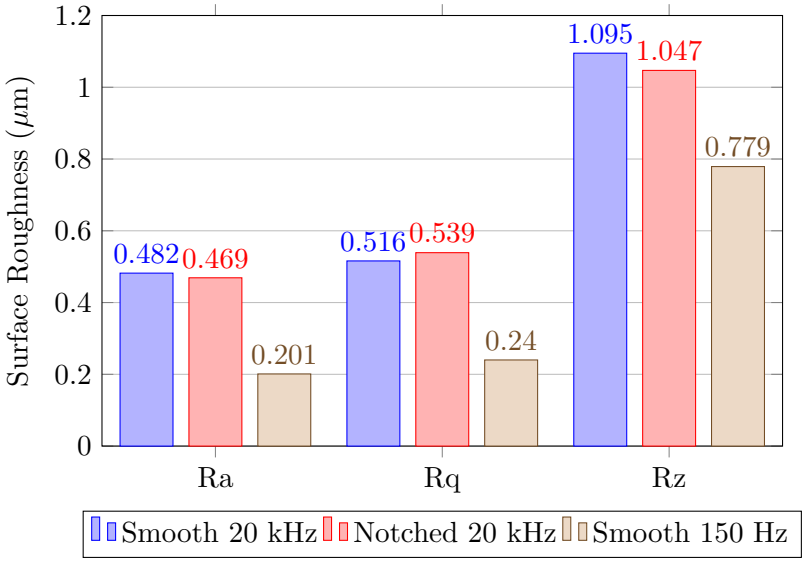


Figure 4.4.24: Average SR in the circumferential direction for the smooth specimens for testing at 20 kHz and 150 Hz, along with the notched specimens for 20 kHz.

4.5 Experimental apparatus for 20 kHz tests

The machine used for testing at 20 kHz was the is the USF-2000 from the japanese manufacturer Shimadzu, which is presented at Figure 4.5.1. Figure 4.5.2 shows the connections in the experimental apparatus, along with the different components.



Figure 4.5.1: Shimadzu USF-2000 Machine with its peripheral equipments

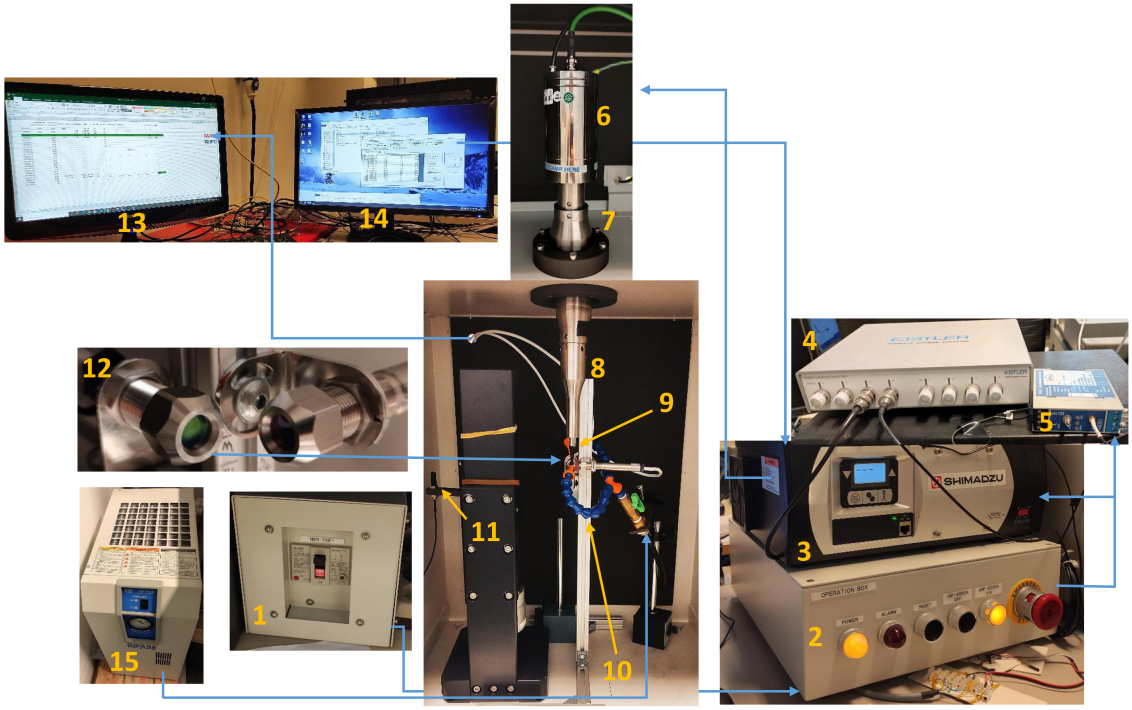


Figure 4.5.2: UFT Machine. Labels: 1- Current stabilizer; 2- Operation box; 3- Signal Generator; 4- DAQ box from Kistler; 5- Eddy current signal generator; 6- Piezoelectric Transducer; 7- Booster; 8- Horn; 9- Hourglass Specimen; 10- Compressed air nozzle (and valve); 11- Electromagnetic probe; 12- Pyrometers; 13- PC to monitor the temperature; 14- PC to control the test and register its values; 15- Air dryer

The current stabiliser supplies power to all components and peripherals of the machine including the computer. The Signal Generator, Transducer, Booster and Specimen

functions were detailed on Chapter 2.4.

The Operation Box serves the purpose of turning the machine on/off and beholds the emergency button. The Eddy Current Generator reads the signal from the probe, when it is placed under the specimen, and transforms it for the Kistler DAQ. This last is used to calibrate the machine and obtain the system gain for the specimen to be tested. The Eddy Current Generator (ECL101-U8-SMM-3.0) has a resolution of 500 nm for the 80 kHz bandwidth, and the range of 2.00 mm and near gap of 0.35 mm. Its typical linearity is 0.50 % of the range.

The compressed air is dried and it cools down the transducer. Plus, when the green valve switch is open, it prevents the specimen from overheating, keeping it around 30 ^{o}C during the fatigue test. The pyrometers measure the temperature on the right and back of the specimen. It must be precisely at 10 mm from the test piece to only acquire its temperature. The hourglass specimen is painted black to have emissivity compatible with the pyrometers, that additionally brings cooling.

The pyrometers are not suitable for measurements on metals due to the emissivity and reflectivity of the reflectance on the sample's surface. This is overcome by painting the surface black, making it possible to use the pyrometers and obtain correct measurements. It was made an adjustment of the emissivity by painting a metal plate with the same paint and recording the temperature acquired by the pyrometer and a thermocouple during the plate heating.

4.5.1 Sequence to execute a UHCF test in the Shimadzu USF-2000

To turn on the UHCF system, it is necessary to follow the sequence detailed in Table 4.5.1.

Table 4.5.1: Sequence to turn on the experimental apparatus

Step	Task	Device on Fig. 4.5.2
1	Empty the water reservoir of the air dehumidifier.	15
2	Open the compressed air feeding valve.	
3	Turn on the current stabilizer.	1
4	Turn on the air dryer.	15
5	Turn on the computers (and monitors).	13 & 14
6	Check with the torque wrench and the special tool that the horn is tight to 25 Nm.	7 & 8
7	Turn on operation box, which turns on the ultrasonic power supply that controls the piezoelectric.	2 & 3
8	Run Supersonic (the testing software).	

Step 6 is important to ensure the manufacturer's specified torque and because some stress may be applied when performing task 7. Owing to the use of the adaptor tool used with the torque wrench (on Fig. 4.5.3b), the 21.4 Nm on the torque wrench corresponds to the specified 25 Nm. This is determined in the Component Dynamometer Type 9272, from Kistler, using the steel adaptor of Figure 4.5.3a. Then, the horn is tightened to the booster like it is shown in Fig. 4.5.3c, using the tools of Fig. 4.5.3b and the torque wrench. The Booster is held in place with the black accessory in order to not damage the machine and the Horn is tightened in the normal direction.



(a) (b) (c)

Figure 4.5.3: Accessory to calibrate the torque wrench for 25 Nm (a), tools to tighten the horn (b) and tightening direction (c).

For task 6 and 7, it is important to guarantee that in the event of movement/vibration of the Horn, at system startup, there is no contact between the components inside the machine, namely with the probe. Having these steps, a "Check frequency" is usually done to verify the machine's resonance frequency.

Following this, the sequence to tighten the specimen in the Horn is illustrated on Figure 4.5.4.

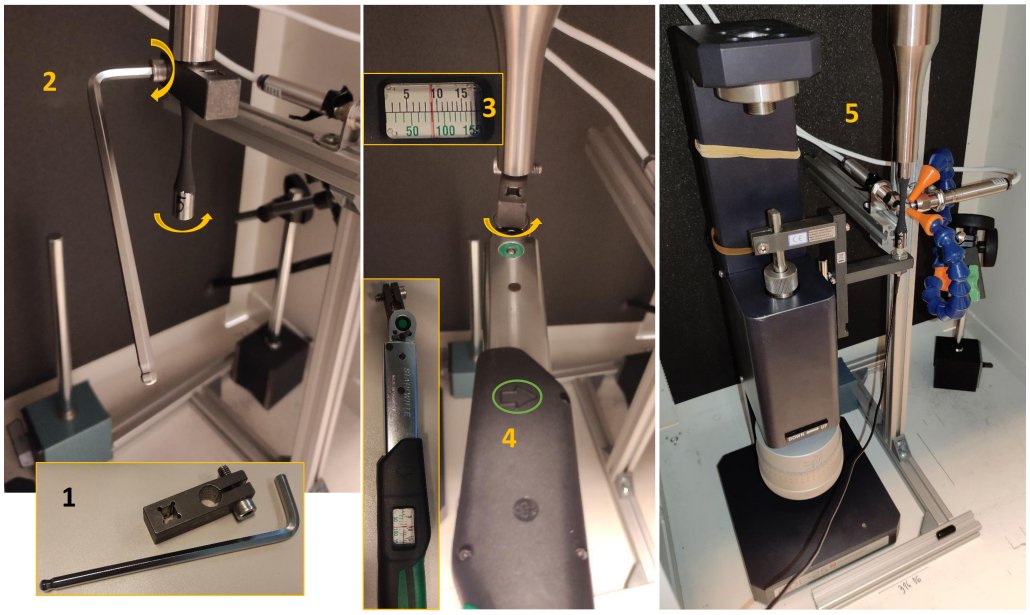


Figure 4.5.4: Sequence to tighten the specimen in the machine and probe placement

First, the test piece is screwed by hand on the top part in order to avoid torsion on the specimen. Then, the tool (1) is passed through the specimen and tightened with the 5 mm hex key (1), being careful not to lean the tool against the Horn. Afterwards, 9.0 Nm (3) at the torque wrench (4) ensures the correct torque, which corresponds in reality to 10 Nm (because of the tool used). It is tightened clockwise until 2 clicks are heard.

Then, it is removed and the tool (1) is unscrewed. It is a good practice to verify the tightening before putting the probe below the specimen. For that, the compressed air valve is opened and the specimen is vibrated by a small pulse close to the test load (for example, 40 % of the maximum power for the smooth specimens) to assure it will not unscrew. Next, assemble the experimental apparatus and place the electromagnetic probe under the specimen carefully without touching anything (5).

Moving forward, the Shimadzu probe which is connected to the DAQ Kistler LabAmp Type 5165A, number 11 and 4 respectively on Figure 4.5.2, enables to calibrate the machine's displacement system. The initial step is to open the Kistler software (DAQ) to adjust the probe until it displays 4 V, register its height with a resolution of 0.001 mm and then repeat the process for 6 V. An Excel spreadsheet calculates gain of the probe, fundamental to measure the displacement. It is usually around 189 μm/V, but is dependent on the probe's position and the material.

Next step, is to obtain data for construction of a calibration curve, to introduce in Supersonic. This curve is necessary so that the control system of the machine defines the power to be delivered to obtain desired nominal stress. The displacement is acquired for low loads and interpolated for higher loads. The first test at 20 %, followed by the 40 % of the maximum machine's power is executed while the DAQ reads the displacement, which generates a data file. The 15 % load is executed through "Check Frequency" to obtain one more point for the next step. Supersonic then adjusts for each estimated load value the corresponding power. The data file is then read by a Scilabs Fourier Function Transformation program that provides on Figure 4.5.5, the displacement's amplitude and the resonance frequency.

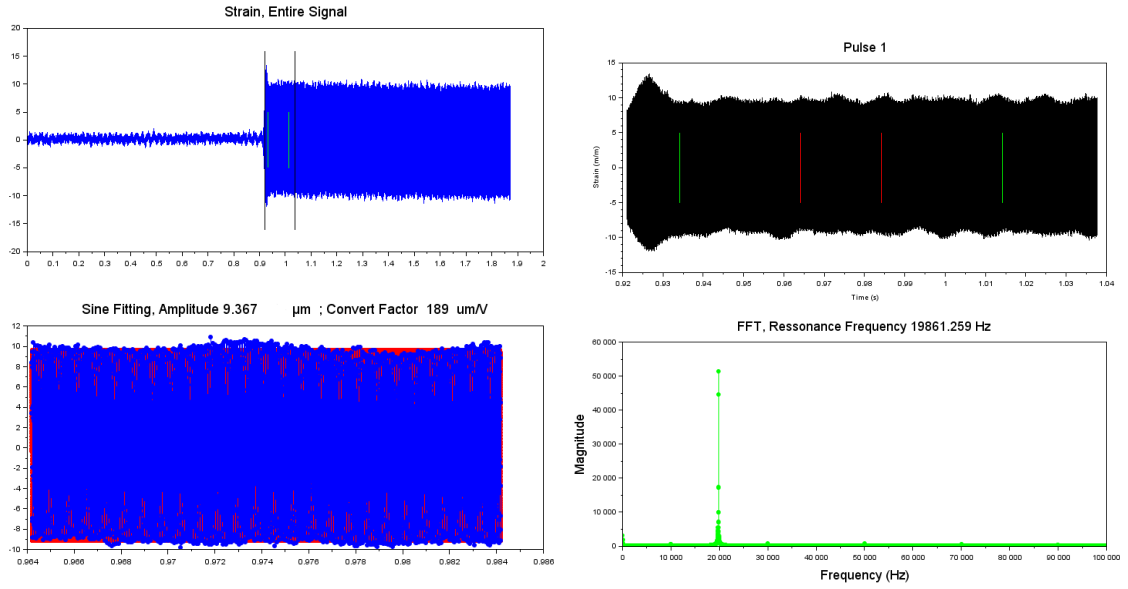


Figure 4.5.5: Example of the data for 15 % load of the specimen P17. Displacement amplitude is 9.37 μm

The three distinct points in the displacement-load percentage plot (Fig. 4.5.6) provide a linear regression that allows to determine other level's approximate maximum displacement. The 60 % of the maximum power is not performed to avoid the yield of the specimen.

Table 4.5.2: Calibration data smooth specimen P21

Power %	Displacement μm
0	-0.06
15	9.37
19.87	12.61
39.93	25.28
60	38.29
80	51.01
100	63.74

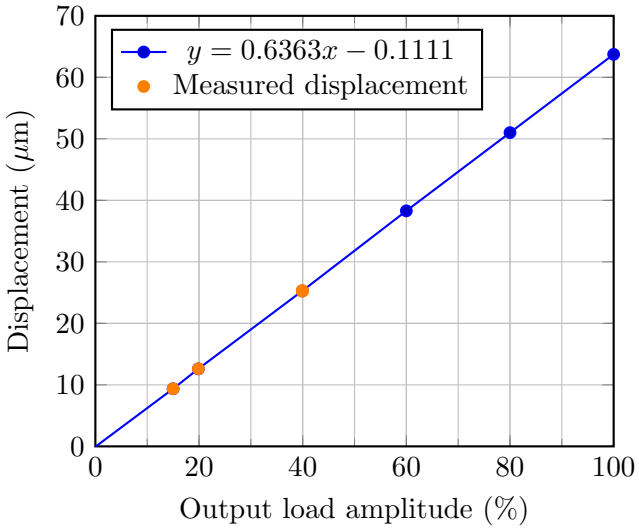


Figure 4.5.6: Calibration curve for the specimen P21

Filling the data for 20 %, 40 % and 60 % in the software (Fig. 4.5.7) as in Table 4.5.2, the Supersonic calculates the load (%) to apply according to the displacement for the required stress.

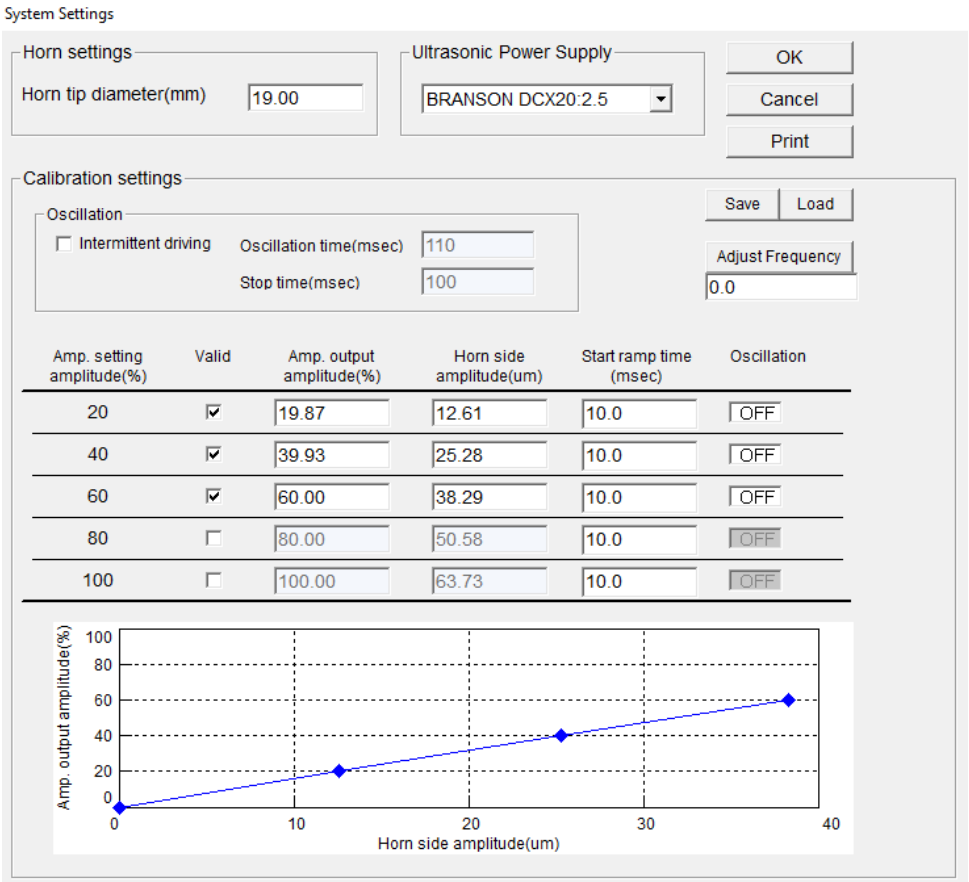
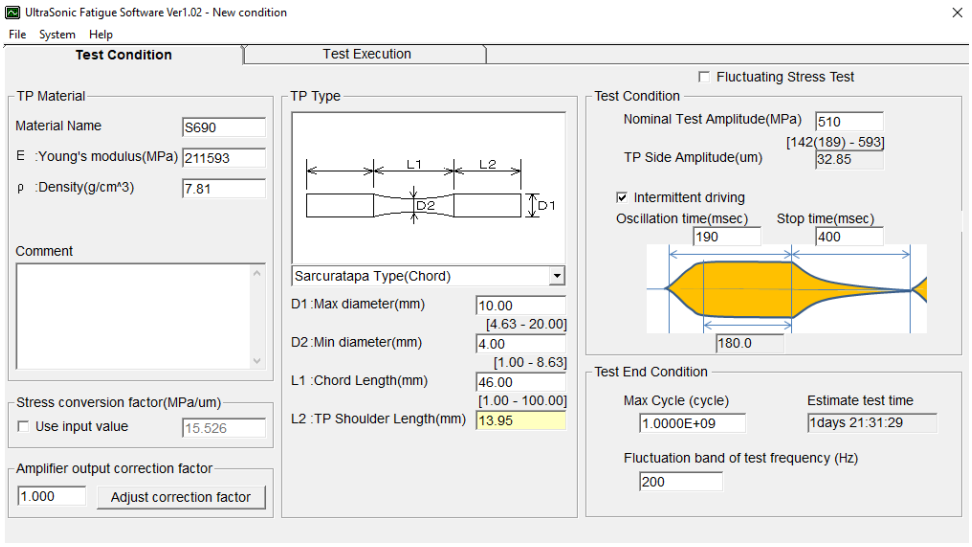


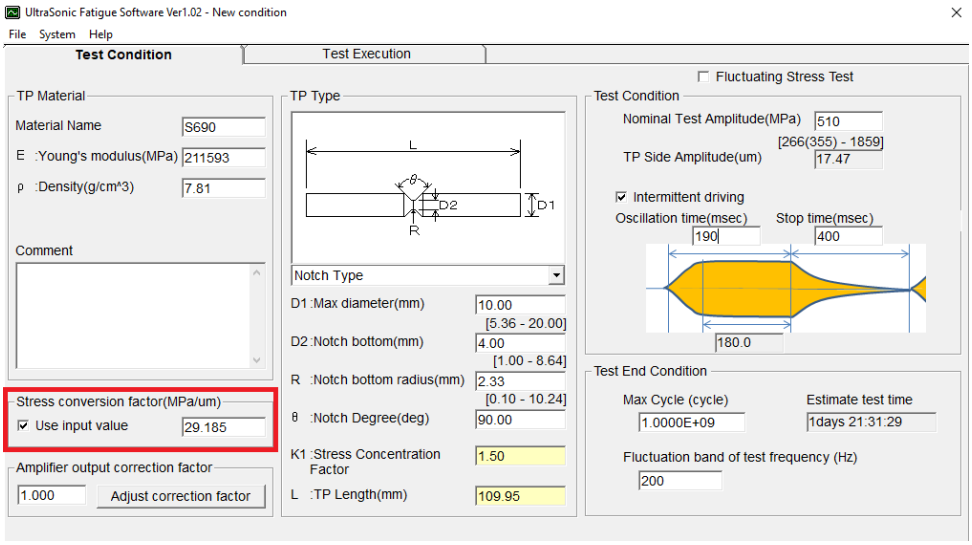
Figure 4.5.7: Supersonic system settings page where the calibration is performed and the data for horn amplitude is introduced

Next, on the Test Condition page (Fig. 4.5.8a) the properties of the material are introduced on the left and on the middle, the specimen's dimensions. According to these properties, the software calculates the stress conversion factor (bottom left) and applies the displacement for the nominal stress amplitude, on the right. The stop time (T_{off}) on a new material is relatively high since it is unknown which temperature it will achieve. The 33 ºC was adopted as the reference temperature to set T_{on} and T_{off}, in order to have a compromise between test speed and temperature. Hence, on winter the T_{off} is shorter than the one on Fig. 4.5.8a and the experimental test can be done faster. Nevertheless, the oscillation time should not drop below the 110 ms because the machine is not able to measure precisely short cycle times.

For the notched specimen it is necessary to change the specimen's type and write the new test variables. Since it was concluded that the FEM has better accuracy than the analytical solution, for notched specimens a stress conversion factor was input manually (Fig. 4.5.8b).



(a) Smooth specimen P17 (20 kHz)



(b) Notched specimen P8 (20 kHz)

Figure 4.5.8: Supersonic test conditions

The test start is done on the test execution page on Fig. 4.5.9. Here the data is displayed with the interval chosen from a start cycle to an end cycle. It shows for each cycles the frequency and the stress amplitude, which are saved after each experimental test.

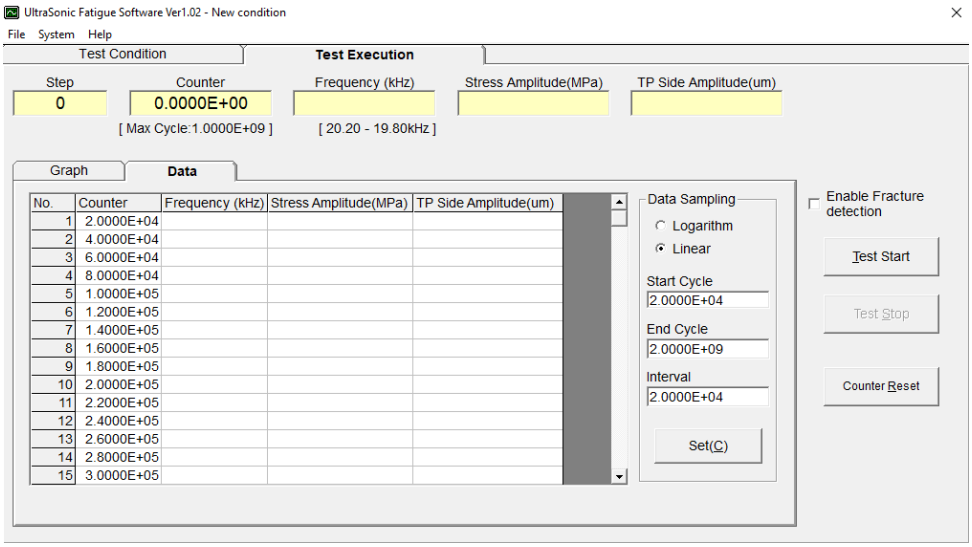


Figure 4.5.9: Supersonic test start page

4.6 Experimental apparatus for 150 Hz tests

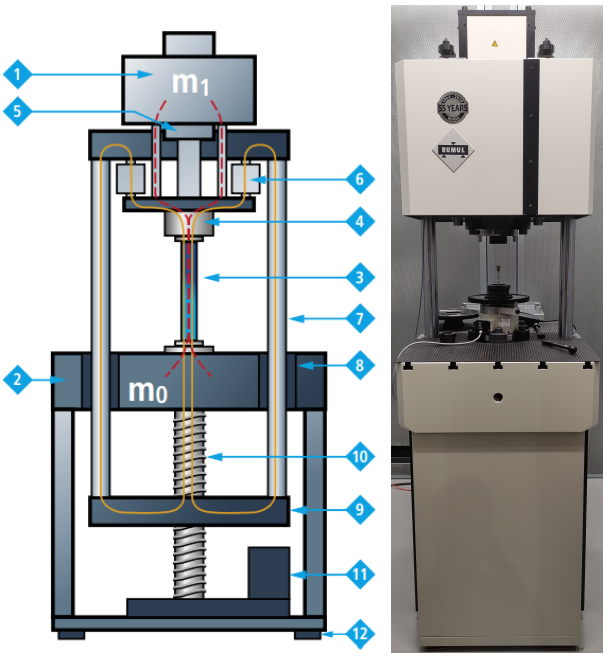
The HCF machine is a Rumul Testronic equipped with a 150 kN load cell (Figure 4.6.1b). It is a resonance machine that allows to perform tests for lower cycles with a high accuracy that, depending on nominal load, type of specimen and activated masses of the oscillating system (adjustable in 8 steps) the operating frequency ranges from 40 Hz to 260 Hz. This is achieved with 3 known masses on top of the machine that can each occupy 2 positions, allowing to vary the test frequency (Rumul, 2022).

This machine can stress specimens or structures with a dynamic load superimposed to a static load. The static load is applied by a ball spindle (10 on Fig. 4.6.1a) with a preloaded double-nut which is driven by a low-backlash gearbox and a servomotor. Thanks to this preloaded double-nut the static load can be adjusted during the dynamic operation in the complete range of the nominal load (100% compression up to 100% tension). This enables to perform experimental tests at any selected stress ratio R (Rumul, 2022).

The dynamic part mainly consists of the mass m_1 (1), the counter mass m_0 (2), the elasticity of specimen (3), springs and all other elasticities and masses within the dynamic load flow. These parts form the oscillating system (resonator) which is controlled and excited by the Rumul Magnodyn drive in its resonant frequency. The short and optimized load flow between the two masses assures a good transfer of the load and a high amplification of the energy fed in (Qualitest, 2022; Rumul, 2022). The load is measured by means of Rumul load cells.

Table 4.6.1: Legend Rumul system

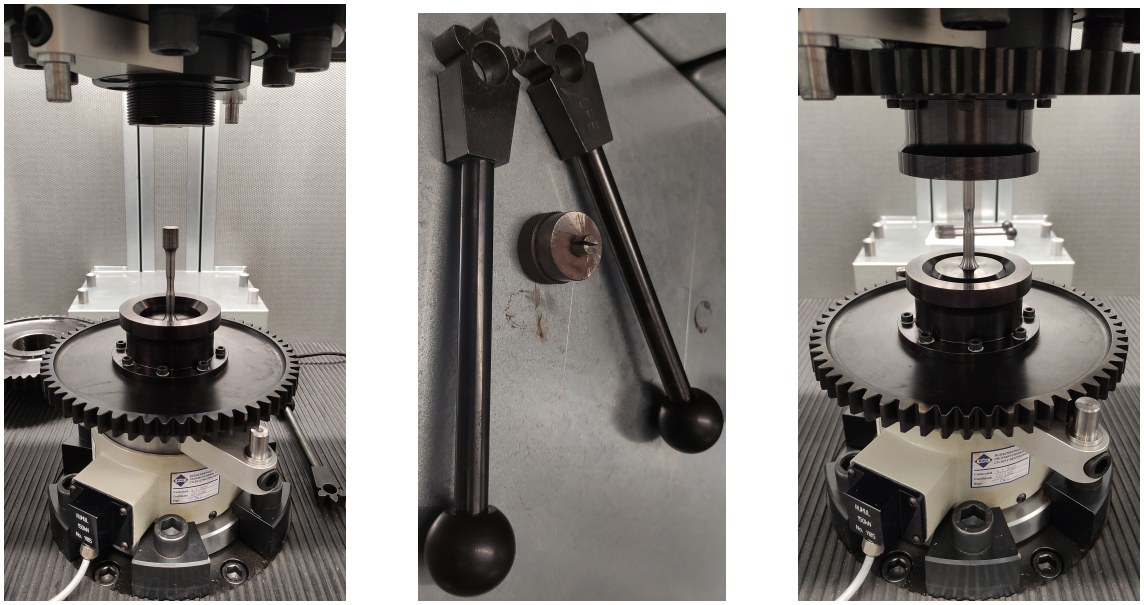
1	Main mass m_1 variable in 8 steps
2	Counter mass m_0 (T-slotted table)
3	Specimen
4	Rumul load cell
5	Rumul Magnodyn excitation system
6	Preload springs for static load
7	Load frame columns
8	Ball bushings
9	Movable lower cross head
10	Screw spindle
11	Spindle drive with servomotor
12	Vibration absorbing supports



(a) (b)

Figure 4.6.1: Resonance system scheme (a) and Rumul Testronic 150 kN (b) (Rumul, 2022)

It allows to start the experimental test with a preload, since the specimens are threaded on the top and bottom grip. The specimen has to thread and pass the grip to lean on the accessory that will transfer the vibrations. In other words, the specimen is axially fixed against the grey accessory of Figure 4.6.2b by threading the external gear that pushes the grip and consequently the specimen down. The final tightening is done with the tool of Figure 4.6.2b. This procedure is done firstly on the bottom and then, by lowering the top part of the machine, the top gear is threaded (Figure 4.6.2).



(a) (b) (c)

Figure 4.6.2: Specimen assembly on the machine (a); Tools to tighten the grip and specimen to the accessory (b); running test position (c)

The top part of the machine is responsible for the frequency generation, while the bottom holds the load cell that measures the force and with the input specimen diameter, calculates the stress to meet the input value.

For this experimental test setup, the specimens were designed to maintain the load ratio $R = -1$ from the VHCF.

4.7 Stress validation for 20 kHz tests

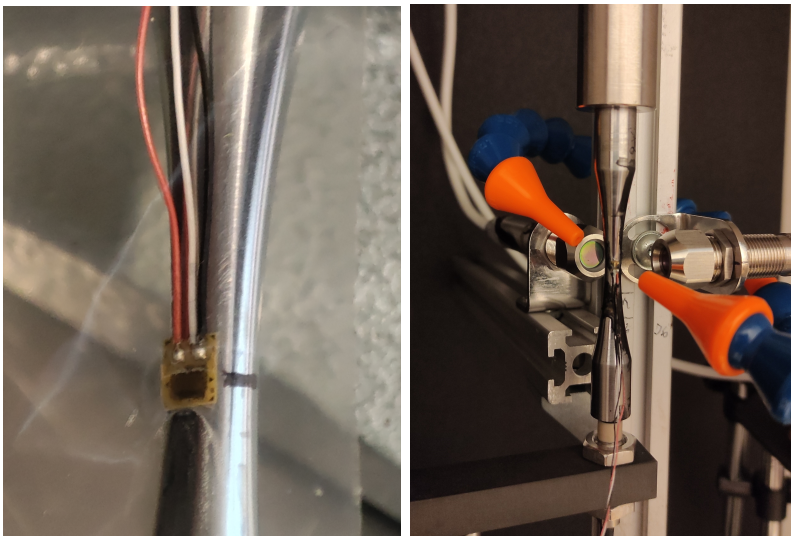
Strain gauges are essential to validate the experimental campaign, notably, certify if the stress Supersonic presents is the real stress on the specimen. Since the stress on specimen's surface is practically the nominal (for the smooth specimens), the stress calculated by the gauge strain must be close to the nominal.

The notched specimen surface stress is crucial to determine and verify if it is 1.15 times the nominal (Table 3.4.4).

The stress validation is not required for the 150 Hz smooth specimens since the Rumul machine has a load cell.

4.7.1 Strain gauge preparation

To glue the strain gauge, first the specimen's surface was degreased with acetone. Then, abrasion/scrubbing with P4000 grit and a drop of M-Prep Conditioner A. Afterwards, the surface was cleaned with M-Prep Neutralizer 5A with a gauze in one direction. Then, the strain gauge was placed on the glue tape with the welds facing towards the glue. The tape with the strain gauge was then stick to the test piece centre (critical section) previously marked. The grid of the strain gauge must be as close as possible to the centre (Fig. 4.7.1a). The assembly on the machine is on Fig. 4.7.1b.



(a) (b)

Figure 4.7.1: Strain gauge (C5K-06-S5145-350-33F) gluing (a) and the smooth specimen assembled on the machine (b)

After ensuring there were no air bubbles, the tape was bent by the solder wires, revealing the strain gauge. This was to put the M-Bond 200 catalyst on the gauge (passed before 10 times on the bottleneck). The catalyst dried in one minute. The crucial part was to place the M-Bond 200 adhesive on the gauge and to press with during 1 min.

The final step is to remove the tape and check with a multimeter if it presents the correct 350 Ω resistance between the red and black wire. The gauge specifications are on Micro-Measurements (2022b) and detailed instructions on Micro-Measurements (2022a).

Following Elsys instructions a half bridge 6 wire was mounted. However, without the internal resistor and implementing the circuit outside it becomes a quarter bridge circuit with an external dummy strain gauge. There are two quarter bridge circuits, one actively measures strain, the other is mounted to complete the circuit. This is on Figure 4.7.2, the dummy allows to compensate the temperature effect (HBM, 2022). For acquisition of the voltage difference, it was used a DAQ Elsys Strain Gauge Amplifier MK2 (on the right side of Fig. 4.5.1) together with the Kistler software. The gauge factor (G_f) is 1.93 or 1.90, depending on the box chosen, and the Elsys Strain Gauge Amplifier MK2 defined gain (G_{amp}) is 10.

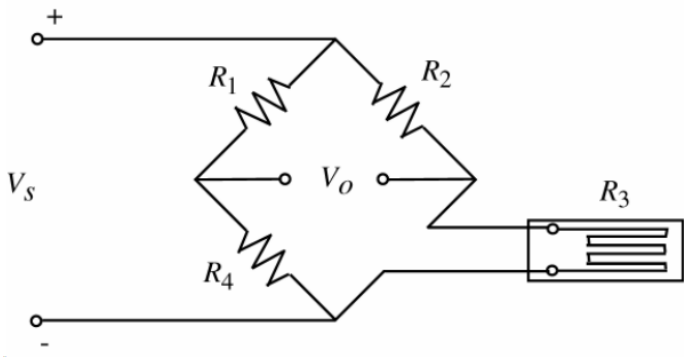


Figure 4.7.2: Quarter bridge-one active gauge (Thitima, 2022)

The gauge factor is given by, where L_G stands for the resistor length:

$$G_f = \frac{\Delta R_3/R_3}{\Delta L_G/L_G} = \frac{\Delta R_3/R_3}{\varepsilon} \tag{4.14}$$

The output voltage (V_0) from Figure 4.7.2 is dependent on the supply voltage V_s and since the resistors have the same resistance (Grech, 2014):

$$V_0 = \left(\frac{-\Delta R_3/R_3}{R_1 + R_2 + R_3 + \Delta R_3/R_3 + R_4}\right) V_s \approx \left(\frac{-\Delta R_3/R_3}{4}\right) V_s \tag{4.15}$$

So, implementing the gauge factor and the gauge amplifier factor on Eq. 4.15, the strain comes in Eq. 4.16b.

$$V_0 = -\frac{G_f \varepsilon}{4} G_{amp} V_s \tag{4.16a}$$

$$strain(\varepsilon) = -\frac{4\frac{V_0}{V_s}}{G_f G_{amp}} \tag{4.16b}$$

The stress is then obtained by multiplying the measured strain by the Young Modulus. The Scilabs Fourier Function Transformation program reads the 20 kHz wave and provides the highest value.

4.7.2 Measurement results with strain gauges on smooth specimens (20 kHz)

The Shimadzu USF-2000 maximum nominal stress is 1000 MPa, so the applied power in percentage corresponds to a stress in function of the 1000 MPa. For each value, it is obtained a strain that corresponds to a stress on Table 4.7.1. There is an uncertainty when the strain gauge is not loaded of about 4 MPa.

Table 4.7.1: Strain gauge measurements on specimen P26

Time sequence ms		Nominal stress MPa	Gauge stress MPa	Error MPa	Error %
Continuous		15% = 150	151	1	0.67
$T_{on} = 200$	$T_{off} = 5000$	20% = 200	203	3	1.50
$T_{on} = 200$	$T_{off} = 5000$	40% = 400	410	10	2.50
$T_{on} = 200$	$T_{off} = 600$	520	523	3	0.58

It is concluded the Supersonic stress is accurate and that at 40 % there was an punctual difference.

Finally, the specimen P26 test load was defined as 520 MPa, in order to measure the strain while testing and prevent the gauge from burning. However, from the S-N curve, this level required a time sequence to prevent the specimen from overheating. This was larger than usual (Table 4.7.1) to ensure the strain gauge would not be burnt and/or affected by the temperature. Figure 4.7.3 displays the data from P26.

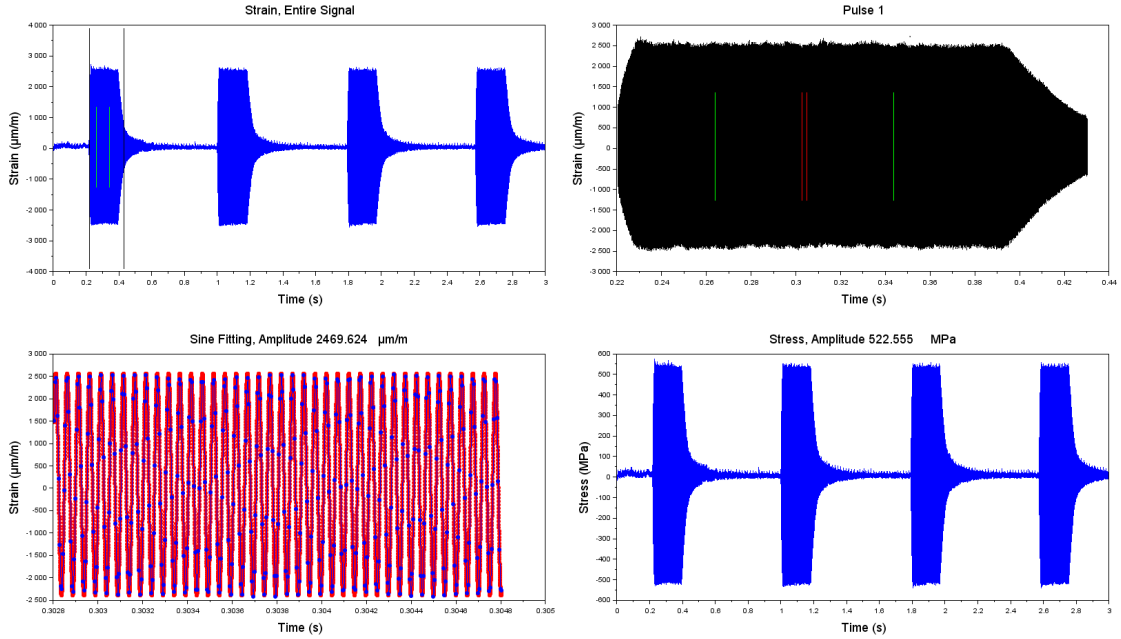


Figure 4.7.3: Strain measured on P26 and corresponding stress

When the stop time was reduced for $T_{off} = 400$ ms the subsequent values where 529 MPa and 526 MPa, in only 3 minutes. So, it is perceived that due to the other strain gauge of the bridge not being next to the specimen affects the measurement, because it does not compensate the strain gauge heating. The gauge in the specimen is deeply affected by the temperature. This was also supported by the next test that was 3 minutes after which presented an impossible stress of 1530 MPa.

4.7.3 Measurement results with strain gauges on notched specimens (20 kHz)

The notched specimens present a major challenge regarding the stress validation. The maximum strain of the strain gauge is $\pm$ 1.5 %, which cannot be guaranteed due to the notch radius that, in addition, makes it difficult to glue the gauge on the test piece surface.

First, it was defined the stress conversion factor of 29.185 MPa/μm using the ratio between the nominal stress and displacement from Table 3.4.4. This conversion is used in Supersonic instead of the intrinsic equations reviewed on Section 3.1.4.

The experimental strain acquisition is in Figure 4.7.4. Two strain gauges were used, one on the critical section and one on the cylindrical part, 40.74 mm from the specimen's top end. This last strain gauge was added to verify if the data of the first gauge was affected by the possible bending, resulting from the gluing process on the notch which presents a geometry that is a mixture of concave and convex. This surface is quite different from the convex and flat geometries for which extensometers are normally used.

Similarly to what is done for the critical section, the FEM stress of the node corresponding to the strain gauge location is taken. Then, a stress conversion factor of 3.721 MPa/μm is calculated using the applied displacement of the FEM model. This provides an estimation of the stress on that point (σ_{cyl}) by means of multiplying the factor by the probe displacement.

The first step, as for the smooth specimens, was to calibrate the machine for notched specimens, since a power percentage on Shimadzu, will correspond to a different displacement on the specimen's free end. The displacement (on Table 4.7.2) was measured by

the probe for 15 % and 20%, however the 40 % displacement was obtained by the linear relation because it would break the specimen. This brings a higher uncertainty on the stress measured since less points are used for the linear regression.

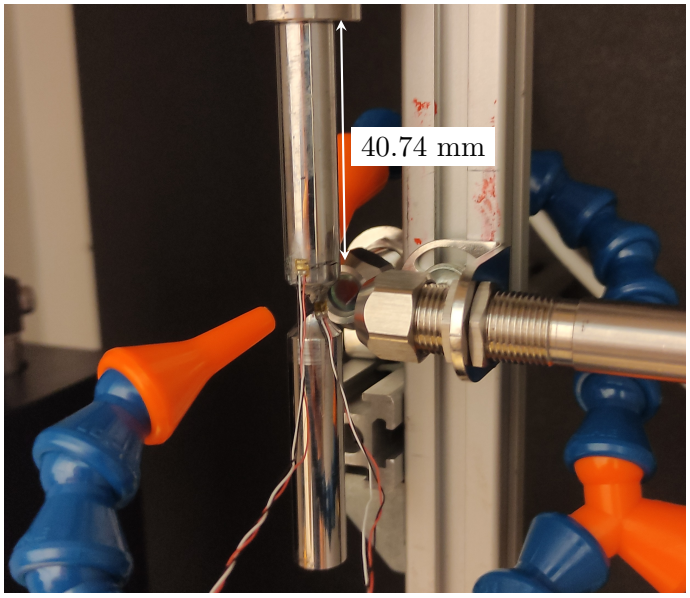


Figure 4.7.4: Strain gauges on the notched specimen P7

The calibration of Table 4.7.2 was used for all the specimens. The stress and strain of P2 on the critical section are on Table 4.7.3.

Table 4.7.2: Calibration data for notched specimens

Load %	Displacement ($y = 0.6912x - 1.4281$) μm
15	8.94
19.89	12.32
40	26.22

Table 4.7.3: Strain gauge on the critical section results for notched specimen P2

Machine displacement μm	σ_{nom} MPa	σ_{max} MPa	σ_{Gauge} MPa	Absolute error MPa	Relative error %
9.22	269	309	311	2	0.52
12.37	361	415	400	-15	-3.70
12.94	378	434	417	-17	-3.98
14.05	410	472	440	-32	-6.73
15.01	438	504	481	-23	-4.49
15.36	448	516	497	-18	-3.56
15.66	457	526	514	-12	-2.23
15.76	460	529	520	-9	-1.69

The predicted nominal stress is obtained by multiplying the displacement Supersonic

reports by the conversion factor. The maximum stress is calculated through the real $K_t = 1.15$. However, the calculated stress on the gauge (σ_{Gauge}), which is the product between the strain (ε_{Gauge}) and E revealed a lack of consistency in the stress error relatively to the σ_{max}. For this reason, the correct σ_{nom} was calculated with the probe measured displacement and numerical model in Table 4.7.4.

Table 4.7.4: Results for the strain gauge in function of the probe displacement on the critical section for the notched specimen P2

U μm	σ_{nom} MPa	σ_{max} MPa	σ_{Gauge} MPa	Absolute error MPa	Relative error %
9.22	269	309	311	2	0.52
12.37	361	415	400	-15	-3.70
12.88	376	432	417	-15	-3.54
13.61	397	457	440	-17	-3.71
14.84	433	498	481	-17	-3.40
15.27	446	513	497	-15	-2.99
15.71	458	527	514	-13	-2.56
15.96	466	536	520	-16	-2.92

When the probe was placed under the specimen to ensure the displacement measured was correct, it was acknowledged the error was approximately 16 MPa, 3 %. Still, this could be affected by the possible errors of the Young moduli determination. So, the difference between the maximum strain (ε_{max}) on the specimen's surface on the FEM model and the one measured by the gauge (ε_{Gauge}) was analysed on Table 4.7.5.

Table 4.7.5: Strain gauge results compared with the strain of the FEM model on the critical section for notched specimen P2

σ_{Gauge} MPa	ε_{Gauge} μm/m	FEM ε_{max} μm/m	σ_{max} ($E\varepsilon$) MPa	Strain error μm/m	%	Stress error MPa
311	1469.714	1422.414	301	47.300	3.33	10
400	1888.731	1908.172	404	-19.441	-1.02	-4
417	1971.672	1987.628	421	-15.957	-0.85	-4
440	2078.692	2100.281	444	-21.589	-1.03	-4
481	2274.033	2290.094	485	-16.061	-0.70	-4
497	2349.594	2356.451	499	-6.857	-0.29	-2
514	2428.551	2424.629	513	3.922	0.16	1
520	2453.397	2462.931	521	-9.534	-0.39	-1

An unexpected error bellow 1 % for the strain was obtained and for the stress, the maximum absolute error was 4 MPa. To sum up, the stress in function of the probe displacement can be observed on Figure 4.7.5.

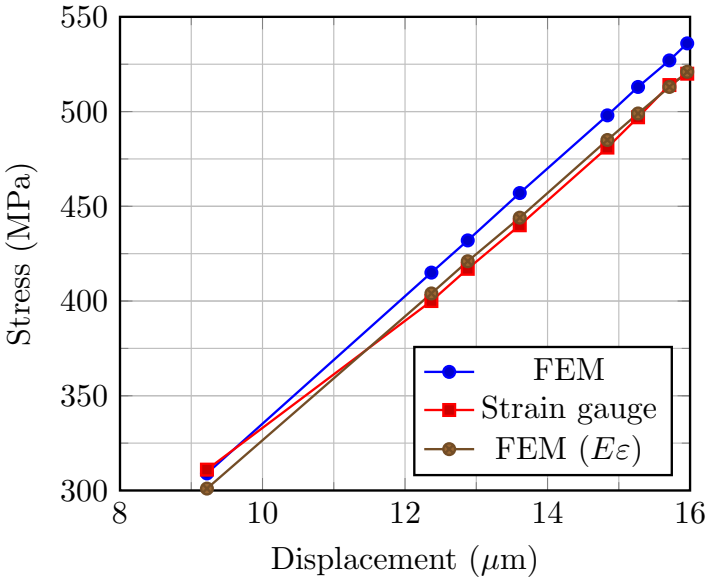


Figure 4.7.5: Stress predicted by FEM and calculated for the gauge on the notch in function of the probe displacement for the notched specimen P2

For P2, on the critical section, the stress calculated through the strain gauge data is closer to the FEM stress obtained via $E\varepsilon$ than the maximum provided by the model. On the cylindrical part of the specimen (Fig. 4.7.4), there were 2 strain gauges positioned on the cylindrical part because the first broke down after 3 trials. The nominal stress is the value introduced on the machine. The results are on Table 4.7.6, where the stress (σ_{cyl}) and strain (ε_{cyl}) predicted by FEM for the cylindrical region are compared to the experimental.

Table 4.7.6: Cylindrical stress and strain compared with the FEM model for the specimen P2

σ_{nom}	U	ε_{Gauge}	σ_{Gauge}	σ_{cyl}	Stress error		ε_{cyl}	Strain error	
MPa	μm	μm/m	MPa	MPa	MPa	%	μm/m	μm/m	%
253	8.66	159.107	34	33	1	4.46	158.505	0.60	0.38
349	11.95	209.765	44	44	0	-0.19	218.723	-8.96	-4.10
450	15.42	254.765	54	57	-3	-4.83	278.574	-23.81	-8.55
264	9.05	159.107	34	34	0	0.61	192.000	-32.89	-17.13
368	12.62	224.456	48	47	1	1.13	210.303	14.15	6.73
380	12.49	258.964	55	47	8	17.70	228.606	30.36	13.28
410	13.92	261.045	55	52	3	6.57	254.780	6.27	2.46
450	15.12	350.139	74	56	18	31.53	276.744	73.40	26.52
460	16.22	323.040	68	60	8	13.25	296.877	26.16	8.81

The predicted stress of Table 4.7.6 is close to σ_{Gauge}. The stress on the cylindrical section is 10 times lower than the critical section. This measurement errors became more important because the absolute signal we read is lower.

For the second round of measurements, it was decided to study a wider range of stress levels with a constant increment between them on the cylindrical region. On Table 4.7.7,

it is shown the displacement acquired for each nominal stress in order to get an accurate estimation of the FEM strain and stress.

Table 4.7.7: Cylindrical stress and strain compared with the FEM model for a wider range of stress levels with constant increment, for the specimen P2

σ_{nom}	U	ε_{Gauge}	σ_{Gauge}	σ_{cyl}	Stress error		ε_{cyl}	Strain error	
MPa	μm	μm/m	MPa	MPa	MPa	%	μm/m	μm/m	%
276	9.56	206.462	44	36	8	22.84	174.93	31.53	18.02
368	12.17	239.947	51	45	5	12.09	222.80	17.15	7.70
395	13.16	260.405	55	49	6	12.51	240.90	19.50	8.09
423	14.08	278.384	59	52	7	13.23	257.64	20.75	8.05
450	15.33	285.243	60	57	3	6.00	280.66	4.58	1.63
478	16.03	308.404	65	60	6	9.37	293.49	14.92	5.08
506	16.37	319.555	68	61	7	11.00	299.64	19.92	6.65

The stress calculated had an error below 10 MPa, 14 %. This is disregarding the first value that corresponds to 15 % since the machine does not have an accurate functioning at low powers. The stress error calculated considering the strain of the FEM model is once again closer to the stress obtained from the strain gauge, as it is seen in Table 4.7.8.

Table 4.7.8: Determination of the cylindrical stress difference regarding the FEM stress calculated from the strain for the specimen P2

Measurement 1			Measurement 2		
σ_{Gauge}	σ_{cyl} $(E\varepsilon)$	Stress error	σ_{Gauge}	σ_{cyl} $(E\varepsilon)$	Stress error
MPa	MPa	MPa	MPa	MPa	MPa
34	34	0	44	37	7
44	46	-2	51	47	4
54	60	-6	55	51	4
34	35	-1	59	55	4
48	48	0	60	59	1
55	49	6	65	62	3
55	54	1	68	63	5
68	63	5			

The lower error on Table 4.7.8 suggests that once again the product of the FEM strain and Young Modulus is closer to the stress calculated based on the strain measurements with the strain gauges.

The measurements on the cylindrical region turned out less accurate than the critical section, most likely owed to the background noise of the stress acquisition. On Figure 4.7.6, the cylindrical section stress for the first measurement of Table 4.7.6 and the second of Table 4.7.7 is plotted in function of the displacement measured on the free end of the specimen.

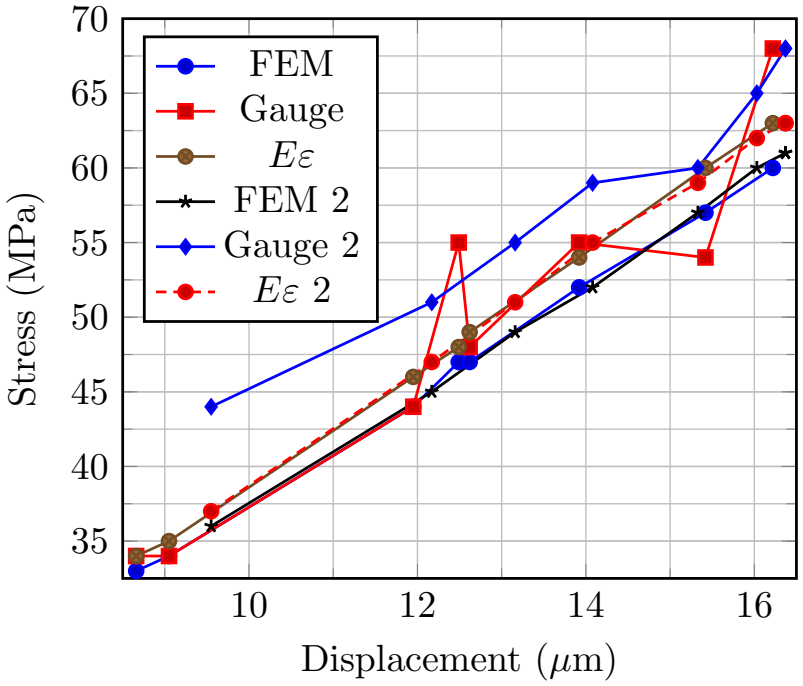


Figure 4.7.6: Stress predicted by FEM and calculated for the gauge on the cylindrical region in function of the probe displacement for the notched specimen P2, for measurement 1 and 2

Taking into account Figure 4.7.6, the stress given by the product of the Young Modulus by the strain is visually perceived closer to the measured value. It is a curve with higher slope than the direct stress form the FEM model. The results from the first measurements have a higher variability but are closer to the predicted, meanwhile the second measurements have a shift upwards yet are more consistent. This can be affected by the uncertainty of the machine at low displacements.

To reinforce the stress confirmation, two strain gauges were glued to the test pieces P7 and P8, but only for the P8 was possible to measure the cylindrical stress. For P7 the signal acquired had too much noise so the result was discarded. The nominal stress introduced in the machine for the P7 was 460 MPa and for the P8, 510 MPa, which turned out to be higher than calculated with the probe displacement.

Table 4.7.9: Notched specimens P7 and P8 calculated stress

Nº	σ_{nom}	U	σ_{max}	σ_{Gauge}	Stress error		ε_{max}	ε_{Gauge}	Strain error	
-	MPa	μm	MPa	MPa	MPa	%	μm	μm	μm	%
7	443	15.18	509	490	-19	-3.84	2342.30	2318.93	-23.37	-1.00
8	491	16.83	587	565	-22	-3.90	2597.57	2466.82	-130.76	-5.00
Nº	σ_{nom}	U	σ_{cyl}	σ_{Gauge}	Stress error		ε_{cyl}	ε_{Gauge}	Strain error	
-	MPa	μm	MPa	MPa	MPa	%	μm	μm	μm	%
8	491	16.83	62	44	-18	-29.65	207.22	306.56	99.34	47.94

The last results of Table 4.7.9 were found to be consistent in comparison with the P2 of Table 4.7.4. The three specimens had a maximum relative error of 4 % on the notch

site. Possibly due to the background noise, the stress on the cylindrical part for P8 had a high variation.

To summarize, the stress variability computed by the strain measurements on the notch is around 10 MPa, being affected by: the machine's uncertainty, specimen's curved surface, inaccurate adhesive layer thickness and temperature variability.

For smaller displacements the errors are reduced which validates the numerical solution. A large part of the observed error can be attributed to deviations of the machine itself and some errors in the calibration, since the conversion factor is very large, which causes any error in the displacement to be amplified for this type of specimen.

Overall, the results are satisfactory.

Chapter 5

Results and discussion

This chapter presents the results together with the discussion for the smooth specimens at 20 kHz and 150 Hz and for notched specimens tested at 20 kHz. The S-N curves are presented along with the probability of survival curve. Details of the analysis of surface crack and fracture under Scanning Electron Microscopy are presented.

The specimens with $K_t = 1.5$ were not manufactured due to the lack of time, so the results were not included in this thesis.

5.1 Fatigue S-N curve - Frequency effect on S690 steel

The main assignment of this dissertation was to obtain with high accuracy the S-N curve of the S690 High Strength Steel. The fatigue life for smooth specimens at 150 Hz and 20 kHz are portrayed on Figure 5.1.1.

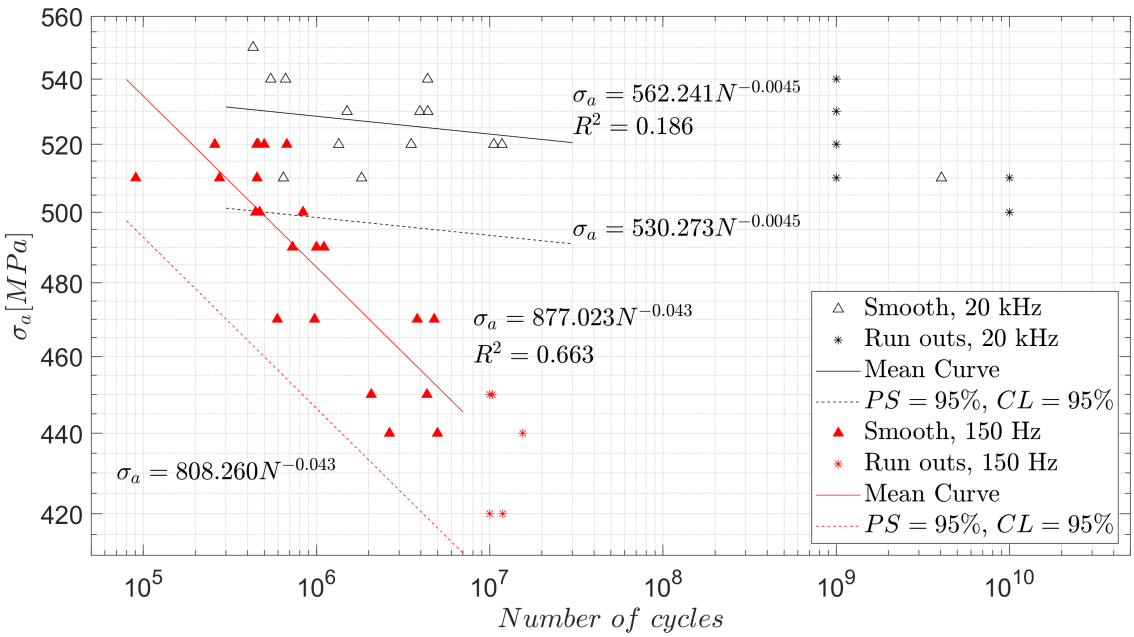


Figure 5.1.1: S-N curve of the S690 obtained for smooth specimens at 20 kHz and 150 Hz

The probability of survival (PS) of 95 % with a confidence level (CL) of 95 % is also displayed on Figure 5.1.1, according to the equations of Chapter 2.1.1. It is deduced both

survival curves are significantly below the S-N curve and define a safe fatigue life for each stress level.

The fatigue limit for smooth specimens tested at 20 kHz was 500 MPa while at 150 Hz it was 420 MPa, being 16 % lower. All specimens failed before 2E7 or survived 1E9 cycles. A similar conclusion was taken in the work developed by Schönbauer et al. (2021) but their specimens of Ck45M steel, in the UFT at 19 kHz, failed before 1E6. Rodrigues da Costa et al. (2020) deduced the same for the ER9 steel grade in the ultrasonic regime, depicted on Figure 2.3.12. It must be noted that low fatigue life results at 20 kHz (of Fig. 5.1.1) are not very trustable since the machine is intended to test in the VHCF regime. Regarding the smooth specimens, it was clear that the second batch of specimens characterized by a better surface quality had much longer fatigue lives.

Palin-Luc and Jeddi (2018), in Fig. 2.3.6, found out for the JIS S15C steel ($Rm = 441$ MPa) there was a fatigue limit drop of 50 MPa (20 %) testing at 140 Hz in comparison to the ultrasonic regime (20 kHz). Since the percentage decrease was higher than the experimental results of Fig. 5.1.1, it is plausible that steels with higher ultimate tensile strength are less prone to the frequency effect.

There is a fatigue limit drop for the 150 Hz smooth specimen of 65 MPa from 1E6 to 1E7. If the tests were extended to 1E9 with the same fatigue limit decrease, then they would be in accordance to what was reported by Bathias (1999), exposed on Section 2.2.

Furthermore, the tests at 150 Hz prove indubitably there is a frequency effect on the S690 steel when testing at 20 kHz. As it is seen on Figure 5.1.1, there is an upwards shifts of the fatigue limit (stress) for the same fatigue life (number of cycles). Despite this, they converge for the same stress level at $N = 1.036$E5 cycles.

In most cases, a size effect exists, i.e., the fatigue strength of large members is lower than that of small specimens. It is extremely difficult to determine this phenomenon because it requires preparing geometrically similar specimens of increasing diameter that have the same metallurgical structure and residual stress distribution throughout the cross section. Changing the size of a fatigue specimen usually results in a larger surface area that propitiates fatigue failures to initiate at the surface. Thus, experimental data on the size effect in fatigue typically show that the fatigue limit decreases with increasing specimen diameter (Boyer, 1997). This, together with the frequency effect (discussed on Chapter 2.3), brings the fatigue limit of the material down for larger specimens and 150 Hz frequency.

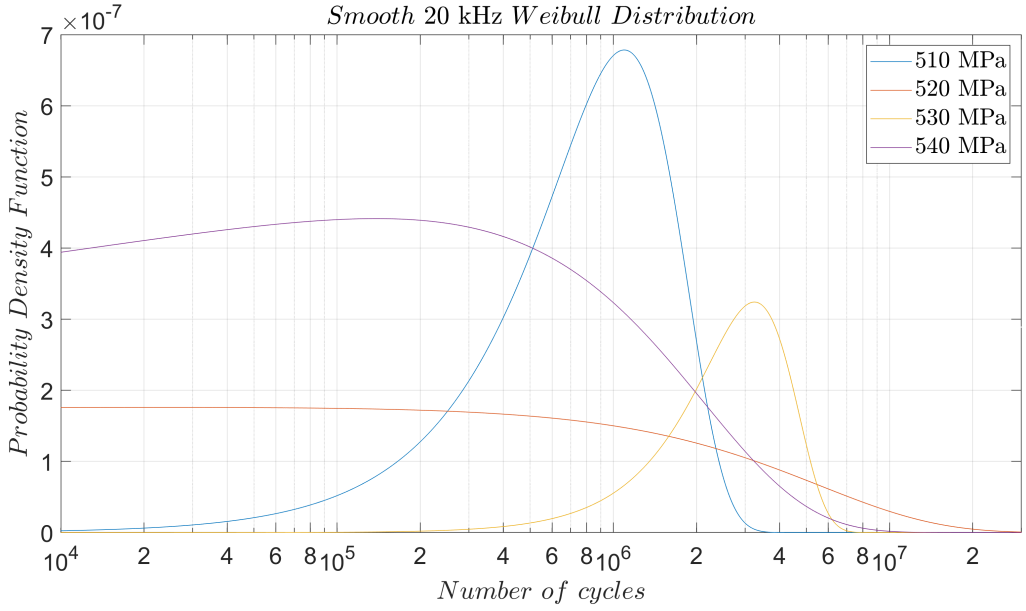
At ultrasonic testing regime the S-N curve is almost a plateau while there is a higher slope observed at 150 Hz. Besides this, the 20 kHz data is more scattered and also the curve less approximated sice the R^2 is lower.

A considerable higher number of run-outs was obtained at 20 kHz since this test was more sensitive to the specimen's manufacturing/polishing quality, as it is pointed out on Table 5.1.1. For the smooth specimens at 20 kHz, the run-out conditions were at 1E9 cycles (2 days), while for the specimens at 150 Hz the maximum number of cycles was 1E7, corresponding to 18 hours.

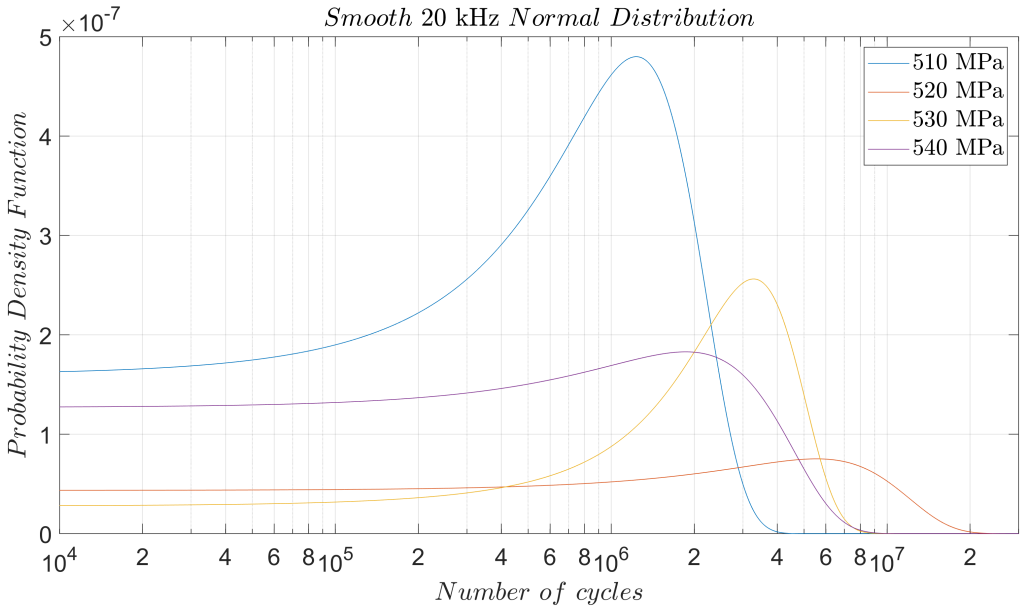
Table 5.1.1: Run-outs for smooth specimens at 20 kHz (1E9) and at 150 Hz (1E7)

Stress MPa	Run-outs Smooth (20 kHz) -	Stress MPa	Run-outs smooth (150 Hz) -
500	1	420	2
510	3	440	1
520	2	450	2
530	2		
540	1		

A method to study the probability of fatigue failure is to fit Weibull and Normal distributions, respectively in Figure 5.1.2 for smooth specimens at 20 kHz, using Matlab intrinsic functions. The probability density function gives the most probable fatigue life for a determined stress level. It is also characterized by increasing the assuredness level with the proximity of fatigue life data at the same stress level.



(a)

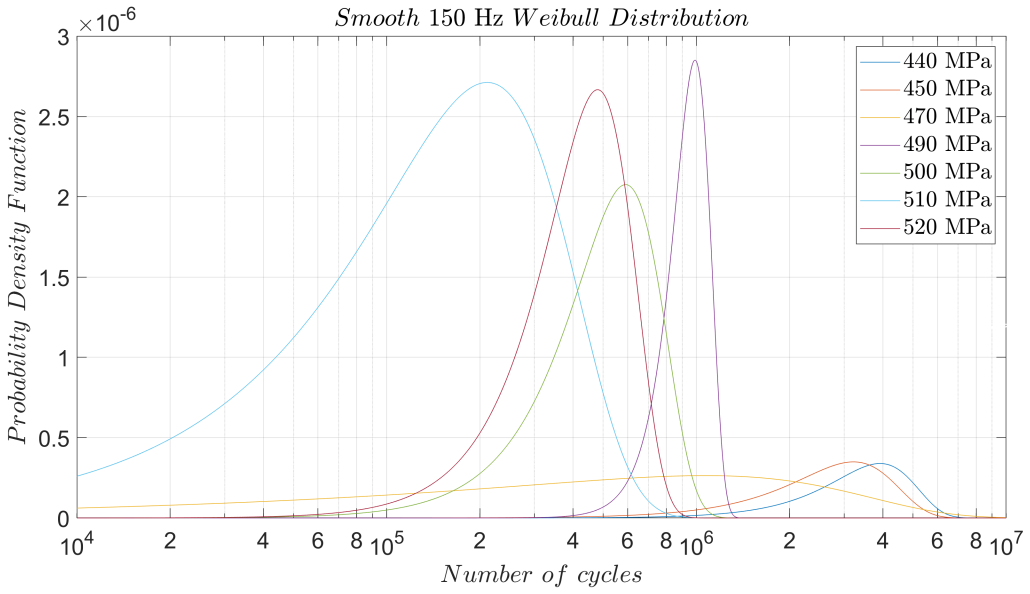


(b)

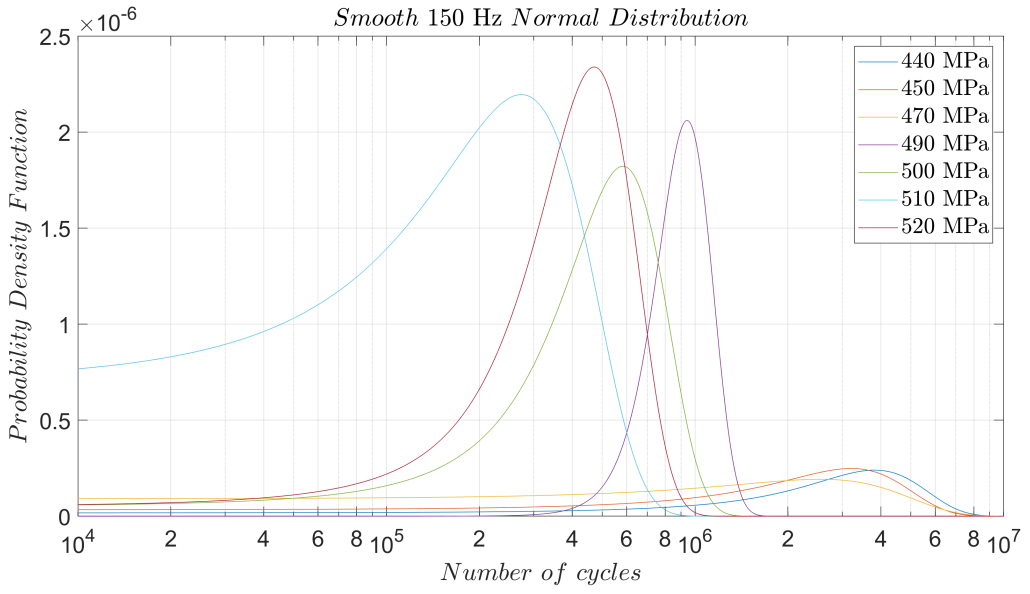
Figure 5.1.2: Weibull (a) and Normal (b) Probability Density Functions for the 20 kHz smooth specimens for each load

For both distributions, the run outs are not considered, thus the stress level of 510 MPa appears to behold the lowest probable fatigue life. Respecting the Weibull distribution, the 530 MPa presents the highest probable fatigue life, followed by 510 MPa, 520 MPa and 540 MPa. Contrarily, the Normal distribution states there is a probability of higher fatigue life for 520 MPa, followed by 530 MPa, 540 MPa and 510 MPa. This is against the expected results of the fatigue life being proportionate to the stress level.

On Figure 5.1.3 it is made the same analysis of the Weibull and Normal distributions for the specimens tested at 150 Hz.



(a)



(b)

Figure 5.1.3: Weibull (a) and Normal (b) Probability Density Functions for the smooth specimens at 150 Hz for each load

For the smooth specimens at 150 Hz specimens of Figure 5.1.3 there is a linear relationship, i.e., higher loads translate into low fatigue lives, in exception for 510 MPa that presents a lower fatigue life than at 520 MPa. This is justifiable by a groove on the specimen's surface even after polishing, dictating its failure outside the middle of the test piece and before 1E5 at 510 MPa.

For 20 kHz, the Shimadzu machine has no load control, it applies power according to a displacement. Furthermore, it has slender specimens and is more sensitive to the surface roughness. Therefore, the distributions are more scattered and not linear as it was verified for the smooth specimens tested at 150 Hz.

5.2 Fatigue S-N curve - Notch effect on S690 steel at 20 kHz

The S-N curve of the notched specimens, compared to the smooth, reveals the high impact of a stress concentration factor on this material in the ultrasonic regime. In Figure 5.2.1 it is considered the specimens which had a strain gauge and in Fig. 5.2.2 they are not. It is seen the removed points flatten the curve significantly.

The S-N curve points of the notched specimens have the stress determined by the conversion factor (29.185 MPa/μm) times the displacement acquired with the probe. This is justified by the inconstant stress implemented by the machine and the calibration uncertainty.

It was verified that the specimens with strain gauge failed sooner than others at the same stress level, due to the surface preparation. This included sanding the critical section to stick the strain gauge, leading to a smaller section and consequently a higher stress concentration in the sanding scratches.

Either S-N curves of the notched specimens have a stress shift downwards, i.e, notoriously a lower fatigue limit of 440 MPa with a higher slope. The nominal stress of the S-N curve is however lower than the maximum peak stress at the specimen's surface. Putting in perspective, the S-N curve without the specimens for the stress validation has a much higher slope than the curve including all notched specimens.

The probability of survival curves are not represented since they were far away from the experimental points, as it is perceived from Table 5.2.1.

Table 5.2.1: Probability of survival curves equations for the notched specimens

Figure	Curve $PS = 95\%, CL = 95\%$
5.2.1	$\sigma_a = 469.478N^{-0.0131}$
5.2.2	$\sigma_a = 554.554N^{-0.0254}$

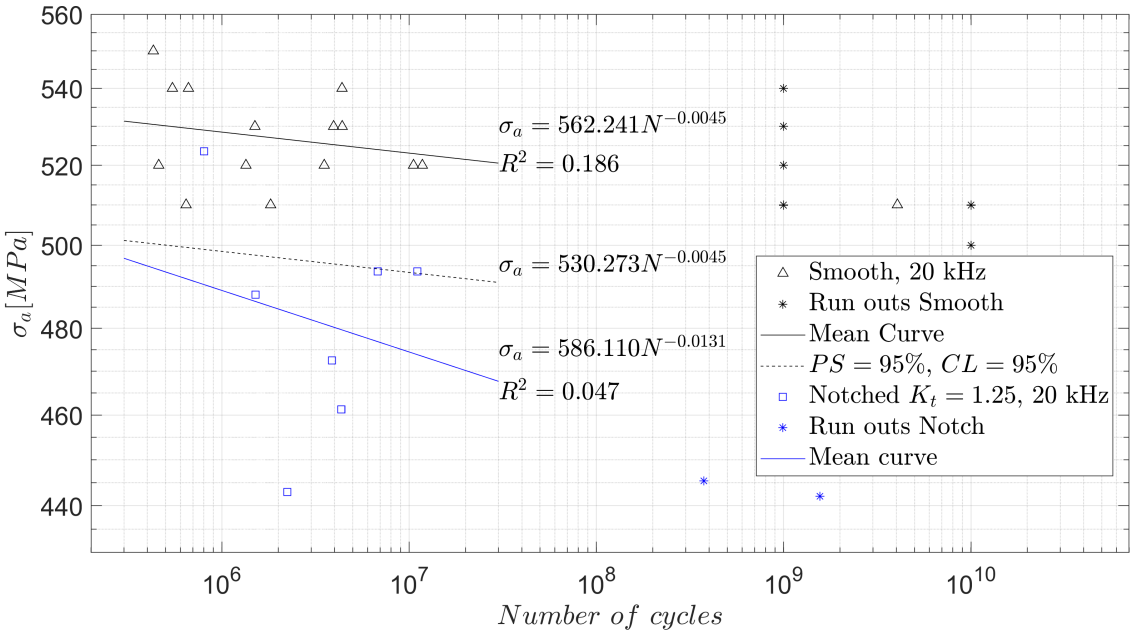


Figure 5.2.1: S-N curve of the tests at 20 kHz for smooth and all notched ($K_t = 1.25$) specimens

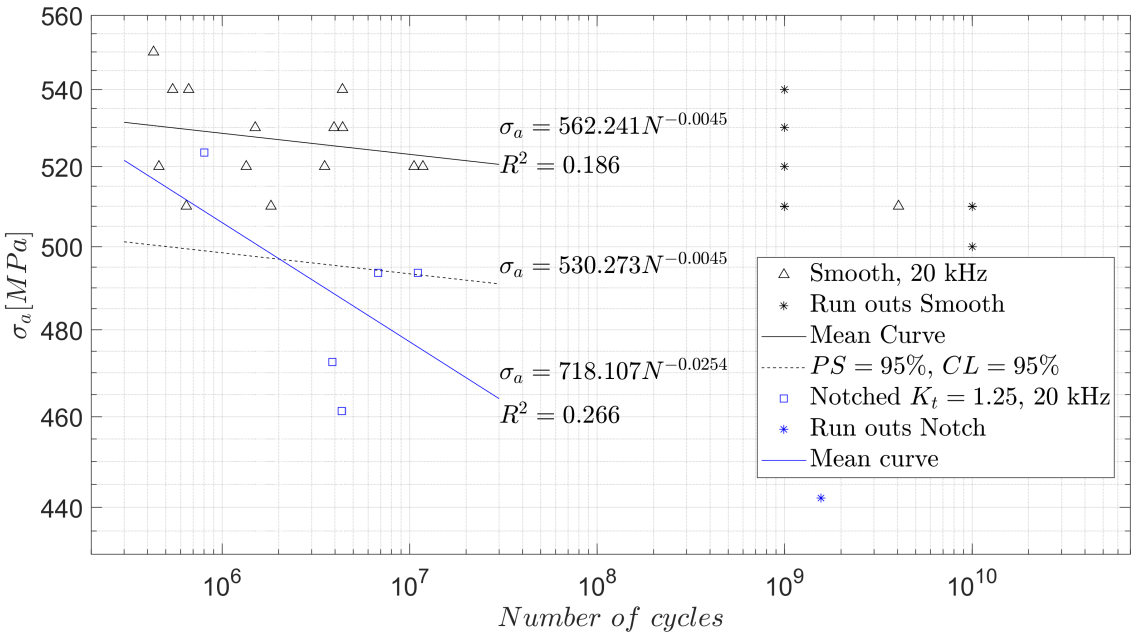


Figure 5.2.2: S-N curve of the tests at 20 kHz for smooth and only the notched ($K_t = 1.25$) specimens without the strain gauge

The S-N curves of the notched specimens have a high R^2 because, besides the high variability of the 20 kHz tests, there are only 9 or 6 fatigue points considered for the curve.

There is a fatigue limit drop of 60 MPa for the experimental results of Fig. 5.2.1 and 5.2.2. Ebara (2017) on Figure 2.6.5 had a fatigue limit drop of 50 MPa (12.5 %) while Bathias (2012) had 150 MPa (20 %) decrease at 1E9 on Fig. 2.6.8. Akiniwa et al. (2006) found a reduction of 100 MPa (11 %) on the fatigue limit for notched specimens on Fig. 2.6.7. Non-withstanding, for the S690 notched specimens, the fatigue limit reduction was only 60 MPa, that is a 12 % in comparison with the smooth specimens (20 kHz).

There were observed 2 run-outs on the notched specimens at 20 kHz for 460 MPa, even for one specimen that had a strain gauge.

The notch concentrator factor and the notch sensitivity are on Figure 5.2.3 in function of the number of cycles, for both S-N curves of the notched specimens, with and without the specimens that had a strain gauge.

Figure 5.2.3 exhibits that the material becomes more sensitive to a notch as its fatigue life increases. Disregarding the specimens with strain gauges, the S690 is not affected by the notch until 1E5.

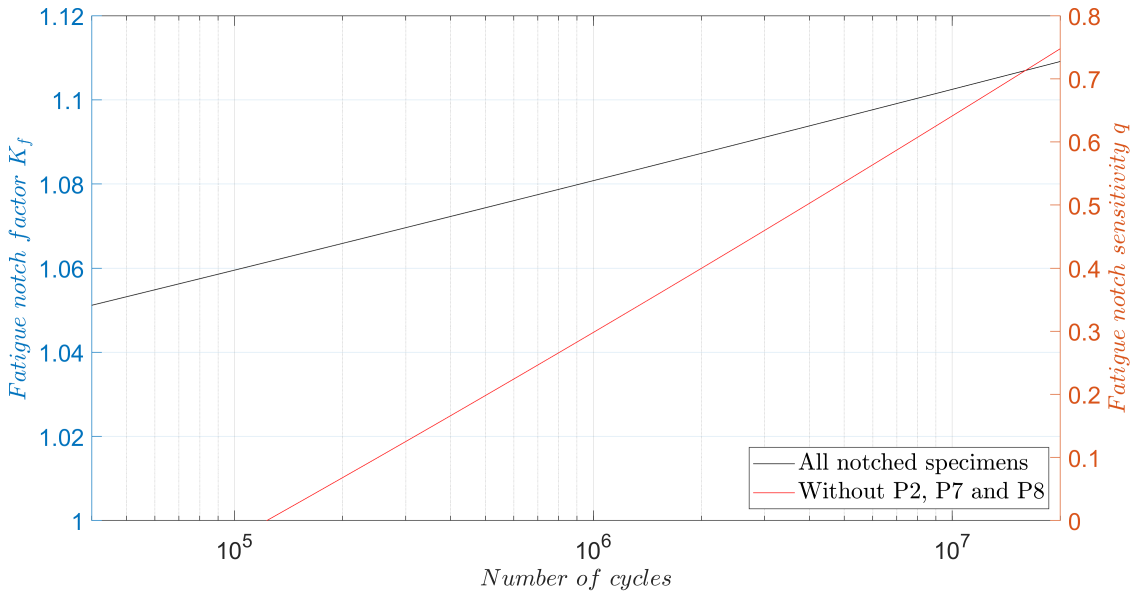


Figure 5.2.3: K_f and q in function of the number of cycles

The K_t and q are presented on Table 5.2.2 for both S-N curves at the fatigue limit 2E7.

Table 5.2.2: K_f and q for the S690 for $K_t = 1.15$ at 2E7

With strain gauge		Without strain gauge	
K_f	q	K_f	q
1.109	0.723	1.112	0.748

The S690 steel is, regarding the fatigue tests, highly sensitive to a notch factor since the q is above 70 %.

5.3 Mean curve estimation

The fatigue life can be determined based on the S690 characteristics. The Vickers Hardness of the S690 was measured in the Emco Test M4U-O75 machine resulting in 280.02 ± 0.95 HV. This translates into a predicted fatigue limit of 448.04 ± 28 MPa, using equation 2.17. This is close to the fatigue limit of 420 MPa at 150 Hz but farther than the 500 MPa fatigue limit at 20 kHz due to the frequency effect.

Moreover, the fatigue limit in function of the number of cycles was estimated and compared with the experimental results on smooth specimens at 150 Hz and 20 kHz (excluding the run-outs), on Figure 5.3.1. The methods for the curves are reviewed on Section 2.8.2. The constants used for each curve are on Table H.0.1, at Appendix H.

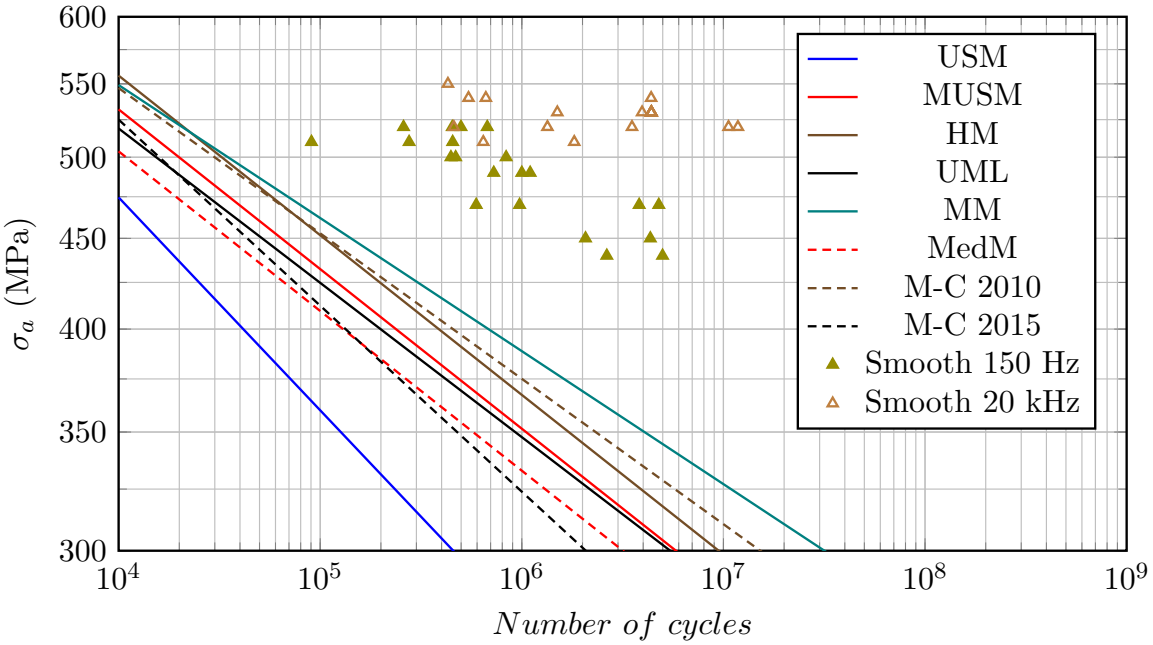


Figure 5.3.1: Fatigue estimation curves in comparison with the experimental data from: USM- Universal Slopes Method, MUSM- Modified Universal Slopes Method, HM- Hardness Method, UML- Uniform Law Material, MM- Mitchell's Method, MedM- Medians Method, Manson-Coffin 2010, Manson-Coffin 2015

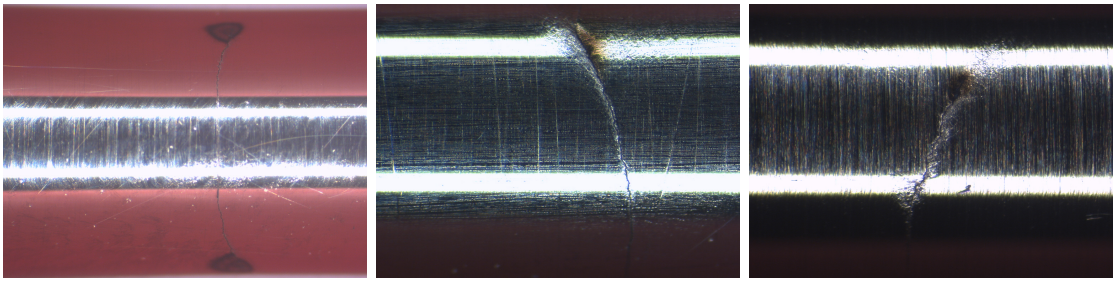
From Figure 5.3.1, it is perceived the analytical models computed with the mechanical properties of the S690 steel are significantly distant from the experimental fatigue limit for both frequencies, which can be deduced as a lack of accuracy from the models. Despite this, the predictions based on the literature are below the experimental fatigue limit, which is good to guarantee a safety coefficient.

5.4 Surface crack analysis

The fatigue crack appearance on the specimen is highly dependent on its loading and fatigue life. These are studied extensively on this section.

5.4.1 Smooth specimens tested at 20 kHz fatigue surface crack analysis

The images for the crack appearance of the 20 kHz smooth specimens were taken on the magnifying eye microscope and are presented on Figure 5.4.1.



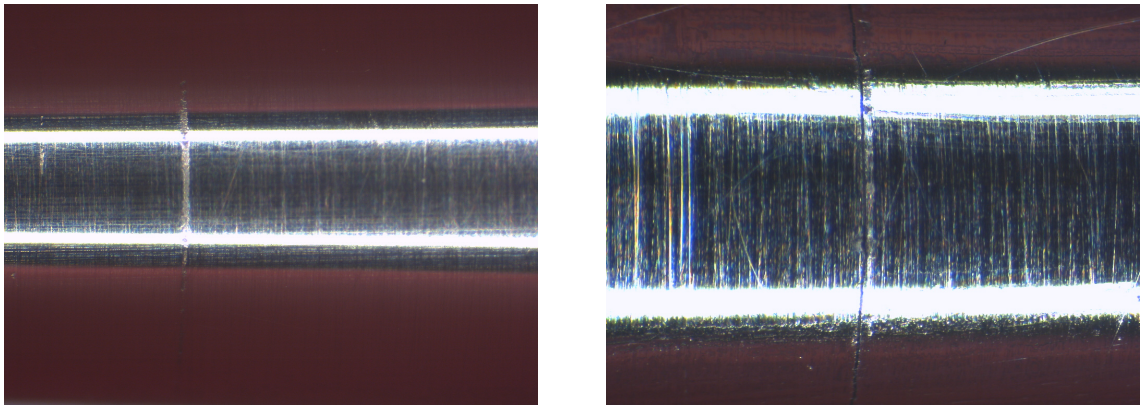
(a) (b) (c)

Figure 5.4.1: Crack shapes: (a) P8 (×19) (S = 550 MPa, N = 4.3E5), (b) P15 (×40) (S = 510 MPa, N = 1.82E6) and (c) P22 (×40) (S = 520 MPa, N = 1.18E7)

It is noticed that the crack always ends with a burnt zone. The crack occurs and due to the 20 kHz, its temperature reaches more than 120 ^{o}C, because some cycles are done until Supersonic stops the test. The temperature is monitored on the pyrometers software, Optris Compact Connect 1.10.18.

The crack is believed to assume curved shape, independently of the load the specimen is subjected to or the fatigue life it has (Fig. 5.4.1a), if higher loads are applied. The outer part of the fatigue crack, since the specimen is not flat, has a concave shape with the concavity towards the specimen's thread probably since the other part of the test piece gets looser.

In the case of P22 versus P15, it is verified that higher loads do not mean lower fatigue life. The surface quality of the specimens is a major factor deteriorating their fatigue life. On Figure 5.4.2, another hourglass specimen crack can be seen.

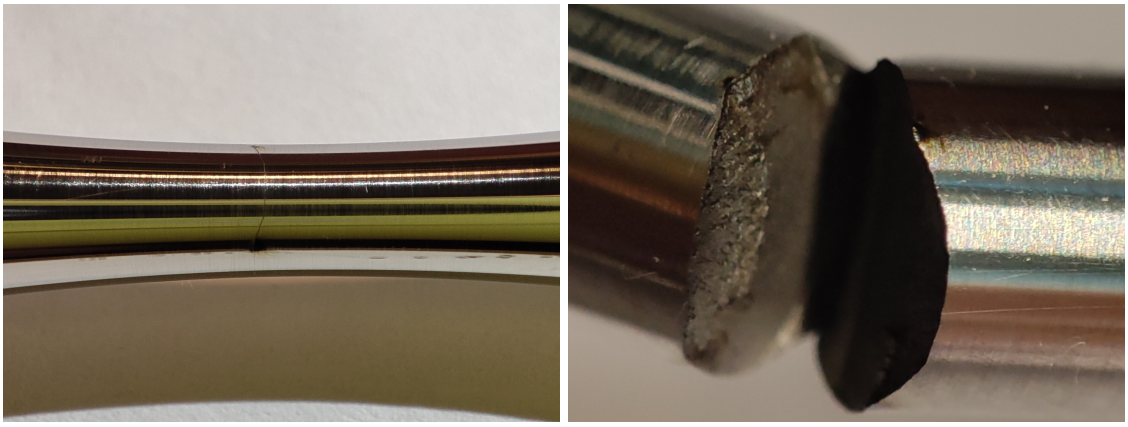


(a) (b)

Figure 5.4.2: Crack shapes for smooth specimen (20 kHz): (a) P14 (×20) before and (b) P14 (×40) after test (S = 510 MPa, N = 6.44E5)

The P14, although being tested at 510 MPa, a load considered low enough for a run-out, failed in HCF due to the deep groove generated in the machining (Fig. 5.4.2). This is because the groove causes a reduction of the cross section, that leads to a higher nominal stress being applied.

On Figure 5.4.3 the characteristic burnt pattern and curved crack shape can be observed, as well as the sequence to open the specimen by hand.



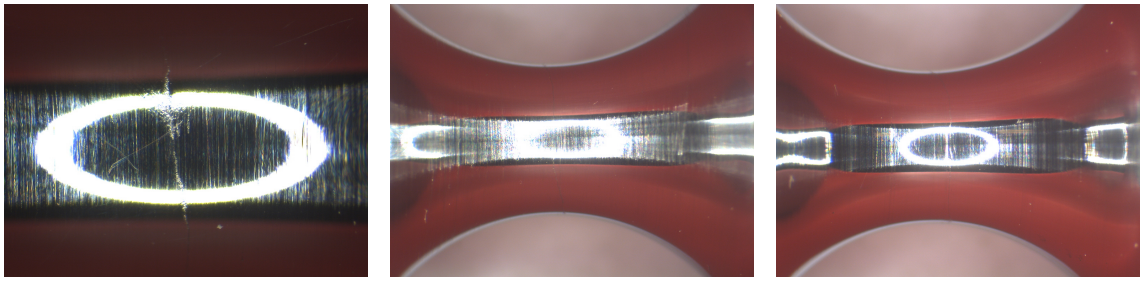
(a) (b)

Figure 5.4.3: Sequence to open the specimen P4 ($S = 520$ MPa, $N = 1.34$E6)

The specimens have reduced minimal sections. The crack occupies about 25 % of the specimen's area which makes difficult to open and split it into two parts by hand. The "Check Frequency" option, besides confirming the specimen has a crack, it facilitates the opening, since it opens the crack until more than 50 % of the cross section area. These two ways create a ductile facture surface whether using liquid nitrogen allows to open by hand and obtain a brittle surface fracture.

5.4.2 Notched specimens (20 kHz) fatigue surface crack

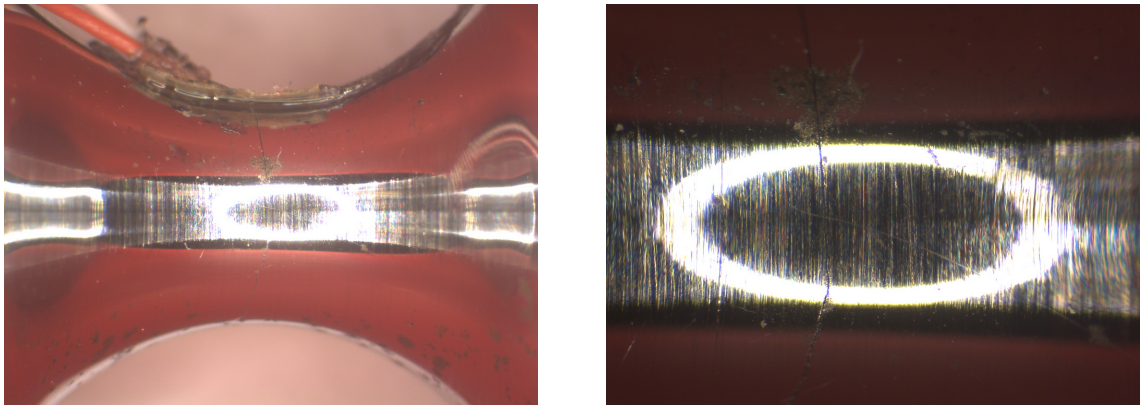
The notched specimens fatigue crack (Figure 5.4.4) is characterized by the lack of a burnt end. Owing to the stress concentration factor, the specimen breaks much faster and the temperature does not go above 70 ^{o}C.



(a) (b) (c)

Figure 5.4.4: Crack shapes for notched $K_t = 1.25$ specimen (20 kHz): (a) P3 ×30 ($S = 530$ MPa, $N = 8.03$E5), (b) P4 ×10 ($S = 510$ MPa, $N = 1.11$E7) and (c) P6 ×10 ($S = 490$ MPa, $N = 3.88$E6)

The fatigue crack is practically perpendicular to the specimen's axis independently of the load, as it is seen on Fig. 5.4.4. The specimen P7 tested with a strain gauge had its fatigue crack grown under it, on Figure 5.4.5. Consequently, the gauge and the procedure to place it surely aided the crack grow.

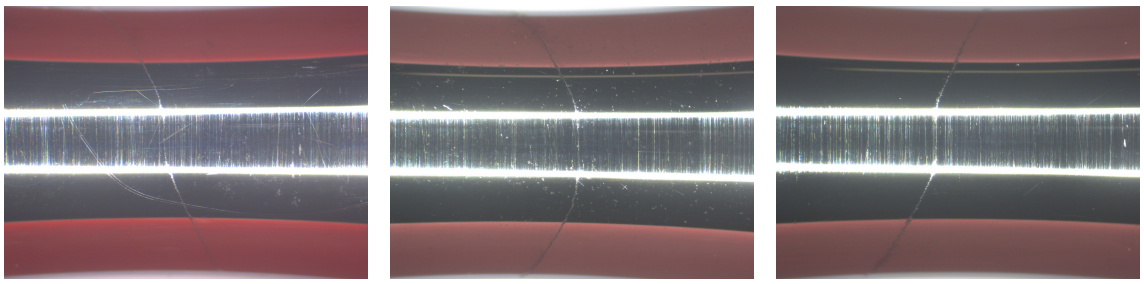


(a) (b)

Figure 5.4.5: Crack shapes for notched $K_t = 1.25$ specimen (20 kHz): P7 (a) ×10 and (b) ×30 ($S = 460$ MPa, $N = 2.24E6$)

5.4.3 Smooth specimens (150 Hz) fatigue surface crack

The surface crack for the specimens tested at 150 Hz (Fig. 5.4.6) are similar to the ones submitted to 20 kHz, with the outstanding dissimilarity being the lack of burnt area since the frequency is around 133 times lower.



(a) (b) (c)

Figure 5.4.6: Crack shapes for smooth specimens at 150 Hz (×10): (a) P5 ($S = 470$ MPa, $N = 4.78E6$), (b) P9 ($S = 510$ MPa, $N = 4.54E5$) and (c) P18 ($S = 490$ MPa, $N = 1.00E6$)

Some specimens present a crack with the curved shape, having an almost transversal part on the middle of the specimen where the crack initiates. In other specimens, the fatigue crack propagation is in opposite directions after being stationary perpendicular to the specimen' axis on the middle. Crack initiation nearly always initiated at one of the larger grains at the surface having its favoured slip system in the same direction as the maximum shear direction of the fatigue load, i.e. 45^{o} inclination to the load direction. This is because plastic deformation by shear is easier at a free surface than in the middle of the material. This persistent slip bands will move back and forth and finally initiate a crack (Hansson, 2012).

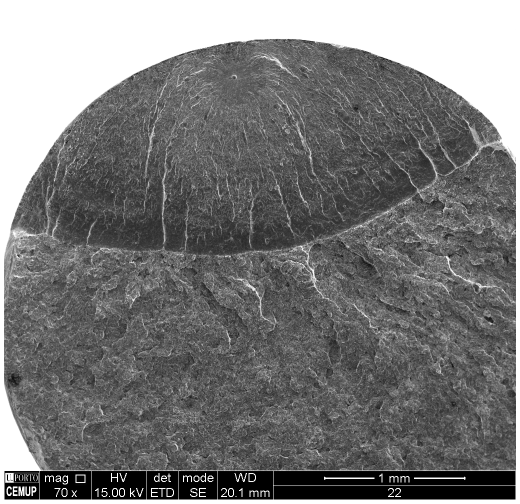
5.5 Fracture surfaces

The fracture surfaces were primarily observed on the magnifying eye. Moreover, the Scanning Electron Microscopy (SEM) analysis, on CEMUP (Materials Centre of the University

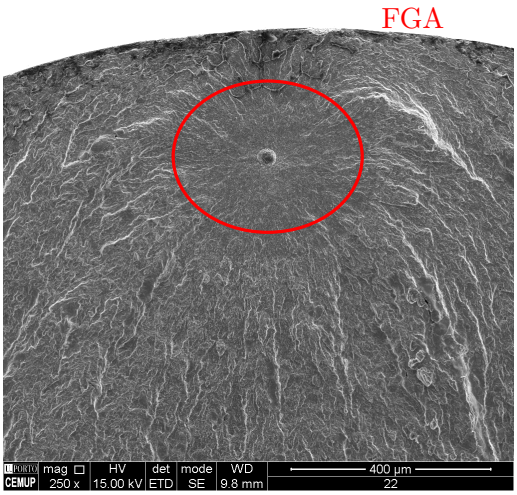
of Porto) provided better images and was useful to analyse the surface's composition and its inclusions. The darker images provided by SEM are obtained by Everhart-Thornley Detector (ETD) and the brighter images by Backscattered-Electron Detector (BSED).

5.5.1 Smooth specimens (20 kHz) fatigue fracture surfaces

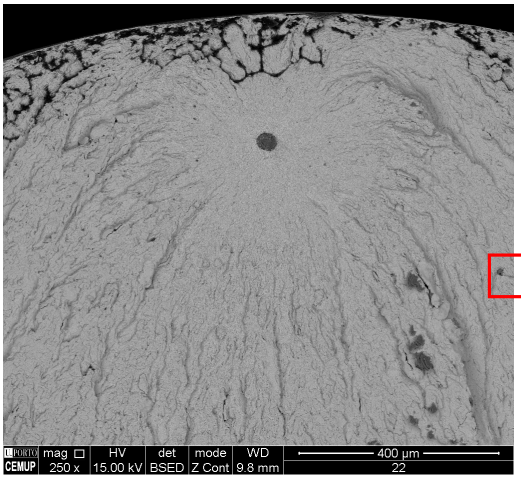
The only smooth specimen at 20 kHz fractured due to a metallic inclusion was the P22, revealed on Figure 5.5.1. The specimen P22 was broken using liquid nitrogen, hence on Figure 5.5.1a the surface appears smooth even outside the fatigue failure zone. The fracture surface at ×70 magnification enables to distinguish the fatigue fracture surface from the fracture due to static stress. The fish-eye is shown in Figures 5.5.1b and 5.5.1c where it is visible the less rough area (fine grained area) and the striations originating from the inclusion. At ×250 magnification, it is seen in more detail the small grain that gives rise to the propagation of an internal crack, with the characteristic fish-eye appearance. Figure 5.5.1c highlights the oil contamination suffered by the specimen near the surface. A smaller impurity is observed in Figure 5.5.1d with ×2000 magnification.



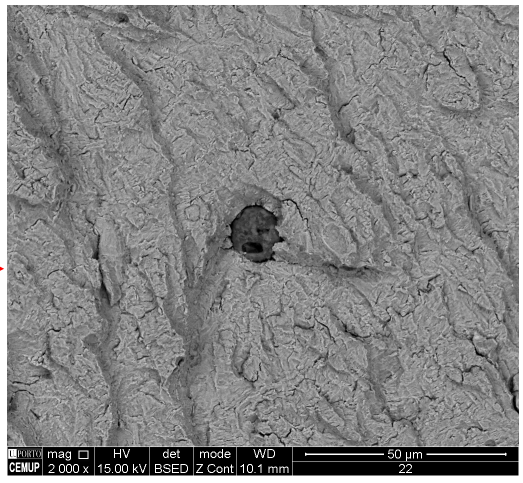
(a) Fracture surface (1 mm)



(b) Fish-eye (400 μm)



(c) BSED of the fish-eye (400 μm)



(d) Inclusion detail (50 μm)

Figure 5.5.1: SEM images of P22 (S_f = 520 MPa, N = 1.18E7) with different scales.

The higher number of cycles the specimen P22 endured (1E7) corroborates the fatigue fracture mode at VHCF discussed on Chapter 2.

Figure 5.5.1, shows with more detail that the inclusion has an oval geometry. Table 5.5.1 displays its dimensions and distance to the surface, besides its composition determined by Energy-Dispersive X-ray Spectroscopy (EDS). It separates the characteristic x-rays of different elements into an energy spectrum that is analysed in order to determine the abundance of specific elements.

Table 5.5.1: Inclusions size (5 measurements) and composition

Fig.	L μm	T μm	T Surface μm
5.5.1d	13.841	11.699	-
5.5.2	39.046	34.556	244.292
Fig.	Chemical composition		
5.5.1d	Al_2O_3, CaO & SO_2		
5.5.2	Al, CaO & ZrO_2		

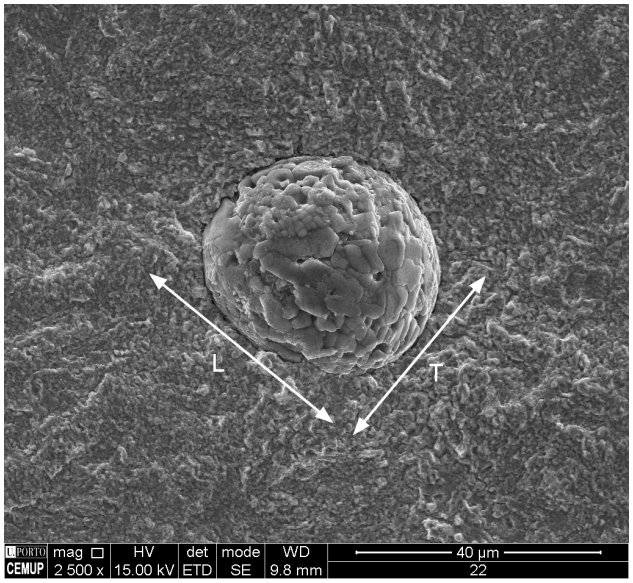
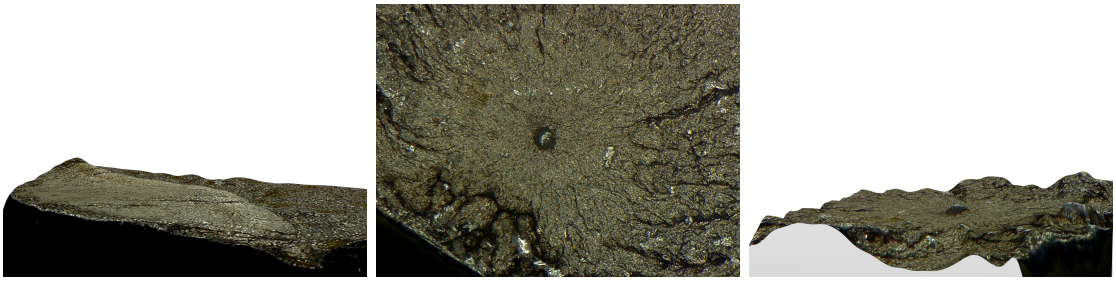


Figure 5.5.2: Detail of the metallic inclusion (40 μm scale) ($S_f = 520$ MPa, $N = 1.18$E7)

The inclusion of Figure 5.5.2 was the only cause of internal failure and the largest impurity found. It is an aluminium inclusion together with dioxides of sulphur and zirconium. This last element is the only which was not present on the S690 composition (Table 4.1.3). Zou et al. (2022) states an increase of aluminium, the majority of the inclusion of Fig. 5.5.2, reduces the content of O and N, which reflects the strong ability of de-oxidation and denitrification. With the low content of Al, Al_2O_3 oxide inclusions are easily formed in the structure. They are round and small in size and show no plasticity, behaving in a brittle manner (Zou et al., 2022).

The Leica Digital Microscope DVM6 was employed to retrieve 3D images and get an estimative of the fracture's surface roughness.

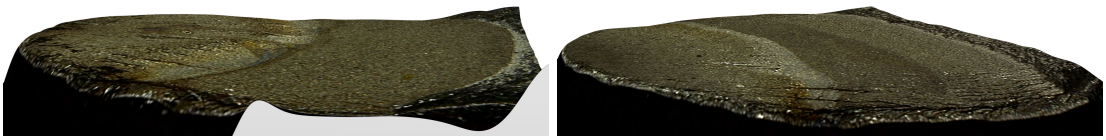
Regarding Fig. 5.5.3b, through Leica Application Suite v4.3, the average SR was 50 μm obtained with a peak of 70 μm at the inclusion. Figure 5.5.3a makes the surface to appear practically flat while Fig. 5.5.3b reveals the rough striations more clearly. On top of that, Figure 5.5.3a shows in 3D the inclusion peak surrounded primarily by a smooth area and then by the rough striations.



(a) (b) (c)

Figure 5.5.3: Tridimensional images of the inclusion surface area on P22 ($S_f = 520$ MPa, $N = 1.18$E7)

Images of P8 and P14 were also taken, on Figures 5.5.4a and 5.5.4b. These show that there is a down bump from the beach mark until the point of crack initiation. Furthermore, the P8 was submitted to a load 7.84 % higher which translates qualitatively into a rougher surface with more striations.



(a) (b)

Figure 5.5.4: Tridimensional images of fracture surfaces on (a) P8 ($S_f = 550$ MPa, $N =$ 4.30E+05) and (b) P14 ($S_f = 510$ MPa, $N = 6.44$E+05)

In a similar way of what was done for P22, the SR of P8 was analysed on Figure 5.5.5. It elucidates the difference from the fracture area, around 900 μm, in comparison with the middle part, in average 700 μm.

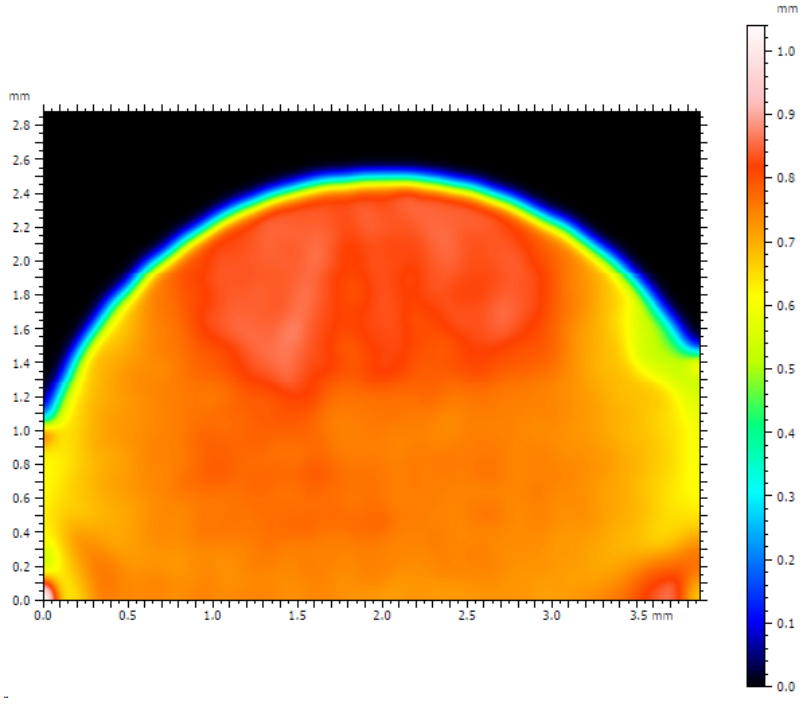
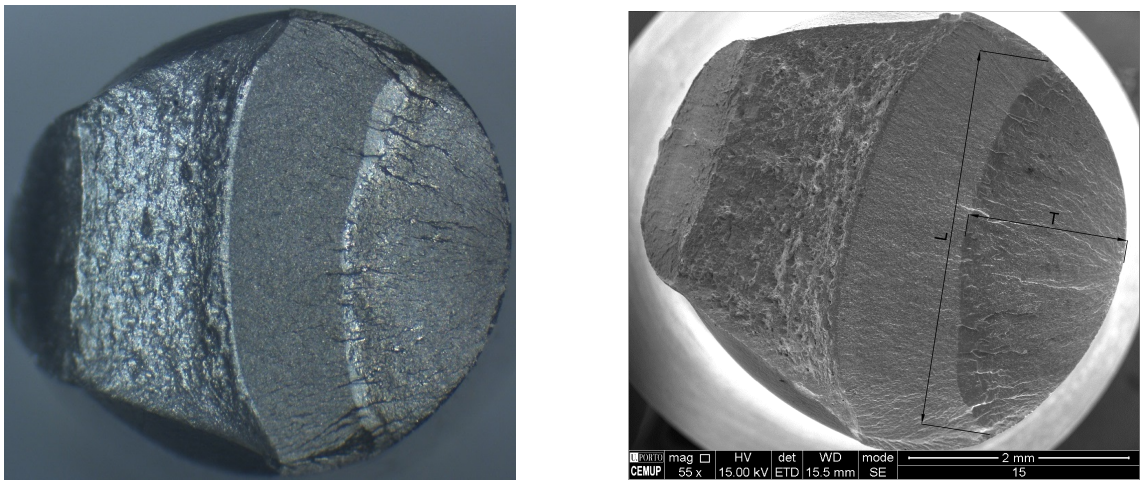


Figure 5.5.5: Topographic image acquired on P8 ($S_f = 550$ MPa, $N = 4.30\text{E}{+}05$) through Leica Application Suite

On Figure 5.5.6 the difference between the images acquired with the magnifying eye and during SEM are highlighted, particularly for P15.



(a) (b)

Figure 5.5.6: Magnifying eye (a) and SEM (b) images of P15 smooth specimen at 20 kHz ($S_f = 510$ MPa, $N = 1.82\text{E}6$) with scale of 2 mm.

On Fig. 5.5.6, there are three different surface roughness distinct areas. The first on (a) is due to the ductile fracture of the specimen done by hand. The middle area is very smooth resulting from the "Check Frequency" and ends in a beach mark characterized by the white colour. The fracture zone is rougher. As the fracture began at the surface where there is the maximum stress, the striations point to that site. Striations/crack-front markings are produced on the fracture surface that show the incremental growth

of a fatigue crack. The term striation generally refers to ductile striations, which are rounded bands on the fracture surface separated by depressions or fissures and can have the same appearance on both sides of the mating surfaces of the fatigue crack. The beach mark is also called macroscopic progression markings, often visible as a result of changes in microscopic roughness, which is associated with changes in the extent of deformation around crack tips owing to variations in stress-intensity parameters (here caused by "Check frequency") (Lynch, 2007). The fracture crack ends are described by deformation of the material and a darker burnt zone due to the friction in this area before the test end.

Table 5.5.2 presents the measurements of the fatigue crack longitudinal and transversally, like defined on Fig. 5.5.6.

Table 5.5.2: Longitudinal and transversal length of the fracture surface for smooth specimens at 20 kHz

σ_{nom} MPa	N cycles	Specimen	Longitudinal μm	Transversal μm
510	6.44E+05	P14	3480.559	1526.368
	1.82E+06	P15	3473.609	1437.480
	4.05E+09	P17	3407.788	1427.733
520	1.34E+06	P4	3269.613	1284.364
	4.60E+05	P7	3228.770	1472.694
	1.18E+07	P22	3570.072	1532.068
530	3.95E+06	P10	3436.973	1427.408
	1.50E+06	P23	3190.588	1424.601
540	5.44E+05	P18	3538.561	1512.094
550	4.30E+05	P8	3277.778	1393.492

According to Table 5.5.2, for the first level of stress, 510 MPa, the higher the fatigue life, the lower the size of fatigue crack. Curiously, the opposite happens for 520 MPa and 530 MPa. It is interesting to discover how the size of the fatigue crack is influenced by the stress applied, on Figure 5.5.7.

Apart from the 540 MPa stress, the size of the fatigue crack diminishes slightly with the stress load increase. This must be related with the general lower fatigue life at higher loads, shown in the S-N curve on Fig. 5.1.1. Lower cycles inhibits the crack propagation, leaving smaller failure crack dimensions. For lower loads, the fatigue crack grows more until it reaches the fracture toughness than for low loads.

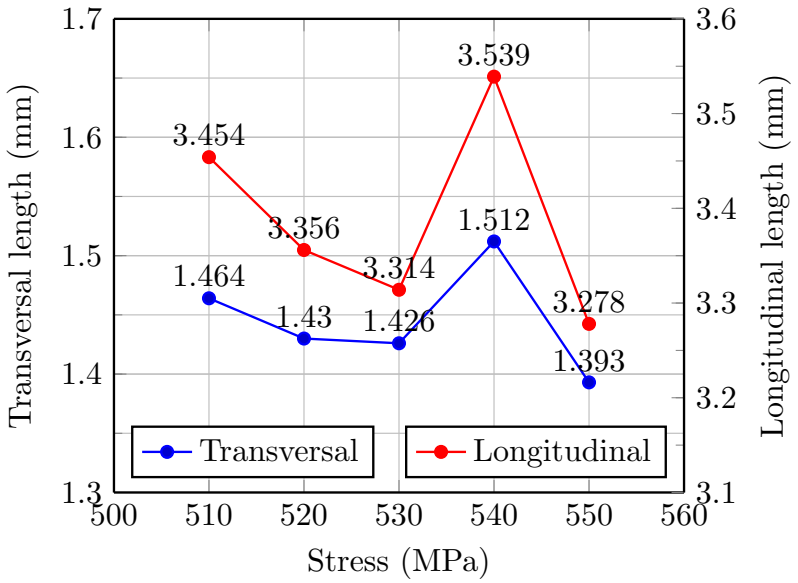
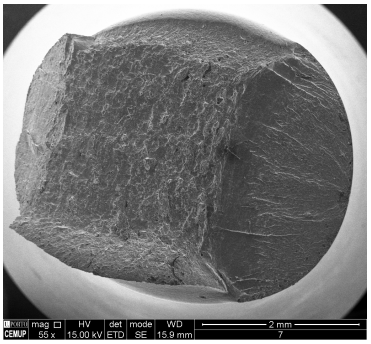


Figure 5.5.7: Fatigue crack average size according to the stress load for smooth specimens at 20 kHz

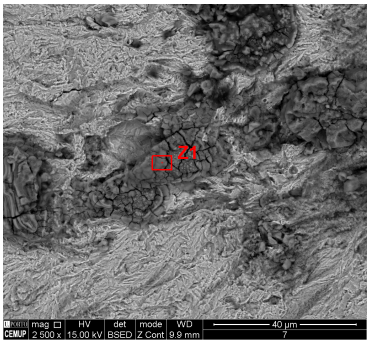
Moving on, SEM images for more specimens are exposed on Figure 5.5.8. Some specimens have their inclusions listed by the most predominant to the least.

Particularly for P15 specimen was detected the darker spots characterized by FeO. The fracture surfaces have very similar shapes except for P7 that has a higher ductile fracture area since it was broken by hand without performing a “Check Frequency”. The aluminium is an expected inclusion, contrariwise to the calcium that is not stated in the material composition. The dark spots near the surface are oil used to protect the specimen from corrosion that got in the crack and contaminated it in some specimens.

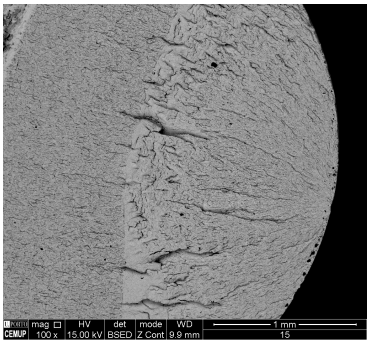
In Figure 5.5.8, the P18 appears to have a rougher surface than the P17. This originated in the higher stress level used for P18 and also lower cycles. The smoother surface roughness of low loads is also reinforced by the middle section of the specimen (that was submitted to 150 MPa). However, the number of cycles also conditions the fatigue surface.



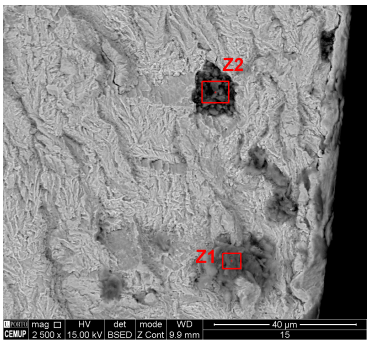
(a) P7 (2 mm)



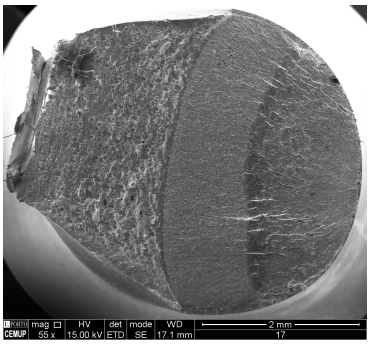
(b) P7 (40 μm). FeO



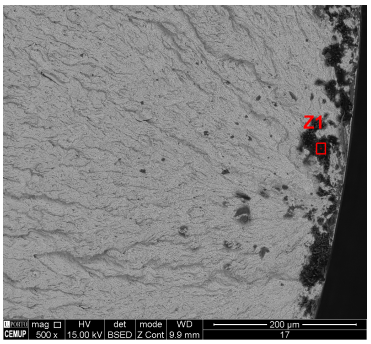
(c) P15 (1 mm)



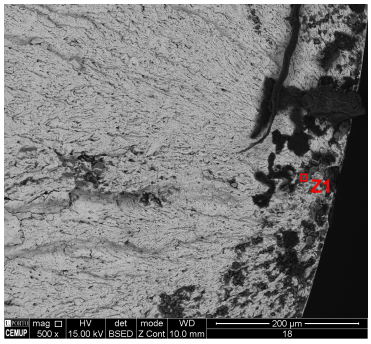
(d) P15 (40 μm). Z1-Al. Z2-CaO, C & Al_2O_3



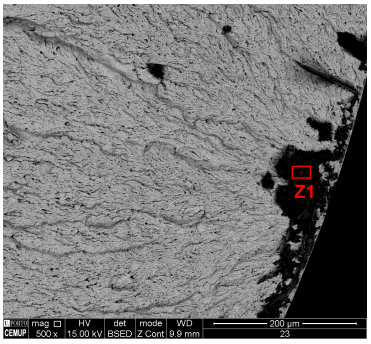
(e) P17 (2 mm)



(f) P17 (200 μm). C, CaO, FeO & Al_2O_3



(g) P18 (200 μm). Al



(h) P23 (200 μm). C, CaO

Figure 5.5.8: SEM images of the smooth specimens (20 kHz)

5.5.2 Notched specimens (20 kHz) fatigue fracture surfaces

The notched specimens presented the fatigue surfaces on Figure 5.5.9.



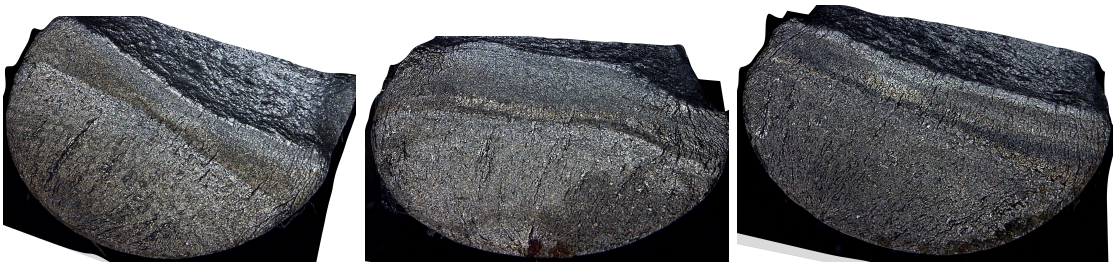
(a) (b) (c)

Figure 5.5.9: Leica DVM6 fracture surfaces of the notched specimens ×100: (a) P4 (S_f = 510 MPa, N = 1.11E7), (b) P7 (S_f = 460 MPa, N = 2.24E6) and (c) P10 (S_f = 490 MPa, N = 4.34E6)

The fracture zone ends in a beach mark and again due to the "Check Frequency", there is a smooth area in the middle however smaller than on the hourglass specimen. The fatigue crack ends in a straight line, contrarily to the curve of smooth specimen that is the most common outcome. This happens since the higher maximum stress lead to a fatigue crack propagation until the middle of the specimen, characterized by this shape (see Fig. 2.2.6).

A higher stress level originates a rougher surface with more striations (Fig. 5.5.9a) than at lower loads. Moreover, a smoother surface is obtained when a higher fatigue life is achieved (Fig. 5.5.9c).

The 3D view of the fracture surface on Figure 5.5.10 shows an almost flat shape and reinforces the striations initiation on the surface. The darker stain signalizes the fatigue crack end.



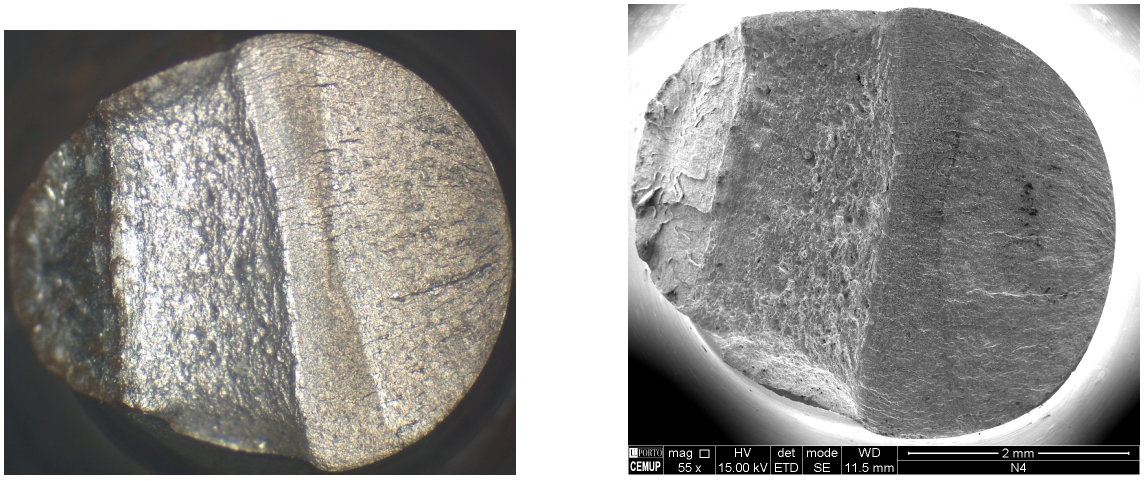
(a) (b) (c)

Figure 5.5.10: Leica DVM6 fracture surfaces of the notched specimens ×100: (a) P4 (S_f = 510 MPa, N = 1.11E7), (b) P7 (S_f = 460 MPa, N = 2.24E6) and (c) P10 (S_f = 490 MPa, N = 4.34E6)

The topographical image is not the most reliable method to acquire the surface roughness, however it gives an approximation of 250, 500 and 500 μm, respectively for the three specimens.

On Figure 5.5.11 the differences between the images acquired with the magnifying eye microscope and during SEM are highlighted for P4. There are presented the three distinct surface roughness areas. In comparison with the hourglass specimens, the smooth "Check Frequency" area is smaller since the normal stress on the notched specimen's surface decreases as the fatigue crack propagates towards the other side of the specimen. Additionally, the transition between the fatigue crack and the yielded region is practically straight instead of curved like for the smooth specimens, because the stress is higher for

greater radius. The fracture zone is rougher and ends in a beach mark characterized by the white colour, although more fainted on this type of specimen. The striations point to the specimen's surface where the fatigue crack initiated. As it was proved by Fig. 5.4.4, on the notched specimen on Figure 5.5.11 there are no burnt marks or relevant yield marks on the surface crack end.



(a) (b)

Figure 5.5.11: Magnifying eye (a) and SEM (b) images of P4 notched specimen at 20 kHz ($S = 530$ MPa, $N = 8.03E5$) with scale of 2 mm

Table 5.5.3 presents the measurements of the fatigue crack longitudinal and transversally for the notched specimens.

Table 5.5.3: Longitudinal and transversal length of the fracture surface for notched specimens at 20 kHz

σ_{nom} MPa	σ_{nom} corrected MPa	N cycles	Specimen -	Longitudinal μm	Transversal μm
460	443	6.44E+05	P7	3823.377	1881.077
490	461	1.34E+06	P10	3883.958	1763.651
510	494	1.11E+07	P4	3677.621	1581.782
530	524	3.95E+06	P3	3657.567	1569.157

According to Table 5.5.3, except for the longitudinal length of P10, higher stress levels translate into a smaller fatigue cracks. The same deductions can be presumed for the transversal length. In contrast the smooth specimens (20 kHz), the notched crack is around 342 μm (10.40 %) and 143 μm (10.04 %) longer, respectively longitudinal and transversally, for 530 MPa. Regarding the 510 MPa, the difference stays in 224 μm (5.84 %) and 118 μm (8.04 %). Figure 5.5.12 shows the length reduction trend found for the notched specimen crack in function of the load level.

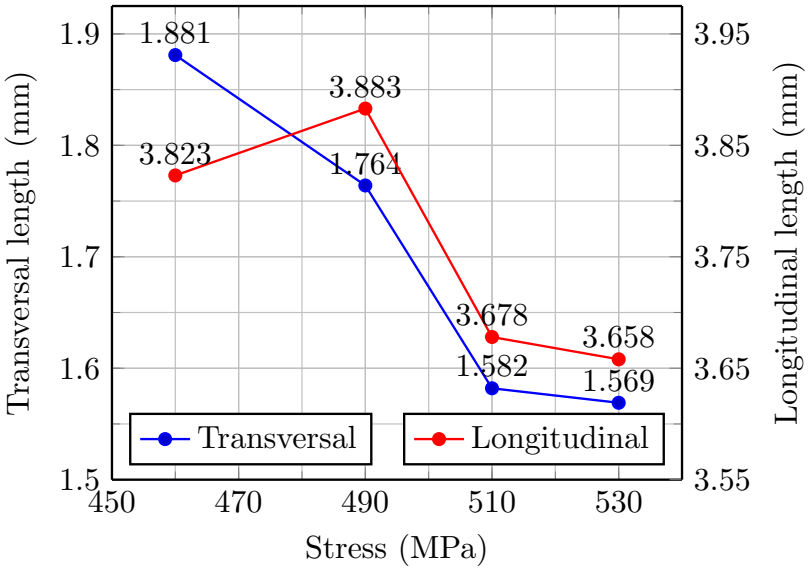
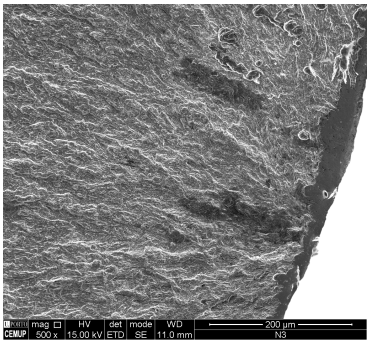


Figure 5.5.12: Fatigue crack average size according to the stress load for notched specimens at 20 kHz

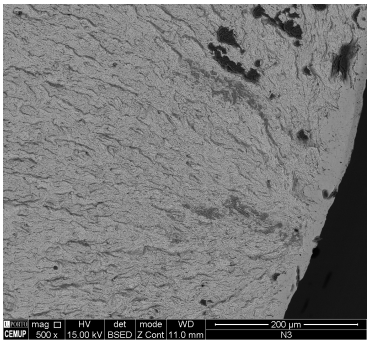
The SEM images are exposed on Figure 5.5.13 where, the inclusions listed by the most predominant to the least. For P3, both images show the flat border that means both halves touched maybe during the "Check Frequency" or owing to the highest load. BSED on Fig. 5.5.13b elucidates the inclusions of iron oxide in grey and aluminium in black.

Analysing P4 on Figure 5.5.13c, there are oil contaminations (carbon), while on Fig. 5.5.13d it is seen an unusual iron wire with aluminium on the background. In contrast to P3 or P4, the specimen P7 has a smoother transition between the 2 crack propagation zones because the load applied was lower (Fig. 5.5.13e). It is seen again on Fig. 5.5.13f on the initiation zone, the grey iron oxide (corrosion) and aluminium particles.

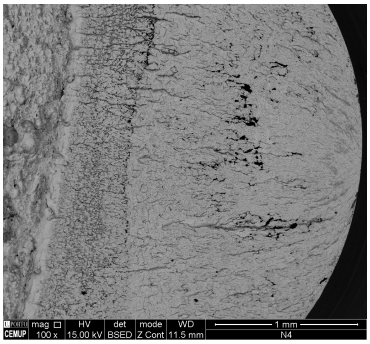
The P10 has its border smashed (Fig. 5.5.13g and 5.5.13h) like it was seen for P3. It seems to have an initiation band instead of only a point. This specimen presents again iron oxide, particularly around an the aluminium particle marked on Fig. 5.5.13h.



(a) P3 (200 μm). FeO & Al



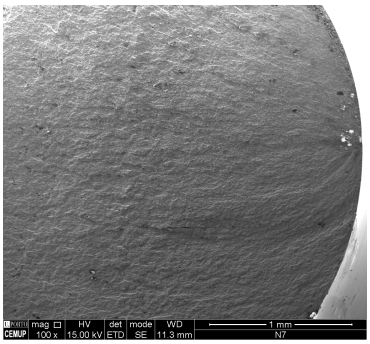
(b) P3 (200 μm). FeO & Al



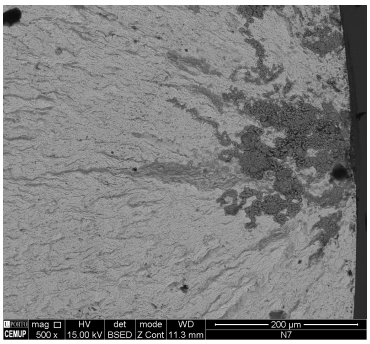
(c) P4 (1 mm). FeO & Al



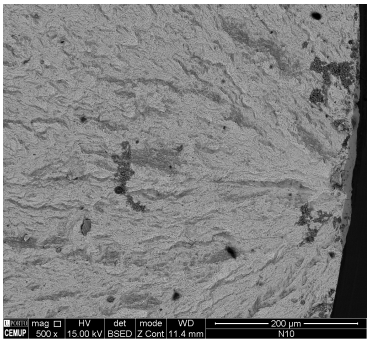
(d) P4 (10 μm). Fe & Al



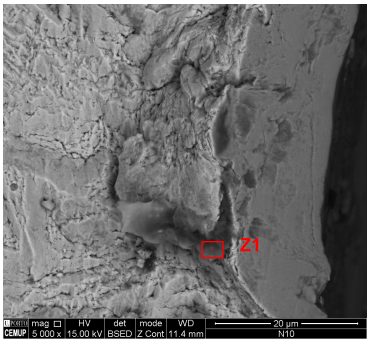
(e) P7 (1 mm). FeO & Al



(f) P7 (200 μm). FeO & Al



(g) P10 (200 μm). FeO & Al



(h) P10 (20 μm). Al

Figure 5.5.13: SEM images of the notched specimens (20 kHz)

5.5.3 Smooth specimens (150 Hz) fatigue fracture surfaces

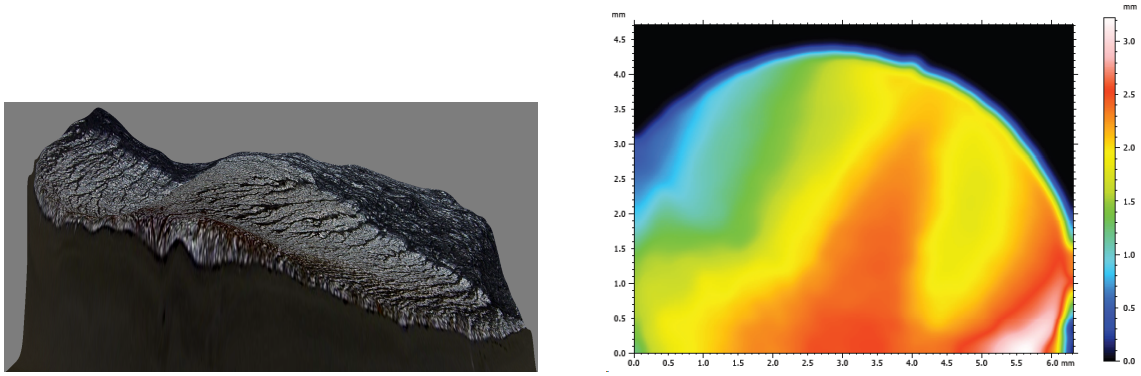
The smooth specimens for 150 Hz have different surface fractures than the ultrasonic testing, on Figure 5.5.14.



(a) (b) (c)

Figure 5.5.14: Leica DVM6 fracture surfaces of smooth specimens at 150 Hz (×68): (a) P5 (S_f = 470 MPa, N = 4.78E6), (b) P20 (S_f = 520 MPa, N = 4.52E5) and (c) P23 (S_f = 440 MPa, N = 4.99E6)

On Figure 5.5.14, a high amount of striations is observed for the higher load (Fig. 5.5.14b) and subsequent less stretch marks for lower loads. It is confirmed the fatigue surfaces have practically the same shape and area. The stain on Fig. 5.5.14a is a contamination by the oil used to preserve the specimen from corrosion. The fracture surface had the same shape as the one verified for smooth specimens.

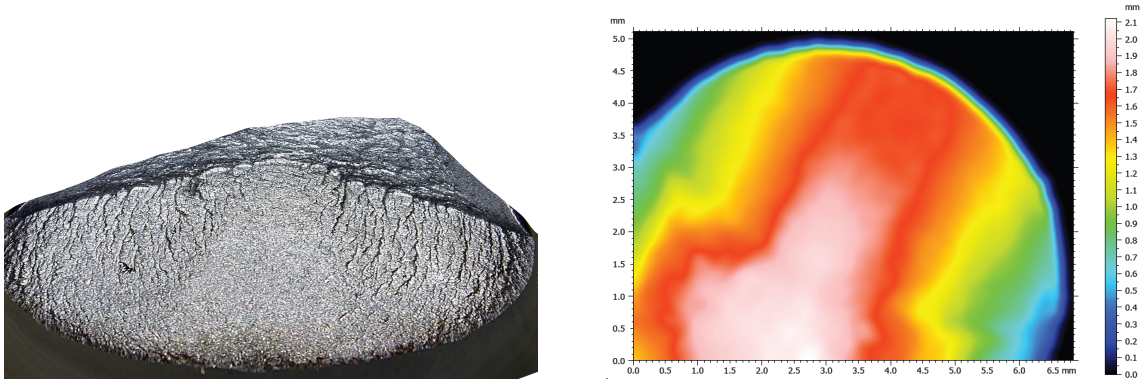


(a) (b)

Figure 5.5.15: Leica DVM6 fracture surface of the smooth specimen for 150 Hz (×68) (a) P20 (S_f = 470 MPa, N = 4.78E6) and (b) topographic image (of Fig. 5.5.14b)

From Figure 5.5.15 it is seen in 3D the fatigue crack is not flat and it has a 2 mm vertical drop. Whereas, for the specimens with different crack shapes like the one on Figure 5.4.6b, the 3D shape on Figure 5.5.16a reveals a dumbbell shape likewise what is seen after a tensile test.

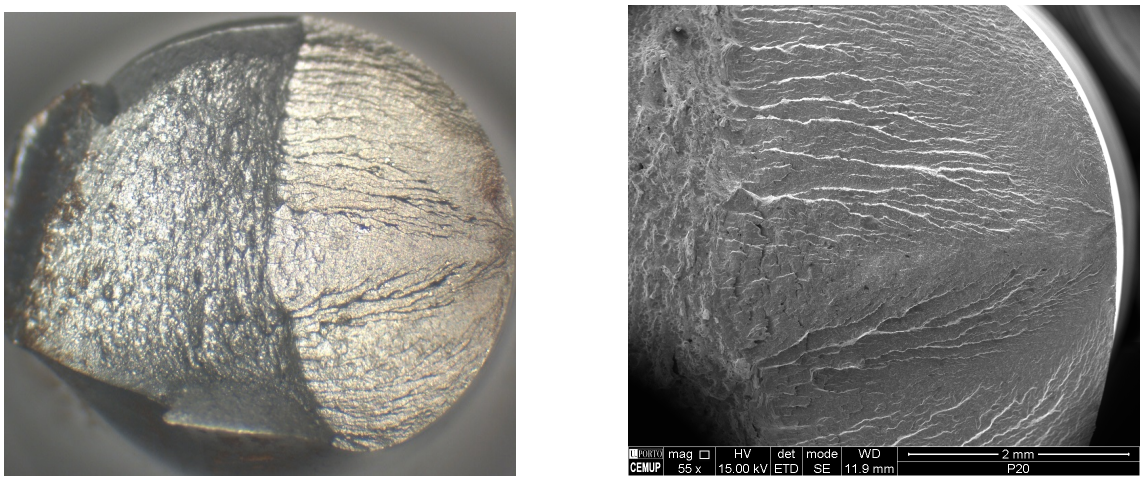
The topographical image of Figure 5.5.16b reinforces the higher area on the middle of the specimen that decreases until its surface.



(a) (b)

Figure 5.5.16: Leica DVM6 fracture surface of the smooth specimens for 150 Hz (×68): (a) P23 ($S_f = 440$ MPa, $N = 4.99E6$) and (b) topographic image (of Fig. 5.5.14c)

For the smooth specimens at 150 Hz, the SEM image on Figure 5.5.17b were difficult to acquire for low amplifications due to the specimen's length. This specimen has only 2 distinguishable zones and, in particular for P20, has a flat area on the middle of the fatigue crack. There are neither beach marks nor burnt zones for this type of specimens, in discrepancy for the smooth at 20 kHz. For P23 on Figure 5.5.17 it is notable the striations symmetry that occurred.



(a) (b)

Figure 5.5.17: Magnifying eye (a) and SEM (b) images of P20 smooth specimen at 150 Hz ($S = 520$ MPa, $N = 4.52E5$) with scale of 2 mm

Table 5.5.4 presents the measurements of the fatigue crack longitudinal and transversally for the smooth specimens at 150 Hz.

Paying attention to the data exposed on Table 5.5.4, the transversal length diminishes with the raise of stress applied on the specimen. As it was seen for Fig. 5.5.17b, due to the height and diameter of half the smooth specimen for 150 Hz, it was impossible to extract images of the whole surface. Hence, the longitudinal length was acquired with the magnifying eye images but gave inconsistent values. It turned out to be useful only to calculate the average value of 6824.899 μm. The longitudinal length measurement is also affected by the deformed end of the crack tip. In analogy to the smooth specimens at 20

kHz, these have clearly fatigue cracks of larger dimensions but this increase is not linear in function of the higher diameter or area.

Table 5.5.4: Longitudinal and transversal length of the fracture surface for smooth specimens at 150 Hz

σ_{nom} MPa	N cycles	Specimen -	Longitudinal μm	Transversal μm
440	4.99E+06	P23	6756.325	3738.942
470	4.78E+06	P5	6827.697	3347.424
470	9.75E+05	P10	6842.706	3504.451
510	2.76E+05	P7	6812.568	3494.691
520	4.52E+05	P20	6885.197	3425.233

On Figure 5.5.18, it is possible to have a better perception of the crack's length crack trend to decrease in function of the stress applied.

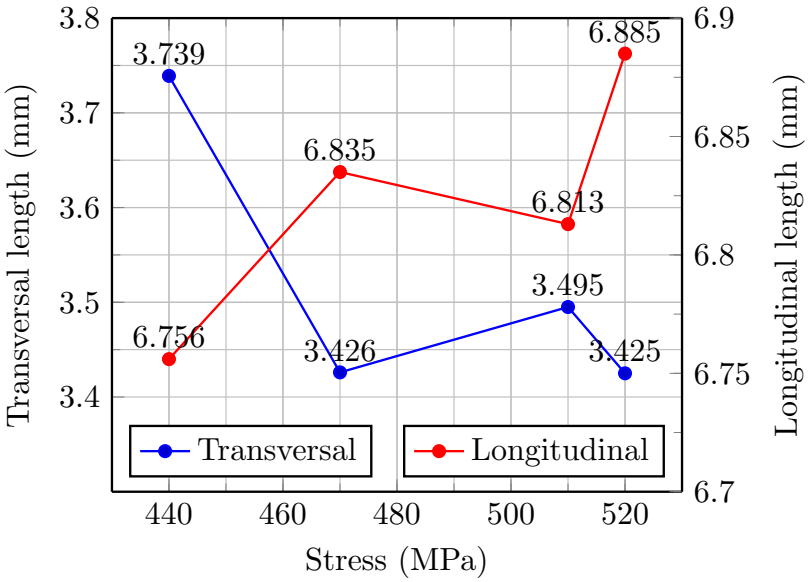


Figure 5.5.18: Fatigue crack average size according to the stress load for smooth specimens at 150 Hz

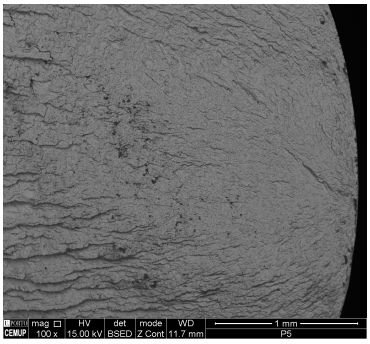
The smooth specimens for 150 Hz have their SEM images of the fracture surfaces presented on Figure 5.5.19.

Studying the P5, it was found one more time iron oxide and aluminium contamination on the crack initiation (Fig. 5.5.19a), perhaps from the aluminium foil used to cover the surface. Alternatively, P7 (on Figures 5.5.19c and 5.5.19d) revealed a surface without contaminations and fairly regular, since it was the last one to be broken and did not contact oil.

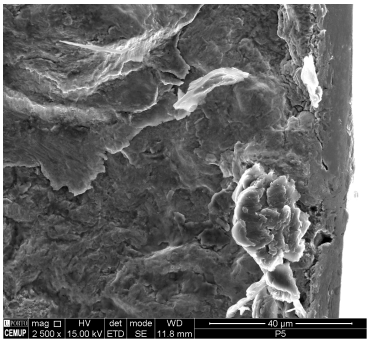
The specimen P10 had a lower number of cycles than P5 and P23. This is originated by the crack initiation on the surface aluminium inclusion of Figure 5.5.19f, which is perceived to be right on the specimen's border and to have facilitated its failure.

The specimen P20 had a good quality despite the oxidation and the inclusion constituted mainly by aluminium and residual quantities of calcium dioxide and zirconium (Fig.

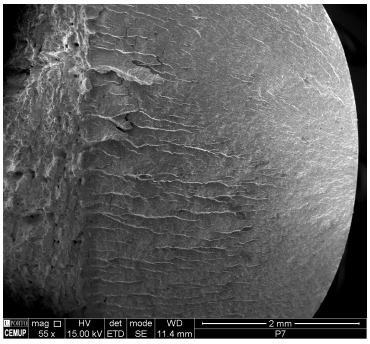
5.5.19h). The P23 had equally an almost symmetric striations distribution. This specimen presented random particles (black dots on Fig. 5.5.19j) of Al, Ca and Ti, besides the FeO. In addition, on Fig. 5.5.19j, there is a debris of aluminium that seems to be placed on the surface due to an external contamination.



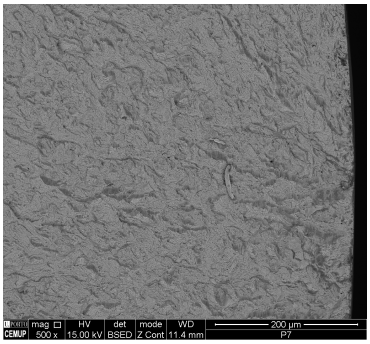
(a) P5 (1 mm). FeO & Al



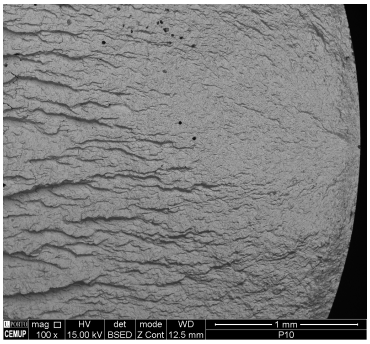
(b) P5 (40 μm). FeO & Al



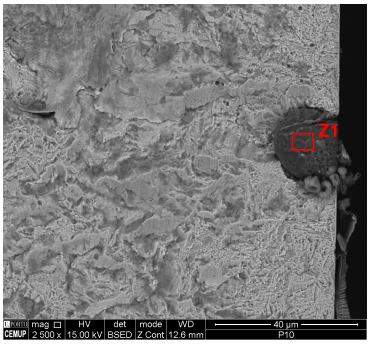
(c) P7 (1 mm).



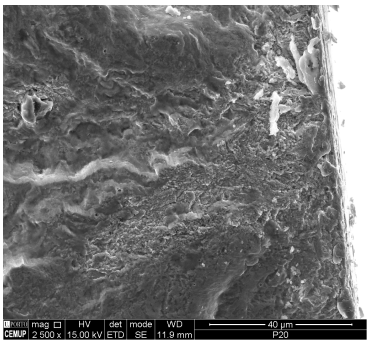
(d) P7 (40 μm).



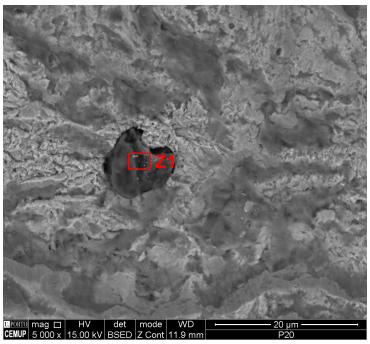
(e) P10 (1 mm). FeO & Al



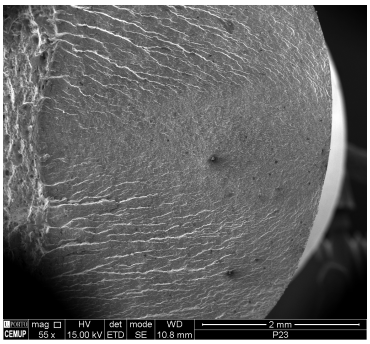
(f) P10 (40 μm). Al, CaO



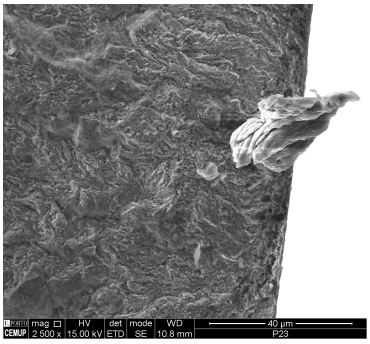
(g) P20 (40 μm). FeO & Al



(h) P20 (20 μm). Al, CaO & Zr



(i) P23 (2 mm). FeO & Al



(j) P23 (40 μm). FeO & Al

Figure 5.5.19: SEM images of the smooth specimens (150 Hz)

Chapter 6

Conclusion

6.1 Conclusions

The work developed consisted in studying the frequency effect of the S690 steel by means of testing smooth specimens at 20 kHz and 150 Hz. In addition, the notch design analytical formulation was investigated and the notch effect determination was carried out through fatigue testing at 20 kHz with a notch factor of 1.15.

The analytical model for the smooth/hourglass specimens is appropriate to estimate the nominal stress. However, it is not reliable to reach the desired resonance frequency. So, it must only be used to estimate the initial dimensions of the specimens. Then, on the FEM modelling is applied to tune the required test frequency and the definitive dimensions to be manufactured. The experimental validation also allows a further refinement of specimen geometry.

The analytical model developed for the notched specimens gives close values to the Shimadzu model, since both reduce a bidimensional problem to unidimensional. Thus, the analytical model should only be used in the beginning of the test piece design to have a starting dimension of the specimen. The dimensions should then be adjusted using FEM for the resonance frequency desired. The Shimadzu formulation for the stress concentration factor (K_t) was found to be overestimated by analysing the transverse stresses within the cross section of specimens by finite element analysis.

The machine (booster and horn) accounts for the bigger mass element of the resonant system. Hence, due to the temperature increase, the resonance frequency of the machine decreased, making the resonance frequency of the specimens also lower.

The strain gauges, glued with an adhesive to the surface of the specimen's critical area, confirmed the applied stress, and validated the Shimadzu machine control outputs, namely the applied voltage.

A fatigue limit of 500 MPa in the ultrasonic fatigue testing (20 kHz) was obtained for the smooth/hourglass specimens at 1E9 cycles. However, due to the poor surface quality (surface scratches) of the first batch of smooth specimens, a higher data scatter was observed, resulting in less predictable results. For the smooth specimens tested at 150 Hz, the fatigue limit observed was 420 MPa at 1E7 cycles, i.e., 80 MPa (16 %) lower. This proved the presence of a size and/or a frequency effect on the fatigue tests. Furthermore, the material is proved to be highly sensitive to a notch, specially in the VHCF regime. A fatigue limit of 440 MPa was found for the notched specimens at 20 kHz at 1E9 cycles, 60 MPa (12 %) lower than the obtained for smooth specimens. This fatigue limit reveals a fatigue notch sensitivity q of 74.8 %.

Only one surface crack of the 20 kHz smooth specimens had origin in an internal inclu-

sion ($\sigma_f = 520$ MPa, $N = 1.18E7$), i.e., the majority exhibited fatigue failures originated at surface cracks. It was noticed that higher stress levels propitiate smaller fatigue crack sizes, since there was less time for the crack to grow and material toughness was achieved sooner. The external observation on all specimens of this type revealed the crack had a concave shape with the concavity towards the thread.

The smooth specimens tested at 150 Hz had the external/surface crack tips branching either with the same direction at 45° or with opposite directions.

6.2 Future Work

In order to improve the work developed during this master thesis elaboration, the following tasks are suggested:

- Perform new fatigue tests on the smooth specimens beholding a better surface quality as well as the application of new optimized manufacturing parameters that induce fewer defects and better quality in test samples and study the S-N curves of both batches separately;
- Perform uniaxial fatigue tests for the run-out smooth specimens at 150 Hz until 1E8 cycles, for at least 3 points on the fatigue limit level and lower stress tests. This can be extended to run-outs at other stress amplitudes. Verify if there is failure or it does not happen, likewise for 20 kHz;
- Extend the experimental program at 20 kHz for alternating amplitude fatigue tests for low-high and high-low cycles sequences;
- Redesign the notched specimens to allow fatigue testing above the 20 % of the machine power for all desired loads. Consequently, implement more severe stress concentration factors on notched specimens;
- Test more notched specimens (20 kHz) to determine an accurate S-N curve for this type of test pieces;
- Manufacture the second notched specimens with higher notching severity;
- Find an appropriate formulation to determine the real stress concentration factor (K_t);
- Establish a relationship between the results at 20 kHz and 150 Hz test frequencies to accurately estimate the material's life according to the applied stress. In addition, investigate how to quantify either the influence of size or the frequency effect that causes the same fatigue lives in tests on smooth specimens (150 Hz and 20 kHz).

References

Abou Jaoude, A. (2015, 01). Analytic and linear prognostic model for a vehicle suspension system subject to fatigue. *Systems Science and Control Engineering 3*, 81–98.

Akiniwa, Y., N. Miyamoto, H. Tsuru, and K. Tanaka (2006). Notch effect on fatigue strength reduction of bearing steel in the very high cycle regime. *International Journal of Fatigue 28*(11), 1555–1565. Third International Conference on Very High Cycle Fatigue (VHCF-3).

Anes, V., D. Montalvão, A. Ribeiro, M. Freitas, and M. Fonte (2011, 06). Design and instrumentation of an ultrasonic fatigue testing machine. In *5th International Conference on Very High Cycle Fatigue*, pp. 1–6.

APREN (2022). Electricity Generation by Energy Sources in Mainland Portugal in 2022. Report, Associação Portuguesa de Energias Renováveis, Portugal. Accessed July 2, 2022. https://www.apren.pt/en/renewable-energies/production.

ASTM International (2013). ASTM 1823-2013: Standard Terminology Relating to Fatigue and Fracture Testing. Standard, American Society for Testing and Materials, West Conshohocken,PA. Accessed May 10, 2022. https://www.astm.org/e1823-13.html.

ASTM International (2016). ASTM E8/E8M-16: Standard Test Methods for Tension Testing of Metallic Materials. Standard, American Society for Testing and Materials, West Conshohocken,PA. Accessed June 26, 2022. https://www.astm.org/.

ASTM International (2022). ASTM 1876-2022: Standard Test Method for Dynamic Young's Modulus, Shear Modulus, and Poisson's Ratio by Impulse Excitation of Vibration. Standard, American Society for Testing and Materials, West Conshohocken,PA. Accessed June 10, 2022. https://www.astm.org/e1876-21.html.

Bannantine, J., J. Corner, and J. Handrock (2022). Fundamentals of metal fatigue analysis. Accessed March 26, 2022. http://mbarkey.eng.ua.edu/courses/AEM649/CH1.pdf.

Basan, R., M. Franulovic, D. Rubesa, and I. Prebil (2011, 12). Implementation of strain-life fatigue parameters estimation methods in a web-based system. *Procedia Engineering 10*, 2369–2374.

Basan, R., D. Rubesa, M. Franulović, and T. Marohnic (2015, 12). Some considerations on the evaluation of methods for the estimation of fatigue parameters from monotonic properties. *Procedia Engineering 101*, 18–25.

Basquin, O. H. (1910). The exponential law of endurance tests. *Proceedings. ASTM* (59), 10(II):625–630.

Bathias (1999). There is no infinite fatigue life in metallic materials. *Fatigue & Fracture of Engineering Materials & Structures 22*(7), 559–565.

Bathias, C. (2012). Gigacycle fatigue of bearing steels. *Materials Science and Technology 28*(1), 27–33.

Bathias, C. and P. Paris (2004). *Gigacycle Fatigue in Mechanical Practice*. Taylor & Francis.

Bathias, J.-C. (2014). *Fatigue limit in metals / Claude Bathias.* Focus Series. London, England: ISTE Ltd.

Berger, C., B. Pyttel, and D. Schwerdt (2008). Beyond hcf – is there a fatigue limit? *Materialwissenschaft und Werkstofftechnik 39*(10), 769–776.

Bergström, J., N. Hallbäck, M. Sadek, C. Burman, S. Plano, B. Weber, S. Münstermann, K. Gillner, O. Polit, L. Gallimard, T. Palin-Luc, M. Ouarabi, K.-H. Lang, S. Becker, R. E. Eguizabal, and B. Escauriaza (2018). Influence of cycling frquency on fatigue strengh and crack growth of engineering steels for demanding applications (FREQTIGUE). Technical report, European Commission Research, Brussels.

Bjorhovde, R. (2004). Development and use of high performance steel. *Journal of Constructional Steel Research 60*(3), 393–400. Eurosteel 2002 Third European Conference on Steel Structures.

Bjørheim, F., D. G. Pavlou, and S. C. Siriwardane (2022). Nonlinear fatigue life prediction model based on the theory of the s-n fatigue damage envelope. *Fatigue & Fracture of Engineering Materials & Structures n/a*(n/a), 1480–1493.

Boyer, H. E. A. S. f. M. (1997). *Atlas of fatigue curves*, pp. 1–10. Ohio: ASM International.

Bäumel, A. A., T. Seeger, and C. Boller (1990). *Materials data for cyclic loading, Supplement 1.* Number 61 in Materials science monographs. Elsevier.

Cadoni, E. and D. Forni (2020). Strain-rate effects on s690ql high strength steel under tensile loading. *Journal of Constructional Steel Research 175*, 106348.

Campbell, F. (2008). *Elements of Metallurgy and Engineering Alloys*, Chapter 10, pp. 244–264. ASM International.

Caresta, M. (2022). Vibrations of a free-free beam. Accessed April 10, 2022. http://www.varg.unsw.edu.au/resources.htm.

Casagrande, A., G. Cammarota, and L. Micele (2011). Relationship between fatigue limit and vickers hardness in steels. *Materials Science and Engineering: A 528*(9), 3468–3473.

Christ, M., X. Guo, R. Sharma, T. Li, W. Bleck, and U. Reisgen (2020). Hydrogen embrittlement susceptibility of gas metal arc welded joints from a high-strength low-alloy steel grade S690QL. *Steel Research International 91*(11), 2000131.

Chung, K.-F., H.-C. Ho, Y. fei Hu, K. Wang, X. Liu, M. Xiao, and D. A. Nethercot (2020). Experimental evidence on structural adequacy of high strength s690 steel welded joints with different heat input energy. *Engineering Structures 204*, 110051.

Costa, P., M. Vieira, L. Reis, A. Ribeiro, and M. de Freitas (2017). New specimen and horn design for combined tension and torsion ultrasonic fatigue testing in the very high cycle fatigue regime. *International Journal of Fatigue 103*, 248–257.

Cui, W., X. Huang, and F. Wang (2014, 01). *Towards a Unified Fatigue Life Prediction Method for Marine Structures*, pp. 7–12. Advanced topics in science and technology China. Heidelberg: Springer-Verlag Berlin Heidelberg.

D. Pilkey, W. (2007, 12). Peterson's stress concentration factors, second edition. pp. 37–38,63–64.

Daniel, R. and T. Paulus (2019). Chapter 7 - structural analysis. In R. Daniel and T. Paulus (Eds.), *Lock Gates and Other Closures in Hydraulic Projects*, pp. 461–530. Butterworth-Heinemann.

de Jesus, A. M., R. Matos, B. F. Fontoura, C. Rebelo, L. Simões da Silva, and M. Veljkovic (2012). A comparison of the fatigue behavior between s355 and s690 steel grades. *Journal of Constructional Steel Research 79*, 140–150.

Dimitrov, D. and J. Argirov (2014). Ultrasonic fatigue testing of high strength 33nicrmov14-5 steel. *Journal of Materials Science and Technology ISSN 0861-9786 22*, 236–244.

Dobosy, Á. and D. J. Lukács (2014, 9). Fatigue resistance of welded joints of S690QL high strength steels. In *Young welding Professionals International Conference (YPIC)*, Budapest, Hungary.

Dong, W., T. Moan, and Z. Gao (2011). Long-term fatigue analysis of multi-planar tubular joints for jacket-type offshore wind turbine in time domain. *Engineering Structures 33*, 2002–2014.

Ebara, R. (2017). Some influencing variables on internal fatigue crack initiation in structural materials. *Fatigue & Fracture of Engineering Materials & Structures 40*(11), 1752–1761.

Ebara, R., Y. Yamada, and A. Goto (1982, 06). Corrosion fatigue behaviour of 13cr stainless steel and ti-6al-4v at ultrasonic frequency. *Ultrasonic fatigue. Philadelphia: The Metall Society of AIME*, 349–64.

Elangeswaran, C., K. Gurung, R. Koch, A. Cutolo, and B. Van Hooreweder (2020). Post-treatment selection for tailored fatigue performance of 18ni300 maraging steel manufactured by laser powder bed fusion. *Fatigue & Fracture of Engineering Materials & Structures 43*(10), 2359–2375.

Emerson Industrial Automation (2022). Ultrasonic horn catalog. Accessed March 26, 2022. https://www.emerson.com/documents/automation/catalog-ultrasonic-horn-branson-en-us-160126.pdf.

European Standard (2019). BS EN 10025-2:2019: Hot rolled products of structural steels- Technical delivery conditions for non-alloy structural steels. Standard, European Commitee for Standardization, Brussels. Accessed June 10, 2022. https://www.en-standard.eu/bs-en-10025-2-2019-hot-rolled-products-of-structural-steels-technical-delivery-conditions-for-non-alloy-structural-steels/.

Fatemi, A. and L. Yang (1998). Cumulative fatigue damage and life prediction theories: a survey of the state of the art for homogeneous materials. *International Journal of Fatigue 20*(1), 9–34.

Fu, L., G. Xu, Y. Yan, J. Yang, and J. Xie (2018, 08). The application and research progress of high strength and high performance steel in building structure. *IOP Conference Series: Materials Science and Engineering 392*, 022008.

Furuya, Y., H. Hirukawa, and E. Takeuchi (2019). Gigacycle fatigue in high strength steels. *Science and Technology of Advanced Materials 20*(1), 643–656. doi: 10.1080/14686996.2019.1610904.

Furuya, Y., S. Matsuoka, T. Abe, and K. Yamaguchi (2002). Gigacycle fatigue properties for high-strength low-alloy steel at 100 hz, 600 hz, and 20 khz. *Scripta Materialia 46*(2), 157–162.

Galar, D. and U. Kumar (2017). Chapter 6 - prognosis. In D. Galar and U. Kumar (Eds.), *eMaintenance*, pp. 311–370. Academic Press.

Gallego-Juarez, J. A. (1989, oct). Piezoelectric ceramics and ultrasonic transducers. *Journal of Physics E: Scientific Instruments 22*(10), 804–816.

Gao, G., Q. Xu, H. Guo, X. Gui, B. Zhang, and B. Bai (2019). Effect of inclusion and microstructure on the very high cycle fatigue behaviors of high strength bainite/martensite multiphase steels. *Materials Science and Engineering: A 739*, 404–414.

Grech, D. (2014, 11). *Development of a Quasi-concertina MEMS sensor for the characterisation of biopolymers.* Ph. D. thesis, University of Southampton, Southampton, UK.

Guennec, B., A. Ueno, T. Sakai, M. Takanashi, and Y. Itabashi (2014). Effect of the loading frequency on fatigue properties of jis s15c low carbon steel and some discussions based on micro-plasticity behavior. *International Journal of Fatigue 66*, 29–38. Cited By :49 Export Date: 13 February 2022.

Guo, Y., H. Ho, K. Chung, and A. Elghazouli (2020). Cyclic deformation characteristics of s355 and s690 steels under different loading protocols. *Engineering Structures 221*, 111093.

Hans, E. (2003). Influence of notches on fatigue behaviour of pm steels. Master's thesis, Luleå University of Technology's. Accessed June 26, 2022. http://urn.kb.se/resolve?urn=urn:nbn:se:ltu:diva-54142.

Hansson, T. (2012). Fatigue failure mechanisms and fatigue testing. Report, North Atlantic Treaty Organization- Science and Technology Organization, Sweden. Accessed July 2, 2022. https://www.sto.nato.int/publications/STO

Harte, R. and G. P. Van Zijl (2007). Structural stability of concrete wind turbines and solar chimney towers exposed to dynamic wind action. *Journal of Wind Engineering and Industrial Aerodynamics 95*(9), 1079–1096.

Hartman, Derek (2013). Robust model for fatigue life estimation from monotonic properties data for steels. Master's thesis, University of Waterloo, Waterloo, Ontario, Canada.

HBM (2022). The wheatstone bridge circuit. Accessed June 17, 2022. https://www.hbm.com/en/7163/wheatstone-bridge-circuit/.

Heim, R. (2020, 01). *Structural Durability: Methods and Concepts: Enabling Cost and Mass Efficient Products*, pp. 116–117. Springer Cham.

Ilie, P., X. Lesperance, and A. Ince (2020). Development of an ultrasonic fatigue testing system for gigacycle fatigue. *Material Design & Processing Communications 2*(6), e120.

IMOA (2011). Molybdenum in Irons and Steels for Clean and Green Power Generation. Report, International Molybdenum Association, Belgium. Accessed June 8, 2022. https://www.imoa.info/.

Inegi (2022). Inegi – instituto de ciência e inovação em engenharia mecânica e engenharia industrial. Accessed April 5, 2022. http://www.inegi.pt/en/.

ISO (1997). ISO 4287:1997: Geometric Product Specification (GPS). Surface Texture Profile Method: Terms, Definition and Surface Texture Parameters. Standard, International Organization for Standardization, Geneva, CH. Accessed May 10, 2022. https://www.iso.org/standard/10132.html.

ISO (2006). ISO 1099:2006: Metallic Materials–Fatigue Testing–Axial Force-controlled Method. Standard, International Organization for Standardization, Geneva, CH. Accessed June 28, 2022. https://www.iso.org/standard/36108.html.

ISO (2012). ISO 12107:2012 (E). Metallic Materials—Fatigue Testing—Statistical Planning and Analysis of Data. Standard, International Organization for Standardization, ISO Copyright office: Geneva, Switzerlan. Accessed June 15, 2022. https://www.iso.org/standard/50242.html.

ISO (2021). ISO 6344-3:2021(en) Coated abrasives — Determination and designation of grain size distribution — Part 3: Microgrit sizes P240 to P5000. Standard, International Organization for Standardization, ISO Copyright office: Geneva, Switzerlan. Accessed May 15, 2022. https://www.iso.org/standard/78219.html.

Kolsky, H. (1964). Stress waves in solids. *Journal of Sound and Vibration 1*(1), 88–110.

Krasovskyy, A. and A. Virta (2014). Fracture mechanics based estimation of fatigue life of welds. *Procedia Engineering 74*, 27–32. XVII International Colloquium on Mechanical Fatigue of Metals (ICMFM17).

Lee, Y.-L. (2005). 2 - fatigue damage theories. In Y.-L. Lee, J. Pan, R. B. Hathaway, and M. E. Barkey (Eds.), *Fatigue Testing and Analysis*, pp. 57–76. Burlington: Butterworth-Heinemann.

Liao, D., S.-P. Zhu, J. A. Correia, A. M. De Jesus, and F. Berto (2020). Recent advances on notch effects in metal fatigue: A review. *Fatigue & Fracture of Engineering Materials & Structures 43*(4), 637–659.

Lindblom, B. E. (1970). Fatigue notch-sensitivity of nodular cast iron in comparison to steel. *Transactions of the Iron and Steel Institute of Japan 10*(2), 73–77.

Liu, X. (2019). *Predicting fatigue life of welded joints under variable amplitude loading spectra*. Ph. D. thesis, Brunel University London.

Liu, X., K.-F. Chung, H. C. Ho, M. Xiao, Z.-X. Hou, and D. Nethercot (2018, 11). Mechanical behavior of high strength s690-qt steel welded sections with various heat input energy. *Engineering Structures 175*, 245–256.

Lynch, S. (2007). Progression markings, striations, and crack-arrest markings on fracture surfaces. *Materials Science and Engineering: A 468-470*, 74–80. The McEvily Symposium: Fatigue and Fracture of Traditional and Advanced Materials, TMS 2006.

Ma, T.-Y., X. Liu, Y.-F. Hu, K.-F. Chung, and G.-Q. Li (2018). Structural behaviour of slender columns of high strength s690 steel welded h-sections under compression. *Engineering Structures 157*, 75–85.

Manson, S. S. (1965). Fatigue: A complex subject—some simple approximations. *Experimental Mechanics 5*(4), 193–226.

Marques, J. M. E., D. Benasciutti, A. Niesłony, and J. Slavič (2021). An overview of fatigue testing systems for metals under uniaxial and multiaxial random loadings. *Metals 11*(3).

Marti, N., V. Favier, N. Saintier, and F. Gregori (2015). Investigating fatigue frequency effects on single phase ductile materials. *Procedia Engineering 133*, 294–298. Fatigue Design 2015, International Conference Proceedings, 6th Edition.

Mason, W. P. (1956). Internal friction and fatigue in metals at large strain amplitudes. *The Journal of the Acoustical Society of America 28*(6), 1207–1218.

Matlab (2022). Weibull distribution. Accessed June 25, 2022. https://www.mathworks.com/help/stats/weibull-distribution.html.

Mayer, H., E. Tschegg, and S. Stanzl-Tschegg (1996, 01). High cycle torsion fatigue of ceramic materials under combined loading conditions (cyclic torsion + static compression). *Multiaxial Fatigue and Design (ESIS 21)*, 411–421.

Meggiolaro, M. and J. Castro (2004). Statistical evaluation of strain-life fatigue crack initiation predictions. *International Journal of Fatigue 26*(5), 463–476.

Mendes, P., J. Correia, A. De Jesus, B. Ávila, H. Carvalho, and F. Berto (2021, 01). A brief review of fatigue design criteria on offshore wind turbine support structures. *Frattura ed Integrità Strutturale 55*, 302–315.

Micro-Measurements (2022a). Instruction bulletin b-127. Accessed June 17, 2022. http://www.vishaypg.com/docs/11127/11127B127.pdf.

Micro-Measurements (2022b). Strain gauge s5145. Accessed June 17, 2022. https://micro-measurements.com/pca/detail/s5145.

Miner, M. A. (1945, 09). Cumulative Damage in Fatigue. *Journal of Applied Mechanics 12*(3), A159–A164.

Mitchell, M. R. (1979). Fundamentals of modern fatigue analysis for design. *Fatigue and Microstructure, Metals Park 110*, 385–437.

Mitutoyo (2022). Surftest surface roughness testers. Accessed May 25, 2022. https://www2.mitutoyo.co.jp/eng/products/menu/QuickGuide.

Monteiro, P. M. V. (2019). Fatigue resistance of butt welds of structural steels in wind turbine towers. Master's thesis, Faculty of Engineering of University of Porto.

Murakami, Y., T. Nomoto, and T. Ueda (1999). Factors influencing the mechanism of superlong fatigue failure in steels. *Fatigue & Fracture of Engineering Materials & Structures 22*, 581–590.

Muralidharan, U. and S. S. Manson (1988). A modified universal slopes equation for estimation of fatigue characteristics of metals. *Journal of Engineering Materials and Technology-Transactions of The ASME 110*, 55–58.

Nakajima, M., K. Tokaji, H. Itoga, and T. Shimizu (2002). Fatigue life under variable amplitude loading in a high strength steel showing step-wise s-n curve. In *ECF 14, Fracture Mechanics beyond 2000, Proc. of the 14th Bienniel Conference on Fracture (ECF 14), Cracow, Poland, 8-13 September 2002.*

Neppiras (1959). Techniques and equipment for fatigue testing at very high frequencies. *Proceedings of the 62nd Annual Meeting of ASTM, Philadelphia* (59), 59:691–710.

Nihei, M., E. Sasaki, M. Kanao, and M. Inagaki (1979). Statistical analysis for the influence of the toe shapes of the weld and the welding conditions on the fatigue strength of arc welded joints with covered electrode. *Journal of the Society of Naval Architects of Japan 1979*, 393–406.

Nishijima and Kanazawa (1999). Stepwise s-n curve and fish-eye failure in gigacycle fatigue. *Fatigue & Fracture of Engineering Materials & Structures 22*(7), 601–607.

Nonaka, I., S. Setowaki, and Y. Ichikawa (2014). Effect of load frequency on high cycle fatigue strength of bullet train axle steel. *International Journal of Fatigue 60*, 43–47. New Advances in VHCF.

Nova, N. S. B. (2018). Utilização de aços de alta resistência em estruturas especiais-aplicação a um caso de estudo. Master's thesis, Faculty of Engineering of University of Porto.

NYSERDA (2022). Determination study for offshore wind. Accessed March 31, 2022. https://portal.nyserda.ny.gov/servlet/servlet.FileDownload?file=00P8z000000kvGhEAI.

Ong, J. (1993). An evaluation of existing methods for the prediction of axial fatigue life from tensile data. *International Journal of Fatigue 15*(1), 13–19.

Orvis, K. H. and H. D. Grissino-Mayer (2002). Standardizing the reporting of abrasive papers used to surface tree-ring samples. *Tree-Ring Research*.

Palbit (2022). Tool dcmt-mw. Accessed June 8, 2022. https://www.palbit.pt/.

Palin-Luc, T. and D. Jeddi (2018). The gigacycle fatigue strength of steels: a review of structural and operating factors. *Procedia Structural Integrity 13*, 1545–1553.

Paris, P. and F. Erdogan (1963, 12). A Critical Analysis of Crack Propagation Laws. *Journal of Basic Engineering 85*(4), 528–533.

Pedro, J. J. O., A. J. Reis, and C. Baptista (2017). 16.04: High strength steel (hss) s690 in highway bridges: Comparative design. *ce/papers 1*(2-3), 4059–4068.

Pineau, A. and S. Forest (2017). Effects of inclusions on the very high cycle fatigue behaviour of steels. *Fatigue & Fracture of Engineering Materials & Structures 40*(11), 1694–1707.

Pinto, H., M. Corpas, J. A. Guio, A. R. Pyzalla, A. Jahn, and J. Standfuß (2009). Microstructure and Residual Stress Formation in Induction-Assisted Laser Welding of the Steel S690QL. *Steel Research International 80*(1), 39–49.

Pluvinage, G. (2003, 01). *Fracture and Fatigue Emanating from Stress Concentrators*, pp. 189–190. Springer Netherlands.

Portal da Inovação (2022). INEGI – Instituto de Ciência e Inovação em Engenharia Mecânica e Engenharia Industrial. Accessed April 5, 2022. https://www.portaldainovacao.pt.

Qian, G., Y. Hong, and C. Zhou (2010). Investigation of high cycle and very-high-cycle fatigue behaviors for a structural steel with smooth and notched specimens. *Engineering Failure Analysis 17*(7), 1517–1525.

Qiang, X., F. Bijlaard, and H. Kolstein (2012a). Dependence of mechanical properties of high strength steel s690 on elevated temperatures. *Construction and Building Materials 30*, 73–79.

Qiang, X., F. S. Bijlaard, and H. Kolstein (2012b). Post-fire mechanical properties of high strength structural steels s460 and s690. *Engineering Structures 35*, 1–10.

Qingyuan, W. and H. Zhiyong (2013). *Super-Long Life Fatigue*, pp. 3387–3397. Boston, MA: Springer US.

Qualitest (2022). Resonant fatigue testing machines. Accessed June 8, 2022. https://www.worldoftest.com/resonant-fatigue-testing-machines.

Ribeiro, A., A. Jesus, J. Costa, L. Borrego, and J. Maeiro (2011). Variable amplitude fatigue crack growth modelling. *Revista da Associação Portuguesa de Análise Experimental de Tensões ISSN 1646*, 7078.

Ritz, F. and T. Beck (2017). Influence of mean stress and notches on the very high cycle fatigue behaviour and crack initiation of a low-pressure steam turbine steel. *Fatigue & Fracture of Engineering Materials & Structures 40*(11), 1762–1771.

Rodrigues, J. D. (2020). *Apontamentos de Vibrações de Sistemas Mecânicos*. FEUP-DEMEc.

Rodrigues da Costa, P., R. Nwawe, H. Soares, L. Reis, M. Freitas, Y. Chen, and D. Montalvão (2020). Review of multiaxial testing for very high cycle fatigue: From 'conventional' to ultrasonic machines. *Machines 20*, 25.

Roessle, M. L. and A. Fatemi (2000). Strain-controlled fatigue properties of steels and some simple approximations. *International Journal of Fatigue 22*, 495–511.

Rumul (2022). Testronic. Accessed June 7, 2022. https://www.rumul.ch/.

Sadek, M., J. Bergström, N. Hallbäck, C. Burman, R. Elvira, and B. Escauriaza (2020). Fatigue strength and fracture mechanisms in the very-high-cycle-fatigue regime of automotive steels. *Steel Research International 91*(8), 2000060.

Schijve, J. (Ed.) (2009, 01). *Fatigue under Variable-Amplitude Loading*, pp. 295–328. Dordrecht: Springer Netherlands.

Schönbauer, B. M., S. Ghosh, J. Kömi, T. Frondelius, and H. Mayer (2021). Influence of small defects and nonmetallic inclusions on the high and very high cycle fatigue strength of an ultrahigh-strength steel. *Fatigue & Fracture of Engineering Materials & Structures 44*(11), 2990–3007.

Setowaki, S., Y. Ichikawa, and I. Nonaka (2011, 01). Effect of frequency on high cycle fatigue strength of railway axle steel. *Proc of VHCF 5 Congress, Berlin, Germany*, 153–8.

Sharifi, Y. and R. Rahgozar (2009, 12). Fatigue notch factor in steel bridges due to corrosion. *Archives of Civil and Mechanical Engineering 9*, 75–83.

Sharma, A., M. C. Oh, and B. Ahn (2020). Recent advances in very high cycle fatigue behavior of metals and alloys—a review. *Metals 10*(9), 1200.

Shi, S. (2015). Evaluating the structural integrity of high strength low alloy steels considered for shipbuilding using acoustic emission. Master's thesis, University of Birmingham. M.Res.

Shiozawa, K., Y. Morii, S. Nishino, and L. Lu (2006). Subsurface crack initiation and propagation mechanism in high-strength steel in a very high cycle fatigue regime. *International Journal of Fatigue 28*(11), 1521–1532. Third International Conference on Very High Cycle Fatigue (VHCF-3).

Smithells, C. J. (2004). 21 - mechanical testing. In W. Gale and T. Totemeier (Eds.), *Smithells Metals Reference Book (Eighth Edition)* (Eighth Edition ed.)., pp. 21–1–21–23. Oxford: Butterworth-Heinemann.

Stanzl, S. (1981). A new experimental method for measuring life time and crack growth of materials under multi-stage and random loadings. *Ultrasonics 19*(6), 269–272.

Stanzl-Tschegg, S. (2014, 03). Very high cycle fatigue measuring techniques. *International Journal of Fatigue 60*, 2–17.

Stanzl-Tschegg, S., H. Mayer, and E. Tschegg (1993, 07). High frequency method for torsion fatigue testing. *Ultrasonics 31*, 275–280.

Stanzl-Tschegg, S. E. and H. Mayer (2001). Fatigue and fatigue crack growth of aluminium alloys at very high numbers of cycles. *International Journal of Fatigue 23*, 231–237.

Stanzl-Tschegg, S. E., H. Mayer, and A. Stich (2002). Variable amplitude loading in the very high-cycle fatigue regime. *Fatigue & Fracture of Engineering Materials & Structures 25*(8-9), 887–896.

Steel, C. (2022). En 10025-6 grade s690ql plates. Accessed February 26, 2022. https://www.csecplates.com/en-10025-6-grade-s690ql-plate-stockists-suppliers.html.

Thiruvengadam (1972). Corrosion fatigue at high frequencies and high hydrostatic pressures. *518*, 139–54.

Thitima, J. (2022). 2103-602 measurement and instrumentation. Accessed June 17, 2022. http://pioneer.netserv.chula.ac.th/ jthitima/602/strain

Torizuka, S., M. Kuntz, Y. Furuya, and M. Bacher-Hoechst (2012). Effect of tensile strength and microstructure on notch-fatigue properties of ultrafine-grained steels. *ISIJ International 52*, 910–914.

Tschegg, E., H. Mayer, M. Czegley, and S. Stanzl-Tschegg (1991, 01). Influence of a constant mode iii load on mode i fatigue crack growth threshold. *Fatigue under Biaxial and Multiaxial Loading*, 213–222.

Tschegg, E. and S. Stanzl-Tschegg (1990, 01). Fatigue crack propagation under rotating bending. *Proc Int Fatigue Series "fatigue 90 2*, 1217–1222.

Tsutsumi, N., Y. Murakami, and V. Doquet (2009). Effect of test frequency on fatigue strength of low carbon steel. *Fatigue & Fracture of Engineering Materials & Structures 32*(6), 473–483.

Union Stahl (2022). Aços de alta resistência. Accessed April 25, 2022. https://www.unionstahl.com/gama-de-produtos/acos-de-alta-resistencia/?lang=pt-pt.

Wagener, R., T. Melz, C. Fischer, M. Matthias, and H. Kaufmann (2011). New experimental methods for investigating variable amplitude loading effects in hcf and vhcf regimes. *Materialwissenschaft und Werkstofftechnik 42*(10), 929–933.

Weibull, W. (1951). A statistical distribution function of wide applicability. *Journal of Applied Mechanics 18*, 293–297.

WindEurope (2022). Wind energy in Europe. Report, WindEurope. Accessed July 2, 2022. https://windeurope.org/intelligence-platform/product/wind-energy-in-europe-2021-statistics-and-the-outlook-for-2022-2026/.

World Steel Association (2022). February 2022 crude steel production. Accessed March 31, 2022. https://worldsteel.org/media-centre/press-releases/2022/february-2022-crude-steel-production/.

Xiong, Z., E. Peng, L. Zeng, and Q. Xu (2021, 7). Giga-cycle fatigue behavior of the nuclear structure of 316l weldments. *Frontiers in Energy Research 9*, 1–8.

Zhang, L., F. Wang, Y. Liang, and O. Zhao (2020). Experimental and numerical studies of press-braked s690 high strength steel channel section beams. *Thin-Walled Structures 148*, 106499.

Zhang, Y., K. Lockwood, P. Bates, and D. DuQuesnay (2015). Fatigue properties of vibration-welded postindustrial waste nylon with glass fibers at room and elevated temperatures. *Polymer Engineering & Science 55*(4), 799–806.

Zhao, M., S. Chiew, and C. K. Lee (2013, 01). Fatigue behavior of rectangular built-up hollow section joint made of high strength steel s690. *Proceedings of the 13th East Asia-Pacific Conference on Structural Engineering and Construction, EASEC 2013*.

Zhao, M., T. Wu, Z. Zhao, L. Liu, G. Luo, and W. Chen (2020). Ultrasonic fatigue device and behavior of high-temperature superalloy inconel 718 with self-heating phenomenon. *Applied Sciences 10*, 8761.

Zhao, Z., F. Zhang, C. Dong, X. Yang, and B. Chen (2020). Initiation and early-stage growth of internal fatigue cracking under very-high-cycle fatigue regime at high temperature. *Metallurgical and Materials Transactions A 51*(4), 1575–1592.

Zimmermann, M. (2018). *Very High Cycle Fatigue*, pp. 1–38. Singapore: Springer Singapore.

Zou, Z., Z. Liu, X. Ai, and D. Wu (2022). Effect of Aluminum on Microstructure and Mechanical Properties of Weld Metal of Q960 Steel. *Crystals 12*(1), 1–13.

Appendix A

Technical drawings

This Appendix displays the technical drawings made for the three specimens for the Shimadzu machine: the smooth/hourglass, notched specimens with stress concentration factors $K_t = 1.25$ and $K_t = 1.5$. Then, the booster is illustrated, followed by the horn.

Also, the smooth specimen tested in Rumul at 150 Hz is presented.

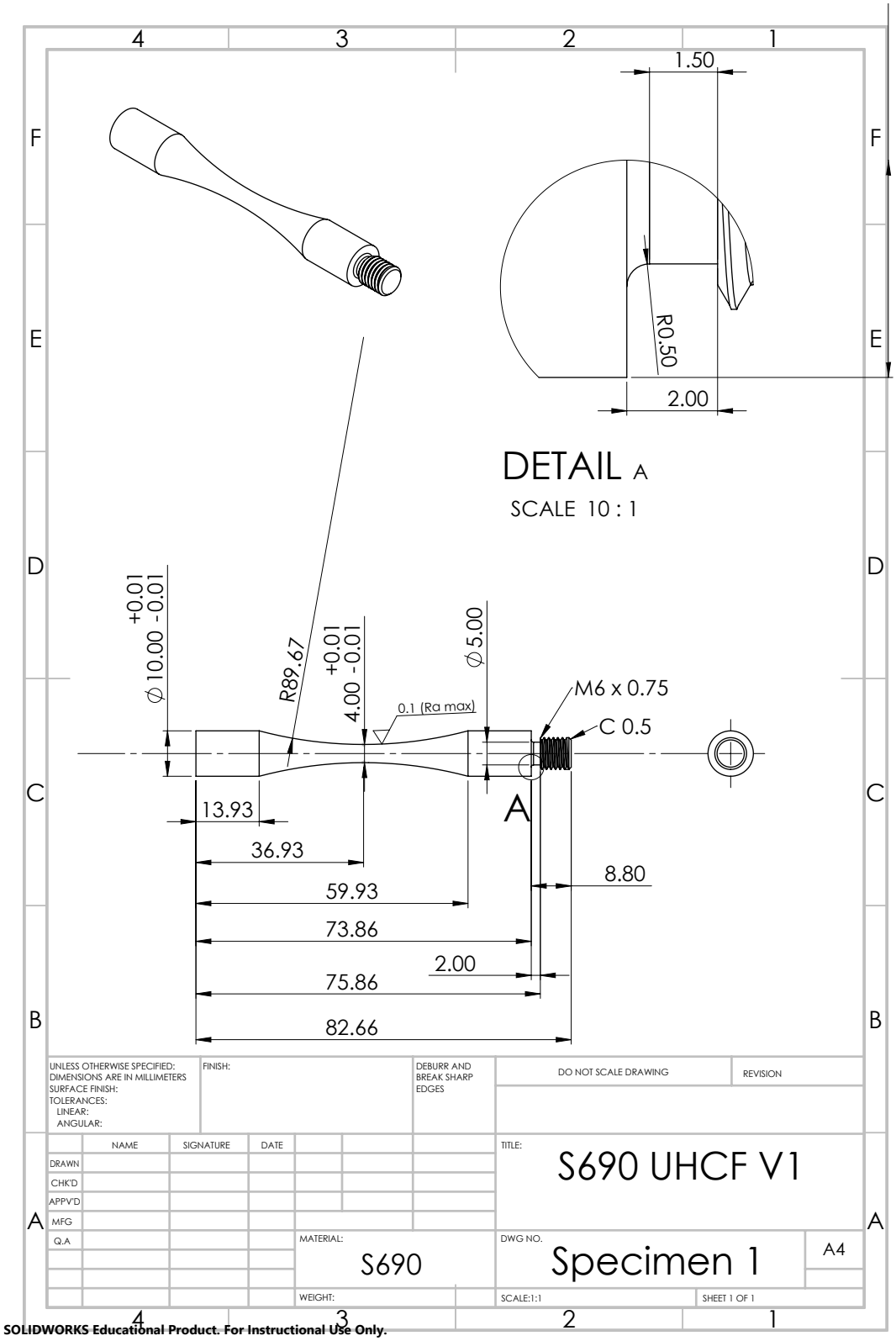


Figure A.0.1: Technical drawing of the smooth specimen (20 kHz)

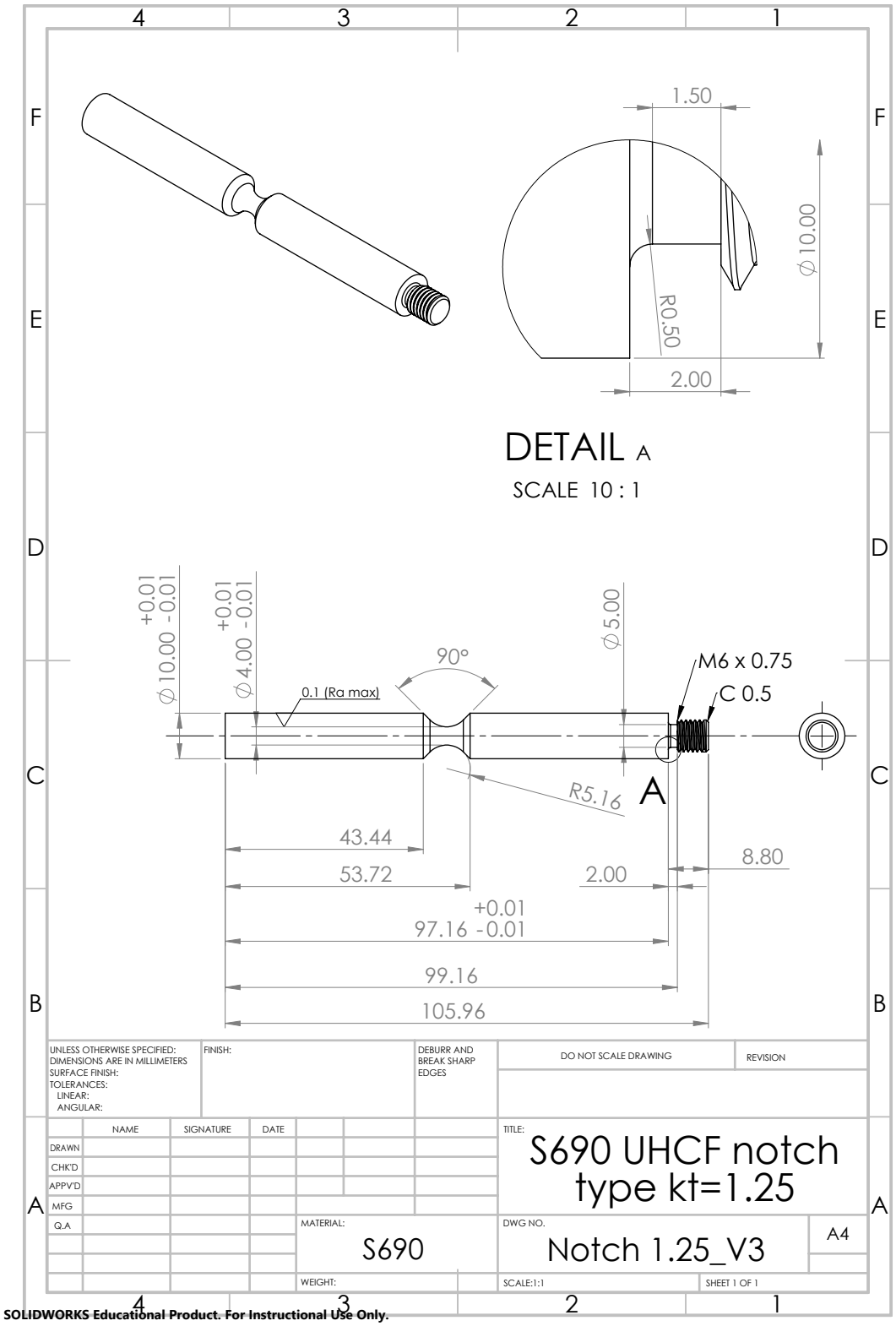


Figure A.0.2: Technical drawing of the notched specimen with $K_t = 1.25$ and the corrected dimensions for the 20 kHz

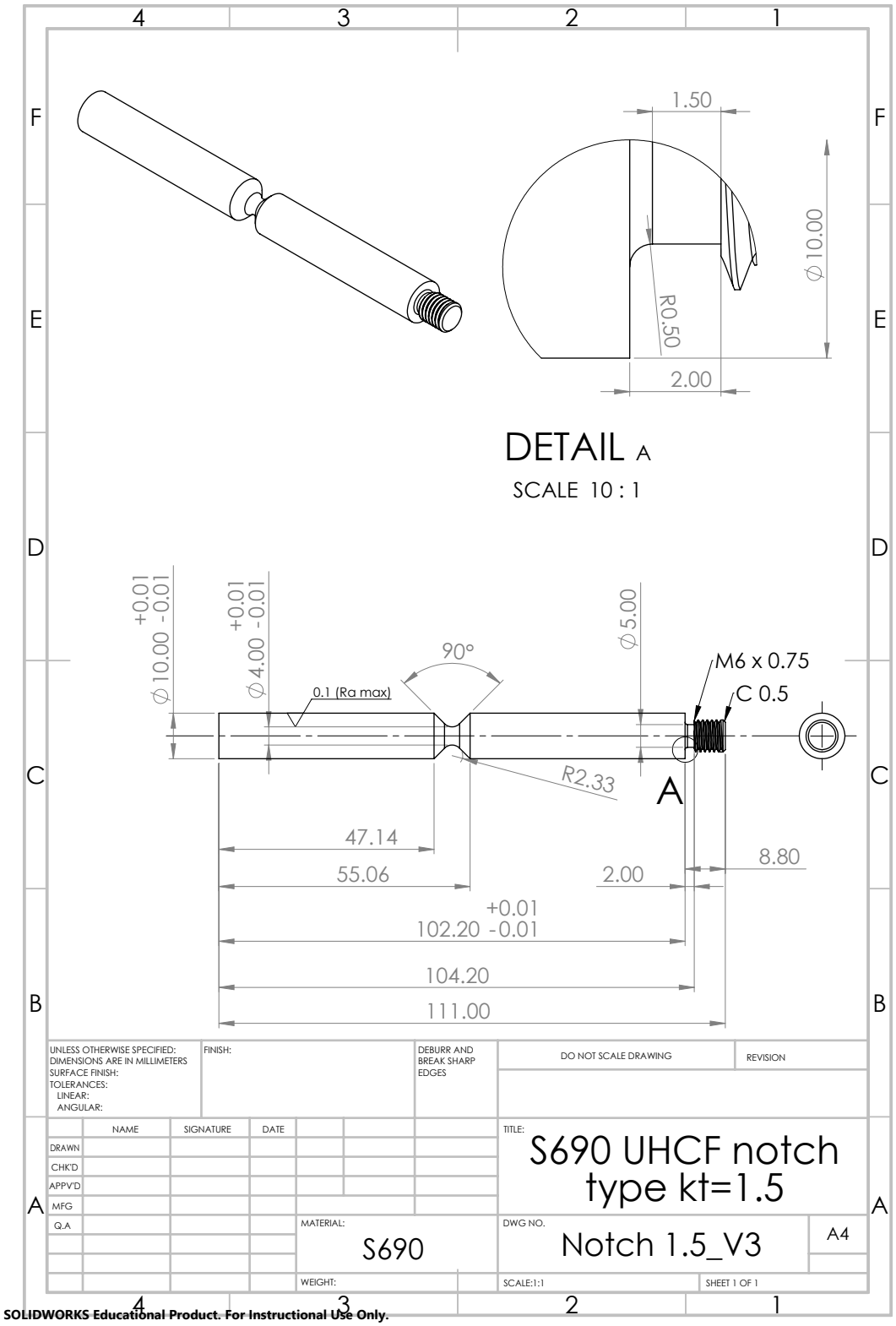


Figure A.0.3: Technical drawing of the notched specimen with $K_t = 1.50$ and the corrected dimensions for 20 kHz

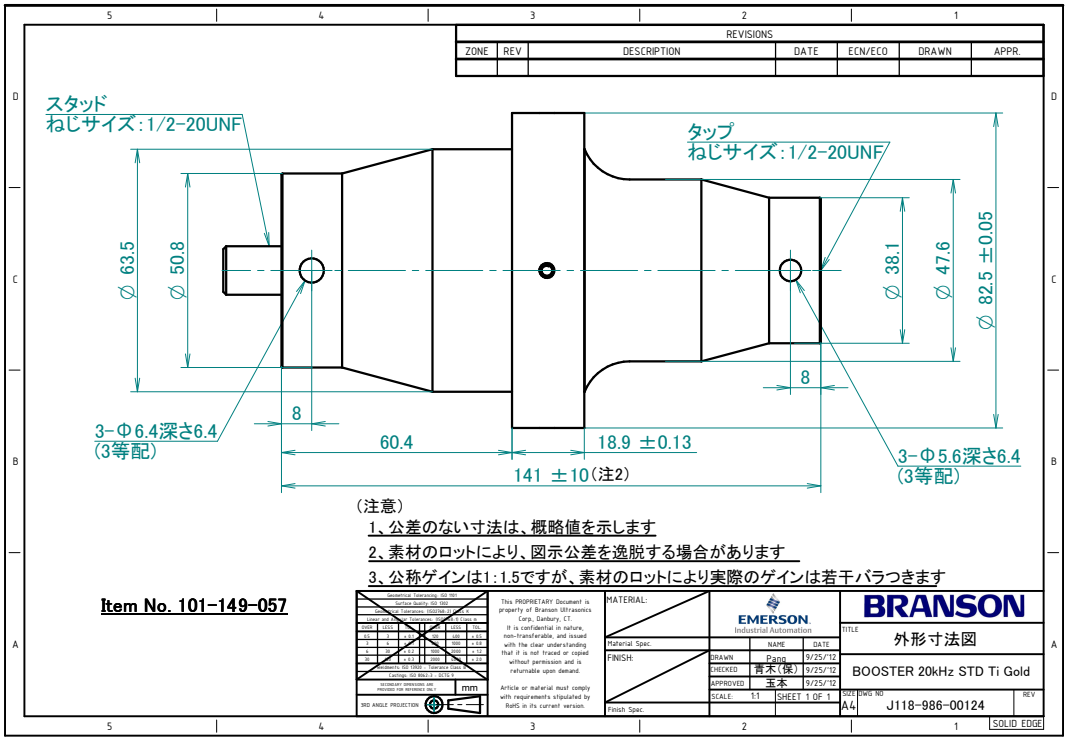


Figure A.0.4: Technical drawing of the booster of the Shimadzu UHSF-2000

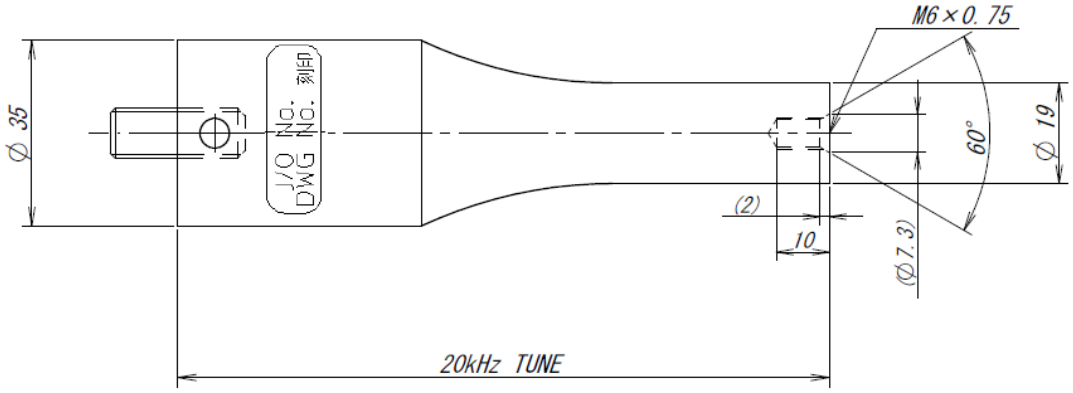


Figure A.0.5: Horn dimensions of the Shimadzu UHSF-2000

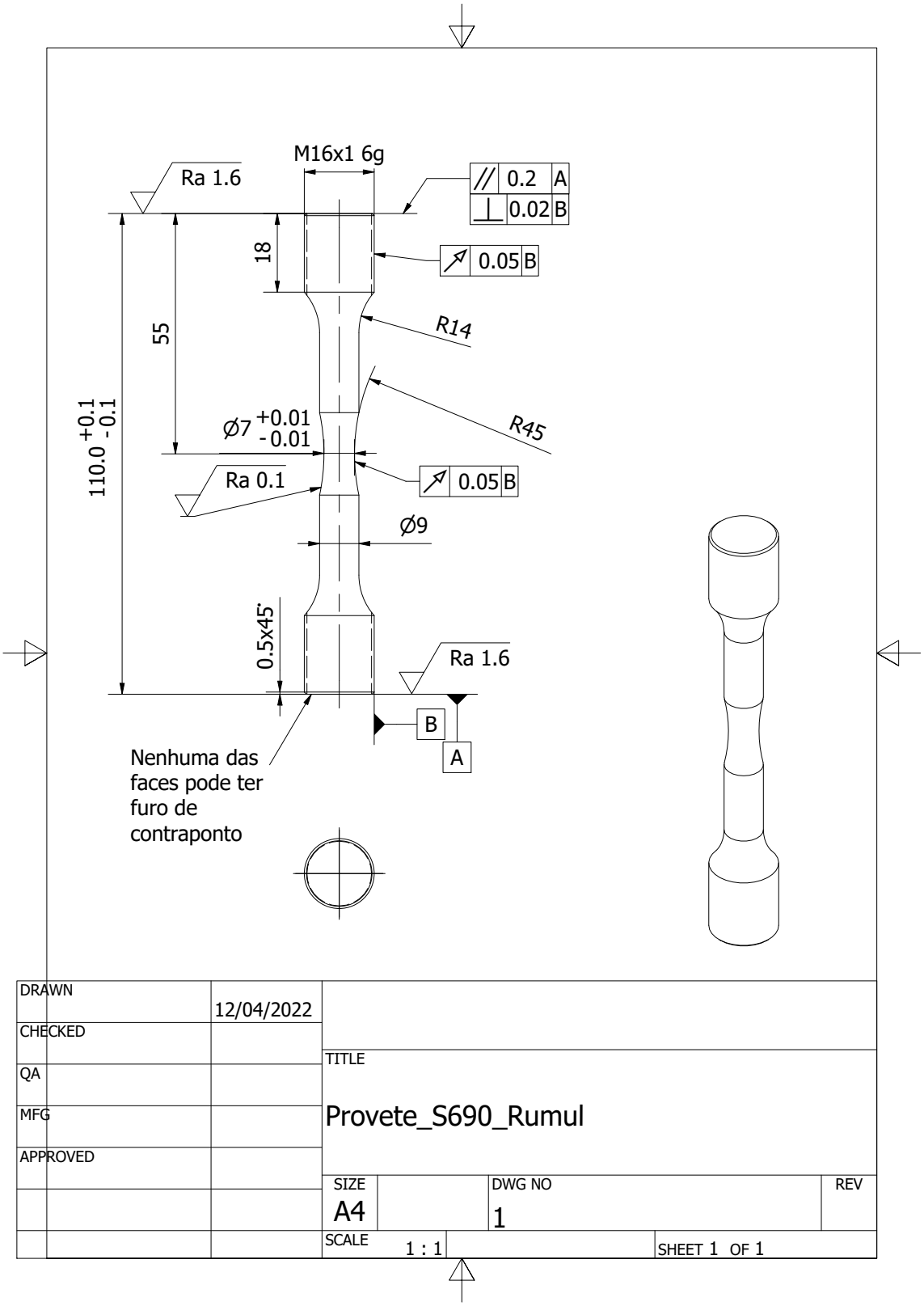
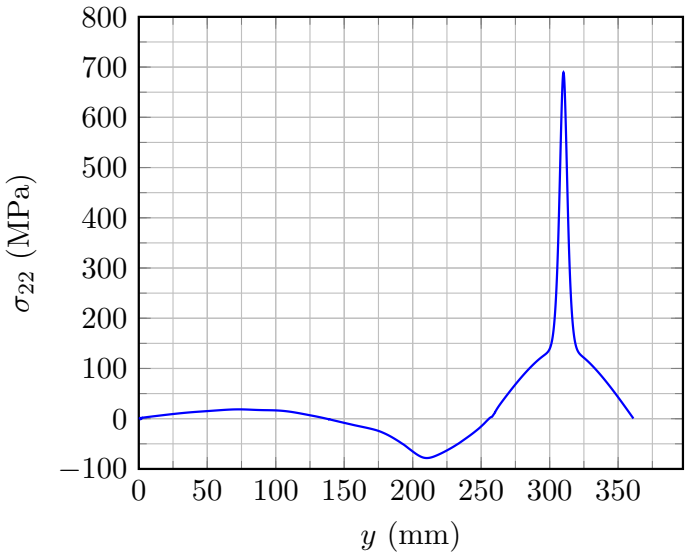


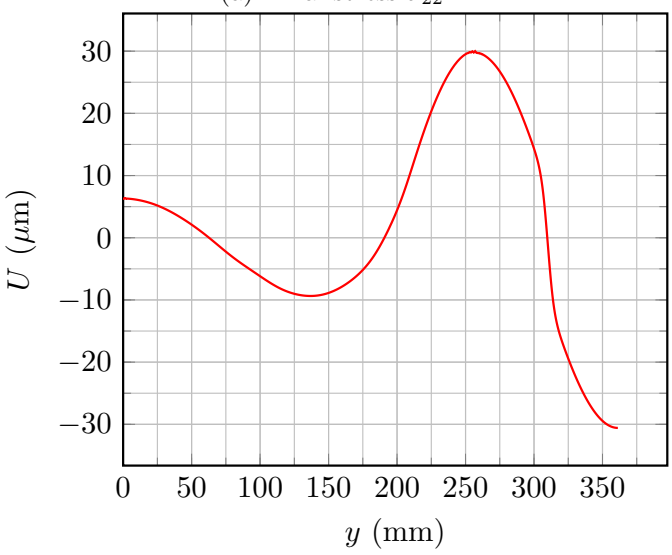
Figure A.0.6: Technical drawing of the S690 smooth specimen (150 Hz)

Appendix B

FEM results for the notched specimens (20 kHz)



(a) Axial stress σ_{22}

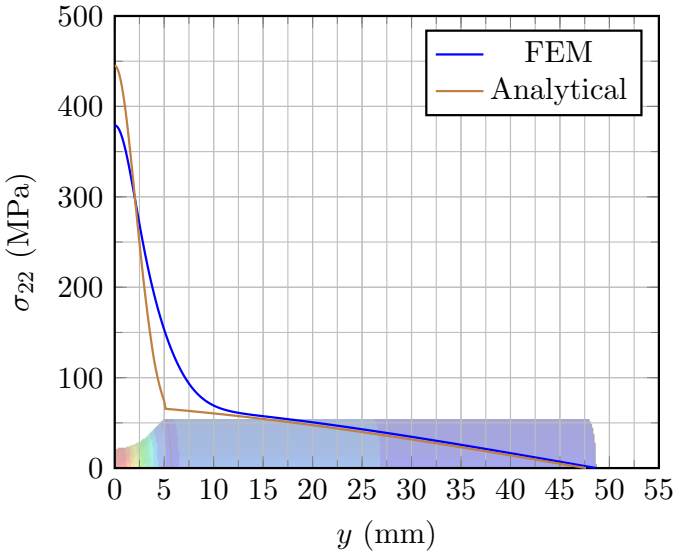


(b) Axial displacement U_2

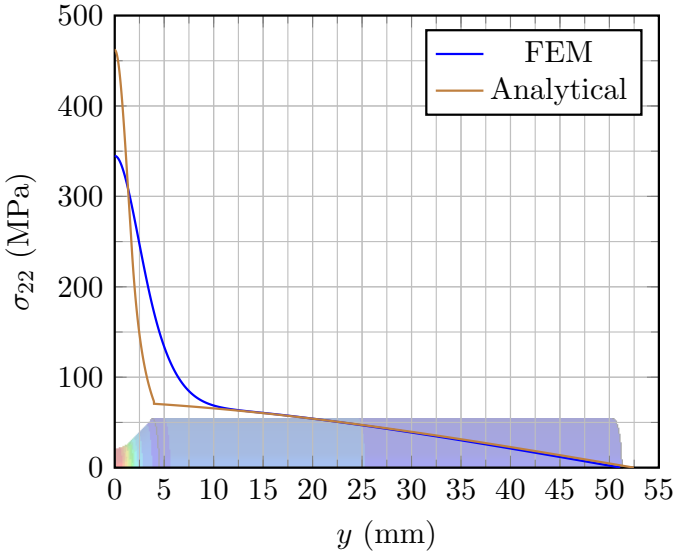
Figure B.0.1: FEM results for the 20 kHz notched specimen with K_t=1.5 ($A_0 = 30\mu$m)

Appendix C

FEM results comparison with the analytical solution (20 kHz)



(a) Specimen $K_t = 1.25$ for the predicted $L_1 = 46.85$ mm and $L = 51.98$ mm ($A_0 = 15\mu$m)



(b) Specimen $K_t = 1.50$ for the predicted $L_1 = 51.68$ mm and $L = 55.64$ mm ($A_0 = 15\mu$m)

Figure C.0.1: Stress for half the notched specimen (20 kHz) by FEM and analytical solution

Table C.0.1: Constants and values calculated for the analytical determination of the stress in the notched specimens (20 kHz)

Variable	Input				Unit
	Notch $K_t = 1.25$		Notch $K_t = 1.50$		
$\theta/2$	$\pi/4$				rad
D_2	0.004				m
D_1	0.010				m
E	2.1159E+11				Pa
A_0	0.000015				m
k	24.1514				rad/m
R	0.00516		0.00233		m
l_s	0.0051373		0.0039651		m
$L_3 = R\cos(\theta)$	0.003649		0.001648		m
$y(R\cos(\theta))$	0.003511		0.002682		m
α_b	318.6764		488.1459		rad/m
$\tan(kR\cos(\theta))$	0.088349		0.039812		-
β	317.73683		487.53303		rad/m
$\frac{C_4}{C_3}$	-34.14433		-113.30400		-
	Output				
L_1	0.047629	0.04344	0.052471	0.04714	m
$L = l_s + L_1$	0.105533	**0.09716**	0.112871	**0.10220**	m
C_3	-1.89376E-08	-2.31160E-08	-4.55747E-09	-6.3894E-09	m^2
C_4	6.46613E-07	7.89282E-07	5.16379E-07	7.23944E-07	m^2
C_5	3.30874E-06	4.03878E-06	2.23926E-06	3.13935E-06	m
Strain ($x = 0$)	0.002102771	0.002566725	0.002183489	0.003061169	-
Stress ($x = 0$)	444932324.8	543102053.0	462011888.0	647723017.8	Pa
Stress ($x = 0$)	**445**	**543**	**462**	**648**	MPa
	Shimadzu values				
Stress ($x = 0$)	479				MPa
L	104.64		109.91		mm
Experimental L	97.16		102.20		mm

Appendix D

FEM cross section stress results

Table D.0.1: Trendline power equations for the horizontal stress distribution for the 20 kHz notched specimens ($R^2 = 1$)

Notch Kt	A_0	Stress Equation for $0 \leq r \leq 2$
-	μm	MPa
1.25	15	$\sigma(r) = 1.849r^4 + 0.2384r^3 + 23.707r^2 + 0.5028r + 379.07$
1.5		$\sigma(r) = 16.138r^4 - 27.331r^3 + 59.197r^2 - 5.8058r + 345.04$
1.25	30	$\sigma(r) = 3.6979r^4 + 0.4769r^3 + 47.415r^2 + 1.0056r + 758.14$
1.5		$\sigma(r) = 32.276r^4 - 54.662r^3 + 118.39r^2 - 11.612r + 690.08$
1.25	50	$\sigma(r) = 6.1632r^4 + 0.7948r^3 + 79.025r^2 + 1.676r + 1263.6$
1.5		$\sigma(r) = 53.793r^4 - 91.103r^3 + 197.32r^2 - 19.353r + 1150.1$

Appendix E

Smooth/hourglass specimens (20 kHz) data

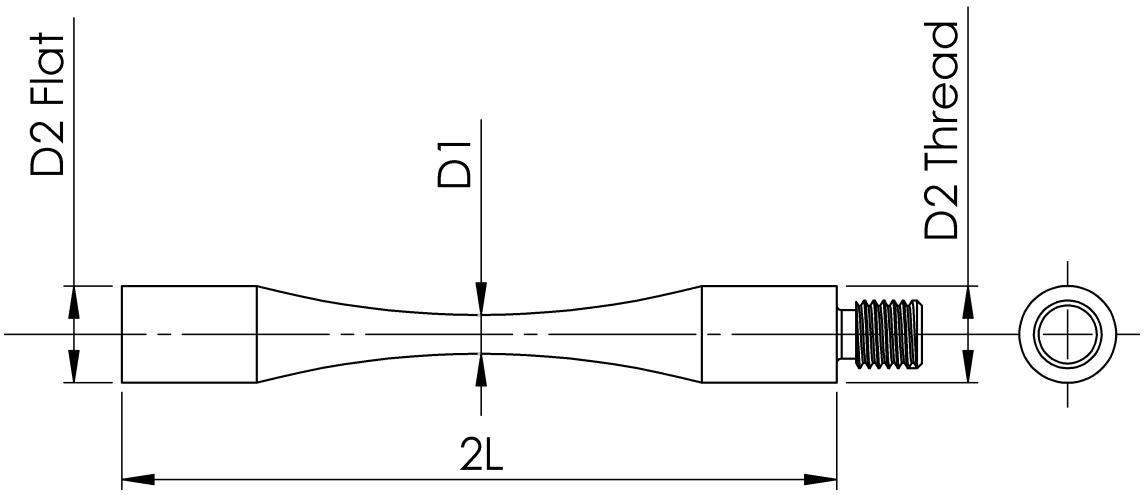


Figure E.0.1: Legend for the dimensions of Table E.0.1

Table E.0.1: Smooth/hourglass specimens (20 kHz) P3 to P34 dimensions (the average of 3 measurements for each variable)

Specimen -	Frequency f Hz	D_2 Thread mm	D_2 Flat mm	D_1 mm	$2L$ mm
3	19.92	10.048	10.045	4.056	73.89
4	19.89	10.052	10.045	4.078	73.88
5	19.87	10.064	10.042	4.035	73.92
6	19.89	10.059	10.033	4.060	73.89
7	19.89	10.048	10.047	4.043	73.94
8	19.89	10.036	10.039	4.039	73.91
9	19.89	10.042	10.032	4.044	73.92
10	19.89	10.051	10.046	4.038	73.92
11	19.88	10.057	10.037	4.046	73.88
12	19.89	10.051	10.036	4.052	73.94
13	19.89	10.052	10.049	4.054	73.91
14	19.87	10.049	10.002	4.046	73.92

Continued on next page

Table E.0.1: Continued from previous page

Specimen -	Frequency f Hz	D_2 Thread mm	D_2 Flat mm	D_1 mm	Total Length mm
15	19.88	10.060	10.056	4.045	73.90
16	19.89	10.053	10.015	4.051	73.88
17	19.89	10.054	10.036	4.052	73.91
18	19.89	10.057	10.041	4.053	73.87
19	19.88	10.064	10.054	4.057	73.92
20	19.88	10.057	10.048	4.045	73.91
21	19.88	10.064	10.022	4.046	73.90
22	19.87	10.051	10.021	4.043	73.93
23	19.86	10.068	10.066	4.036	73.90
24	19.88	10.051	10.063	4.050	73.91
25	19.84	10.014	10.019	4.018	73.86
26	19.85	10.008	10.014	4.003	73.86
27	19.86	10.016	10.011	4.011	73.86
28	19.85	10.016	10.005	4.007	73.86
29	19.84	10.005	10.010	4.011	73.89
30	19.85	10.014	10.004	4.008	73.85
31	19.85	10.003	10.006	4.009	73.86
32	19.85	10.013	10.006	4.008	73.87
33	19.85	10.011	10.007	4.007	73.88
34	19.85	10.006	9.998	4.005	73.88

Table E.0.2: Smooth/hourglass specimens (20 kHz) P3 to P34 results data

Nº -	f Hz	Polished f Hz	Final f Hz	N_f cycles	S_N MPa	Run-out -	T_{on} ms	T_{off} ms
3	19.92	-	19.88	1.00E+09	510	Yes	200	250
4	19.89	19.88	19.87	1.34E+06	520	No	250	200
5	19.87	19.84	19.84	6.63E+05	540	No	200	300
6	19.89	19.88	19.88	1.00E+09	530	Yes	190	400
7	19.89	19.86	19.86	4.60E+05	520		200	300
8	19.89	19.87	19.85	4.30E+05	550	No	190	400
9	19.89	19.85	19.85	6.22E+08	530	No	200	300
10	19.89	19.85	19.84	3.95E+06	530	No	190	400
11	19.88							
12	19.89	19.87	19.85	1.00E+09	530	Yes	190	400
13	19.89	19.87	19.87	1.00E+09	520	Yes	190	400
14	19.87	19.87	19.85	6.44E+05	510	No	190	400
15	19.88	19.87	19.86	1.82E+06	510	No	190	400
16	19.89	19.88	19.86	1.00E+10	500	Yes	190	400
17	19.89	19.88	19.88	4.05E+09	510	No	190	400
18	19.89	19.87	19.86	5.44E+05	540	No	190	400
19	19.88	19.86	19.86	4.38E+06	540	Yes	190	400
20	19.88	19.86	19.84	1.06E+07	520	No	190	400
21	19.88	19.86	19.85	1.00E+10	510	Yes	190	450
22	19.87	19.86	19.81	1.18E+07	520	No	200	300
23	19.86	19.85	19.85	1.50E+06	530	No	190	400
24	19.88	19.87	19.87	3.52E+06	520	No	190	400
25	19.84	19.84	19.84	4.39E+06	520	No	190	400
26	19.85	19.85	19.84	1.00E+09	520	Yes	190	400
27	19.86	19.85	19.85	1.00E+09	540	Yes	190	400

Table E.0.3: Surface roughness of the smooth/hourglass specimens (20 kHz) before polishing (3 measurements for each)

Specimen	Ra μm	Rq μm	Rz μm
4	0.237	0.327	2.076
5	0.260	0.484	4.223
7	0.361	0.535	3.984
14	0.148	0.232	0.148
23	0.106	0.148	1.118
Average	0.2222	0.3452	2.621

Table E.0.4: Surface roughness of the smooth/hourglass specimens (20 kHz) after testing in both directions (3 measurements for each)

Specimen	Longitudinal SR			Circumferential SR		
	Ra	Rq	Rz	Ra	Rq	Rz
	μm	μm	μm	μm	μm	μm
4	0.059	0.076	0.398	0.472	0.504	1.192
5	0.020	0.025	0.158	0.461	0.494	1.001
6	0.045	0.061	0.393	0.454	0.484	1.192
7	0.054	0.068	0.360	0.562	0.595	1.035
8	0.040	0.051	0.291	0.468	0.494	0.878
9	0.071	0.088	0.432	0.448	0.472	0.938
10	0.025	0.035	0.239	0.561	0.614	1.464
14	0.063	0.079	0.336	0.512	0.545	0.995
15	0.034	0.043	0.244	0.506	0.542	1.326
16	0.058	0.087	0.618	0.485	0.501	0.919
17	0.090	0.119	0.660	0.493	0.543	1.120
18	0.040	0.051	0.242	0.502	0.545	1.368
19	0.041	0.052	0.298	0.478	0.528	1.197
20	0.032	0.043	0.279	0.476	0.534	1.512
21	0.049	0.068	0.378	0.439	0.464	0.966
22	0.054	0.071	0.413	0.476	0.534	1.512
23	0.057	0.072	0.356	0.453	0.478	0.951
24	0.024	0.031	0.185	0.468	0.487	0.774
25	0.022	0.029	0.193	0.467	0.492	0.970
Average	0.0462	0.0605	0.3498	0.4820	0.5158	1.0954

Appendix F

Smooth specimens (150 Hz) data

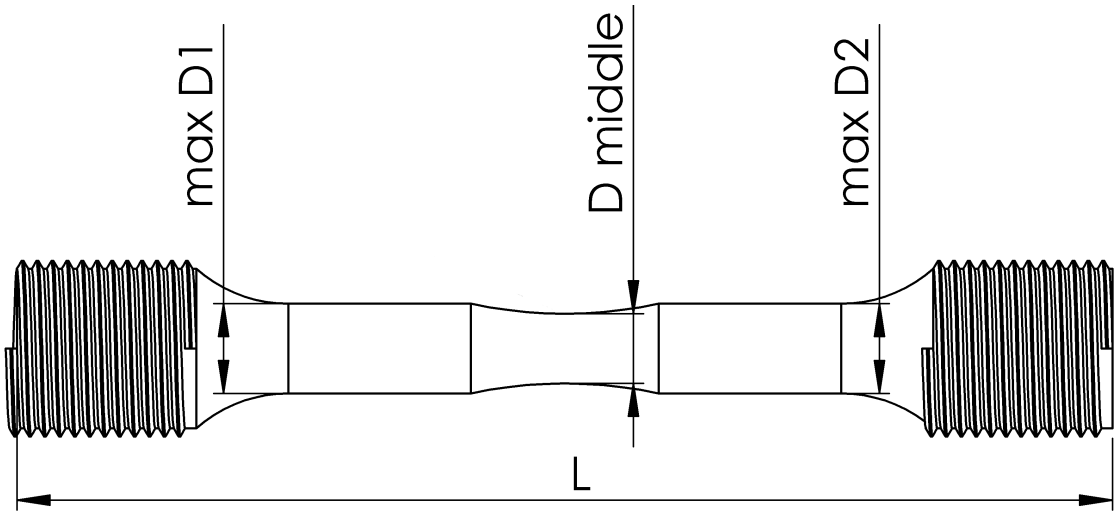


Figure F.0.1: Legend for the dimensions of Table F.0.1

Table F.0.1: Smooth specimens (150 kHz) P1 to P21 dimensions (the average of 3 measurements for each variable)

Specimen -	D middle mm	L mm	max D 1 mm	max D 2 mm
1	109.583	7.063	9.041	9.044
2	109.900	7.013	9.007	9.019
3	110.107	7.054	9.044	9.044
4	109.977	7.020	9.019	9.013
5	109.430	7.064	9.047	9.042
6	109.487	6.989	8.991	8.956
7	109.830	7.073	9.046	9.048
8	110.010	7.065	9.055	9.053
9	109.897	7.060	9.034	9.038
10	109.297	7.060	9.038	9.032
11	110.073	7.037	9.030	9.028
12	109.657	7.039	9.030	9.036

Continued on next page

Table F.0.1: Continued from previous page

Specimen -	D middle mm	L mm	max D 1 mm	max D 2 mm
13	109.683	7.005	9.041	9.042
14	109.543	7.064	9.054	9.051
15	110.023	7.056	9.048	9.043
16	109.507	7.047	9.027	9.023
17	110.143	7.056	9.040	9.035
18	109.677	7.061	9.040	9.031
19	109.873	7.057	9.039	9.032
20	109.567	6.927	8.932	8.909
21	107.883	7.057	9.006	8.973

Table F.0.2: Smooth specimens (150 Hz) P1 to P24 results data

Specimen -	N_f cycles	S_N MPa	Run-out -
Test	1.00E+07	450	Yes
Test	4.70E+05	500	No
P1	7.26E+05	490	No
P2	1.00E+07	420	Yes
P3	8.36E+05	500	No
P4	1.10E+06	490	No
P5	4.78E+06	470	No
P6	9.05E+04	510	No
P7	2.76E+05	510	No
P8	1.19E+07	420	Yes
P9	4.54E+05	510	No
P10	9.75E+05	470	No
P11	1.04E+07	450	Yes
P12	2.07E+06	450	No
P13	3.82E+06	470	No
P14	4.34E+06	450	No
P15	1.55E+07	440	Yes
P16	2.59E+05	520	No
P17	4.45E+05	500	No
P18	1.00E+06	490	No
P19	5.94E+05	470	No
P20	4.52E+05	520	No
P21	6.74E+05	520	No
P22	4.99E+05	520	No
P23	4.99E+06	440	No
P24	2.64E+06	440	No

Table F.0.3: Surface roughness of the smooth specimens (150 kHz) after testing (the average of 3 measurements for each variable)

Specimen	Longitudinal SR			Circumferential SR		
	Ra μm	Rq μm	Rz μm	Ra μm	Rq μm	Rz μm
1	0.026	0.035	0.228	0.288	0.327	1.152
3	0.065	0.083	0.408	0.345	0.464	1.202
4	0.031	0.040	0.251	0.275	0.370	1.597
5	0.060	0.074	0.371	0.107	0.128	0.458
6	0.032	0.040	0.221	0.158	0.177	0.515
7	0.026	0.035	0.216	0.267	0.299	0.825
9	0.026	0.033	0.179	0.103	0.122	0.419
10	0.021	0.026	0.156	0.134	0.153	0.429
17	0.059	0.074	0.360	0.114	0.132	0.423
18	0.026	0.033	0.196	0.231	0.253	0.672
19	0.082	0.100	0.475	0.182	0.218	0.878
Average	0.0413	0.0522	0.2783	0.2005	0.2402	0.7790

Appendix G

Notched specimens (20 kHz) data

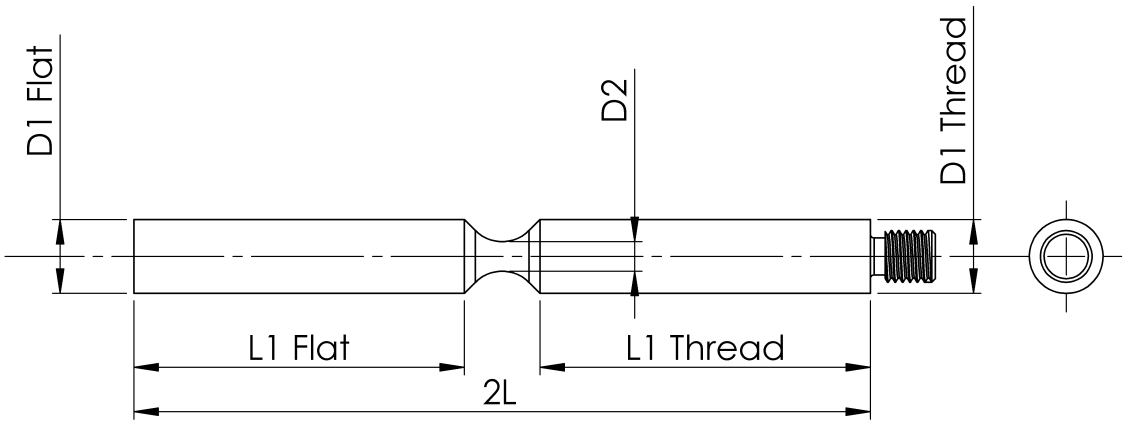


Figure G.0.1: Legend for the dimensions of Table G.0.1

Table G.0.1: Notched specimens $K_t = 1.25$ (20 kHz) P2 to P10 dimensions (the average of 3 measurements for each variable)

Specimen -	Frequency f Hz	D_2 mm	D_1 Thread mm	D_1 Flat mm	L_1 Flat mm	L_1 Thread mm	$2L$ mm
2	19.95	4.000	10.012	10.013	43.44	43.43	97.11
3	19.98	4.013	10.017	10.022	43.52	43.52	97.11
4	19.96	4.015	10.010	10.009	43.59	43.55	97.13
5	19.97	3.990	10.008	10.009	43.55	43.53	97.11
6	19.98	4.004	10.003	10.013	43.58	43.57	97.13
7	19.98	4.000	10.001	10.013	43.56	43.44	97.15
8	-	4.030	10.009	10.013	43.66	43.37	97.16
9	-	4.033	10.015	10.015	43.42	43.49	97.13
10	-	4.035	10.013	10.018	43.39	43.47	97.14

Table G.0.2: Notched specimens $K_t = 1.25$ (20 kHz) P2 to P10 results

Nº -	Polished f Hz	Final f Hz	N -	S_N MPa	S_N by U MPa	Run-out -	T_{on} ms	T_{off} ms
2	19.95	19.95	3.75E+08	460	445	Yes	190	410
3	19.99	19.98	8.03E+05	530	524	No	190	410
4	19.98	19.98	1.11E+07	510	488	No	190	410
5	19.98	19.96	6.78E+06	510	488	No	190	410
6	19.99	19.98	3.88E+06	490	461	No	190	410
7	19.99	19.99	2.24E+06	460	443	No	190	410
8	19.99	19.99	1.51E+06	510	488	No	190	410
9	19.99	20	1.56E+09	460	442	Yes	190	410
10	20	19.99	4.34E+06	490	461	No	190	410

Appendix H

Fatigue limit estimation

Table H.0.1: Constant for the estimation of the fatigue life of the material based on its mechanical properties

	Unit	MUSM	USM	UML		Unit	MM	MMM	MedM
R_m	MPa	819	819	819	R_m	MPa	819	819	819
C_e	-	0.623	1.9018	1.5	σ_f	MPa	1154	1154	1228.5
b	-	-0.09	-0.12	-0.087	b	-	-0.07499	-0.0833	-0.09
d	-	0.832							

	Unit	HM		Unit	M-C 2010	M-C 2015
Hardness	HV/HB	288/266	Hardness	HV/HB	280/266	280/266
b	-	-0.09	σ_f/E	-	0.00612	0.00629
			b	-	-0.0806	-0.08265
			Hardness 1	HB	220	276
			Hardness 2	HB	276	293
Constants to estimate $y = mx + b$			σ_f/E 1	-	0.005	0.006
for the 280 HV parameters			σ_f/E 2	-	0.0063	0.005618
			b 1	-	-0.081	-0.0864
			b 2	-	-0.08	-0.081